Correlating Interfacial Structure and Magnetism in Thin-Film Oxide Heterostructures Using Transmission Electron Microscopy and Polarized Neutron Reflectometry

A Thesis

Submitted to the Faculty

of

Drexel University

by

Steven Richard Spurgeon

in partial fulfillment of the

requirements for the degree

of

Doctor of Philosophy

October 2014

Dedications

This thesis is dedicated to my Lord and Savior Jesus Christ, as well as my wife, Jennifer, and my family—without their love this work would not have been possible.

For now we see in a mirror dimly, but then face to face.
Now I know in part; then I shall know fully,
even as I have been fully known.

1 Corinthians 13:12

Acknowledgments

The past five years have been an immensely rewarding but formidable challenge, an emotional and intellectual whirlwind with calm skies rarely in sight. The research presented in this thesis would not have been possible without the support of my colleagues, friends, and family. It has been a privilege to work with my advisor, Mitra Taheri, whose wit and wisdom have guided me throughout my work. I am indebted to the many past and present members of our research group, including Chris Winkler, Greg Vetterick, Ian McDonald, Chris Barr, Matt Hartshorne, Katie Jo Sunday, James Hart, and others. I am also fortunate to have been financially supported by both NSF IGERT and DoD NDSEG Fellowships.

Knowledge is not forged in quiet isolation but in the fiery furnace of debate and criticism. I have received guidance from many brilliant and helpful scientists, including Brian Kirby, Sam Lofland, Steve May, James Rondinelli, Craig Jonson, Ed Basgall, Jonathan Spanier, Quentin Ramasse, Demie Kepaptsoglou, Prasanna Balachandran, Rebecca Sichel-Tissot, Eun Ju Moon, Mark Scafetta, Babak Anasori, Philipp Hunger, Amalie Donius, Darin Tallman, Guannan Chen, Min Hyun, and others.

The doctoral process has been tremendously humbling; it is a relentless diminishing of the self that culminates in an acute awareness of just how much one needs others. Over the years I have come to depend on the kindness, encouragement, and advice of my friends, who helped me move forward when I alone could not. These include Terry Shyu, Dennis Watson, Cliff Kang, Anita Lai, Micky Kim, Emily Schutsky, Dan Kim, Eddie and Sharon Sharick, Paul Tzen, Susie Cha, Brian Pyles, and others.

Finally, I am most thankful for the love of my wife, Jennifer, my brother, Justin, and my parents, Richard and Brigitte. At every stage of this process they have been ceaselessly supportive and understanding. They filled me up after I had poured myself out time and time again, and they spurred me on to run the race set before me. For these manifold blessings, both seen and unseen, I am eternally grateful.

Steven R. Spurgeon

Philadelphia, PA

Table of Contents

List of Tables

List of Figures

Abstract

Correlating Interfacial Structure and Magnetism in Thin-Film Oxide Heterostructures Using Transmission Electron Microscopy and Polarized Neutron Reflectometry
Steven Richard Spurgeon
Mitra L. Taheri

Oxide thin-films have attracted considerable attention for a new generation of spintronics devices, where both electron charge and spin are used to transport information. However, a poor understanding of the local features that mediate magnetization and coupling in these materials has greatly limited their deployment into new information and communication technologies. This thesis describes direct, local measurements of structure-property relationships in ferrous thin-films and $La_{1-x}Sr_xMnO_3$ (LSMO) / $Pb(Zr_xTi_{1-x})O_3$ (PZT) thin-film heterostructures using spatially-resolved characterization techniques.

In the first part of this thesis we explore the properties of ferrous spintronic thin-films. These films serve as a model system to establish a suite of interfacial characterization techniques for subsequent studies. We then study the static behavior of LSMO / PZT devices with polarization set by the underlying substrate. Using transmission electron microscopy and geometric phase analysis we reveal the presence of significant local strain gradients in these films for the first time. Electron energy loss spectroscopy mapping of the LSMO / PZT interface reveals Mn valence changes induced by charge-transfer screening. Bulk magnetometry and polarized neutron reflectometry indicate that these chemical and strain changes are associated with a graded magnetization across the LSMO layer. Density functional theory calculations are presented, which show that strain and charge-transfer screening act locally to suppress magnetization in the LSMO by changing the Mn orbital polarization.

In the second half of this thesis, we explore asymmetric screening effects on magnetization LSMO / PZT composites. We find that the local ferroelectric polarization can vary widely and that this may be responsible for reduced charge-transfer effects, as well as magnetic phase gradients at interfaces. From this information and electron energy loss spectroscopy, we construct a map of the magnetic phases at the interface. Collectively these results show that we must move toward high-resolution local probes of structure and magnetism to achieve deterministic control of functional thin-film oxides.

Chapter 1: Introduction

1.1 Motivation

The field of spintronics promises to revolutionize the design of electronics, enabling more robust and efficient computing architectures. Spintronics devices utilize both electron spin and charge to convey information in the solid-state.[1] The advantages of solid-state electrically-switched magnetic memory are numerous: such memory is predicted to have faster access times, higher rewritability, reduced energy consumption, and no chance of mechanical failure.[2] Designers have already envisioned other devices such as spin switches that enable tuning of spin polarization under the application of an electric current, but candidate materials for such devices are still being actively pursued.[3] Thin-film heterostructures deposited using advanced growth techniques, such as molecular beam epitaxy and pulsed laser deposition, show great potential for these applications.[4,5] These techniques make it possible to deposit a ferromagnet onto a ferroelectric substrate with atomic level precision and control. Coupling between the two layers can be achieved through several mechanisms, including piezoelectric strain of a substrate lattice-matched to a piezomagnetic layer, exchange bias between ferromagnetic and antiferromagnetic multiferroic layers, as well as charge screening at ferromagnet-dielectric interfaces.[6–8] The coupling between magnetic and electronic order is broadly termed magnetoelectricity. As the size of thin-film systems converges on the characteristic length scales of physical phenomena such as magnetic exchange, new and poorly understood physics begins to emerge. Symmetry breaking at interfaces is also responsible for induced changes in interfacial electronic structure and magnetic order. Artificial heterostructures have opened up an entirely new field of research, since even minor changes in local structure and chemistry can have profound effects on magnetoelectric coupling.[9,10]

The use of artificial magnetoelectric heterostructures in solid-state memory technology is currently hindered by a poor understanding of the atomic-scale structural, chemical, and magnetic features that mediate magnetoelectricity. Transmission electron microscopy offers a simultaneous high spatial resolution probe of interface structure and chemistry; this wealth of information can be combined with

bulk magnetometry and interface-sensitive polarized neutron reflectometry to produce a complete understanding of heterostructure behavior. This static characterization will provide the framework to understand dynamic behavior in simplified device structures, leading to deterministic control of coupling behavior and device performance. More broadly, the methods and suite of characterization techniques assembled for this study can be applied to structure-property studies of other nanoscale magnetic systems.

1.2 Organization of the Thesis

This thesis is organized into the following structure:

Background In this chapter we introduce the concept of spintronics and discuss the various oxide materials that have been pursued for such applications. We describe the magnetic and ferroelectric properties of these materials, as well as the phenomenology of magnetoelectricity. We conclude with a discussion of coupling mechanisms in artificial magnetoelectric heterostructures and a summary of the current challenges in the field.

Techniques and Methods In this chapter we describe the techniques and methods used in the course of this work. These techniques may be broadly divided into structural and magnetic characterization. We explain the complementary approach of electron microscopy and neutron scattering and the insights to be gained from local probes.

Interface Effects on Magnetization in Ferrous Thin-Films In this chapter we describe our preliminary studies of Fe / MgO thin-film bilayers for spintronic applications. We use this as a model system to assemble a comprehensive set of structural and magnetic characterization techniques to correlate structure and magnetism in thin-films. This chapter lays the groundwork for the subsequent studies described in this thesis.

Substrate-Induced Polarization Effects in LSMO / PZT In this chapter we discuss the artificial magnetoelectric heterostructure LSMO / PZT. Using a substrate-controlled poling technique, we induce different charge and strain states at the interface in this system. We then characterize local

structure, chemistry, and strain state, which we correlate to magnetic properties, to develop a comprehensive model for magnetoelectric coupling in these materials.

Screening-Induced Magnetic Phase Gradients at at LSMO / PZT Interfaces In this chapter we use electron energy loss spectroscopy to directly visualize the charge-transfer effect and its asymmetry with polarization at interfaces in LSMO / PZT. We map the local electronic and magnetic phases at the interface and argue that device designs must account for this asymmetric behavior.

Conclusions and Future Work In this chapter we summarize the primary findings of this thesis. We explain how this informs a more complex and comprehensive model of coupling in spintronic systems, and we suggest avenues for future study.

Appendix A: Strain Effects on Magnetization in Ferrous Thin-Films In this chapter we discuss ongoing studies of ferrite bilayers, in which we disentangle strain and chemical effects on magnetization.

Appendix B: Interface Effects on Magnetization in Ferrous Thin-Films In this chapter we discuss the methods used in our study of interface effects on magnetization in ferrous thin-films.

Appendix C: Substrate-Induced Polarization Effects in LSMO / PZT In this chapter we provide further details on bulk magnetometry, ferromagnetic Curie temperature measurements, and our polarized neutron reflectometry analysis.

Appendix D: Screening-Induced Magnetic Phase Gradients at LSMO / PZT Interfaces In this chapter we discuss our measurements of local ferroelectric polarization in detail. We describe EELS and XPS measurements, as well as the details of our DFT calculations.

Chapter 2: Background

2.1 Introduction

In this section we first discuss the emerging field of spintronics and summarize the properties of the materials studied in this thesis. Structure-property relationships in the ferrous and manganite systems are discussed; we then introduce the concept of magnetoelectricity and describe its theoretical and physical underpinnings. We next describe the phenomenology of artificial magnetoelectric (ME) heterostructures and the coupling modes operating in these materials. Finally we conclude with a discussion of the current challenges in the field and the motivation for the present work.

2.2 Spintronics and Device Applications

For the past hundred years the electronics paradigm has relied on the transport of charge through a device to convey logic. This paradigm has enabled many of the ubiquitous technologies we use today, including the integrated circuit and radio communications. Until recently only the charge of the electron was put to use in such devices; the electron spin was almost completely neglected. In the late 1980s this changed with the discovery of giant magnetoresistance (GMR) by Albert Fert and Peter Grünberg.[11,12] The authors synthesized a thin-film trilayer consisting of a non-magnetic Cr spacer sandwiched between two ferromagnetic (FM) thin-film Fe layers; by tuning the thickness of the Cr layer they showed it is possible to switch the coupling of the Fe layers from FM to antiferromagnetic (AF).[12] This AF ordering results in a high resistance state, because both spin states of conduction electrons travel the same mean free path. By applying an external magnetic field the Fe layers can again be FM coupled, inducing a low resistance state by increasing the mean free path of one spin state, as shown in Figure 2.1.[13] Fert and Grünberg received the 2007 Nobel Prize for their work, although the connection between electron spin and conduction had been discussed and demonstrated decades before by Mott *et al.*[14–16]

The discovery of GMR spurred the development of advanced, high-density hard disk storage technologies.[17] At the same time advances in thin-film growth and atomic-scale characterization gave re-

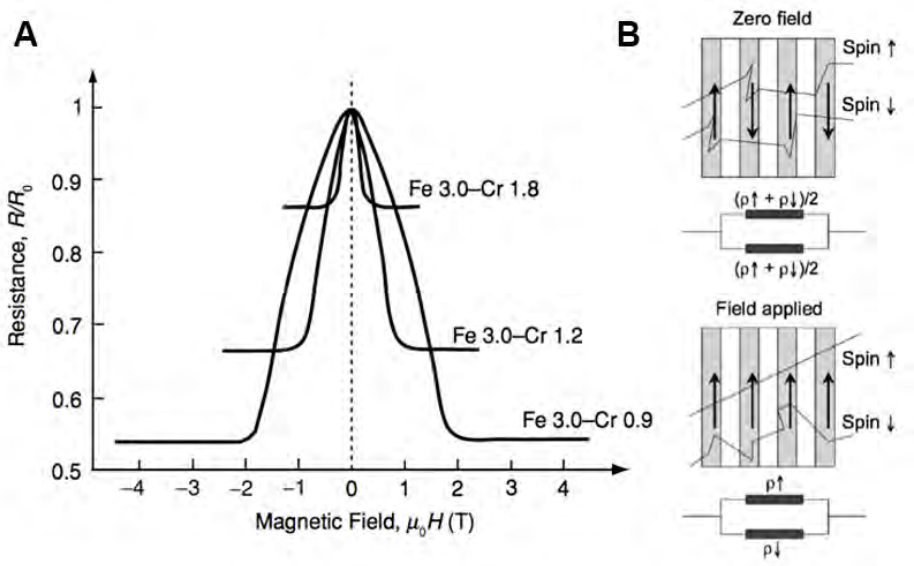

Figure 2.1: (A) Increase in resistance caused by increasing Cr spacer thickness, resulting from a transition from FM to AF coupling. (B) Illustration of the GMR effect, in which a high-resistance AF state is tuned to a low-resistance FM state by the application of an external magnetic field.[13,15]

searchers unprecedented synthesis and analysis capabilities.[18,19] This fortunate confluence of events sparked renewed interest in the connection between spin and charge, giving birth to the field of spintronics. This field, broadly described in Figure 2.2, encompasses many devices and materials systems. Many new kinds of devices based on spintronics have been proposed, including racetrack memory and spin valves.[17] While not all of these have come to fruition, each has furthered the understanding of basic physics and paved the way for successive generations of devices. Among the most promising of these devices, MEs have recently attracted considerable attention, since they offer the potential to tune magnetization directly by applying an electric field. These materials and their properties are the focus of this thesis.

2.3 Functional Thin-Film Oxides

The class of thin-film oxides spans a range of diverse functionalities, structures, and properties. These materials are used in many of the important devices we interact with each day, including hard drives, integrated circuits, transducers, and other logic devices. Their drive to the forefront of materials science has been enabled by novel growth techniques and improved characterization methods. Here we focus

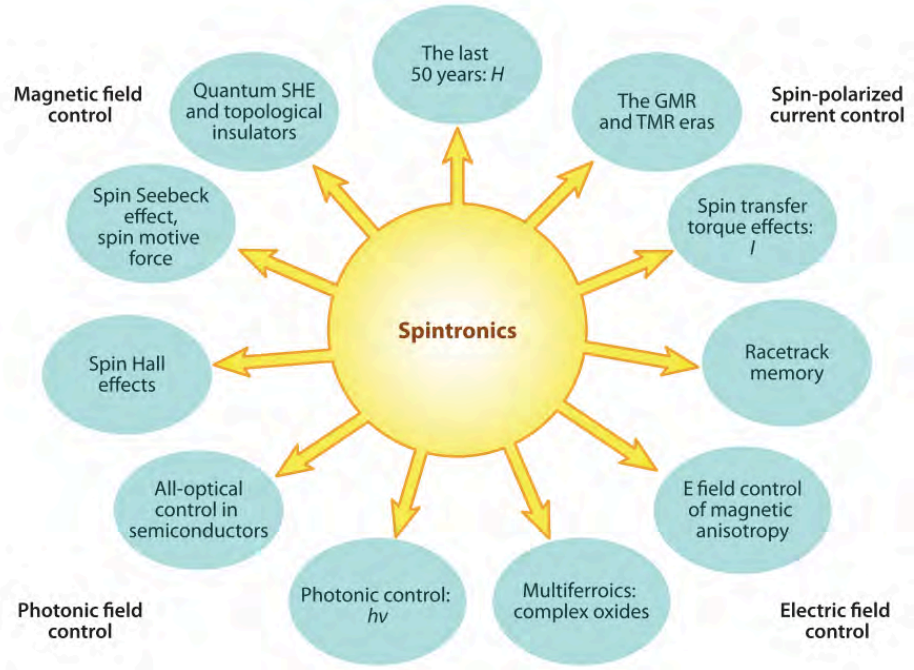

Figure 2.2: Overview of the many facets of spintronics technologies. Of particular interest in this thesis is electric field control of magnetization.[17]

on three classes of oxides: namely, iron oxides, the rare-earth manganites, and the lead titanates. These systems have attracted considerable attention for the next generation of spintronic memories and are a playground for exploring novel phenomena at interfaces.

2.3.1 Ferrous Thin-Film Oxides

Iron and iron oxides are among the oldest known magnetic materials: magnetite-rich lodestone was used in the first compasses developed by the Chinese as early as the 11th century.[13] Iron and its alloys have found widespread use in electromagnetic cores for transformers and motors, magnetic tape for data storage, and more. Most recently, with the advent of advanced thin-film growth techniques, it has become possible to synthesize highly pure Fe thin-films. Heterostructures of Fe and MgO exhibit very large tunneling magnetoresistive (TMR) properties that are well-suited for use in hard drive read heads and other sensing applications.[20–22] Monolayer-thin Fe films display a significantly enhanced magnetization that may be tuned by the application of an electric field and shows promise for ME logic.[23,24] By understanding the structure-property relationships in this system, we will be able to engineer materials

for the next generation of spintronics devices.

Structure of Ferrous Thin-Films

In the last few decades advanced deposition techniques have been used to fabricate increasingly pristine iron films, with precise control over stoichiometry and film structure. Atomic Fe has an electronic configuration (Ar) $3d^6 4s^2$, with four unpaired $3d$ electrons yielding a magnetic moment of 4 μ_B; however, in a solid, crystal-field splitting leads to the formation of a broad $4s$ band and a narrow $3d$ band. Charge transfer between the $4s \rightarrow 3d$ bands results in a net (Ar) $3d^{7.4} 4s^{0.6}$ configuration.[13] Below a critical temperature of 1044 K, α-Fe assumes a body-centered cubic (BCC) structure with nearly perfectly paired inner- and $4s$ shells. The $3d$ band configuration is $3d^{\uparrow 4.8} 3d^{\downarrow 2.6}$, resulting in a net magnetic moment of 2.2 μ_B.[13] This magnetic ordering is highly sensitive to lattice strain, oxidation state, and surface morphology—Table 2.1 shows the diversity of ordering types for different ferrous compounds.

Table 2.1: Magnetic ordering of various ferrous compounds.[13]

Ordering Type	Compound	Magnetic Moment (μ_B)
Ferrimagnet	γ-Fe_2O_3	5.0
Ferromagnet	α-Fe	2.2
	YFe_2	1.45
Antiferromagnet	γ-Fe	Unstable
Pauli Paramagnet	YFe_2Si_2	0
Diamagnet	FeS_2	0

To induce these different magnetic states, Fe has been grown on a range of substrates, including Si (001), GaAs (001), and MgO (001).[25–27] In the case of MgO (001), there is a mismatch between BCC α-Fe ($Im\bar{3}m \mid a = 2.87$ Å) and rocksalt MgO ($Fm\bar{3}m \mid a = 4.22$ Å) lattice parameters, resulting in 45° in-plane rotation during growth.[27] This epitaxial relationship $\big(\text{Fe}\,[100](001) \parallel \text{MgO}\,[110](001)\big)$, shown in Figure 2.3, leads to an approximately 3.8% in-plane tensile strain. Although this strain is small, it can lead to the formation of islands instead of a continuous film during growth. By varying the deposition conditions it is possible to control the morphology and structure of these films, ranging from discrete nanoscale islands (Volmer-Weber) to continuous films, or mixed island-film (Stranski-Krastanov) structures.[27–29]

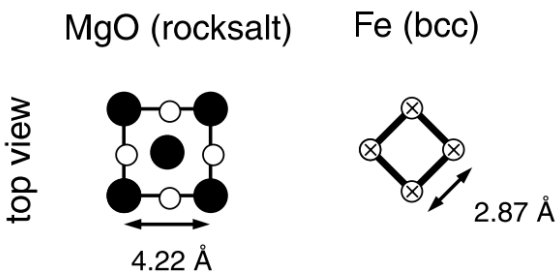

Figure 2.3: Illustration of the Fe [100](001) || MgO [110](001) epitaxial growth relationship between BCC α-Fe and rocksalt MgO (001).[27]

Magnetic Structure-Property Relationships

While an all-encompassing discussion of thin-film magnetism is beyond the scope of the present work,* it is worthwhile to consider the effect of the aforementioned film morphology changes on the magnetization of ferrous thin-films. The properties of these materials often differ markedly from the bulk and show a dependence on nanostructuring.[31] This can be understood by considering the expansion of the magnetocrystalline anisotropy (MCA),

$$\frac{E_a}{V} = K_1 \sin^2\theta + K_2 \sin^4\theta + K_2' \sin^4\theta \cos 4\phi + K_3 \sin^6\theta + K_3'' \sin^6\theta \cos 4\phi \tag{2.1}$$

where K_1 is the uniaxial anisotropy constant, $K_2 - K_3$ are higher-order anisotropy constants that depend on crystal symmetry, and θ is the relative orientation of the crystal and applied field.[32] Examples of the calculated energy surfaces for cubic FMs are shown in Figure 2.4. It is clear that modification of the crystal symmetry, by abrupt termination at a surface or the introduction of surface roughness for instance, will affect this anisotropy. The demagnetizing fields associated with roughness will act to impose a uniaxial anisotropy, the relative contribution of which scales inversely with film thickness ($t \propto d^{-1}$).[33] Precise control of interfaces and roughness may then be used as a means to tune the MCA and fundamental magnetic hysteresis of ferrous thin-films. Achieving this control necessitates an integrated, atomic-scale approach to materials fabrication and characterization of structure and magnetic properties.

*The interested reader is referred to Falicov *et al.* for more information.[30]

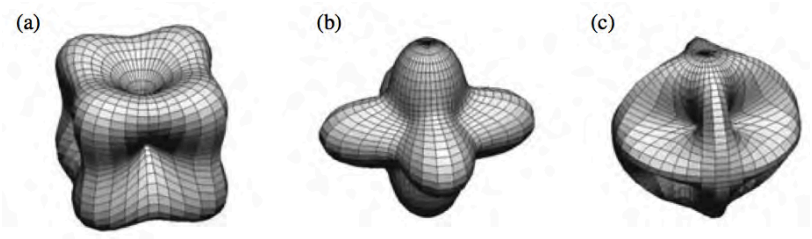

Figure 2.4: Example of the energy surfaces for various cubic ferromagnet systems.[32]

2.3.2 Rare-Earth Manganites

In the past two decades the field of oxide chemistry has been dominated by studies of superconducting cuprates and colossal magnetoresistive materials, such as the doped manganites ("Re"$_{1-x}$"A"$_x$$MnO_3$, where "Re" is a rare-earth such as La and "A" is a divalent cation such as Sr or Ca).[34] These compounds can be grown with high purity and may be readily interfaced into precise, atomically-sharp heterostructures. The magnanites are notable for the rich variety of electronic and magnetic phases they exhibit, as well as their tunability by strain, charge, chemical doping, and other stimuli.[35] They have been studied for a range of applications, including magnetic memory, photovoltaics, fuel cells, and thermoelectrics.[36] The magnetic "attraction" of the manganites arises from the various kinds of exchange coupling they exhibit—namely, super exchange and double-exchange—and the intimate connection between these coupling modes and local structure.[35–37] Understanding and controlling these interactions by coupling the manganites to other systems is the focus of this thesis.

Structure of the $La_{1-x}Sr_xMnO_3$ Compounds

Of all the manganites, $La_{1-x}Sr_xMnO_3$ (LSMO) in particular has attracted much attention, because of its large bandwidth, high Curie temperature, and the potential to induce first-order electronic phase transformations through controlled doping and strain modulation.[37,38] This compound can be understood as a solid solution of the end members $LaMnO_3$ (LMO) and $SrMnO_3$ (SMO), with formal valences $La^{3+}Mn^{3+}O_3^{2-}$ and $Sr^{2+}Mn^{4+}O_3^{2-}$, which yields a mixed-valence state $(La^{3+}_{1-x}Sr^{2+}_x)(Mn^{3+}_{1-x}Mn^{4+}_xO_3)$.[37] LSMO is part of the perovskite class, which is able to accommodate lattice distortions by lowering its symmetry from cubic to rhombohedral, tetragonal, orthorhombic, and monoclinic phases.[35] This results

from two effects, namely the Jahn-Teller distortion and the size mismatch between *A*-site cations. The former lifts the orbital degeneracy of the $Mn^{3+}O_6$ octahedra, concomitant with a tetragonal elongation of the lattice along the z direction; this distortion acts to stabilize the occupancy of the lowest e_g orbital.[35] The latter effect arises from internal chemical pressure in the lattice, which responds by cooperative rotations and tilting of MnO_6 octahedra. This is described by the Goldschmidt tolerance factor,

$$t = \frac{r_A + r_O}{\sqrt{2}(r_B + R_O)} \tag{2.2}$$

where r_A, r_B, and r_O are the ionic radii of the A, B, and O species, respectively.[39] The end member LMO possesses an orthorhombic *Pnma* structure, which consists of six-fold coordinated rare-earth La cations at corner positions and body-centered Mn ions surrounded by oxygen octahedra; the crystal field splits the five Mn 3*d* orbitals into a t_{2g} triplet and e_g doublet state.[40–42] This structure, shown in Figure 2.5, possesses an electron configuration of $t_{2g}^3 e_g^1$; in this configuration the t_{2g}^3 ($S = 3/2$) electrons may be considered localized because of poor hybridization with O 2*p* states, while the e_g^1 electron ($S = 1/2$) is strongly hybridized and may be itinerant or localized.[35,43–45] Controlled doping of divalent Sr^{2+} ions for La^{3+} ions in LMO causes an effective increase in the proportion of Mn^{4+} ions, introducing itinerant holes in the e_g state and inducing a phase transition to an rhombohedral $R\bar{3}c$ structure. This charge doping sensitivity results in a rich variety of magnetic and electronic phases, as shown in Figure 2.6, ranging from a charge-ordered insulating state at low Sr doping and temperatures to an AF metallic state at Sr doping in excess of x ≈ 0.5.[36] Below x ≈ 0.5 doping the $t_{2g}^{\uparrow}$ band is fully occupied, while the $e_g^{\uparrow}$ band is only partially occupied. The O 2*p* states, however, are fully occupied and their hybridization with the Mn e_g states determines the electronic structure near the Fermi level. Because of the band gap between the minority spin states and the O 2*p* band, the spin-polarized density of states only has majority carriers at the Fermi level and LSMO is considered a half-metal.[35]

Exchange Mechanisms in the Manganites

The diverse array of phases shown in Figure 2.6 results from two kinds of magnetic exchange interactions: superexchange and double-exchange. Both of these mechanisms depend on the occupancy and

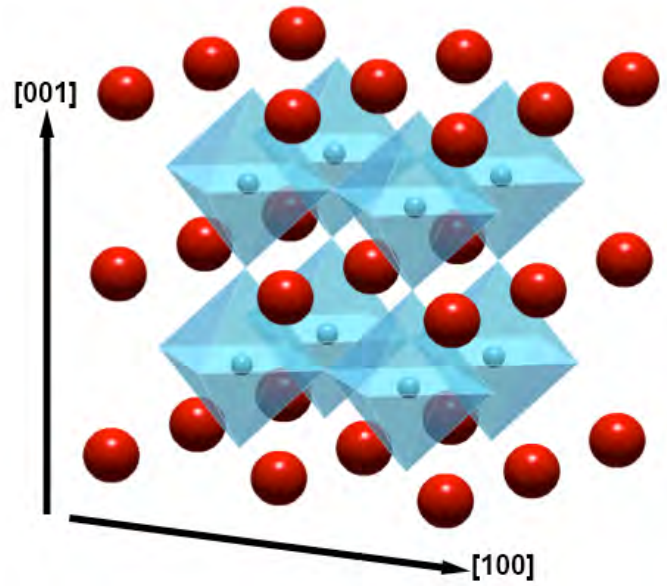

Figure 2.5: Schematic of the $LaMnO_3$ *Pnma* parent perovskite structure. La atoms are shown in red, Mn atoms are shown in light blue, and O octahedra are shaded.

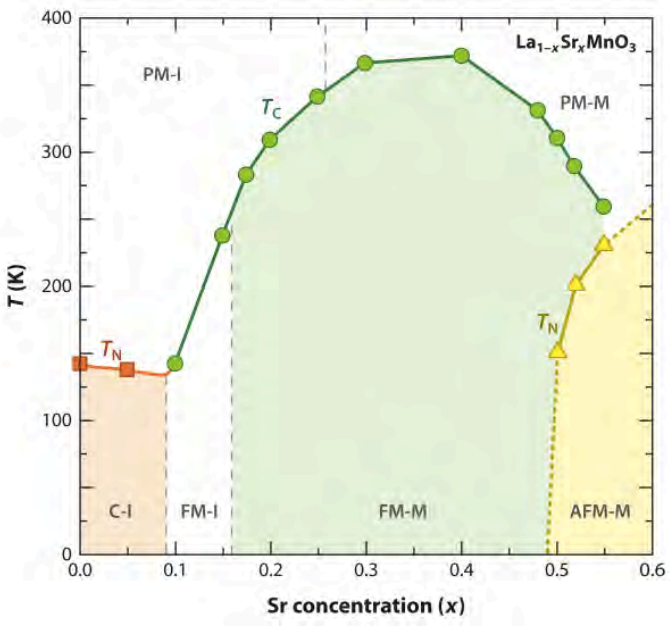

Figure 2.6: Bulk phase diagram of the $La_{1-x}Sr_xMnO_3$ system. I = Insulating, M = Metallic, PM = Paramagnetic, FM = Ferromagnetic, AFM = Antiferromagnetic, and C = Charge-ordered phases.[36]

orbital degeneracy of the 3d states and are mediated by O 2p orbitals. In superexchange a singly-occupied 3d orbital gives rise to the virtual transfer of two electrons and the spread of electrons from O 2p orbitals to unoccupied Mn 3d orbitals.[13] This results in a lower energy AF spin configuration, as shown in Figure 2.7, as is the case for *monovalent* LMO and SMO compounds.

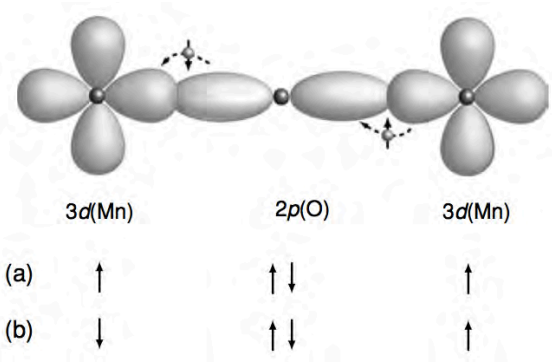

Figure 2.7: Model of superexchange coupling in monovalent manganites. The top shows the hybridization of O 2p and Mn 3d states, while the bottom shows ferromagnetic (a) and antiferromagnetic (b) spin configurations, the latter of which is lower energy because it promotes increased $2p-3d$ hybridization.[13]

If a compound takes a *mixed-valence* state through the doping of divalent Sr^{2+} ions, on the other hand, the double-exchange mechanism will generally give rise to long-range FM ordering, as shown in Figure 2.8. Although the 3d core electrons are localized in a narrow $t_{2g}^{\uparrow}$ band, FM ordering occurs because the fourth d electron occupies a hybridized $e_g^{\uparrow}$ band with O. This hybridization permits hopping from core to core through the $2p-3d$ bonds. When core spins are parallel this hopping is unrestricted, but when they are antiparallel Hund's coupling impedes hopping and imposes a large barrier to delocalization.[13,37,46]

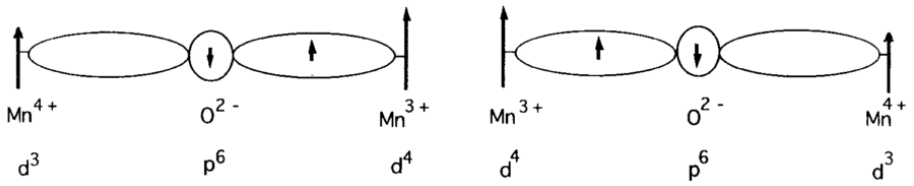

Figure 2.8: Model of double-exchange coupling in mixed-valence manganites. On-site Hund coupling gives rise to parallel alignment of hybridized $e_g^{\uparrow}$ electrons, leading to long-range ferromagnetic order.[37]

As would be expected, this coupling is highly sensitive to the Mn–O–Mn bond angle. The spin-

dependent hopping resonance integral governing this interaction is given by,

$$d_{ij} \approx \epsilon_\sigma \lambda_\sigma^2 \cos\theta \cos\phi / 2 \tag{2.3}$$

where ϵ_σ is the one-electron energy, λ_σ is the covalent-mixing parameter between Mn e_g orbitals and the O $2p$ orbitals, $(180^\circ - \theta)$ is the Mn–O–Mn bond angle, and ϕ is the angle between spins on adjacent Mn^{3+} and Mn^{4+} ions.[35,47] Chemical modifications to the effective Mn valence will greatly affect this coupling, as will any structural distortion that changes bond angles or orbital overlap. Data compiled by various groups show that there is a clear doping dependence on magnetic and electronic order in the system.[44,48,49] The application of strain through constrained epitaxial growth can also tune the electrical resistivity and FM Curie temperature of the manganites.[6,50–53] Recently the reversible tuning of this strain using piezoelectric sbustrates has been demonstrated with great success.[54–58] These features offer various handles to tune the magnetic properties of the manganites, making them quite attractive for device applications.

2.3.3 Piezoelectric Lead Titanates

Piezoelectrics, materials which develop an electrical polarization under the application of strain, are among the most prolific oxide materials. They find use in applications as diverse as transducers, sensors, microgrippers, energy harvesting, and medicine.[59] Although $BaTiO_3$ (BTO) was the first ceramic material in which ferroelectricity was discovered, in the 1950s solid solutions of $Pb(Zr_xTi_{1-x})O_3$ (PZT) were also found to be ferroelectric (FE)—they soon became the dominant piezoelectric system.[60] In recent years there has been a push toward more environmentally-friendly, Pb-free compounds, but PZT is still highly prized for its large piezoelectric coefficient and is used in the present work.

Structure of the $Pb(Zr_xTi_{1-x})O_3$ Compounds

$Pb(Zr_xTi_{1-x})O_3$ is the most ubiquitous of the piezoelectrics because of its high piezoelectric and coupling coefficients, which were first measured by Berlincourt *et al.* in the 1950s.[61] At high temperatures it possesses a cubic $Pm\bar{3}m$-type structure, but at lower temperatures it is generally rhombohedral $R3c$, tetragonal $P4mm$, or monoclinic Cm.[62–64] The cubic PZT structure is similar to that of LSMO, albeit with

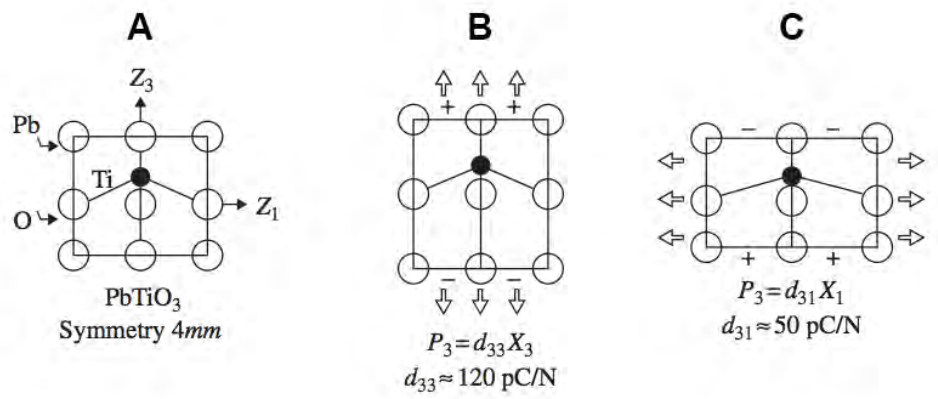

Figure 2.9: (A) Spontaneous dipole formation in $PbTiO_3$ by off-centering of the Ti^{4+} cation. (B, C) show enhancement of this dipole by the application of external stress.[63]

Pb atoms at the corner positions and Zr / Ti atoms occupying the octahedral positions. Spontaneous off-centering of the Ti^{4+} cation breaks the centrosymmetry of the cubic structure at low-temperatures and results in a dipole; this dipole may be enhanced by the application of stress, as shown in Figure 2.9, particularly in the vicinity of the morphotropic phase boundary (MPB).[63] Alternatively, an electric field may be applied to strain the lattice by further displacing the charge center in the crystal.

In particular, near the MPB ($0.455 \leq x \leq 0.48$), there is a symmetry-breaking transition from rhombohedral to tetragonal phases, with a concomitant rotation of FE polarization (Figure 2.10).[60,63,65] The FE polarization vectors in rhombohedral PZT intersect at 71° and 109°, giving rise to domain walls on {110} and {100} planes. Alternatively, the vectors in the tetragonal phase intersect at 90°, giving rise to walls on {110} planes.[66] The piezoelectric strain has been shown to lie along the directions of the monoclinic distortion instead of the polar axis, which explains PZT's exceptional electro-mechanical properties around the MPB.[67]

The Piezoelectric Effect

The piezeoelectric effect relates polarization (a vector) to stress (a second rank tensor) as,

$$\mathbf{P_j} = d_{jkl} \hat{X}_{kl} \tag{2.4}$$

where $\mathbf{P_j}$ is the polarization, $\hat{X}_{kl}$ is the stress tensor, and d_{jkl} is the general piezoelectric coefficient.[63]

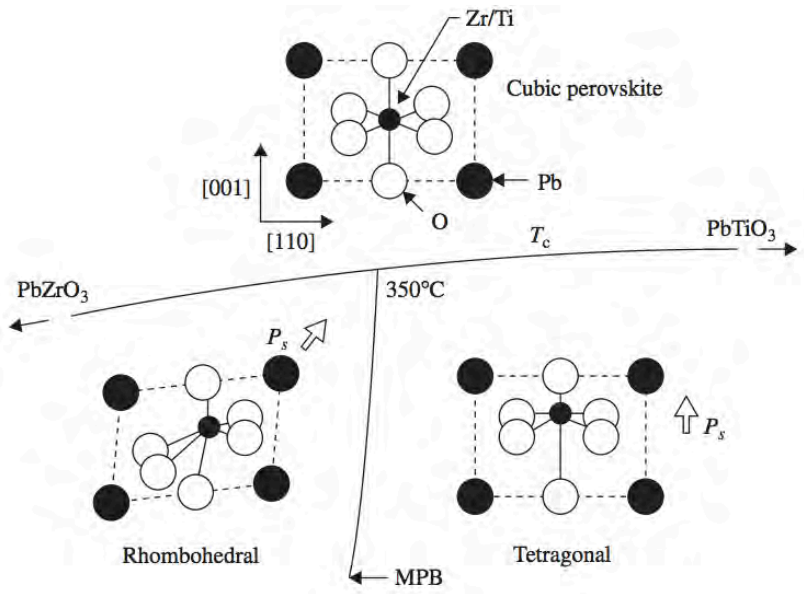

Figure 2.10: Phase diagram of the PZT system, showing the morphotropic phase boundary (MPB) near x ≈ 0.46, as well as the rotation of the polarization direction during the symmetry-breaking rhombohedral-to-tetragonal phase transition.[63]

Equation 2.4 can be transformed to a different coordinate system, yielding a polar third rank tensor for the piezoelectric coefficient,

$$\hat{d}'_{imn} = a_{ij} a_{mk} a_{nl} d_{jkl} \tag{2.5}$$

The symmetry of this stress tensor reduces an initial 27 components to only 18 independent components, which may be expanded as,

$$\begin{pmatrix} P_1 \\ P_2 \\ P_3 \end{pmatrix} = \begin{pmatrix} d_{11} & d_{12} & d_{13} & d_{14} & d_{15} & d_{16} \\ d_{21} & d_{22} & d_{23} & d_{24} & d_{25} & d_{26} \\ d_{31} & d_{32} & d_{33} & d_{34} & d_{35} & d_{36} \end{pmatrix} \begin{pmatrix} X_1 \\ X_2 \\ X_3 \\ X_4 \\ X_5 \\ X_6 \end{pmatrix} \tag{2.6}$$

From thermodynamic arguments it can be shown that the direct and converse piezoelectric effects are

equal. Moreover, according to Neumann's Principle, the piezoelectric matrix must remain invariant after applying the symmetry of a particular space group.[63] Applying this requirement to the 32 crystal classes and seven Curie groups yields only a limited number of systems that can support piezoelectricity, all of which are noncentrosymmetric and polar.[63] PZT's figure-of-merit (d_{33}) easily surpasses its rivals, as shown in Table 2.2.

Table 2.2: Piezoelectric coefficient (d_{33}) for various compounds.[63]

Material	**Crystal Symmetry**	d_{33} **(pC N^{-1})**
ZnO	$6mm$	12.4
$PbTiO_3$	$4mm$	117
$LiNbO_3$	$3m$	16
$PbNb_2O_6$	$mm2$	60
PZT-5H	∞m	593

From the piezoelectric matrix it is clear that the application of a mechanical stress will affect particular components of the matrix. For instance, the application of tensile stress parallel to the dipole along the [001] direction in Figure 2.9.B enhances the d_{33} component, while tensile stress perpendicular to the dipole along the [100] direction in Figure 2.9.C enhances the d_{31} component.[63] Thus, there is a clear need to understand the relationship between FE polarization, crystal orientation, and the stress-strain response of piezoelectrics.

2.4 Magnetoelectricity

In the past several decades MEs and multiferroics have captivated the oxides community. Research into these materials has been spurred by advances in thin-film growth techniques; these improvements have enabled single atomic layer control of perovskites, which can be layered into precise epitaxial heterostructures with unprecedented levels of control over strain and chemistry.[34] At the same time, aberration-correction has become routine in transmission electron microscopy and it now possible to characterize structure, defects, and chemistry in the oxides down to the picometer level.[68] It is now possible to couple phenomena in these thin-films at interfaces to unlock novel functionalities not found in nature.[36,69,70] This rapidly changing landscape offers a rich and fertile ground for the materials scientist to ply his trade.

2.4.1 The Magnetoelectric Effect

Magnetoelectrics are a source of fascination for both practical and fundamental reasons. Many new kinds of ME logic devices have been proposed, including magnetic tunnel junctions (MTJs) with a ME active layer, as well as devices in which an electric field is used to directly tune magnetization.[7,71] Fundamentally these compounds show promise because of the cross-coupling between magnetization and an applied electric field, even in the absence of a spontaneous polarization.[72] The genesis of magnetoelectricity can be traced back to Röntgen and Curie, who in the 1880s–1890s discussed the magnetization of a moving dielectric in a magnetic field, as well as the symmetry requirements for ME in a crystal.[10,73,74] Debye first used the term "magnetoelectric," but he did not have much success in demonstrating the effect.[75] Single-phase MEs were not discovered until researchers fully understood the implications of time-reversal symmetry-breaking, first described by Curie.[74] Dzyaloshinskii discussed time-reversal symmetry-breaking in Cr_2O_3 and subsequent experimental measurements confirmed the coupling, albeit weak, between magnetization and polarization.[10,76–78] This was followed by the discovery of a number of other ME systems, including Ti_2O_3, $GaFeO_3$, the boracites, and $PbFe_{0.5}Nb_{0.5}O_3$.[79–82] While many more single-phase MEs have since been found, they all suffer from a rather weak coupling between polarization and magnetization.[10]

To better understand this, we must first describe the energetics of the ME effect. The free energy of a ME system is given by,

$$\begin{aligned}\mathscr{F}(\mathbf{E},\mathbf{H}) = F_0 - P_i^S E_i - M_i^S H_i - \frac{1}{2}\epsilon_0\epsilon_{ij}E_iE_j - \frac{1}{2}\mu_0\mu_{ij}H_iH_j \\ -\alpha_{ij}E_iH_j - \frac{1}{2}\beta_{ijk}E_iH_jH_k - \frac{1}{2}\gamma_{ijk}H_iE_jE_k - \cdots\end{aligned} \tag{2.7}$$

where $\mathbf{E}$ and $\mathbf{H}$ are the electric and magnetic fields, respectively. $\mathbf{P}^S$ and $\mathbf{M}^S$ are the spontaneous polarization and magnetization, respectively. $\hat{\epsilon}$ and $\hat{\mu}$ are the electric and magnetic susceptibilities. Finally, $\hat{\alpha}$ corresponds to the linear ME tensor, while $\hat{\beta}$ and $\hat{\gamma}$ correspond to higher-order ME coupling effects.[10] Differentiating this free energy equation with respect to the electric and magnetic fields yields the fol-

lowing relations for the polarization and magnetization, respectively,

$$P_i(\mathbf{E},\mathbf{H}) = -\frac{\partial \mathscr{F}}{\partial E_i} = P_i^S + \epsilon_0 \epsilon_{ij} E_j + \alpha_{ij} H_j + \frac{1}{2}\beta_{ijk} H_j H_k + \gamma_{ijk} H_i E_j - \cdots \tag{2.8}$$

$$M_i(\mathbf{E},\mathbf{H}) = -\frac{\partial \mathscr{F}}{\partial H_i} = M_i^S + \epsilon_0 \epsilon_{ij} H_j + \alpha_{ij} E_i + \beta_{ijk} E_i H_j + \frac{1}{2}\gamma_{ijk} E_j E_k - \cdots \tag{2.9}$$

For a simple linear ME coupling we can describe the relationship between polarization and magnetization as,

$$\mathbf{P} = \hat{\alpha}\mathbf{H} \tag{2.10}$$

$$\mathbf{M} = \hat{\alpha}'\mathbf{E} \tag{2.11}$$

where $\hat{\alpha}$ and $\hat{\alpha}'$ are the ME and EM tensors, respectively, given by,

$$\begin{pmatrix} P_x \\ P_y \\ P_z \end{pmatrix} = \begin{pmatrix} \alpha_{11} & \alpha_{12} & \alpha_{13} \\ \alpha_{21} & \alpha_{22} & \alpha_{23} \\ \alpha_{31} & \alpha_{32} & \alpha_{33} \end{pmatrix} \begin{pmatrix} H_x \\ H_y \\ H_z \end{pmatrix} \tag{2.12}$$

$$\begin{pmatrix} M_x \\ M_y \\ M_z \end{pmatrix} = \begin{pmatrix} \alpha'_{11} & \alpha'_{12} & \alpha'_{13} \\ \alpha'_{21} & \alpha'_{22} & \alpha'_{23} \\ \alpha'_{31} & \alpha'_{32} & \alpha'_{33} \end{pmatrix} \begin{pmatrix} E_x \\ E_y \\ E_z \end{pmatrix} \tag{2.13}$$

for which $\alpha'_{ij} = \alpha_{ji}$ and has units of s m^{-1}.[83]

As already mentioned, Cr_2O_3 and many other single-phase MEs have very small coupling coefficients, which limits their usefulness. Table 2.3 presents a list of some of these compounds; among them, $LiCoPO_4$ and $TbPO_4$ have some of the highest coupling coefficients, but are still less than 40 ps m^{-1}.[10] There has been considerable debate as to why this is the case; it is thought that FM requires transition metal *d* electrons, which suppress off-centering necessary for ferroelectricity.[84] In general, the difference

in magnetic and FE ordering temperatures of these materials have been too great for practical use.[85] For instance, the well-studied ME multiferroic $BiFeO_3$ (BFO) possesses a large spontaneous polarization of 90 μC cm^{-2}, but a Nèel temperature of 643 K and a FE Curie temperature of 1100 K. In other cases, the FE polarization itself is too small to be of use, as in $BiMnO_3$ (P_s = 100 nC cm^{-2}).[71] Research into single-phase MEs is ongoing, but it is clear that alternatives are needed for practical device applications.

Table 2.3: Magnetoelectric coefficients (α) measured for various single-phase magnetoelectrics.[10]

Material	α (ps m^{-1})	Reference
Cr_2O_3	4.13	86
$LiCoPO_4$	30.6	87
$Y_3Fe_5O_{12}$	∼30	88
$TbPO_4$	36.7	89

2.4.2 Artificial Magnetoelectric Heterostructures

As already discussed, the 1990s and early 2000s saw a renaissance in the growth of thin-film oxide materials. Modern-day alchemists such as Ramamoorthy Ramesh and Darrell Schlom developed ways to grow increasingly complex metal-oxide heterostructures with ever-increasing quality, purity, and perfection.[6,18] Their experimental work was buttressed by the groundbreaking theoretical work of J.F. Scott, Craig Fennie, Karin Rabe, and others, who harnessed increasing computing power to forecast promising new systems.[90,91] As these two approaches converged, it was soon realized that disparate properties might be coupled at interfaces to craft powerful new functionalities.[7,9,70] This is shown in Figure 2.11, where mechanical coupling between piezoelectric and piezomagnetic layers mediates electric-field tuning of magnetization.

The class of "artificial" MEs encompasses these kinds of heterostructures. Various geometries have been proposed, such as particles or fibers embedded in a matrix.[7] Early studies utilized unidirectional solidification to synthesize a composite structure with promising properties—the first artificial ME, BTO / $CoFe_2O_4$, possesses ME coefficients up to 720 ps m^{-1}, an order of magnitude higher than the values shown in Table 2.3.[92–94] In the 90s attention turned to laminar thin-film heterostructures because of their relative simplicity and adaptability to conventional lithography processes.[7]

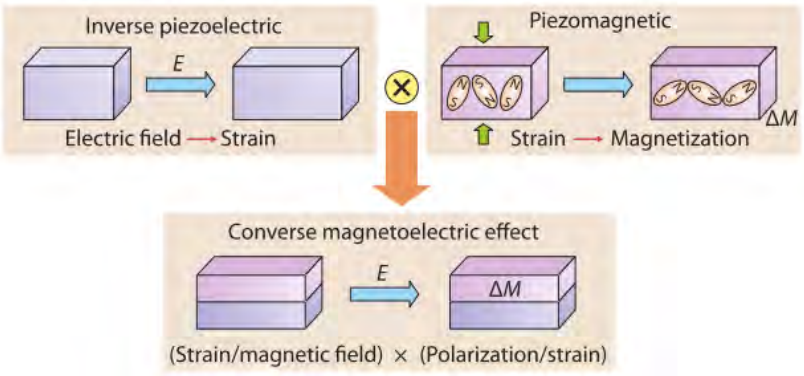

Figure 2.11: Illustration of coupling between a piezoelectric and piezomagnetic layer. The layer in the top left strains under the application of an electric field. If a piezomagnetic is mechanically coupled to this layer, the application of an electric field induces indirect changes in magnetizaton.[7]

2.4.3 Magnetoelectric Coupling Modes

Coupling in artificial ME heterostructures may be mediated by various modes, which may be broadly divided into exchange-, strain-, and charge-mediated coupling.[95] These are summarized in Figure 2.12.

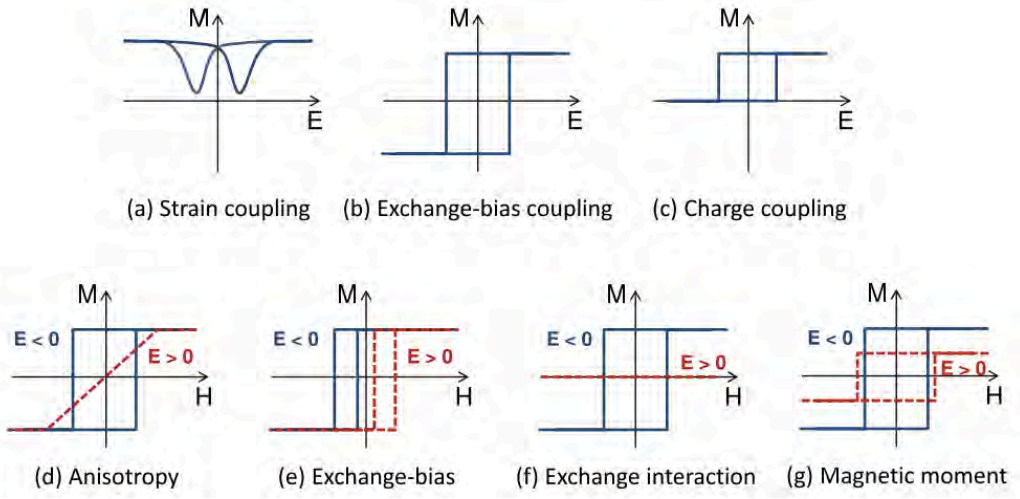

Figure 2.12: (A-C) Illustration of the effects of various kinds of interfacial ME coupling on $M - E$ hysteresis behavior. (D-G) The resulting magnetic hysteresis behavior for different kinds of interfacial coupling mechanisms.[95]

Exchange-Mediated Coupling

Magnetic order in transition metal oxides is mediated by exchange interactions through the hybridization of O $2p$ orbitals with metal $3d$ cations, giving rise to predominantly AF (superexchange) or ferri / FM (double-exchange) order, as described in Section 2.3.2.[95] One would intuitively expect a close

relationship between this magnetic order and local polarization, as is the case for the archetypal ME multiferroic BFO.[96,97] It has been shown that magnetization may be tuned through the exchange bias effect by coupling BFO to an adjacent FM; then, by switching the FE polarization, one can induce changes in this bias.[98]

The phenomenon of magnetic exchange bias (EB) was first discovered in the 1950s by Meiklejohn and Bean in their study of oxidized Co particles.[99,100] Put simply, EB arises from an interfacial exchange interaction between an AF and FM; when a bilayer composite of such materials is heated above the Néel temperature of the AF and then cooled in an external magnetic field, AF spins at the interface act to pin adjacent FM spins.[101] This interaction imposes an extra coercive force on the FM layer, which manifests in a horizontal shift in the hysteresis loop (H_{EB}). Although there have been many proposed models for this behavior, uncompensated interfacial spins are generally regarded as a requirement for EB to occur: if their distribution and orientation in a substrate can be controlled, it should therefore be possible to tune the magnetic behavior of the adjacent FM layer.[102–104] Most single-phase ME multiferroics exhibit AF order and it is conceivable that a material such as BFO could be coupled to a thin FM layer in a heterostructure through the EB mechanism. More importantly, in the case of BFO this AF is strongly tied to the FE polarization, presenting a way to tune the EB.

BFO has been the subject of much study for its simultaneous room-temperature AF and FE character after the Ramesh group published a study in 2003 showing a thin-film FE polarization an order of magnitude larger than in the bulk.[105] At room-temperature BFO is part of a rhombohedral $R3c$ point group ($a_{rh} = 3.965$ Å/ $\alpha_{rh} = 89.3 - 89.4°$) and possesses a perovskite-type unit cell (u.c.), with Bi^{3+} ions at eight-fold coordinated sites and Fe^{3+} ions at six-fold coordinated sites.[106–108] The mismatch between oxygen and bismuth ions can also be described by the Goldschmidt tolerance factor (see Equation 2.2), which predicts buckling of the oxygen octahedra.[39,109] This buckling causes an octahedral tilt of $\omega = 11 - 14°$ around the [111] polarization direction and a resulting Fe–O–Fe bond angle of $\sim 154 - 156°$.[107,108,110] The Fe–O–Fe bond angle has important consequences for magnetic and electronic order in the system, as it dictates both magnetic exchange and orbital overlap, similar to the Mn–O–Mn bond in the manganites (see Section 2.3.2).[111] Catalan *et al.* have proposed a model for the

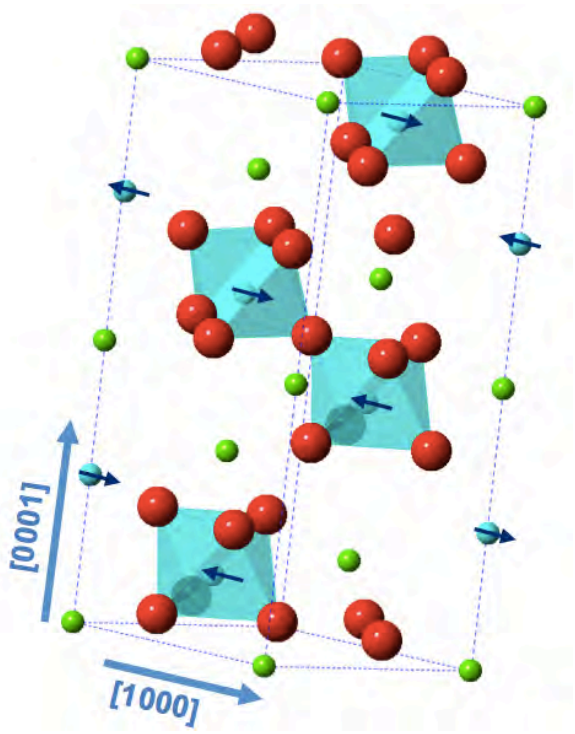

Figure 2.13: Schematic of the BFO structure (in a hexagonal representation) showing tilted pairs of octahedra. Green atoms are Bi ions and turquoise atoms are Fe ions surrounded by red oxygen octahedra. Arrows indicate Mn spins.

metal-insulator transition in BFO that depends on the Fe–O–Fe bond angle.[111] In their model BFO is a charge-transfer insulator with a bandgap controlled by the overlap of O 2*p* and Fe 3*d* bands—a view also supported by the screened-exchange model.[112,113] The Fe–O–Fe angle is controlled by the FE distortion, suggesting that magnetization and polarization may be coupled.[113–115]

When BFO is epitaxially grown in thin-film form on a substrate such as $SrTiO_3$ (001) (STO), a symmetry lowering in-plane contraction and out-of-plane elongation gives rise to a monoclinic structure.[116,117] Both bulk single crystals and thin-films of BFO show a high FE polarization of approximately 100 μC cm^{-2} along the $[111]_{pseudocubic}$ direction that is also relatively insensitive to strain.[114,118] Early work seemed to indicate that in-plane compression gives rise to an enhancement of polarization, but more recent studies have shown that the polarization is largely unaffected by strain state.[105,119,120] This weak strain dependence is due to BFO's relatively small piezoelectric constant of 15–60 pm V^{-1}, compared to 100–1000 pm V^{-1} for other perovskite FEs.[118,121] This small constant makes the material a relatively

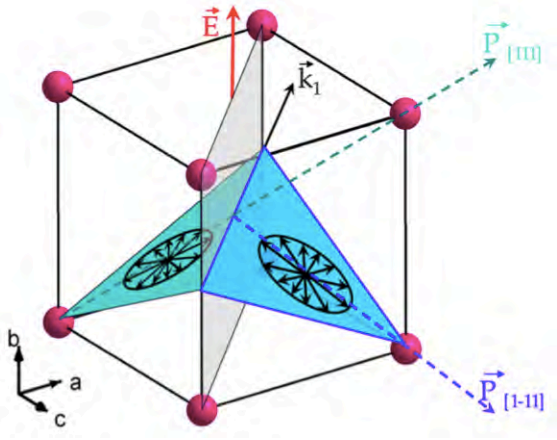

Figure 2.14: Relationship between polarization, spin cycloid propagation direction, and magnetic easy plane. A 71° switch from [111] to [11$\bar{1}$] FE polarization directions induces a switch in the magnetic easy plane.[122]

poor candidate for strain-mediated ME coupling.

Locally BFO is a *G*-type AF, with each Fe^{3+} spin surrounded by six antiparallel spins on its nearest Fe neighbors, as shown in Figure 2.13.[111] ME coupling to the FE polarization gives rise to a weak canted moment and a slight disordering of the *G*-type spin structure. There is an additional long range spin cycloid that repeats over a 62–64 nm distance along a [110] propagation direction and consists of AF ordered sublattices.[122,123] Neutron diffraction studies of monodomain BFO crystals have shown that the spins rotate within the magnetic easy plane defined by the FE polarization ($P \parallel [111]_{\text{pseudocubic}}$) and the cycloid propagation vector ($k \parallel [10\bar{1}]_{\text{pseudocubic}}$).[96,122] Moreover, Lebeugle *et al.* and Lee *et al.* have shown that it is possible to switch the FE polarization and induce a switch in magnetic easy planes (spin-flip). They found that only a change in polarization direction (*i.e.* 71° polarization rotation) affected the magnetic orientation and that merely changing the polarity (*i.e.* 180° rotation) had no effect. This is shown schematically in Figure 2.14. Control of AF ordering alone may be powerful, but such ordering is too difficult to read in memory applications. Since FM ordering provides an easier signal to measure, it is better to couple AF and FM order through the EB phenomenon for device applications.

Coupled oxide heterostructures offer an interesting twist on traditional EB, since the hysteresis behavior of an FM layer can be indirectly controlled by electrical switching of AF order. The use of mul-

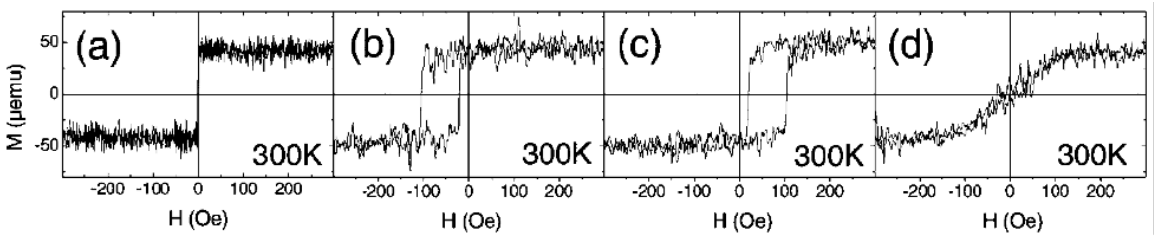

Figure 2.15: Illustration of polarization-induced changes in the hysteresis of a Co layer exchange bias-coupled to a BFO underlayer. (A-D) correspond to different in-plane polarization directions.[127]

tiferroics or FEs in such applications has been explored in the Cr_2O_3 and $YMnO_3$ systems.[124,125] BFO is an ideal candidate for similar use, since a voltage-induced spin-flop could be used to switch between different states of EB. Groups have already observed EB in thin FM films grown on BFO and measured voltage-induced changes in bias.[126–128] Changes in hysteresis behavior are shown to depend on FE polarization in Figure 2.15. Recent studies of BFO / CoFe heterostructures have revealed complex FM magnetic domain structures that depend on the underlying FE domain structure.[129]

The coupling of BFO to manganites such as LSMO is another possibility that is just starting to receive attention.[98] The two systems show high structural compatibility and offer the potential for a well-matched, high quality interface. The ME properties of such a composite are further enhanced by LSMO's colossal magnetoresistance, which makes it appealing for a multifunctional device. Work by You *et al.* has shown that it is possible to induce changes in the uniaxial anisotropy of the LSMO layer by switching striped FE domains in BFO.[130] Recent synchrotron studies have confirmed the presence of a new magnetic phase at the LSMO / BFO interface resulting from orbital reconstruction, but the pinning mechanism that drives EB is not fully understood.[131] Moreover, it is speculated that local factors such as spin anisotropy and interface roughness give rise to a complex magnetic domain structure. From a more fundamental perspective, the size and type of FE domains in BFO is known to play a role in EB coupling, but detailed information is lacking.[71,132]

Charge-Mediated Coupling

Charge-mediated coupling in oxide heterostructures finds its origin in semiconductor field-effect devices, such as metal-oxide-semiconductor field-effect transistors (MOSFETs).[133] These devices were first devel-

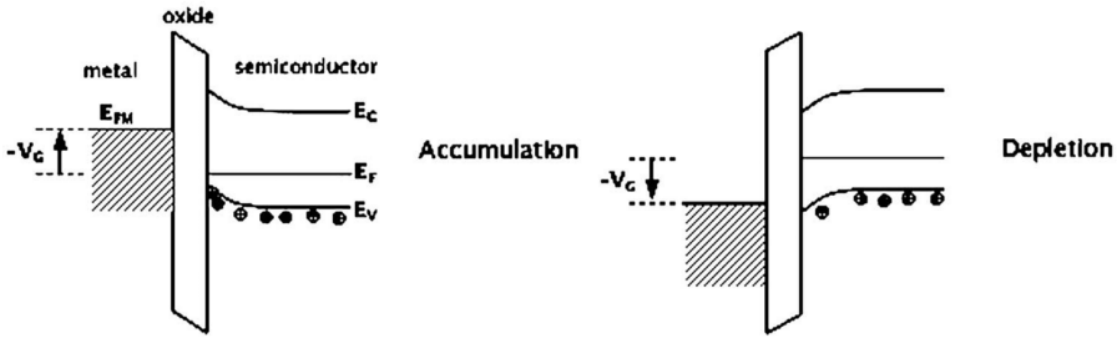

Figure 2.16: Illustration of charge accumulation (top) and depletion (bottom) states in a MOSFET device. The application of a voltage to the gate increases the effective carrier density in the accumulation state and *vice versa* for the depletion state.[133]

oped in the 1970s–1980s and are based on a tripartite design of source and drain terminals, a conducting channel connecting the terminals, and a gate terminal that tunes the resistivity of the conducting channel.[134] The application of an electric field to the gate changes the effective density of the mobile carriers in the conducting channel; when the carrier density is increased, this is termed **accumulation**, while when it is decreased, this is termed **depletion**.[133] An illustration of this behavior is shown in Figure 2.16.

The areal carrier density for such a MOSFET device lies in the range of $10^{12} - 10^{13}$ charges cm^{-2} for a 100 Å channel; with a gate dielectric such as SiO_2 it is possible to tune the effective carrier density by this much—even more with a FE such as PZT.[133] For instance, PZT has a remanent polarization in the range of $\sim 3 \times 10^{14}$ charges cm^{-2}, which is an order of magnitude larger than the breakdown field of SiO_2.[135] This suggests that an FE layer may be used to induce sizable modulations of the carrier density in a metal. However, it should be noted that these modulations are screened quite quickly by free carriers in a metal. One can estimate the expected Thomas-Fermi screening length (λ_{TF}) in a metal using the equation,

$$\lambda_{TF} = \sqrt{\varepsilon b/(4\pi e^2 \partial n/\partial \mu)} \tag{2.14}$$

where ε is the background dielectric constant of the oxide, b is the interplanar spacing, and $n(\mu)$ is the

chemical potential dependence of the charge carrier density.[133] According to this equation, the expected screening length for most metals is on the order of a few u.c. This *theoretically* limits the charge-screening effect to a small layer at the interface.

In the case of charge-mediated ME composites, this field effect is generally used in one of three ways: to directly modify the magnetic moment of a system, to change the magnetic interactions present in the system, or to change the magnetic anisotropy in the system.[95] In the first case, charge-screening by the metal modifies the spin asymmetry at the Fermi level, giving rise to a change in magnetic moment.[136] This has been predicted theoretically in several heterostructures, including Fe / BTO (001) and Fe_3O_4 / BTO, where the ferroelectric causes local bonding changes at the interface.[23,137] It has also been observed in the manganites, particularly $La_{0.8}Sr_{0.2}MnO_3$ / $Pb(Zr_{0.8}Ti_{0.2})MnO_3$, where the bound surface charge from the FE directly affects the adjacent Mn valence.[138]

The second mechanism of charge-mediated coupling tunes the magnetic interactions present in a system. This has been exploited in the case of dilute magnetic semiconductors, such as (In,Mn)As, (Ga,Mn)As, and Mn_xGe_{1-x}, where $p-d$ shell interactions drive magnetic ordering by connecting itinerant carriers to localized Mn dopant spins.[95,139] Bound surface charge from a FE can modulate the carrier density in these compounds and stabilize FM order. Even in the case of metallic complex oxides, such as LSMO, it is possible to induce sizable modulation of carrier densities, albeit across a shorter screening length.[138,140] In these compounds doping of La by a divalent alkaline earth, such as Sr or Ca, removes an e_g carrier from the system and leads to a transition from Mn^{3+} to Mn^{4+} valence—analogous to hole doping.[95] Similarly, the screening of carriers from an adjacent FE can also produce an effective valence change, with associated changes in electronic and magnetic ground states.[141,142]

This mechanism is thought to operate in the LSMO / PZT system, where an interfacial hole charge depletion state gives rise to FM ordering and an accumulation state gives rise to AF ordering at low-temperature (Figure 2.17).[138,143] Vaz *et al.* have proposed that such a spin structure change is necessary to account for the induced magnetization change upon switching the PZT polarization direction; they cite several first principles studies of related LSMO / STO and $La_{0.5}Ba_{0.5}MnO_3$ / BTO systems, in which it is calculated that an AF-*A*-type configuration represents the lowest energy ground state.[144,145] However,

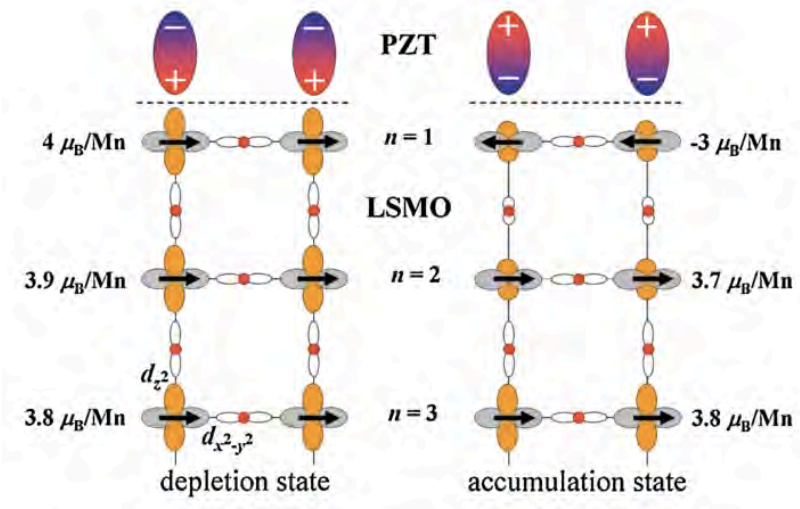

Figure 2.17: Calculated ground-state spin configurations for depletion (left) and accumulation (right) states of the PZT polarization. In the former case the ordering is predicted to be ferromagnetic, while in the latter it is predicted to be antiferromagnetic at low-temperatures.[138]

the rich variety of electronic and magnetic phases present in the manganites complicates this situation; it is far from clear what the temperature dependence of this coupling behavior is. Recently Lu *et al.* have shown that for LSMO / BTO films at room-temperature, a depletion state can actually give rise to a *paramagnetic* (PM) insulating phase, instead of an FM phase.[146]

The third mechanism of charge-mediated coupling occurs when charge screening modifies the magnetic anisotropy of a system. This mechanism is intimately connected to the previous two mechanisms, since a reduction in magnetic moment will affect the magnetostatic energy and a change in the exchange interactions of the system will affect the domain wall formation energy.[95] Moreover, it is expected that a changing orbital occupancy will also change the MCA of a system. These kinds of changes have been demonstrated in various systems, including FePt and FeCo, as well as in ultrathin Fe films;[147,148] very thin layers are more likel to exhibit such coupling, since surface MCA will dominate their behavior.[13]

In summary, while there are various mechanisms of charge-mediated coupling, they are all generally constrained to thin interface layers. In spite of this limitation, these mechanisms can yield sizable magnetoelectric coefficients, as shown in Table 2.4.

Table 2.4: Surface magnetoelectric coefficients (α_S) for two kinds of charge-mediated coupling.[95]

Coupling Type	Material System	α_S (Oe cm^2 V^{-1})	Reference
Exchange	$La_{0.8}Sr_{0.2}MnO_3$ / $Pb(Zr_{0.2}Ti_{0.8})O_3$	-6.3×10^{-9}	138, 140
Magnetic Moment	Fe / MgO (001)	1.1×10^{-13}	8
	Fe_3O_4 / BTO	2×10^{-10}	137
	1 ML Fe / $PbTiO_3$	0.073	23

Strain-Mediated Coupling

Strain-mediated coupling is among the most widely studied mechanisms for linking electronic and magnetic order in ME heterostructures.[6,7,9] Coupling may be achieved in a variety of geometries, such as fibers or particles embedded in a matrix or laminar heterostructures.[9] We shall primarily consider the latter case. Ignoring thermodynamic and growth considerations, it is generally possible to deposit a material onto a substrate of different lattice structure and chemistry. Depending on the structural relationship between the film and substrate, one can grow fully coherent, epitaxial films with minimal threading dislocations. Alternatively, the film may be partially or fully relaxed, leading to large dislocation densities ($\rho \sim 10^{11}$ cm^{-2}) and inhomogeneous properties around the local strain fields associated with such dislocations.[149–151] Strained growth can therefore be used as a means to manipulate the lattice of a film and the most controllable and efficient coupling is achieved through coherent, epitaxial growth.

This approach has been successfully demonstrated in composite structures of BTO and various other systems, including LSMO, LCMO, $SrRuO_3$, and $CoFe_2O_4$.[70,152,153] Upon cooling BTO transitions from cubic to tetragonal (393 K), orthorhombic (278 K), and rhombohedral (183 K) phases, with concomitant changes in lattice parameter.[95] Strain transferred from the substrate to film causes changes in magnetic anisotropy, as well as changes in atomic and electronic structure; in the case of the LSMO system strain gives rise to changes in Mn–O–Mn bonds, as described in Section 2.3.2.[95] This powerful control over magnetic ordering is limited to situations where a sample can be heated or cooled. To be useful a device must be capable of switching between an active and inactive state for a large number of duty cycles. While it is possible in some cases to switch the electrical resistivity and magnetization of a film through a structural phase transformation of the substrate, the design of a high density memory technology with

small local heating elements is problematic.[154]

For more practical control of ordering, one can use an electrically-responsive laminar substrate to dynamically tune strain in a well-controlled fashion, making them an excellent model to understand coupling. Piezoelectrics such as $Pb(Mg_{1/3}Nb_{2/3})O_3$–$PbTiO_3$ (PMN-PT) and PZT have been extensively used with a range of magnetic layers, including LCMO, LBMO, Fe_3O_4, CoFeB, Fe, Ni, and more.[95,155–159] Strain in these structures can act to reorient magnetization through magnetoelastic and magnetostatic contributions, as well as enhance coercivity. Alternatively, strain can act to suppress magnetization by enhancing the Jahn-Teller distortion in the manganites.[160–162]

2.5 Limits of Current Coupling Models

Thin-film ME heterostructures show considerable promise for use in novel spintronic applications, but their implementation is hindered by a poor understanding of interfacial coupling mechanisms. The LSMO / PZT system has received particular attention because of the high sensitivity of magnetic order in LSMO to charge and strain states. Extensive work has been conducted by the Ahn group, who argue that the mechanism of coupling is largely charge-transfer screening dominated.[143] They show that charge carrier modulation in the LSMO induces a change in Mn valency near the interface and they find that coupling results from an interfacial spin reconfiguration resulting from different charge states.[138,163] They also find that the coupling has a strong temperature dependence and is largest near the LSMO magnetic critical temperature at 180 K (for this composition).[140] However, Vaz *et al.* utilize primarily non-local probes to investigate structural and magnetic ordering. Furthermore, they explore only the ultrathin limit (< 4 nm) of LSMO, where charge effects are expected to dominate (see the discussion in Section 2.4.3).

More insight is needed into thicker composites, where strain fluctuations may play a larger role. Various strain states and textures that depend on film thickness have been observed in other manganites, such as $La_{0.8}Ca_{0.2}MnO_3$, with important consequences for magnetic order.[53,164] In general epitaxial strain is thought to enforce a long range tetragonal distortion in the manganites, favoring a particular direction of the Jahn-Teller distortion of the e_g orbitals.[165–167] In LSMO this strained growth gives rise to changes in the metal-insulator transition temperature and FM Curie temperature, as well as

magnetic anisotropy.[168–171] The LSMO / PZT system also shows a thickness and strain dependence on T_C.[42,172] Still other groups have shown that the transport properties of the manganite layer are highly dependent on layer thickness and strain relaxation.[173] The effect of in-plane stress is debated, as recent studies of manganite multilayers have shown a variation in coercive field with interfacial biaxial strain.[50,174] It is speculated that there is some critical thickness at which coupling crosses over from purely charge-transfer-mediated to strain-mediated, but more work is needed.[159] It is clear that there is much uncertainty regarding the nature of coupling, as well as about the relationship between local strain and magnetization.

An additional consideration is the direct relationship between FE polarization and Mn valence changes at interfaces. There is considerable debate over the screening length for charge in this system; calculations of the Thomas-Fermi screening length vary, ranging from 0.2 to 1.9 nm.[135,175] Previous studies have revealed the presence of a dead layer in LSMO that is approximately 2–3 nm thick, depending on the choice of substrate.[176–178] However, prior work has employed primarily non-local X-ray absorption spectroscopy (XAS) techniques to characterize local valence states in LSMO / PZT.[138,143] Because of the intimate relationship between charge screening, electronic phase, and magnetic order, a local, atomically-resolved analysis of such screening is necessary. Lu *et al.* have recently proposed a model in which polarization screening gives rise to the formation of either PM or FM ordering at room-temperature in LSMO / BTO.[146] This contrasts to the low-temperature AF and FM states predicted by Vaz *et al.*, but since few local room-temperature studies of magnetization in this system have been conducted, further work is needed.

In this thesis we present a detailed, *local* study of atomic-scale structure, chemistry, and magnetization in the LSMO / PZT system. We explore composites at and beyond the ultrathin limit using correlated local probes of structure and magnetic order. We assemble a suite of characterization techniques across a range of length scales that allow us to disentangle strain and charge effects on magnetization. This allows us to develop a more comprehensive model of ME coupling in thicker composites. More fundamentally, we explore the underlying electronic effects governing coupling and provide new insight into the magnetic phases present at interfaces in these structures. This new understanding will guide the

implementation of these materials into the spintronics devices of the future, while the methods we have developed may be extended to many other ME composites.

Chapter 3: Techniques and Methods

3.1 Introduction

In this section we describe the techniques employed in this thesis. These techniques can be broadly divided into structural and magnetic characterization, as shown in Figure 3.1. By correlating high-resolution, local probes of structure and magnetism, we are able to map structure-property relationships in these heterostructures.

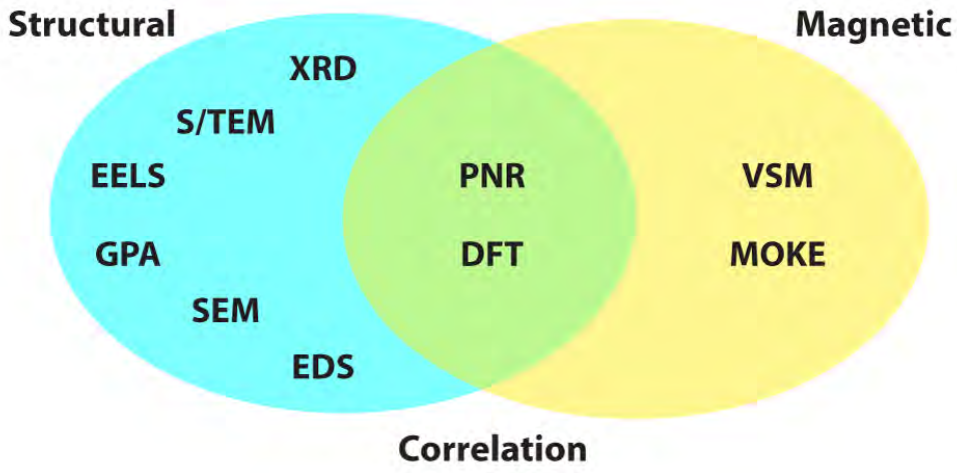

Figure 3.1: Overview of the techniques used in this thesis.

3.2 Thin-Film Growth

There are many techniques for physical vapor deposition (PVD) of thin-films, including pulsed laser deposition (PLD), molecular beam epitaxy (MBE), and sputtering.[179] PLD has been developed in the last several decades and is extensively used to synthesize oxide thin-films and ferroelectrics, since it is possible to deposit high-quality thin-films relatively quickly and easily using this method.[180] Moreover, through careful control of target stoichiometry and growth conditions, it is possible to synthesize extremely sharp, phase-pure epitaxial thin-film heterostructures.[181]

An illustration of the PLD process is shown in Figure 3.2. A basic setup consists of a vacuum chamber,

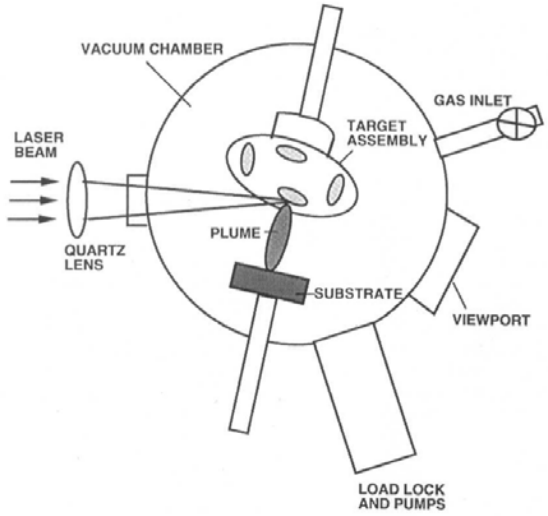

Figure 3.2: Schematic of a PLD chamber, illustrating the vacuum chamber, ablating laser, target carousel, and substrate.[179]

which generally kept at high to ultrahigh vacuum ($10^{-6} - 10^{-8}$ Torr), to minimize surface contamination.[179] The sample substrate is mounted on a block that can heat it up to several hundred °C during deposition. The source of material is a sintered ceramic target typically prepared by mixed-oxide synthesis, mounted on a rotating carousel; each target rotates on the carousel to ensure uniform ablation and it is easy to switch between targets. The vacuum chamber has a window with a quartz focusing lens through which an intense laser beam is focused. This beam is typically generated by a Nd^{3+}:YAG or gas excimer laser, the former of which is typically frequency doubled twice to produce outputs of 355 and 266 nm. Such a laser is capable of delivering $\sim$2 J pulse^{-1} at repetition rates of tens of Hz, which vaporizes the target, forming a plasma plume. Adatoms from the plume are deposited on the substrate, where they form layers or islands, depending on the growth conditions.

The MBE technique is conceptually very similar to PLD; however, the source of growth material is quite different. Rather than ablating a target with a laser, MBE uses Knudsen effusion cells, which are essentially high-temperature crucibles that radiatively heat highly-pure elemental sources to their sublimation temperature.[4] A flux of atoms is emitted from these sources and deposited on a target substrate in concert with the introduction of a small flow of oxygen or ozone. A shutter is placed over each source to precisely time the emission of this flux to achieve very precise monolayer deposition of

compounds. Another technique, sputtering, is also quite similar to MBE; however, instead of heating a source, an electron beam bombards the material to heat it.[4]

3.3 X-Ray Diffraction

The venerable techniques of X-ray diffraction (XRD) allow for facile and non-destructive measurement of important properties, such as lattice parameter, epitaxy, and thin-film layer thickness. Unlike optical radiation, X-rays have a wavelength on the order of Ångströms, the same length scale as the atomic bonds in a solid.[182] Diffraction of collimated, monochromatic X-rays from periodically-spaced atoms in a crystal can be described by the well-known Bragg law,

$$n\lambda = 2dsin\theta \tag{3.1}$$

in which n is the order of the reflection, λ is the wavelength of the incident radiation, d is the lattice spacing, and θ is the angle of incidence of the X-rays.[182] This equation will be satisfied when the total path length of the X-rays is an integral multiple of the lattice spacing, leading to specific angles at which the diffraction will be most intense. For a powder or polycrystalline sample, which contains all possible orientations of lattice planes, the resulting pattern may be indexed to determine the space group and symmetry of the underlying lattice. For epitaxial thin-film heterostructures, the orientation of the underlying substrate generally dictates the orientation of the crystal grown atop it. For a well-defined single-crystal sample, then, only a limited number of diffraction conditions will be accessible for a given tilt of the crystal (Figure 3.3); however, these are generally sufficient to determine the epitaxial relationship between the crystal and substrate.

In the case of a layered heterostructure or superlattice, there is a variant of this technique known as X-ray reflectivity (XRR) that can be used to determine the thickness of the individual layers. When radiation is incident on the surface of a crystal, part of that radiation is refracted and part of it is reflected (both specularly and diffusely). Because the index of refraction for X-rays is less than unity, there exists a critical angle of incidence ($\theta_C \approx 0.2 - 0.4°$) below which this radiation is totally externally reflected.[183] Moreover, in the case of a laminar thin-film heterostructure, the incident radiation will be reflected by

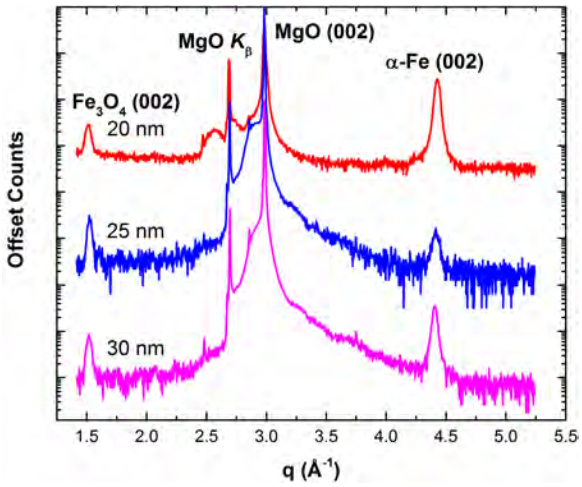

Figure 3.3: $\theta - 2\theta$ diffraction pattern from an Fe / Fe_3O_4 / MgO (001) thin-film heterostructure.

each layer and—due to the path length difference between the layers—these reflected beams will interfere with one another. This results in an oscillating interference pattern, as shown in Figure 3.4. The periodicity of these "Kiessing fringes" is proportional to $2\pi t^{-1}$, where t is the thickness of the respective layer. The determination of structure from such an interference pattern typically begins with some nominal knowledge of layer structure and geometry, as well as known chemical scattering length densities. From this information it is possible to construct a theoretical slab model, where each layer is approximated by a chemical scattering length density, thickness, and roughness. The scattering and diffraction from each layer is then simulated as a function of angle-of-incidence and the resulting reflectivity profile is calculated using the Paratt formalism.[184] This process is repeated until the simulation converges to the measured data.

3.4 Electron Microscopy

The techniques of electron microscopy offer unprecedented levels of analysis of local structure, chemistry, and strain state. These techniques are all complementary and form the characterization backbone of this thesis.

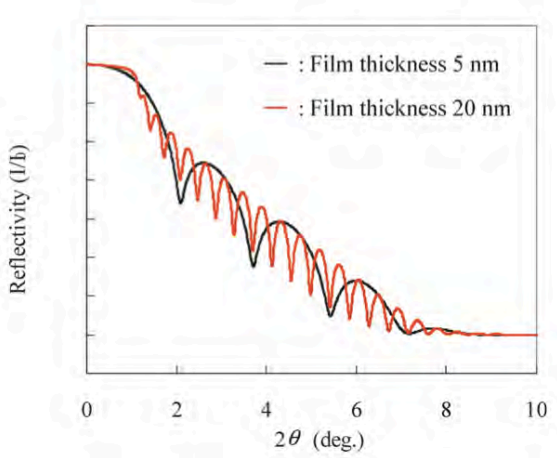

Figure 3.4: Calculated X-ray reflectivity for Au films deposited on Si substrate, illustrating the interference of reflected beams from the multilayer.[183]

3.4.1 Transmission Electron Microscopy

Transmission electron microscopy (TEM) and its related techniques comprise the primary structural and chemical characterization method used in this thesis. The interaction of an electron beam with a thin foil specimen creates a number of simultaneous signals: among these, bright-field images and diffraction patterns can be used to probe the crystal structure of a sample, while characteristic X-rays and electron energy loss spectroscopy (EELS) can be used to determine local changes in chemistry.[185] On most modern instruments a wide variety of information can be collected at once with Ångström or better spatial resolution. At the frontier of electron microscopy, it is possible to generate real-world conditions inside the microscope through customized holders. These include environmental and liquid cells, straining, heating, magnetizing, and electrical biasing holders.[186]

Electrons possess a much smaller wavelength than optical radiation (pm *versus* nm, respectively). As described by de Broglie, electrons can be considered as simultaneously both a particle and wave. According to the Rayleigh criterion, the smallest resolvable distance for a visible light microscope is given by,

$$\delta = \frac{0.61\lambda}{\mu sin\beta} \tag{3.2}$$

where δ is the resolvable distance, λ is the optical wavelength, μ is the refractive index of the viewing medium, and β is the collection semi-angle of the magnifying lens.[185]

One can immediately see that for visible light in the 400–700 nm range, the smallest resolvable feature is on the order of approximately 200–300 nm, much larger than most nanostructures. To resolve a smaller feature size, one would need to shorten the wavelength of the incident radiation, which is not possible with visible light. However, by using electrons instead of light it is possible to shorten this wavelength further. We can estimate the (non-relativistic) equivalence between electron energy and wavelength according to de Broglie as,

$$\lambda = \frac{1.22}{E^{1/2}} \tag{3.3}$$

where λ is wavelength given in nanometers and E is the energy of the electron in eV.[185] For a 100 keV electron this yields a theoretical wavelength of 0.004 nm, which is smaller than an atom. Such energies are routinely attainable in a modern electron microscope, as shown in Figure 3.5. The main parts of the microscope are the electron gun, focusing optics, specimen, and collection optics.[185]

The electron gun consists of a thermionic (typically LaB_6) or field emission (W) source that is kept near ultrahigh vacuum and acts to generate a source of electrons under heating, electric field, or some combination thereof. These electrons are then accelerated to 60–70% of the speed of light under a 100–300 keV potential and passed through a series of collimating and focusing lenses. The beam may be made parallel or converged onto the specimen, where it is scattered elastically and inelastically. It is here that a variety of useful signals are generated, as shown in Figure 3.6; these include characteristic X-rays, scattered electrons, diffracted electrons, secondary electrons, and visible light. Finally, forward-scattered electrons are passed through a series of image collecting optics toward a photodetector that records the intensity of the transmitted beam.

The range of signals simultaneously generated upon interaction between the electron beam and sample, as well as the high spatial resolution of the probe, make TEM a highly effective means to probe local atomic-scale structure and chemistry.

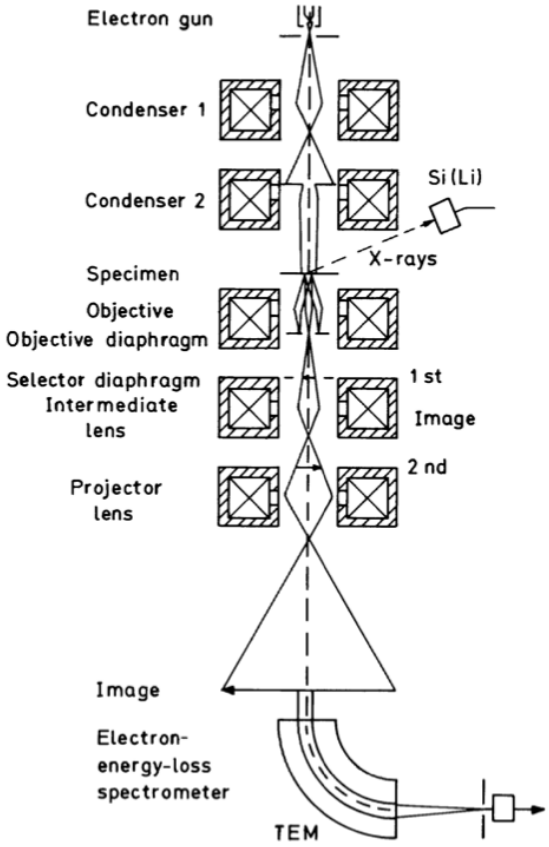

Figure 3.5: Illustration of the TEM lens system showing the electron gun, focusing optics, and collection optics, as well as optional X-ray and EELS detectors.[187]

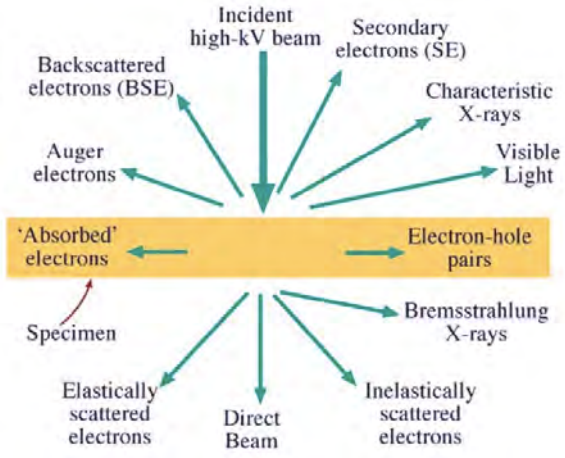

Figure 3.6: Illustration of the signals generated when an electron beam is incident on a thin foil sample.[185]

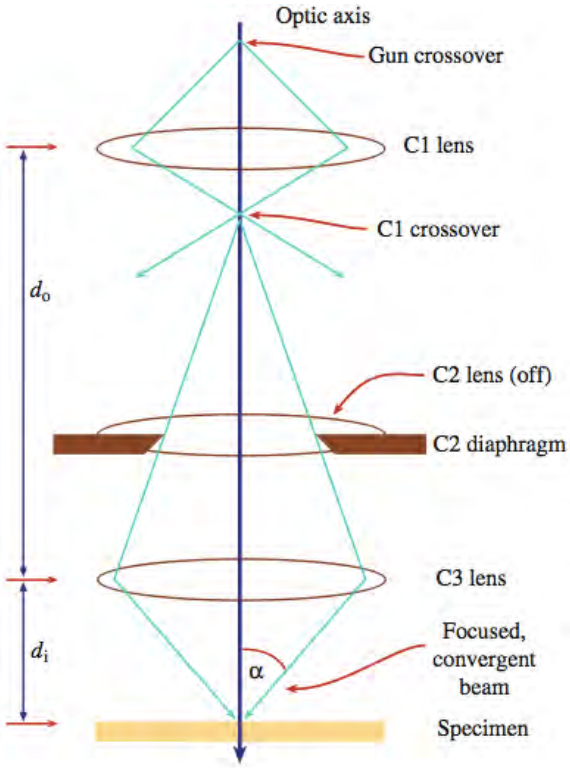

Figure 3.7: Schematic of the incident optics in STEM mode. The C1 and C3 lenses are active, but the C2 lens is turned off. The C1 lens is used to control probe size and current, while the C2 lens aperture is still used to control the convergence angle on the specimen.[185]

3.4.2 Scanning Transmission Electron Microscopy

Scanning TEM is a variant of traditional TEM in which the incident optics are arranged in such a way as to converge the beam at the sample position. In particular, the second condenser lens (C2) is turned off and a third condenser (C3) is used to focus and converge the beam to a small spot on the sample, as shown in Figure 3.7.[185] This results in a convergent beam with a large convergence angle and the smallest possible probe. In STEM mode a series of scan coils (not shown) are used to raster the probe over an area of the sample. This method allows for a highly localized signal to be collected from each part of the specimen and in theory permits higher spatial resolution, but it is prone to scan error and can easily damage beam-sensitive samples.[188]

In spite of its limitations, there are many benefits to using a STEM imaging mode. STEM affords the user the highest possible spatial resolution of any real-space imaging mode, as well as simultaneous

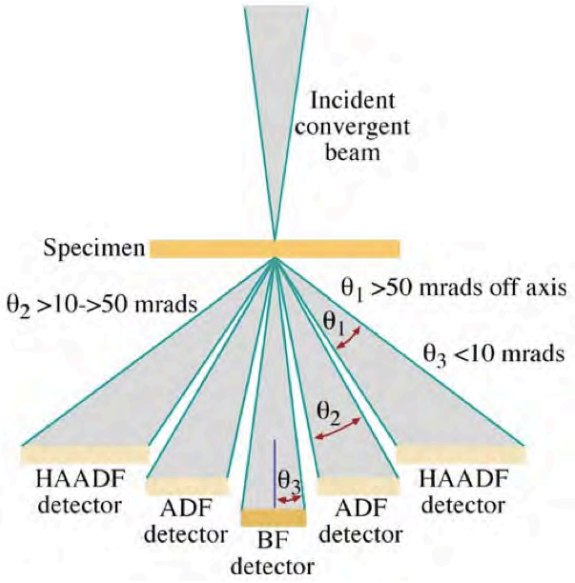

Figure 3.8: Illustration of scattering angles and annular collection apertures for a convergent STEM probe. Scattering in excess of 50 mrad is termed high-angle annular dark field (HAADF) or "Z-contrast" imaging.[185]

measurement of local chemistry, bonding, and valence.[188] In addition, the use of an annular dark field (ADF) detector allows the user to isolate purely elastically scattered electrons. As shown in Figure 3.8, these electrons are scattered to high angles; for angles in excess of 50 mrad, one may use a high-angle annular dark field (HAADF) detector to isolate electrons scattered to high angles. It is found that the probability of such scattering is proportional to the atomic number (Z) of the scattering atom and is sometimes termed "Z-contrast" imaging. This contrast mechanism allows the user to easily distinguish regions of high and low atomic number. For instance, Figure 3.9 displays a PZT sample, in which the bright, large dots mark columns of Pb atoms ($Z = 82$) and the smaller, darker dots mark columns of Zr / Ti atoms ($Z = 40$ / 22).

3.4.3 Transmission Electron Microscopy Image Simulation

The proper interpretation of high-resolution TEM and STEM micrographs is quite difficult, owing to the fact that a generated image results from a complex interaction of factors, including[185]:

- Sample alignment with respect to the electron beam
- Sample thickness

Figure 3.9: STEM-HAADF image of the piezoelectric PZT, with bright Pb columns and darker Zr / Ti columns.

- Objective lens defocus
- Chromatic aberration
- Electron beam coherence

For instance, even small modifications in defocus can invert the contrast of an image, making direct interpretation of bright and dark spots impossible. To address these issues, it is common to simulate images for a variety of sample and beam conditions. These are then compared to the experimental images to enable direct interpretation of contrast. In this way even extremely complex structures, such as zeolites, can be quantitatively interpreted.[189]

The two main image simulation techniques are Bloch wave and multi-slice calculations, also termed real-space and reciprocal-space image simulations, respectively.[185] In the Bloch wave approach, we consider that, while many diffracted beams are formed upon interaction of an electron beam with a highly symmetric crystal, only a small number of Bloch waves give rise to the actual image.[190,191] Mathematically, we can describe the propagation of these waves as,

$$\Psi_{n+1}(\mathbf{r}) = [\Psi_n(\mathbf{r})P_{n+1}(\mathbf{r})] \otimes q_{n+1}(\mathbf{r}) \tag{3.4}$$

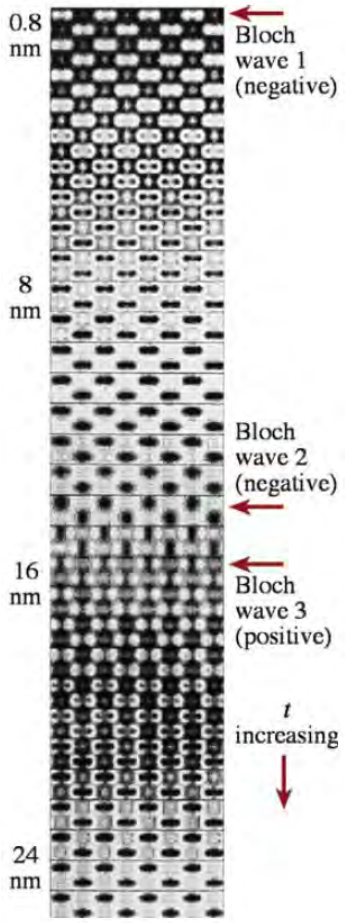

Figure 3.10: Ge lattice images calculated using the Bloch wave approximation.[185] The arrows indicate the contrast resulting from the interaction of one (top arrow), two (middle arrow), and three (bottom arrow) Bloch waves.

where Ψ describes the electron wave, P is the real-space propagator of the electron wave in the microscope, and q is the real-space phase grating (specimen).[185] This allows us to approximate an HRTEM zone-axis image using as few as three Bloch waves, as shown in Figure 3.10. This method is computationally efficient, but it is limited in that we only consider diffracted wave propagation in the forward direction of scattering.[185]

The alternative to Bloch wave calculations is the multi-slice (reciprocal-space) approach. This method, while more computationally-intensive, is generally more accurate, since we calculate all the diffracted beams generated by a point scatterer in the crystal.[185] As its name implies, the multi-slice method subdivides the crystal lattice into a number of projection planes, each of which acts as a diffraction grating.

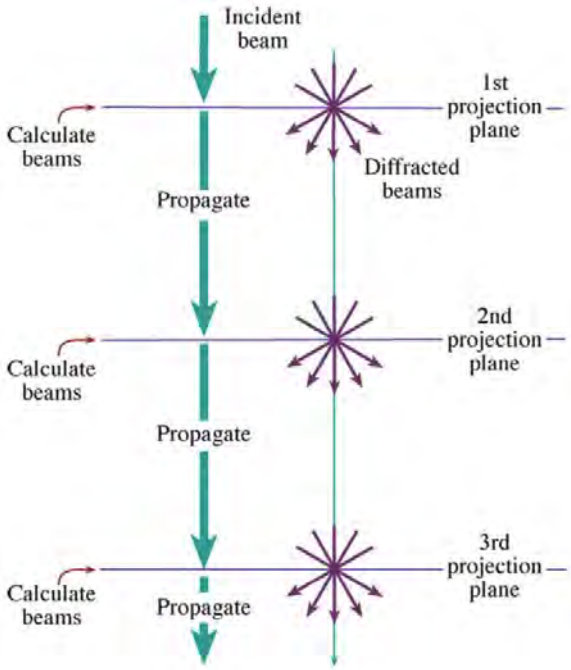

Figure 3.11: Illustration of the multi-slice simulation method. The sample is first approximated by breaking it up into an array of "projection planes." The incident electron beam is then passed through the first of such planes and all the scattered beams in reciprocal space are calculated. These calculated beams are then passed through the second plane and the calculation is repeated. This process is repeated until the beam has passed through all the slices.[185]

As shown in Figure 3.11, the incident beam is propagated through such a plane and all the diffracted beams are calculated. These beams are then passed on through free space to the next projection plane, and the calculation is repeated until the number of planes equals the thickness of the crystal.

It is immediately apparent that the complexity of such a calculation grows rapidly, since we calculate scattering in all of reciprocal space. On a modern desktop computer most multi-slice calculations do not take more than a few hours, so it is generally desirable to use this method. There are many programs that have been developed for image simulation, including JEMS, MacTempasX, and QSTEM.[192–194] The latter program, QSTEM, has been used in this work and employs multi-slice methods to simulate images.

3.4.4 Electron Energy Loss Spectroscopy

As described in Section 3.4.2, many signals are generated when the electron beam interacts with a sample. In particular, some energy is lost to inelastic scattering with the sample, leading to a net reduction in the energy of the incident electron. This electron energy loss (EEL) can be measured using a magnetic

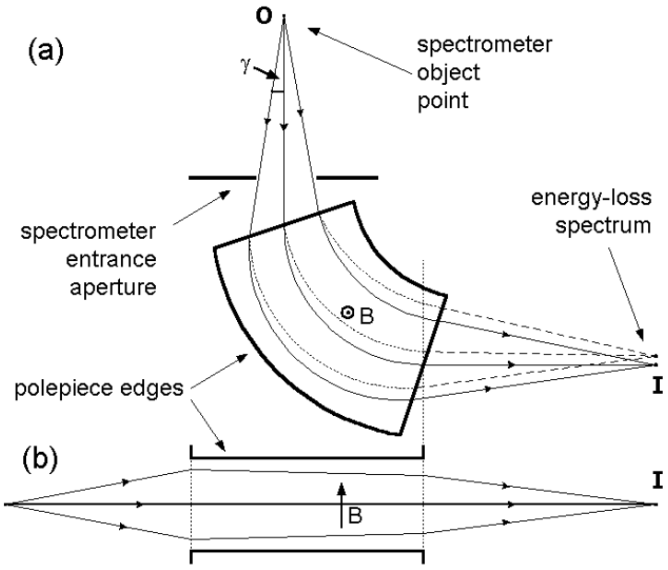

Figure 3.12: Schematic of an EEL spectrometer. (A) Shows the plane perpendicular to the applied magnetic field, with the dashed lines indicating deviations in electron paths due to energy loss. Solid lines indicate zero-loss electrons. (B) Shows the plane parallel to the magnetic field.[195]

prism in a manner analogous to mass spectroscopy, as shown in Figure 3.12.[195] In this setup, a magnetic field on the order of 0.01 T is applied, causing electrons to precess through a 90° angle. The bending radius depends on the electron mass, charge, and velocity, according to,

$$R = \frac{mv}{eB} \tag{3.5}$$

A dispersion of energies therefore results in a range of different bending radii, which can be recorded on a detector to produce an energy-loss spectrum. Such a spectrum is shown in Figure 3.13, which broadly defines three regions of energy loss: the zero-loss, low-loss, and high-loss. The zero-loss peak is intense and contains contributions from both the elastically-scattered and unscattered electrons (or those below the resolution-limit of the detector).[185] The higher energy loss regions correspond to plasmon, intra-atomic, and ionization transitions that can be quite difficult to interpret, but offer a wealth of information about the local chemistry of the sample.[195]

While it is possible to use a conventional TEM imaging mode to capture EEL spectra, in practice STEM imaging is much more common. As previously described, in STEM the C2 lens is turned off and

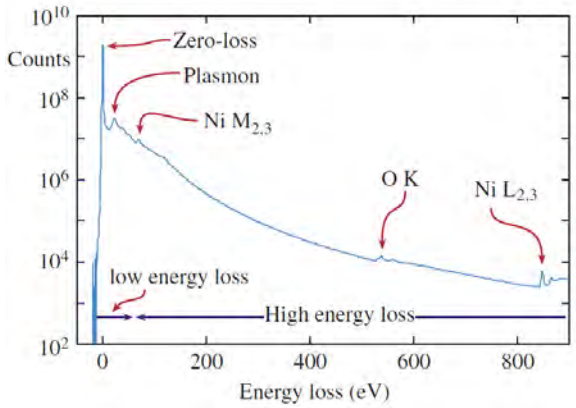

Figure 3.13: Example of an EEL spectrum, with the zero- (elastically-scattered), low-, high-loss regions indicated. The intensity of the low-loss region is orders of magnitude higher than the higher energy loss regions, which fall off in intensity according to a power law.[185]

a C3 lens is used to converge the beam to a small spot on the sample. This spot is then rastered and an EEL spectrum is collected at each point on the sample. This method offers enhanced spatial resolution, as well as the possibility of elemental mapping. Figure 3.14 shows an example of such mapping at an LSMO / STO interface.[196] Using aberration-correction it is possible to achieve better than 0.5 eV energy resolution, with sub-Ångström spatial resolution.[68]

This kind of local chemical information is essential to understand the behavior of oxide thin-films, which typically deviate near surfaces or interfaces. Unlike other chemical analysis techniques, such as energy-dispersive X-ray spectroscopy, EELS offers unrivaled spatial resolution and single-atom sensitivity.[185] This permits direct mapping of local bonding and oxidation states—features that dictate the magnetic and electronic phase of the manganites.[197]

3.4.5 Geometric Phase Analysis

Geometric phase analysis (GPA) allows for direct measurement of local strain using TEM micrographs. In contrast to indirect scattering techniques, such as XRD, this method allows the user to resolve local strain states to better than 0.1% strain, with 1 nm spatial resolution.[198–200] The technique has been primarily applied to studies of strained-silicon transistors, where strain is used to enhance electron mobility.[201] However, it has also been used to explore structural distortions and growth-induced strain effects in the manganites.[202–205]

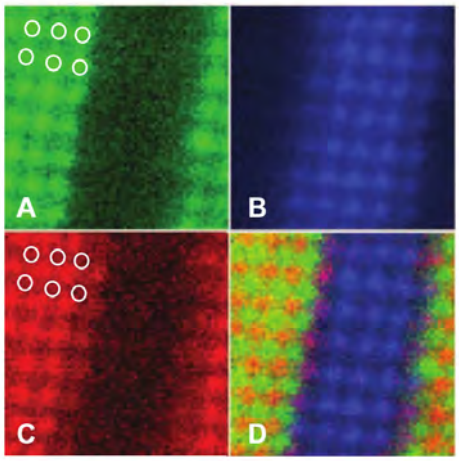

Figure 3.14: Elemental mapping of an $La_{0.7}Sr_{0.3}MnO_3$ / $SrTiO_3$ thin-film heterostructure interface. (A-C) Correspond to the La M, Ti L, and Mn L edges, respectively. (D) Shows a false-color combination of the three maps.[196]

While there are different variants of GPA, they all make use of the phase shift induced by local lattice displacements.[199] First an HRTEM image is taken along a particular zone axis and a region of reference is selected. Displacements relative to this reference region are then calculated using the equation,

$$P_g(\mathbf{r}) = -2\pi \mathbf{g} \cdot \mathbf{u}(\mathbf{r}) \tag{3.6}$$

where $P_g(\mathbf{r})$ is the geometric phase and $\mathbf{u}(\mathbf{r})$ is the component of the displacement vector in the direction of the reciprocal lattice vector $\mathbf{g}$.[199] It is important to note that the displacement is averaged over the entire thickness of the thin foil specimen. After calculating the geometric phase of two non-collinear diffracted beams, it is possible to determine the displacement field according to,

$$\mathbf{u}(\mathbf{r}) = -\frac{1}{2\pi}\left[P_{g_1}(\mathbf{r})\mathbf{a}_1 + P_{g_2}(\mathbf{r})\mathbf{a}_2\right] \tag{3.7}$$

where $\mathbf{a}_1$ and $\mathbf{a}_2$ are the real-space basis vectors for the reciprocal space lattice defined by $\mathbf{g}_1$ and $\mathbf{g}_2$. Differentiating the displacement field yields the two-dimensional deformation tensor (ε_{ij})[199],

$$\varepsilon_{ij} = \frac{1}{2}\left(\frac{\partial u_y}{\partial x} - \frac{\partial u_x}{\partial y}\right) \tag{3.8}$$

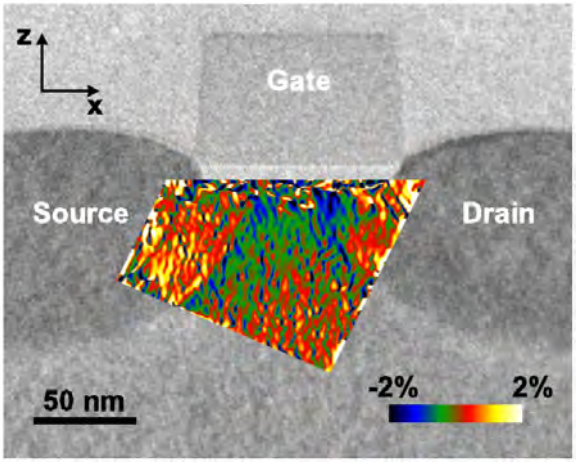

Figure 3.15: Calculation of the strain field in a transistor, with the color map corresponding to the ε_{xx} component of local strain.[201]

The result of such an analysis is shown in Figure 3.15, which shows the strain field around the source and drain of a $Si_{80}Ge_{20}$ transistor.[201] The immense utility of this measurement is clear when one considers that all the strain information has been extracted from one TEM micrograph; moreover, it is possible to simultaneously map local chemistry and defects, which can then be directly correlated to strain.

3.4.6 Scanning Electron Microscopy

The technique of scanning electron microscopy (SEM) is a natural complement to TEM. As its name implies, in this technique a focused electron beam is rastered across the surface of a sample and signals are collected from various points on the sample. This setup is shown in Figure 3.16. In contrast to TEM, which samples beams scattered through a thin foil specimen, SEM operates on the short-range interactions of an incident electron beam with the surface of a material—which generates a variety of useful signals (Figure 3.6).[206]

This limited interaction arises from the inelastic scattering of primary electrons; each collision reduces the energy of the primary electron until they fall to rest and are absorbed into the sample.[188] The penetration depth of the electron is given by the equation,

$$\rho R \approx a E_0^r \tag{3.9}$$

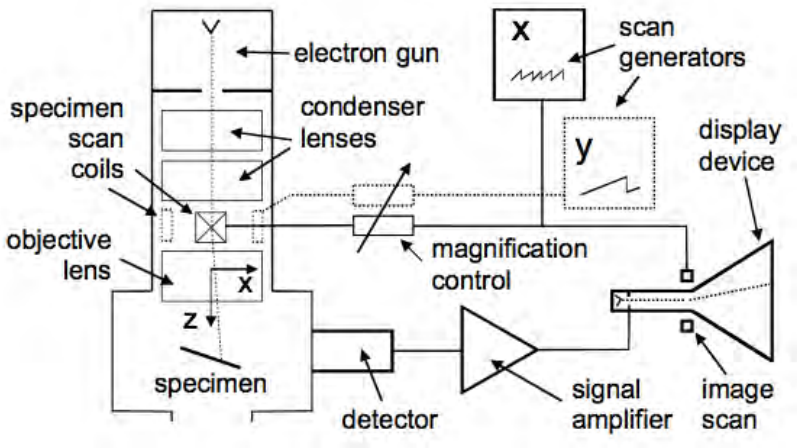

Figure 3.16: Schematic of the scanning electron microscope, illustrating the instrument optics, control system, and detectors.[188]

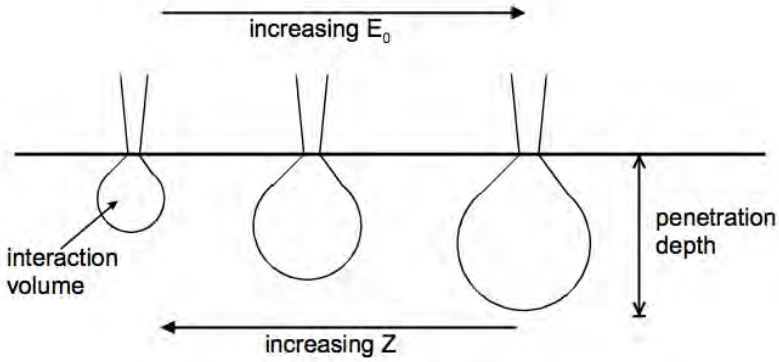

Figure 3.17: Illustration of the secondary electron interaction volume for increasing primary electron energy (E_0) and increasing atomic number (Z).[188]

where R is the electron range, ρ is the density of the sample, E_0^r is the incident electron energy and a is a constant.[206] Typical penetration depths for 10–30 keV electrons range from 0.8–6.4 μm.[188] This equation shows that with increasing atomic number Z the penetration depth will decrease, primarily because of increased backscattered electron generation. The resulting, teardrop-shaped interaction volume is shown in Figure 3.17.

Because of these features of secondary electron generation, SEM is largely limited to probing near the surface of a material. In this regard SEM is an excellent complement to TEM, since it provides a high resolution probe of surface morphology and chemistry (as described in Section 3.4.7), and sample preparation is quite easy—generally the only requirements are a small (1–2 cm) conductive sample.[188]

3.4.7 Energy-Dispersive X-Ray Spectroscopy

As mentioned in the previous section, SEM may be used to resolve both surface morphology and chemistry. When an incident electron is inelastically scattered by a crystal, some of the radiation may be given off in the form of X-rays (Figure 3.6). These X-rays have characteristic energies corresponding to intra-atomic transitions in the scattering atom and are probed in the energy-dispersive X-ray spectroscopy (EDS) technique.[188] According to quantum mechanics, an atom can only absorb or emit energy in certain quanta corresponding to electronic transitions between energy levels.[207] For the hydrogenic atom, the de-excitation process of energy loss and photon emission can be described by the equation,

$$hf = RZ^2\left(\frac{1}{n_l^2} - \frac{1}{n_u^2}\right) \tag{3.10}$$

where n_u and n_l are the upper and lower energy levels in the transition, R is the Rydberg energy (13.6 eV), Z is the atomic number, and hf is the energy of the emitted photon.[188] For non-hydrogenic atoms this calculation is more complex and must account for interactions *between* electrons—nonetheless, each characteristic X-ray emitted corresponds to a specific intra-atomic transition that can be indexed. The full X-ray energy spectrum (shown in Figure 3.18) may then be used as a kind of chemical fingerprint for a particular atom.

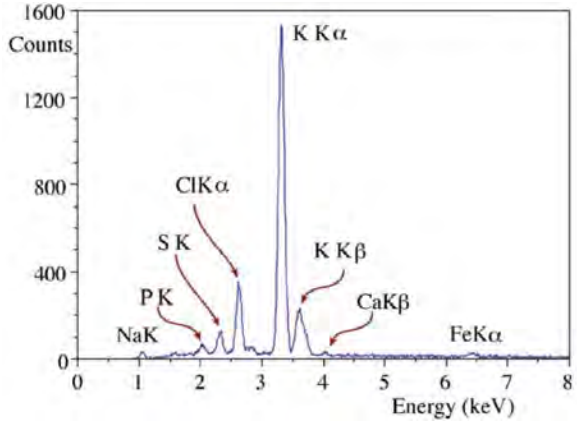

Figure 3.18: X-ray emission spectrum from a cauliflower. The peaks in the spectrum correspond to specific intra-atomic transitions and can be indexed to specific elements.[185]

A chemical map of a region may be constructed by rastering the electron beam across the sample and collecting a full emission spectrum from each point, as shown in Figure 3.19. Such maps can be directly

overlaid onto the local morphology of a sample to identify secondary phases, precipitates, and other features. This method is primarily limited by the number of X-ray photons generated (a small probe yields fewer photons) as well as the incident energy of the electron beam.[188] Moreover, EDS is poorly suited to detecting light elements, because of their small X-ray yield, and requires careful processing to remove background contributions (Bremsstrahlung).[185,188] However, atomic-resolution EDS mapping is now routinely possible using multiple windowless Si-drift detectors available in aberration-corrected microscopes.[208]

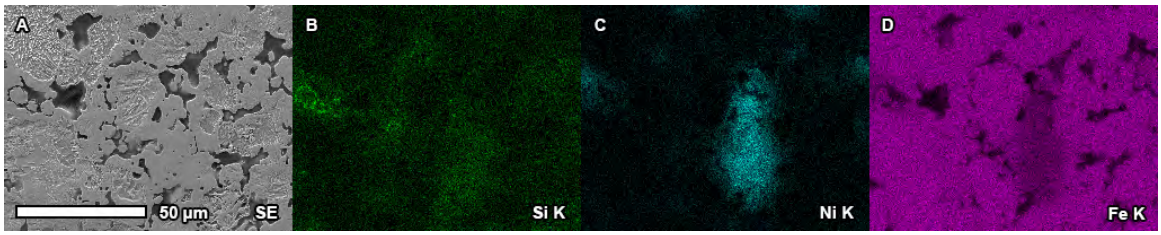

Figure 3.19: (A) Secondary electron image of a ferrous powder metal compact and Ni additive particle. (B-D) Corresponding Si K, Ni K, and Fe K characteristic X-ray maps, clearly distinguishing the Ni particle from the surrounding Fe matrix.[209]

3.5 Magnetometry

We next describe the techniques of bulk and depth-resolved magnetometry employed in this thesis. These techniques are an excellent complement to electron microscopy and offer a means to correlate local structure to magnetization.

3.5.1 Vibrating Sample Magnetometry

To investigate the bulk properties of magnetic thin-film materials, it is necessary to use a highly sensitive magnetometer. The technique of vibrating sample magnetometry (VSM) relies on the flux change in a coil when a magnetized sample is vibrated next to it at approximately 40–100 Hz, as shown in Figure 3.20.[210] The locally varying magnetic field of the sample induces an electromotive force (emf) in the "pickup" coil, which is fed into a lockin amplifier sampling at the frequency of vibration. A magnetic field is applied to the sample and the emf is measured as a function of this field. This is compared to a reference magnet vibrating at the same frequency, which enables measurement of very small magnetic moments (10^{-5} Oe). For thin-film samples it is generally possible to neglect demagnetizing fields and it

is possible to precisely measure the hysteresis of a sample.[210]

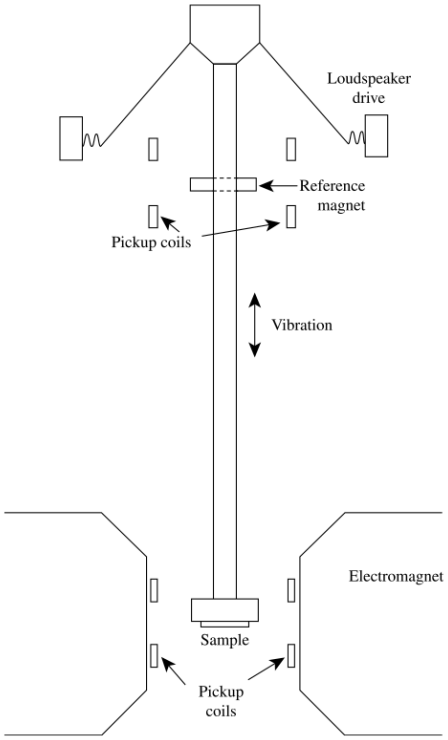

Figure 3.20: Schematic of a vibrating sample magnetometer, showing the reference magnet and sample. The sample is placed in a magnetic field generated by a superconductor, permitting the application of large fields, up to several T.[210]

3.5.2 Magneto-Optical Kerr Effect Magnetometry

In contrast to bulk VSM techniques, the magneto-optical Kerr effect (MOKE) is commonly used to probe the surface magnetization of a material or thin-film. Using this method it is possible to achieve highly sensitive magnetic measurements, down to a monolayer of Fe.[211] In addition to this sensitivity, the effect is robust and can be conducted under various stimuli (such as heat or electric field).[138] It is even possible to distinguish different layers of a magnetic thin-film heterostructure, making this a powerful complement to bulk magnetic characterization methods that sample the overall magnetization of a device.[212,213]

MOKE occurs when a plane-polarized beam of light is specularly reflected off the surface of a magnetic material in the presence of a magnetic field.[214] From a classical perspective, the electric field of the light generates motion of the electrons in the medium: in the absence of an applied magnetic field,

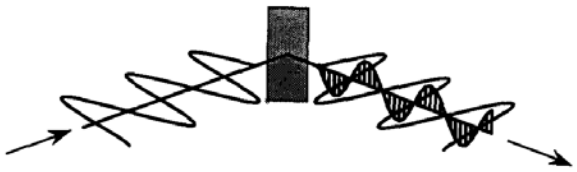

Figure 3.21: Illustration of the decomposition of linearly-polarized light into left- and right-circularly polarized modes upon refraction from a magnetized medium.[214]

the electron orbits experience the same force from both left and right circular polarizations; but when an external magnetic field is applied, an additional Lorentz force exerted on the electrons and the two orbits are no longer the same. Mathematically we may describe this behavior in terms of the dielectric tensor ϵ,

$$\epsilon = N^2 \begin{pmatrix} 1 & iQ & 0 \\ -iQ & 1 & 0 \\ 0 & 0 & 1 \end{pmatrix} \tag{3.11}$$

where N is the refractive index and Q is the magneto-optical (Voigt) constant of the material.[214] In the presence of magnetizing medium the incident light decomposes into left- and right-circularly polarized modes,

$$n = N(1 \pm gQ) \tag{3.12}$$

where g is the direction cosine between the propagation vector of the light and the magnetization, as shown in Figure 3.21.[214]

The more rigorous quantum mechanical model accounts for spin-orbit coupling between the local magnetic field inside the material and the unequal populations of spin-up and spin-down electrons.[211] Using the Heisenberg model and Kramers-Heisenberg dispersion formula, Hulme was able to calculate the different refractive indices for the two polarizations of light caused by the spin-orbit interaction.[215] This model was further refined by Argyres using perturbation theory to give the correct magnitude of splitting.[216]

Practically a MOKE measurement is conducted using a pair of crossed polarizers to determine the degree of rotation from *s* to *p* polarized light reflected off a magnetic sample. MOKE has the advantage of being able to detect tiny magnetic moments ($\sim 10^{-12}$ emu) near the surface of a material and can be equally well applied to multilayers and ultrathin (monolayer) films.[214,217] Measurements can be conducted in ambient conditions, under vacuum, or during heating and cooling cycles. Magnetic fields of up to several T can be applied, as can electrical biases.[163] Information about magnetic hysteresis, surface anisotropy, and interlayer exchange coupling can all be attained with this technique.[218]

3.5.3 Polarized Neutron Reflectometry

Polarized neutron reflectometry (PNR) is a complementary scattering technique for measuring depth-dependent magnetic information across buried heterostructure interfaces.[219] Cold neutrons, generated by a reactor or pulsed source, possess a wavelength between 2–40 Å, making them an excellent probe for condensed matter.[220] Neutrons also possess a nuclear spin that interacts with the magnetic induction present in a sample—yet they are charge neutral and can probe deeply into most materials.[221]

A typical neutron reflectometry experiment is conducted in a manner analogous to the XRR experiment described in Section 3.3. Below the critical edge neutrons will be totally externally reflected; as their angle of incidence is increased they will begin to diffract off the various layers of the crystal, creating a periodic oscillation in the reflectivity. The first Børn approximation of the reflectivity is then given by,

$$R \approx \frac{1}{Q_z^4} |4\pi \sum_{l=1}^{L} [(Nb)_l - (Nb)_{l-1}] exp(iQ_z d_l)|^2 \tag{3.13}$$

where Nb is the chemical scattering length density of the lth layer, Q_z is the momentum transfer vector parallel to the film normal, and d_l is the distance of the lth layer's interface below the surface.[222] In the presence of a magnetic induction **B** the total interaction potential seen by the neutron becomes,

$$U(z) = U_n(z) + U_m(z) = \frac{\hbar^2}{2m} N(z) b(z) + \mathbf{B} \cdot \hat{s} \tag{3.14}$$

where $\hat{s}$ is the neutron spin operator.[222,223] Because the neutron is a spin 1/2 particle, it may take one

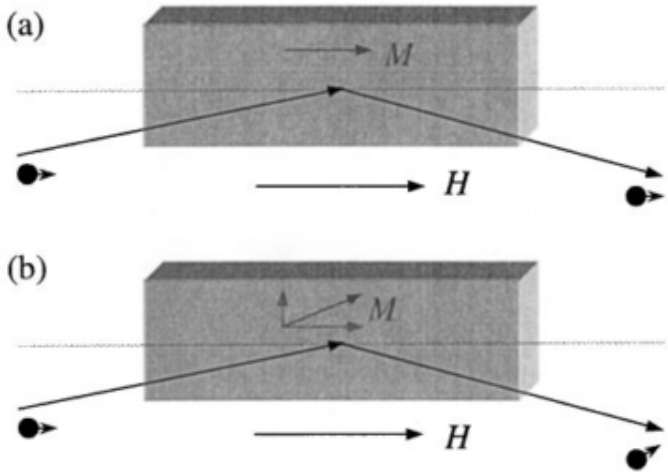

Figure 3.22: Schematic of the reflection of a polarized beam of neutrons from magnetized sample. (A) shows that for uniform **M** parallel to the guide field **H** only non-spin-flip occurs, while (B) shows that when a perpendicular component of **M** is introduced, spin-flip scattering occurs.[222]

of two polarization states with respect to the applied magnetic field (**H**), which we term parallel (+) or antiparallel (−). In a typical neutron reflectometry experiment we first polarize the beam using a known guide field ($\mathbf{H_p}$). The polarized beam then interacts with the local induction of the sample ($\mathbf{B_s}$) and its spin state change is recorded using a third, analyzer field ($\mathbf{H_a}$). For $\mathbf{H_a} \parallel \mathbf{H_p}$ we can then define four reflectivities: two "non-spin-flip" reflectivities, R^{++}, R^{--}, and two "spin-flip" reflectivities, R^{+-}, R^{-+}.[222] This is illustrated in Figure 3.22 for a magnetized sample; simply put, a component of magnetization perpendicular to the guide field will induce neutron spin-flipping.

One can record these four scattering cross-sections as a function of incidence angle to produce a reflectivity profile, as shown in Figure 3.23.A. To fit this profile one constructs a slab model consisting of layers of different chemical and magnetic scattering length density (Figure 3.24). The reflectivity is then calculated using the one-dimensional Schrödinger equation, while iteratively fitting to known film parameters.[219,222,224] The end result is a calculation of nuclear and magnetic scattering length density profiles, the latter of which can be directly translated into local magnetization, as shown in the bottom half of Figure 3.23.

In contrast to bulk magnetic characterization methods such as VSM, which sample all magnetic material, PNR makes it possible to isolate individual magnetic layers down to 2 Å, and measure absolute

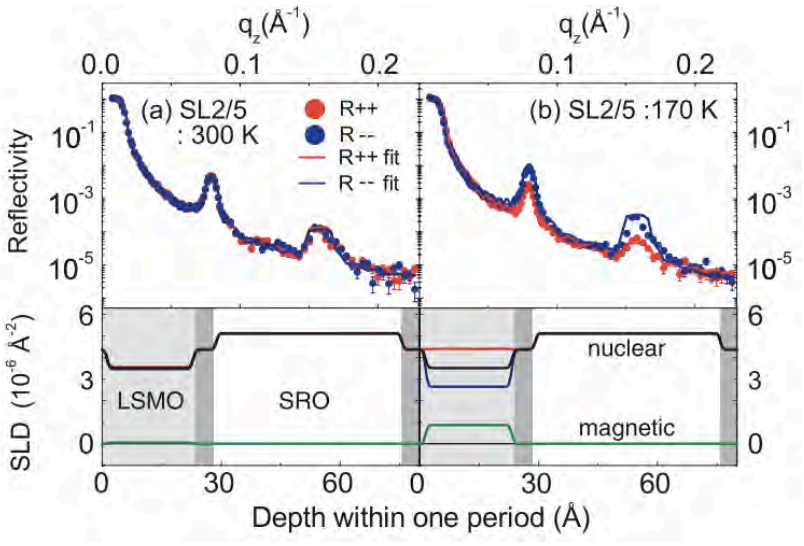

Figure 3.23: An example of polarized neutron reflectometry data collected at 300 (A) and 170 K (B) for an LSMO / SRO superlattice. The resulting magnetization depth profiles are shown in the bottom half of each figure.[225]

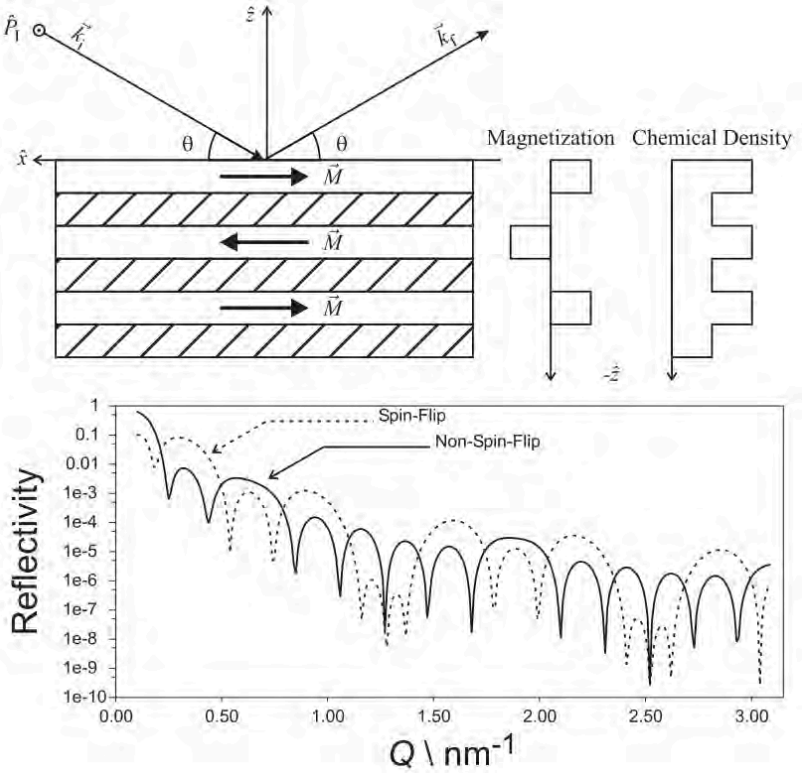

Figure 3.24: Illustration of the slab model of nuclear and magnetic scattering length density used to calculate a reflectivity profile. The measured data are iteratively fit until an accurate model of magnetic and chemical structure is attained.[224]

magnetizations smaller than 30 emu cm^{-3}.[219] PNR is also non-destructive and, since neutrons are so weakly interacting, samples can be placed in various *in situ* holders and environments.[226,227] As already described, neutron models benefit immensely from local information about chemistry and structure, making them an excellent complement to the previously discussed techniques of TEM, EELS, and XRD.

3.6 Density Functional Theory

Density functional theory (DFT) is a powerful computational method for estimating the ground-state energy of an ensemble of atoms.[228] Using DFT it is possible to calculate a variety of physical properties, including the electronic, thermal, optical, and magnetic response of a system.

We begin with the binding energy (E_{bind}) of a simple diatomic molecule, illustrated in Figure 3.25. In this model the binding energy of the system is given by the equation,

$$E_{bind}(R) = E_0(R) + \frac{Z_A Z_B}{R} - E_A - E_B \tag{3.15}$$

where $E_0(R)$ is the ground-state energy, R is the distance between nuclei, and E_A and Z_A are the atomic energy and charge of atoms A and B.[228] The Hamiltonian for N electrons is,

$$\hat{H} = \hat{T} + \hat{V}_{ee} + \hat{V} \tag{3.16}$$

where the kinetic energy operator $\hat{T}$, the electron-electron repulsion operator $\hat{V}_{ee}$, and the one-body operator $\hat{V}$ are defined as follows,

$$\hat{T} = -\frac{1}{2}\sum_{j=1}^{N} \nabla_j^2 \tag{3.17}$$

$$\hat{V}_{ee} = \frac{1}{2}\sum_{i \neq j} \frac{1}{|\mathbf{r}_i - \mathbf{r}_j|} \tag{3.18}$$

$$\hat{V} = \sum_{j=1}^{N} v(\mathbf{r}_j) \tag{3.19}$$

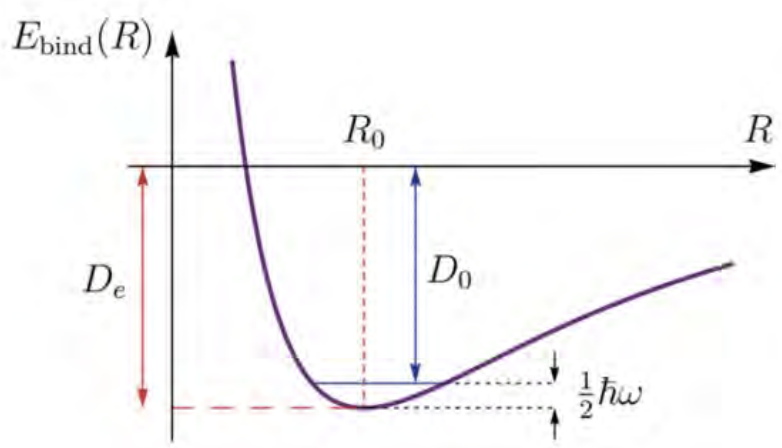

Figure 3.25: Binding energy curve for a diatomic molecule. R_0 is the bond length and $\frac{1}{2}\hbar\omega$ is the zero-point energy.[228]

The ground-state energy must satisfy the variational principle,

$$E = \min_{\Psi} \langle \Psi | \hat{H} | \Psi \rangle \tag{3.20}$$

where the minimization is applied to all antisymmetric N-particle wavefunctions and E is equivalent to $E_0(R)$ in Equation 3.15. Ψ is commonly approximated using a variety of methods, including Hartree-Fock and coupled cluster approximations, Møller-Plesset perturbation theory, and Greens functions.[229–231]

In DFT we define an electron density $n(\mathbf{r})$, such that $n(\mathbf{r})\, d^3r$ is the probability of finding any electron in a volume d^3r about $\mathbf{r}$.[228] We then approximate the kinetic energy density of a non-interacting, spin-unpolarized system as,

$$T^{TF} = a_s \int d^3r n^{5/3}(\mathbf{r}) \tag{3.21}$$

$$a_s = 3(3\pi^2)^{2/3}/10 \tag{3.22}$$

The interelectron repulsion is modeled by the electrostatic self-energy of the charge density (Hartree

energy) as,

$$U = \frac{1}{2}\int d^3r \int d^3r' \frac{n(\mathbf{r})n(\mathbf{r'})}{|\mathbf{r}-\mathbf{r'}|} \tag{3.23}$$

The one-body potential is given by,

$$V = \langle \hat{V} \rangle = \int d^3r\, n(\mathbf{r})v(\mathbf{r}) \tag{3.24}$$

And finally we minimize the sum of these three energies according to the constraint,

$$n(\mathbf{r}) \geq 0 \int d^3r\, n(\mathbf{r}) = N \tag{3.25}$$

This is the basic form of DFT first described by Thomas and Fermi.[232,233] Various other approximations are commonly used, including density functionals, the local spin density approximation (LDA), and the generalized gradient approximation (GGA), which permit more precise determinations of energies.[228] Using these methods it is possible to simulate an array of materials properties that can be correlated to experimental techniques. From these simulations one can isolate various features of a system to determine the major contributor to a phenomenon of interest. Such simulations can also guide materials selection and experimental design; while computationally-intensive, they are often more efficient than laboratory "trial and error" methods.

An example of the power of this technique is given in Figure 3.26. Here DFT is used with the GGA to calculate the magnetic ground state of a $La_{0.7}Sr_{0.3}MnO_3$ / $BaTiO_3$ / $La_{0.5}Ca_{0.5}MnO_3$ / $La_{0.7}Sr_{0.3}MnO_3$ heterostructure.[234] Figures 3.26.A-C show various magnetic configurations assuming different directions of the ferroelectric polarization in the $BaTiO_3$ layer. This information may be compared to experimental results and can provide deep insight into the mechanisms behind magnetoelectric coupling in thin-film oxide heterostructures.

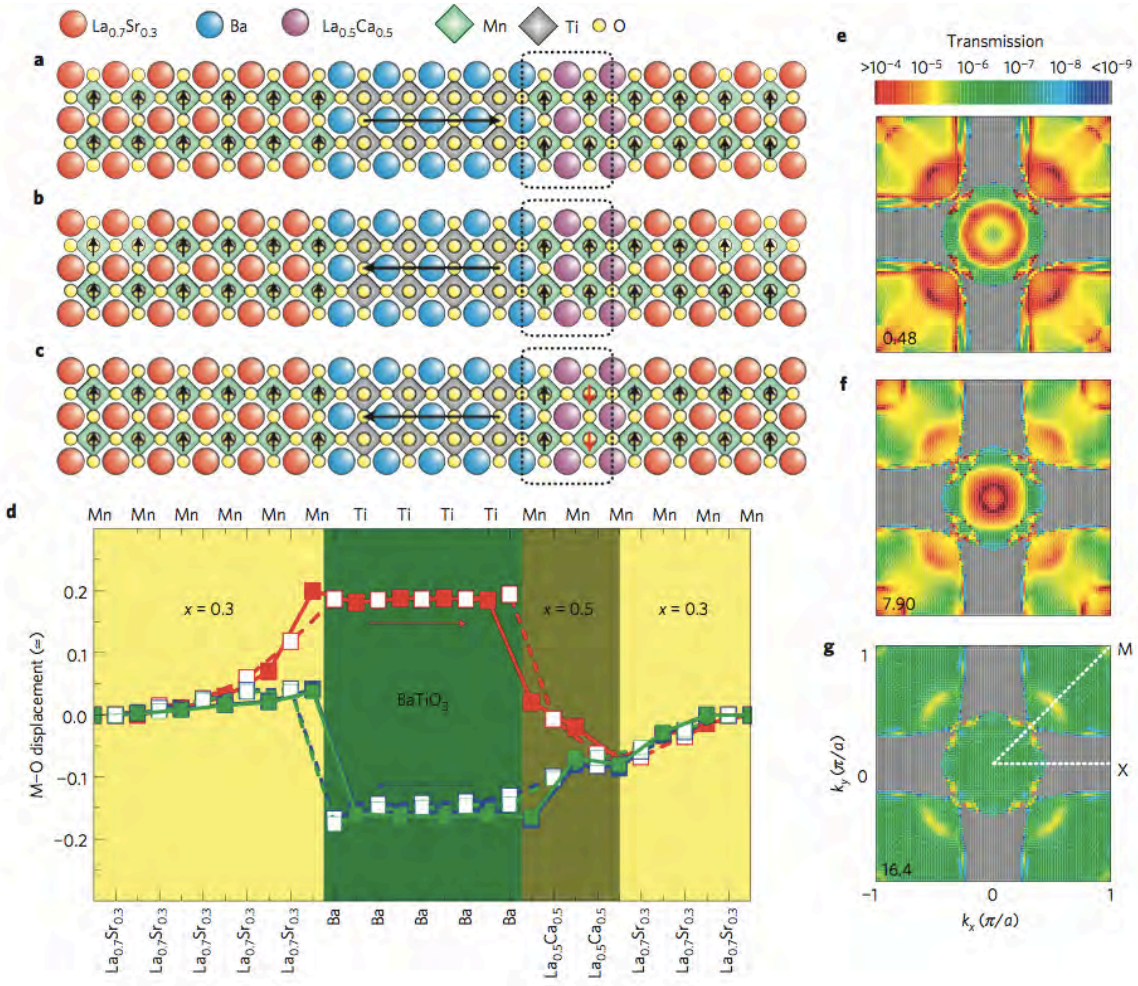

Figure 3.26: DFT-GGA calculations for a $La_{0.7}Sr_{0.3}MnO_3$ / $BaTiO_3$ / $La_{0.5}Ca_{0.5}MnO_3$ / $La_{0.7}Sr_{0.3}MnO_3$ heterostructure. (A-C) show magnetic configurations for different ferroelectric polarizations and ground states. (D) shows the calculated metal-oxygen bond displacements as a function of position. (E-G) are plots of the tunneling transmission in the two-dimensional Brillouin zone for configurations A-C.[234]

Chapter 4: Interface Effects on Magnetization in Ferrous Thin-Films

4.1 Introduction

In this first study we explore the interfacial properties of Fe / MgO thin-film composites. This model system allows us to assemble a set of techniques to correlate local structure, chemistry, and magnetization for the subsequent studies described in this thesis.

Fe / MgO tunnel junctions have received much attention for their use in hard drive read heads and other spintronic applications. This system is particularly interesting because of its magnetoresistive behavior and the abundance and low cost of its constituent elements. However, many questions remain about how the structure and chemistry of the Fe / MgO interface mediates magnetic behavior. In this study we report on transmission electron microscopy, electron energy loss spectroscopy, and magnetic characterization of Fe / MgO composite films with various morphologies. We explore relationships between film morphology, intermixing, and the resulting effects on magnetic structure. We find the presence of oxidation at the Fe / MgO interface, with a detrimental impact on the saturation magnetization of the composite. We also observe changes in coercivity and magnetocrystalline anisotropy with film morphology and thickness. These results will inform the design of MgO-based tunnel junctions and improve our understanding of how processing conditions, resulting in morphological and chemical changes such as oxidation, affect magnetization.

4.2 Background

The Fe / MgO system has been widely studied for its low-dimensional magnetic behavior, as well as its potential use in magnetoresistive tunnel junctions for memory applications. A small lattice mismatch of ~3.5% upon a 45° in-plane rotation of the Fe lattice enables the growth of high-quality films according to the $\left(\mathrm{Fe}\,[100](001) \parallel \mathrm{MgO}\,[110](001)\right)$ orientation relationship.[27,235,236] By varying the deposition temperature and rate, it is possible to grow a wide range of Fe film morphologies, ranging from discrete islands to connected structures and continuous films.[237] Many studies have focused on an enhancement

of magnetization in ultrathin Fe films, as well as magnetoresistive behavior in Fe / MgO / Fe tunnel junctions.[20,24,238,239] More recently the Fe / MgO system has been used as a canvas to explore relationships between microstructure and magnetism for potential device applications.[8,240–242]

It is known that Fe island coverage and interconnectivity can introduce configurational magnetic anisotropy that dominates over MCA.[243] This results in a rounding of hysteresis loops that depends on island size and distribution, interfacial strain, and intermixing at the Fe / MgO interface.[244] There has also been much debate about the potential formation of an interfacial iron oxide layer and its effect on magnetic order.[245–247] Tunnel barrier oxide thickness and composition are crucial design parameters in magnetic tunnel junctions: a competing iron oxide layer could increase the magnetoresistance of the junction to unusable levels and lead to unpredictable device behavior.[248,249] Likewise, the presence of interface defects or intermixing can change the transport behavior of the junction.[250] Electron microscopy is an ideal probe of the Fe / MgO interface, enabling simultaneous high-resolution characterization of chemistry and structure. The use of TEM and EELS makes it possible to identify the presence of any significant oxide layers while also exploring the effect of growth parameters on interdiffusion, roughness, and Fe film morphology. These measurements can then be correlated with changes in MCA measured by bulk magnetometry. This combination of techniques offers an improved understanding of the processing-property relationships necessary for the design of MgO-based spintronics.

4.3 Sample Growth

Samples were first synthesized by electron beam deposition: Fe films of three thicknesses (10, 20, and 30 nm) were then electron beam deposited at 500 °C at a rate of 0.2 nm s^{-1} onto MgO (001) substrates. Each film was subsequently capped in a nominal 5 nm layer of Au, deposited at 30 °C and a rate of 0.5 nm s^{-1}. X-ray diffraction and fluorescence measurements were performed on the samples to confirm the orientation, crystallinity, and thicknesses of the Fe films.

4.4 Electron Microscopy

Bright field cross-section TEM images reveal the Fe island structure and morphology in the films. Figure 4.1 shows TEM images along the MgO <100>, <011>, and <012> zone axes of the films, with Fe

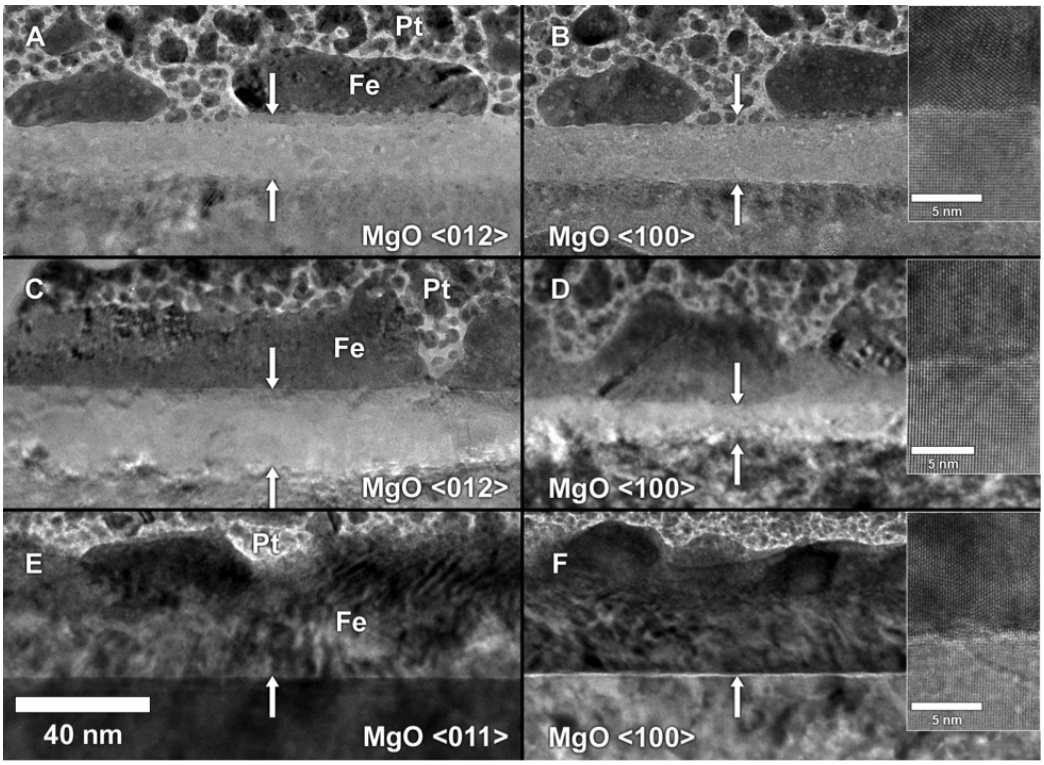

Figure 4.1: Sequence of bright field TEM images illustrating the evolution of Fe island morphology and interconnectivity with increasing Fe thickness along MgO <100>, <011>, and <012> zone axes. A-B, C-D, and E-F correspond to 10, 20, and 30 nm Fe thicknesses, respectively. Insets show high resolution images of each Fe / MgO interface and arrows indicate the boundaries of the Fe / MgO intermixed region.

layer thickness increasing from top to bottom. At the smallest Fe film thickness (Figures 4.1.A and 4.1.B) discrete islands ranging in thickness from 5–10 nm are clearly visible. The islands are spaced approximately 10 nm apart and appear to show faceting along their edges. A region of light contrast is visible between the bottom edge of the islands and the top of the MgO substrate.

As shown in Figures 4.1.C and 4.1.D, as the film thickness increases the islands begin to coarsen and exhibit the formation of small interconnecting regions. The nominal island thickness is 20 nm, with interconnecting regions approximately 5 nm thick and 10 nm wide. The faceting evidenced in the previous film remains, as does the band of light contrast below the islands, which appears thinner in the <100> orientation compared to the <120> orientation. The 30–nm film (Figures 4.1.E and 4.1.F) consists of a 30 nm continuous Fe layer, capped by small Fe islands ranging in size from 5–10 nm. At this point the island caps show more rounded edges instead of the facets previously observed. The layer

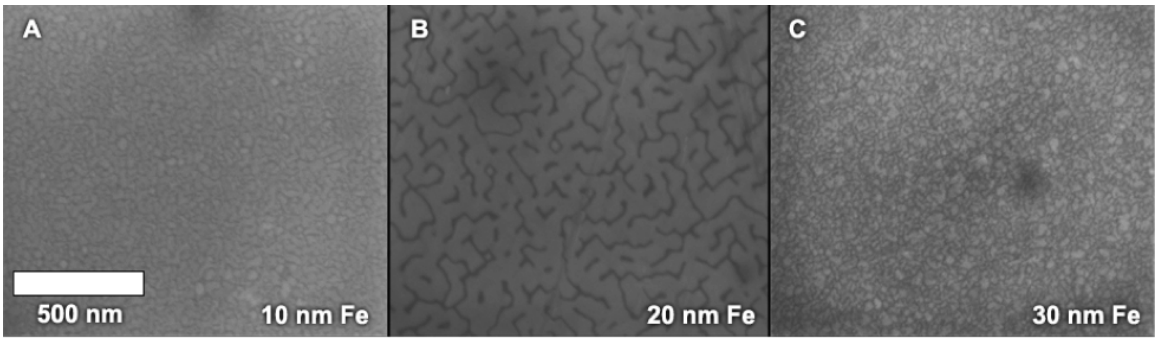

Figure 4.2: SEM plan-view images illustrating the evolution of Fe island morphology with thickness. (A) shows discrete, equiaxed islands. (B) shows connected, anisotropic islands, while (C) shows the appearance of a new layer of discrete, equiaxed islands.

of light contrast at the Fe-MgO interface is not visible in these samples.

High-resolution cross-section TEM micrographs (see insets of Figure 4.1) demonstrate the crystallinity of the Fe islands and MgO substrate, as well as the uniformity and smoothness of the interface. The islands themselves appear to be largely single-crystalline and faceted. The cross-section TEM micrographs are complemented by scanning electron micrographs that offer a two-dimensional plane view of the surface of the films. In Figure 4.2.A the 10–nm Fe film appears to consist of discrete, equiaxed islands ∼25 nm in diameter. The 20–nm Fe film (Figure 4.2.B) exhibits coarsening, enhanced island coverage and elongation of the islands to ∼80 nm. The surface morphology of the ∼30 nm Fe film (Figure 4.2.C) is similar to that of the 10–nm Fe film, consisting of equiaxed islands approximately 30 nm in diameter.

4.5 Chemical Mapping of Interface Valence

Figure 4.3 shows a bright field STEM image, as well as Fe K and Mg K edge STEM-EDS maps for the 20–nm film. The bright field image displays the aforementioned band of light contrast between the Fe islands and the MgO substrate. The accompanying elemental maps show that this band is a transition region of intermixed Fe and Mg approximately 15 nm thick. This appears to indicate diffusion of Mg from the substrate into the Fe layer.

Previous EELS studies have shown that the strong Fe L_3 and L_2 white lines near 710 eV correspond to the transition of electrons from spin-orbit split levels $2p_{3/2}$ and $2p_{1/2}$ to unoccupied $3d$ states.[251,252] The relative intensity of these two peaks is strongly dependent on the d-band occupancy and the Fe

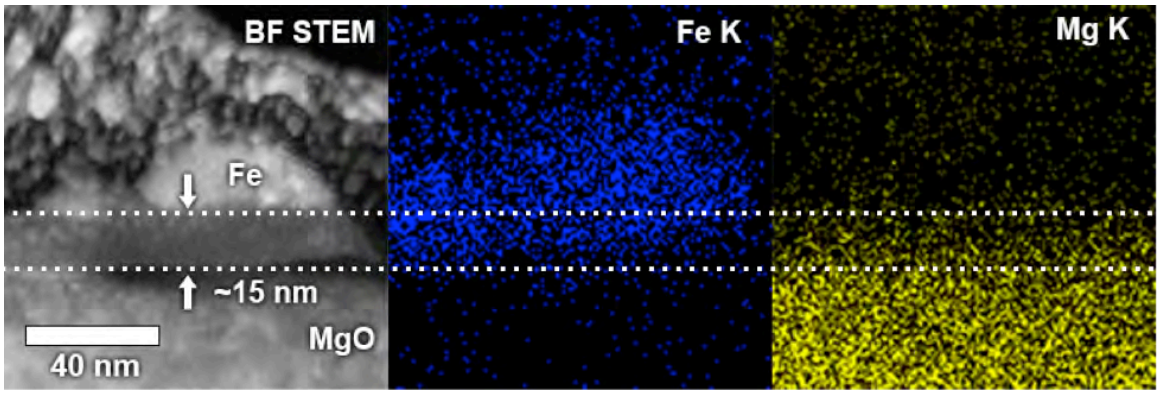

Figure 4.3: STEM-EDS maps of the intermixing of a 20 nm Fe island and the MgO substrate. From left to right, a bright field STEM image, Fe K edge map, and Mg K edge map are shown. The region between the dashed lines corresponds to an intermixed interface layer.

valence.[253,254] By measuring the L_3/L_2 ratio at various points across the Fe / MgO interface it is therefore possible to estimate the degree of oxidation. Since the magnetic properties of Fe depend on the $3d$ occupancy (see Section 2.3.1), this information is essential for understanding the magnetic behavior of the composite.

As shown in Figure 4.4, strong Fe L_3 and L_2 peaks are visible and observed in the film layer away from the interface, as is expected. The ratio of these peaks corresponds to a Fe^{2+} oxidation state (Figure 4.4.B). As the scan moves into the interface region, the intensity of these peaks begins to decay and their ratio changes, indicating a transition to a $Fe^{\sim 2.5+}$ oxidation state. Approximately 8 nm into the transition region the Fe L_3 and L_2 peaks disappear, indicating the absence of Fe. This decrease in L_3 and L_2 intensity is accompanied by an increase in the intensity of the O K edge at ~537 eV, commensurate with the increasing oxygen content of the substrate. The K edge consists of a small pre-peak at ~529 eV that decreases moving from spots 1–4 and indicates a transition from FeO to Fe_2O_3. The strong peak at ~537 eV is largely independent of the oxide phase but indicates the presence of oxygen. Between spots 5–11 a broad peak also forms at ~557 eV that can arise from multiple-loss contributions.[252] These changes in the Fe L and O K edges appear to indicate both oxidation of the Fe layer and intermixing with the underlying MgO substrate.

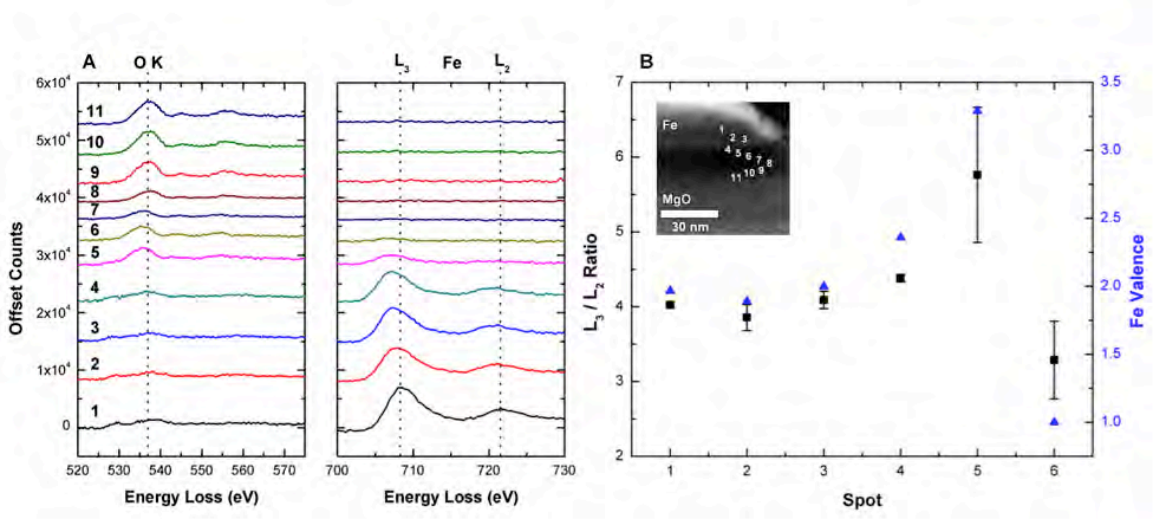

Figure 4.4: STEM-EELS maps of the interface between a 20–nm Fe film and the MgO substrate. (A) shows a series of spectra collected across the intermixed region at the points labeled in the inset of (B). (B) shows the calculated Fe L_3 / L_2 peak ratios (squares) and the estimated Fe valence (triangles) from Cosandey *et al.*[255] Error bars correspond to the goodness of the Gaussian fit to the two peaks at each spot.

4.6 Vibrating Sample Magnetometry

Figure 4.5 shows hysteresis loops for the films measured along <100> and <110> Fe crystallographic directions. The Fe film volume was calculated using X-ray fluorescence measurements for the various film thicknesses. The 10–nm and 20–nm films saturate at 1500 emu cm^{-3}, while the 30–nm film saturates near 1800 emu cm^{-3}. These values are close to the expected bulk saturation of 1700 emu cm^{-3}, but may differ due to oxidation at the interface and experimental error.[210] As shown in Figure 4.5.D, the coercivity increases from approximately ~238 Oe at 10 nm to ~428 Oe at 20 nm and decreases to ~55 Oe at 30 nm.

4.7 Film Coverage During Growth

The evolution of morphology and interface structure in these films can be measured by TEM and SEM micrographs. As shown in Figures 4.1.A and 4.1.B, the thinnest 10–nm Fe film consists of discrete, faceted islands similar in size to those previously observed during growth at 500 °C.[29] Continuing growth transitions to a layer-by-layer mode, as supported by other studies.[244,256] This is supported by images of the 20–nm film, which show that the islands have started to connect into a uniform layer (Figures

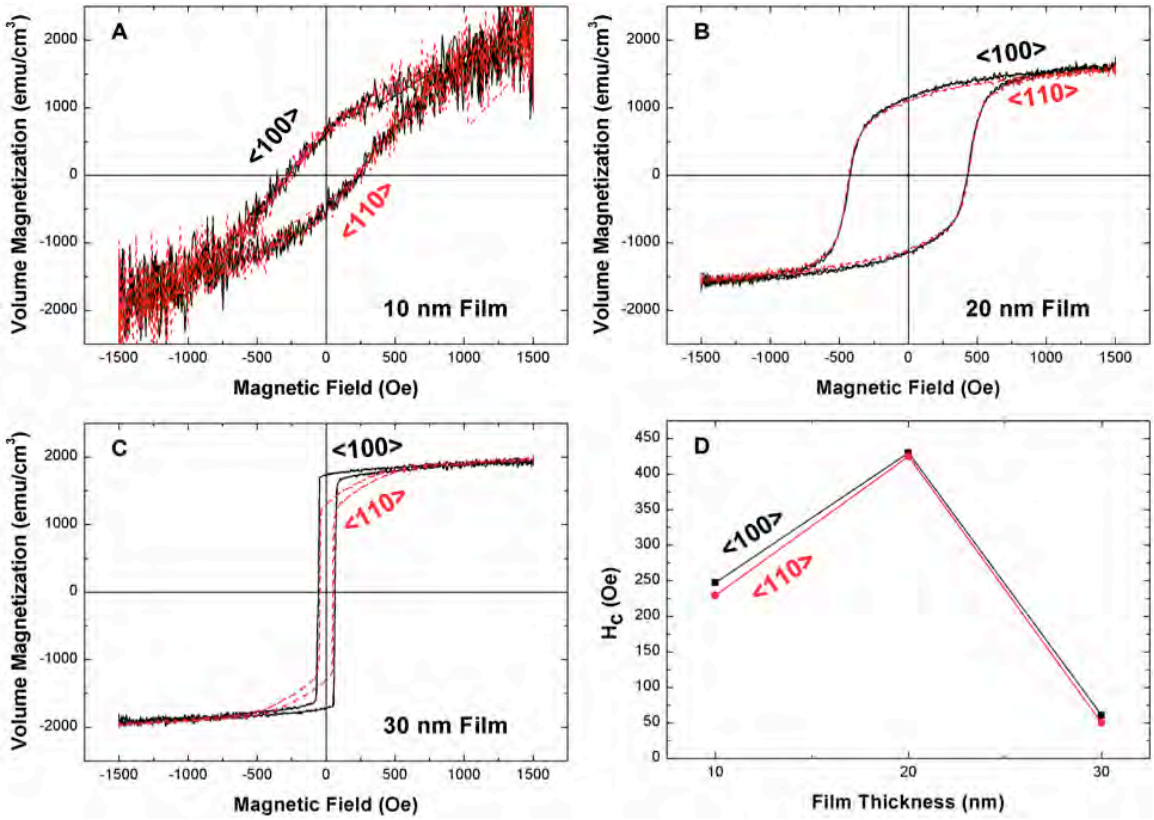

Figure 4.5: In-plane magnetic hysteresis loops for 10, 20 and 30 nm Fe films (A-C, respectively) along the Fe <100> and <110> directions. (A) shows little splitting between the two directions, while in (C) an obvious anisotropy exists between the <100> and <110> directions. (D) shows coercivities along <100> and <110> directions, with a peak at 20 nm.

4.1.C and 4.1.D). For a thickness of 30–nm (Figures 4.1.E and 4.1.F), there is a continuous Fe layer with some surface roughness. Because of the geometry of the sample, it is likely that the interconnectivity corresponds to the coarsening observed in SEM images (Figure 4.2.B). The increase in coverage at 20–nm also compares favorably to the minimum thickness for complete coverage predicted by helium atom scattering.[257] As growth continues the 30–nm film is again equiaxed with an average island size of 30 nm, corresponding to the formation of new Fe islands on a uniform sub-layer.

This behavior may be understood energetically using the model developed by Siegert and Plischke (S&P), which employs Monte Carlo simulations to consider a diffusive current onto a substrate.[258,259] The authors find that Fe is expected to form pyramidal islands with <011>–type facets in the initial stages of high temperature growth. This faceting is seen in TEM micrographs of the thinner samples along the corners of the islands (Figures 4.1.A and 4.1.C). In the S&P model, the faceted islands first nucleate on the free MgO surface and then coarsen according to a power law ($t^{1/4}$, where t = deposition time). Initial growth proceeds in an island growth mode due to the high surface energy of 4.0 J m^{-2} for Fe (001) compared to 1.2 J m^{-2} for MgO (001).[260] Island formation is preferred because of the high electronegativity difference between Fe and O, as well as a high cohesive energy and dielectric constant for MgO.[257] A relatively high monomer diffusion barrier of 0.4 eV has been calculated, which leads to a weak temperature dependence of adatom diffusion below ~220 °C. At low-temperatures adatoms are less mobile and these pyramidal structures remain stable even up to significant Fe thicknesses (200–300 nm).[261] For our high temperature depositions at 500 °C, adatoms are able to overcome the barrier to surface diffusion and coalesce into a uniform layer. Our results are supported by helium atom scattering and infrared absorption studies that find that complete coverage is reached near 20 nm.[257,262]

4.8 Oxide Formation at the Fe / MgO Interface

The two thinner films exhibit a clear region of light contrast below the interface, a possible result of inter-diffusion or oxidation. The diffusion of iron into the substrate is not unexpected at a 500 °C deposition temperature.[263,264] A simple calculation of the expected diffusion length can be conducted, according to

the diffusivity relationship,

$$\tilde{D} = 8.83\, exp\left(\frac{-74.6\, kCal}{RT}\right)\ cm^2\ s^{-1} \tag{4.1}$$

measured by other authors, where R is the ideal gas constant.[265,266] Assuming that the diffusivity is largely independent of composition, we expect that the concentration profile will take the form,

$$C(x,t) = 1 - erf\left(\frac{x}{2\sqrt{\tilde{D}t}}\right) \tag{4.2}$$

where x is the depth normal to the interface and t the time. At the deposition temperature of 500 °C and an approximate deposition time of 30 minutes, the concentration profile has an intermixed region of ∼0.2 nm. The diffusion length estimated by EELS from the drop off in the Fe white line signals is approximately 5–7 nm. The measured value is still an order of magnitude larger than the predicted diffusion length; a possible explanation is that the diffusivity values used in the above calculation were measured for bulk Fe powders and MgO single crystals, while diffusivities are expected to be much larger in reactive thin-film structures.

In addition to spatial information about diffusion, EELS allows one to study the migration of oxygen and oxidation of the Fe film at the interface. The oxidation state of the Fe away from the interface is ∼2+, but approximately 4–5 nm into the transition region it increases to ∼2.5+. This rise is accompanied by a rise in the intensity of the O K edge, indicating the possible formation of a mixed FeO–Fe_2O_3 magnetite phase. The presence of this magnetite region could reduce the saturation magnetization of the film by an amount proportional to the oxidized volume. Assuming a saturation magnetization of 1700 emu cm^{-3} for bulk Fe and 473 emu cm^{-3} for Fe_3O_4 and layer thicknesses of $d_{Fe} \approx 16$ nm and $d_{Fe_3O_4} \approx 4$ nm, we expect a saturation magnetization of ∼1413 emu cm^{-3}, close to the observed saturation of ∼1500 emu cm^{-3}.[13] Thus, EELS results indicate that oxidation could be a possible explanation for the film's reduced magnetization.

4.9 Morphology Effects on Magnetization

MCA can be estimated from measured in-plane magnetic hysteresis loops. The work done W in the magnetization process is equal to the area encompassed by the $M-H$ loop,

$$W = \int_0^M H dM \tag{4.3}$$

For cubic crystals we can define the anisotropy constants as: $K_0 = W_{100}$ and $K_1 = 4(W_{110} - W_{100})$. Because these constants are based on relative changes in loop area, they should not be affected by differences in domain wall motion.[210] For the 20–nm film we estimate $K_1 = 5.9 \times 10^5$ erg cm^{-3} and for the 30–nm film $K_1 = 12 \times 10^5$ erg cm^{-3}. The measured value for the thinner film is on the same order of magnitude as bulk Fe (4.8×10^5 erg cm^{-3}) but the anisotropy for the thicker is more than twice as large (12×10^5 erg cm^{-3}).[267] Martínez-Boubeta *et al.* have proposed that misfit energy introduced by dislocations can introduce an interface contribution to the anisotropy constant.[244,268] However, even the formation of misfit dislocations cannot account for the measured anisotropy value of the 30–nm film.

Other potential sources of anisotropy are interfacial roughness, intermixing, and oxidation of the Fe layer. While the films are relatively smooth, the latter two features have been observed by STEM-EDS and STEM-EELS. The formation of an iron oxide layer in particular could account for some of the observed changes in MCA. Previous studies of Co / Cu / Co / Fe_3O_4 / MgO (001) spin valves have shown that the presence of the oxide layer can induce changes in coercivity and reorient the easy axis of the bottom Co layer.[269] Although the formation of an oxide layer is generally regarded as thermodynamically unfavorable, there have been conflicting reports about its synthesis.[245,247,249] Studies of $CoFe_2O_4$ have shown significant diffusion of Mg into the oxide layer and a resultant reduction in saturation magnetization.[270,271] The transition from Fe^{2+} to $Fe^{2.5+}$ observed in EELS may also be the result of the formation of a mixed valence magnetite phase. Because $MgFe_2O_4$ is a thermodynamically stable spinel phase, its presence at the Fe / MgO interface cannot be entirely precluded.

Changes in the shape of the hysteresis loops may offer insight into the effects of film coverage on the magnetization process. The thinnest film (Figure 4.5.A) exhibits a rounded, sheared loop that progresses

to a squarer loop for the 20–nm film (Figure 4.5.B) and finally a sharp, square loop at a thickness of 30–nm (Figure 4.5.C). The changes in loop shape correlate directly to changes in film morphology and thickness measured by SEM and TEM. Previous work has indicated that the rounding of hysteresis loops results from incomplete film coverage, as well as the introduction of configurational anisotropy from layer-by-layer (Vollmer-Weber) island growth.[244] The squaring of the hysteresis loops correlates to the observed increase in coverage. Likewise, the increasing presence of these anisotropy terms is further supported by a splitting in the <100> and <110> hysteresis loops: at 10–nm, the two loops are similar, but as the film thickness a clear distinction between the two develops. This magnetic behavior coincides with the transition from discrete islands to a uniform layer.

The observed changes in coercivity (Figure 4.5.D) can also be related to film morphology. The thinnest 10–nm film consists of discrete islands with a coercivity of ∼238 Oe that increases to ∼428 Oe at 20–nm as the islands begin to connect. By 30–nm the islands have fully formed into a uniform layer and the coercivity drops to ∼55 Oe. Several effects resulting from the geometry of our samples may explain this behavior. It has been observed in thin-film Co that H_C is highly dependent on coverage and film thickness.[272,273] Coercivity in Co rises with increasing film coverage, but drops once a uniform layer has been formed. We see similar behavior during the transition from a discontinuous island network to a uniform film. This illustrates the importance of surface states and suggests that morphological barriers to domain wall motion can greatly affect coercivity. These conclusions are supported by modeling that predicts significant pinning and nucleation effects near island edges.[274] Studies of granular Fe thin-films also confirm an enhancement of coercivity up to ∼18 nm grain size, followed by a decrease proportional to d^{-1} (where d = film thickness).[275] It is thought that such grains possess a uniaxial surface anisotropy; as the surface/volume ratio decreases, the surface term becomes less dominant. This surface anisotropy may be responsible for suppression of superparamagnetic behavior, which would explain the increase in coercivity going from 30 to 20 nm.[276]

We may also consider local demagnetizing fields present near the island surfaces, which act to oppose the applied magnetic field.[277] Because the demagnetizing field depends on geometry and volume, the changing morphology and increasing thickness may affect H_C between 10– and 20–nm. Lastly, strain and

local chemistry should not be neglected. It is known that the magnetostriction of Fe reverses sign near 20 nm, the result of strain effects with increasing thickness.[31] Similar strain effects have been observed in FeCo, with H_C attaining a peak near 30–nm and decreasing with increasing film thickness, the result of strain gradients that form during growth.[278] We discuss these strain effects further in Appendix A. Interdiffusion between the film and substrate may also introduce additional pinning sites that compete with increasing film coverage.[279]

4.10 Conclusions

Electron micrographs reveal a clear progression in Fe–film morphology as a function of thickness. Discrete islands coarsen and interconnect until a uniform layer is formed, upon which a second layer begins to grow. Cross-section TEM micrographs indicate that the islands are faceted and that the interface between the Fe film and MgO substrate is largely free of dislocations. Micrographs, EELS, and EDS maps show evidence for the intermixing of Fe and Mg at the interface and the formation of an interfacial iron oxide layer, which is consistent with the decreased saturation magnetization of some of the films. Measured changes in coercivity, MCA, and the squaring of the hysteresis loops are related to increases in island coverage and thickness. While the calculated anisotropy constants are on the same order of magnitude as the expected values, there is evidence that the values are also affected by oxidation of the Fe. We propose several mechanisms for the observed coercivity behavior and find a significant dependence on film morphology, consistent with models of domain wall pinning. Future studies with polarized neutron reflectometry, X-ray photoemission spectroscopy, and EELS mapping of the films will make it possible to further quantify the magnetic and chemical nature of the interface with respect to film structure and morphology. These studies will be complemented by local TEM analysis to develop deterministic models of coercivity and hysteresis behavior.

Chapter 5: Substrate-Induced Polarization Effects in LSMO / PZT

5.1 Introduction

In this section we discuss magnetoelectric coupling effects in LSMO / PZT heterostructures. Building off the characterization toolkit established in the previous chapter, we employ a variety of local atomic-scale structural, chemical, and magnetic characterization methods to show that charge and strain coupling effects operate over different length scales. For the first time we are able to disentangle these effects using local probes and we suggest ways to tune coupling by controlling layer geometries.

Magnetoelectric oxide heterostructures are proposed active layers for spintronic memory and logic devices, where information is conveyed through spin transport in the solid-state. Incomplete theories of the coupling between local strain, charge, and magnetic order have limited their deployment into new information and communication technologies. In this study, we report direct, local measurements of strain- and charge-mediated magnetization changes in the $La_{0.7}Sr_{0.3}MnO_3$ / $Pb(Zr_{0.2}Ti_{0.8})O_3$ system using spatially-resolved characterization techniques in both real and reciprocal space. Polarized neutron reflectometry reveals a graded magnetization that results from both local structural distortions and interfacial screening of bound surface charge from the adjacent ferroelectric. Density functional theory calculations support the experimental observation that strain locally suppresses the magnetization through a change in the Mn e_g orbital polarization. We suggest that this local coupling and magnetization suppression may be tuned by controlling the manganite and ferroelectric layer thicknesses, with direct implications for device applications.

5.2 Background

Over the past decade great strides have been made toward electronics that utilize both electron charge and spin.[17,280] For instance, spin-transfer torque memories rely on the injection of a spin-polarized current to flip the magnetization of a free layer in a MTJ.[281,282] Direct control of spin polarization would greatly optimize the performance of such devices, enabling more robust and efficient comput-

ing architectures by conveying information through spin transport in the solid-state.[1,2,283,284] Recent advances in thin-film growth techniques have enabled the synthesis of oxide heterostructures where strain and charge effects are used to reversibly control spin polarization and magnetization at interfaces.[7,34,58,71,285–287] In particular there is growing interest in the connection between strain and magnetism in materials—most notably in the active tuning of magnetization *via* a coupling of local strain gradients and spin states through the so-called "flexomagnetic" effect.[288,289] Flexomagnetism describes the interactions between strain gradients and local spins; the presence of varying local strains may therefore give rise to a sizeable flexomagnetic contribution to magnetization.[288–290]

The current understanding of localized strain and charge-transfer effects on magnetization is limited, since previous studies have relied on non-local probes that are unable to directly map strain and valence changes.[95] Studies of ME heterostructures of the FM, half-metal LSMO and the piezoelectric PZT exemplify the inherent complexity of these systems. Previous work has found that charge-transfer screening of the adjacent ferroelectric layer is largely responsible for coupling in ultrathin (< 4 nm) LSMO films on PZT[138,140,163], while other studies have shown that variations in layer thickness and interfacial strain can also affect magnetization.[173,174,291–294] In these studies the local strain state of the LSMO / PZT interface was not measured. The relationship between interfacial strain and chemistry is also an important consideration in controlling the behavior of these materials, since previous studies have shown that strain fields around dislocations can act as fast paths for interfacial interdiffusion in LSMO / PZT.[295,296] It remains unclear how local strains evolve as a function of layer thickness, how strain and charge-transfer screening act in concert to mediate interfacial magnetization, and, more importantly, how to deterministically control this behavior.

To better understand flexomagnetism and ME coupling in oxides, it is necessary to move beyond bulk probes of strain and magnetization toward local measurements of strain and interfacial charge-transfer screening.[297–299] Here we synthesize heterostructures with different local strain and polarization states. Using a combination of local atomic and magnetic characterization, in conjunction with DFT calculations, we find evidence for significant strain-induced magnetization changes. We show that large strain changes occur throughout the magnetic layer and that they can be tuned by an appropriate choice

of substrate thickness. Furthermore, we show evidence for interfacial charge-transfer screening, which is secondary to dominant strain effects in thicker layers. Our analysis suggests that it is possible to favor a particular coupling mode by an appropriate choice of FM and FE layer thickness. Furthermore, by using local probes of structure and magnetization we are able to resolve strain and magnetization changes within each layer that would be inseparable by bulk techniques.

5.3 Sample Growth

We used a substrate-induced self-poling technique to vary the electrostatic boundary conditions of the bottom electrode interface, so as to pole the PZT away from (on LSMO) or toward (on $SrRuO_3$ (SRO)) the substrate, which we term as poled-up and -down, respectively.[300–304] Using this method it is possible to control the polarization of the PZT without the need for large, leaky planar electrodes that would preclude neutron measurements. Four heterostructures were deposited on single-crystal STO (001) substrates by PLD. Oxide metal underlayers of either LSMO or SRO were deposited on a bulk STO substrate, followed by either a "thick" (23–37 nm) or "thin" (13 nm) $Pb(Zr_{0.2}Ti_{0.8})O_3$ layer, and a cap of ∼10–19 nm LSMO, as shown in Figure 5.4. These thicknesses were chosen to explore the changes in strain profiles associated with gradual relaxation of PZT to the bulk.

5.4 X-Ray Diffraction

Layer geometries were confirmed using XRR, as shown in Figure 5.1. With the layer thicknesses measured *via* TEM as a starting point, the chemical profiles were iteratively refined in the GenX software package.[184] A list of samples is given in Table 5.1.

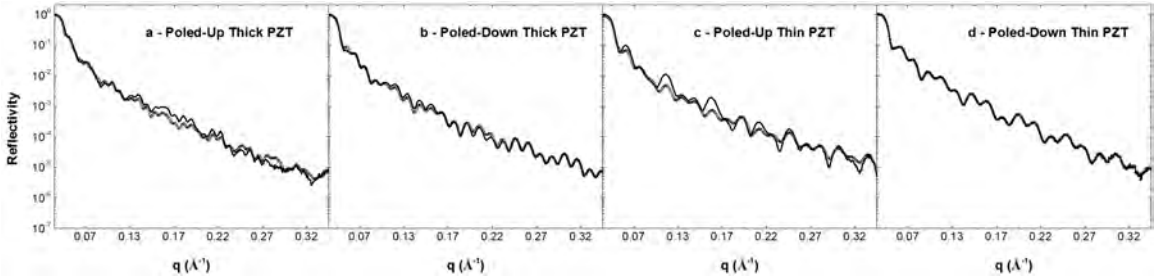

Figure 5.1: X-ray reflectivities (circles) and calculated fits (solid lines) measured with Cu K_α radiation at 298 K.

Table 5.1: Sample thicknesses measured by TEM.

PZT Polarization & Thickness	Top LSMO Thickness (nm)	PZT Thickness (nm)	Underlayer Thickness (nm)
Up Thin	13	13	13 LSMO
Up Thick	19	37	12 LSMO
Down Thin	13	13	8 SRO
Down Thick	10	23	13 SRO

To confirm film quality and epitaxy, reciprocal space maps were conducted on each sample around the STO 103 diffraction condition, as well as in a symmetric $\theta - 2\theta$ condition (Figures 5.2 and 5.3, respectively). The results show that the LSMO 103 diffraction condition is quite broad in-plane, suggesting it is not uniformly strained. There is evidence for some STO substrate mosaic in the poled-down thin PZT sample, but otherwise the samples are all single-crystalline and epitaxial. The strains relative to bulk LSMO measured by this technique are listed in Table 5.2. The poled-up PZT samples exhibit significantly larger in-plane strains (ε_{xx}) than the poled-down PZT samples—it should be noted that these samples consist of two LSMO layers, so this result is the average of strains across both layers.

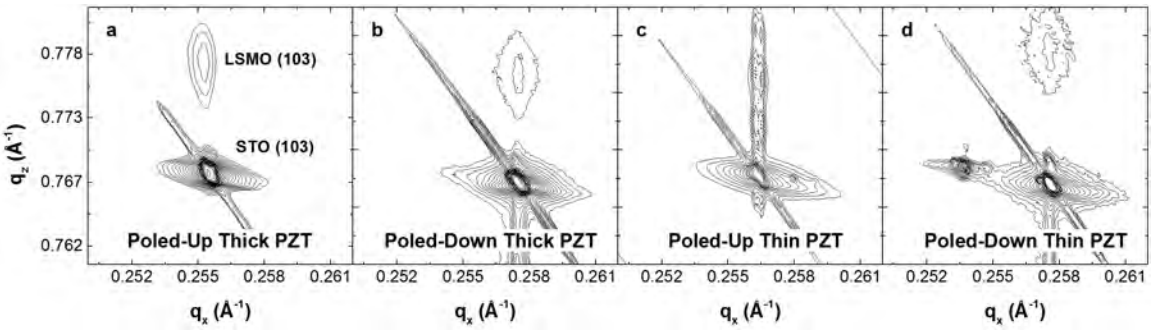

Figure 5.2: X-ray reciprocal space maps measured around the STO 103 diffraction condition using Cu K_α radiation at 298 K. The LSMO 103 peak is visible in the upper-middle portion of each panel. A diagonal analyzer streak is also visible in each of the maps.

Table 5.2: Average LSMO strains measured by XRD relative to bulk LSMO (3.87 Å).

PZT Polarization & Thickness	ε_{xx} (%)	ε_{yy} (%)	LSMO c/a Axial Ratio
Up Thin	0.791	0.0186	0.992
Up Thick	1.25	-0.33	0.984
Down Thin	0.450	-0.430	0.991
Down Thick	0.626	0.00952	0.994

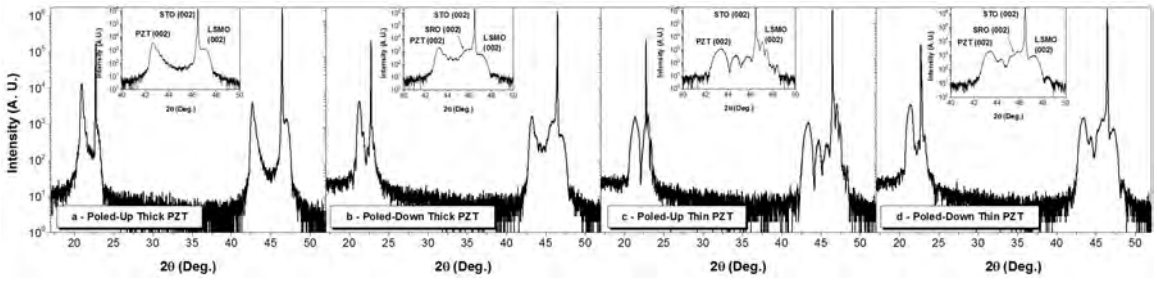

Figure 5.3: Symmetric $\theta - 2\theta$ scans of the (001) and (002) diffraction peaks measured using Cu K_α radiation at 298 K. The insets show detail around the (002) reflections and Kiessig fringes are visible around the PZT (002) peak.

5.5 Scanning Transmission Electron Microscopy

Aberration-corrected STEM was conducted to confirm the quality of the LSMO / PZT interfaces. STEM-HAADF images show that the layer thicknesses are nominally constant in the plane of the film (Figure 5.4). The reversal of the PZT polarization between the LSMO and SRO underlayers is also confirmed locally by measuring the Ti^{4+} cation displacement at several points along the interface (Figure 5.4.C,G).[305] Since all the film layers were grown *in situ*, it was not possible to conduct piezoresponse force microscopy (PFM) measurements without disturbing the pristine interfaces between each layer. XRD shows that in-plane, the films are constrained to the substrate. However, as we later discuss, the local strain state of the top LSMO layer varies greatly depending on the choice of underlayer and PZT thickness.

5.6 Local Ferroelectric Polarization Measurements

To determine the local PZT polarization with better than 8 pm precision, STEM-HAADF images were cross-correlated with the StackReg plugin for the ImageJ analysis program.[306,307] The program takes an input of serially acquired images, performs a cross-correlation routine to align them, and then averages across Z through the stack. It was found that the default rigid-body rotation alignment option worked best since it does not rescale or otherwise distort the images. Likewise, the default Z integration by the average value of each image also yielded the best results, some of which are shown in Figure 5.5.

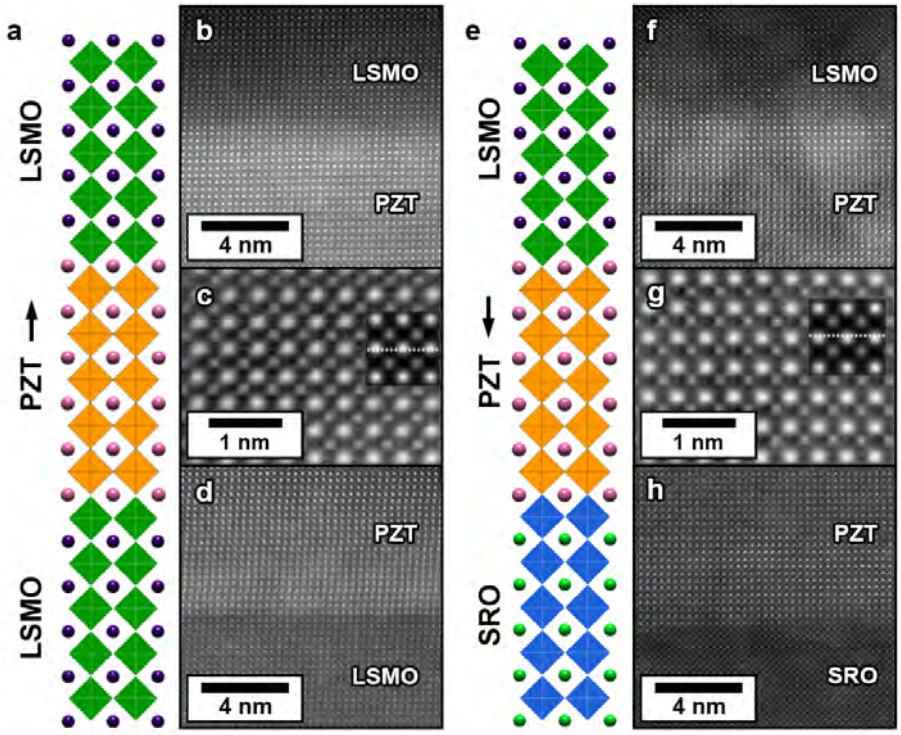

Figure 5.4: (A, E) Illustration of the two film structures used in this study, with the PZT polarization direction indicated by the arrows. Characteristic high-angle annular dark field (STEM-HAADF) images of the top (B, F) and bottom (D, H) PZT interfaces, showing the absence of any extrinsic defects. (C, G) Cross-correlated images of the PZT layer, confirming the change in polarization; the insets are the result of multi-slice simulations, with the horizontal dash corresponding to the center of the unit cell.

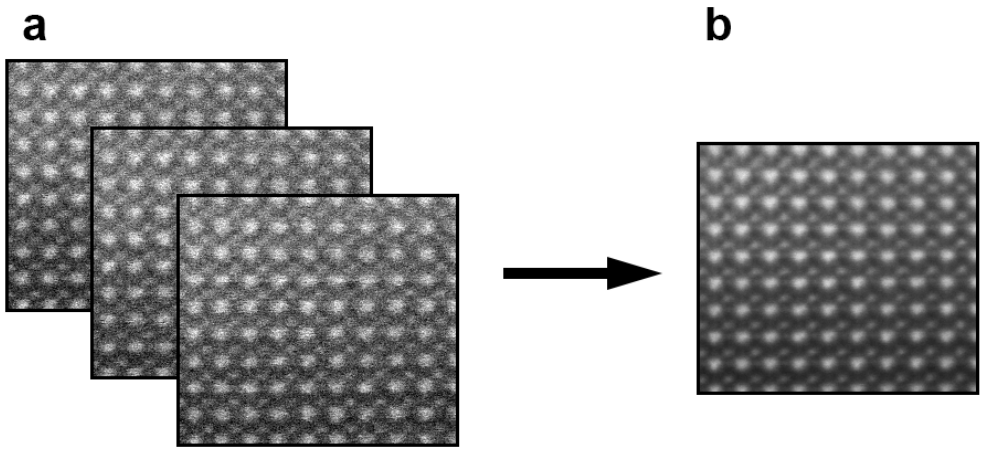

Figure 5.5: Illustration of the cross-correlation and deconvolution routine. (A) A series of acquisitions and (B) The reconstruction of 50 such images acquired over 5 μs intervals.

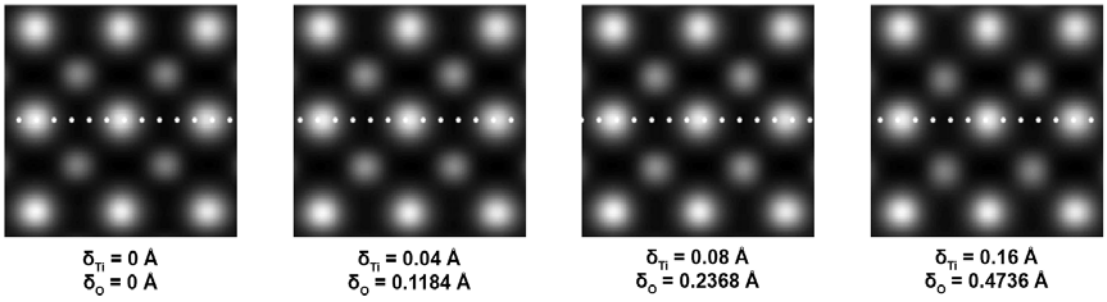

Figure 5.6: Multi-slice calculations conducted for a 16 nm thick PZT layer assuming differing cation displacements from their centrosymmetric positions. The dashed line is added as guide to the eye to show the difference in displacements.

Multi-slice STEM image simulations were then conducted using the QSTEM program.[194] The expected lattice parameters for the $Pb(Zr_{0.2}Ti_{0.8})O_3$ composition of PZT are $a_{PZT} \approx 3.935$ Åand $c_{PZT} \approx 4.132$ Å.[308] From the cation displacements measured by Jia *et al.*, it is possible to estimate the expected relationship between Ti (δ_{Ti}) and O (δ_O) atom displacements as $\delta_O \approx 2.96 \times \delta_{Ti}$.[304] Several structures were constructed and compared to the measured data; these structures are shown in Figure 5.6. The third and fourth figures from the left best fit the experimental STEM-HAADF images.

5.7 Bulk Magnetometry

Macroscopic magnetic hysteresis measurements (Figures 5.7.A,B) reveal a thickness-dependent saturation magnetization (M_S). The data shown have been normalized to the entire thickness of LSMO present in each sample. A remarkable 50% ($\sim$0.6 μ_B Mn^{-1}) difference in M_S occurs between poled-up and -down heterostructures based on thick PZT (Figure 5.7.A). A smaller $10-20\%$ ($0.1-0.2$ μ_B Mn^{-1}) difference in M_S occurs between poled-up and -down heterostructures based on thin PZT (Figure 5.7.B). For comparison, $M_S \approx 1$ μ_B Mn^{-1} is expected for $La_{0.67}Sr_{0.3}MnO_3$ at room-temperature.[146] These differences are also reflected in the Curie temperature (T_C) (Figure 2.C): the samples deposited on the thin PZT have a T_C of $335-342$ K, while the samples on thick PZT show T_C of $328-331$ K, compared to a nominal bulk T_C of $\sim$360 K.[309] Additional magnetometry, including details of alignment effects and more precise measurements of Curie temperature, are given in Appendix C.1.

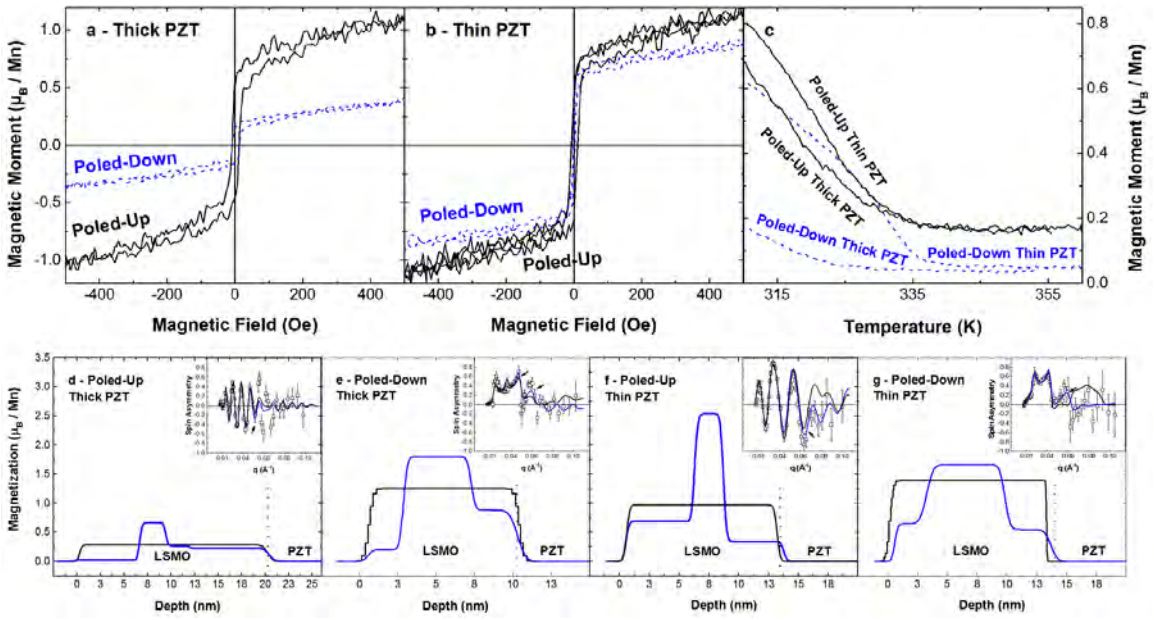

Figure 5.7: Top: (A, B) In-plane vibrating sample magnetometry (VSM) measurements conducted at 305 K along the [100] substrate direction, showing a ∼50% increase in saturation between the poled-up and poled-down thick PZT samples (A) and a 10–20% increase in saturation for the thin PZT samples (B). (C) Moment *versus* temperature measurements conducted in a 100 Oe magnetic field measured on heating show a significant enhancement of T_C with decreasing PZT thickness. Bottom: (D-G) Polarized neutron reflectometry (PNR) magnetization depth profiles measured at 298 K and with an in-plane magnetic field of 1 T along the [100] substrate direction. The insets show the measured spin asymmetry $\frac{R^{++}-R^{--}}{R^{++}+R^{--}}$ and the fits to the data. The vertical dashed lines mark the boundaries between adjacent film layers. The black lines are a model that assumes uniform magnetization throughout each LSMO layer, while the blue lines are a model that allows for graded magnetization through the LSMO. The arrows in the inset show regions of improved fitting. There is a clear suppression of magnetization across the majority of the top LSMO layer in (D), as well as suppression near the vacuum and PZT interfaces in the other samples (E-G).

5.8 Polarized Neutron Reflectometry

To probe the local origin of these magnetization differences, PNR was conducted at 298 K with an in-plane magnetic field of 1 T. Magnetization depth profiles (Figures 5.7.D–G) show that the M_S of the top LSMO layer varies spatially but is generally suppressed near the vacuum surface as well as at the PZT interface, as has been previously observed.[310] Strain-induced distortions of LSMO can suppress T_C and consequently room-temperature magnetization.[50,169,170,311] The suppression of T_C due to strain-induced distortions in LSMO results from changes in the Mn–O–Mn bond angles that govern electron hopping between the Mn e_g states responsible for double-exchange.[162,312,313] Because of the sensitivity of the double-exchange mechanism to strain, local strain fluctuations—if present—may give rise to the graded magnetization profiles observed in PNR. Further details of the PNR fitting and results are given in Appendix C.2.

5.9 Geometric Phase Analysis

GPA was used to test this strain hypothesis by measuring strains directly from TEM micrographs with ∼0.1% accuracy down to the nanometer scale.[199,200] In all samples the in-plane strain is essentially uniform over the 3–5 nm integration window, varying by $< 0.1\%$. We note that there is good agreement between the average GPA-measured c/a axial ratios and those measured by XRD (Table 5.2). The out-of-plane strain relative to bulk unstrained LSMO increases normal to the PZT interface, reaching a maximum at the vacuum surface. Using this technique we are able to map the local c/a axial ratio within each sample (Figure 5.8.B). This analysis reveals that for both thick PZT samples (Figure 5.8.C,D) the c/a of the LSMO increases from ∼0.96 at the PZT interface to $1.01 - 1.03$ at the vacuum surface. This corresponds to a strain gradient of approximately $2.95 - 4.76 \times 10^6$ m^{-1}. The poled-down thin PZT sample (Figure 5.8.F) shows a similar trend, increasing from ∼0.98 at the PZT interface to ∼1.03 at the vacuum surface (a gradient of 4.76×10^6 m^{-1}). However, the poled-up thin PZT sample (Figure 5.8.E) shows a U-shaped profile that drops from ∼1.04 at the PZT interface to ∼0.97 at the middle of the LSMO and increases to ∼1.05 at the vacuum surface. The changes coincide with significantly different c/a ratios in the adjacent PZT layer, which ranges from $1.04 - 1.1$, suggesting that the interfacial strain

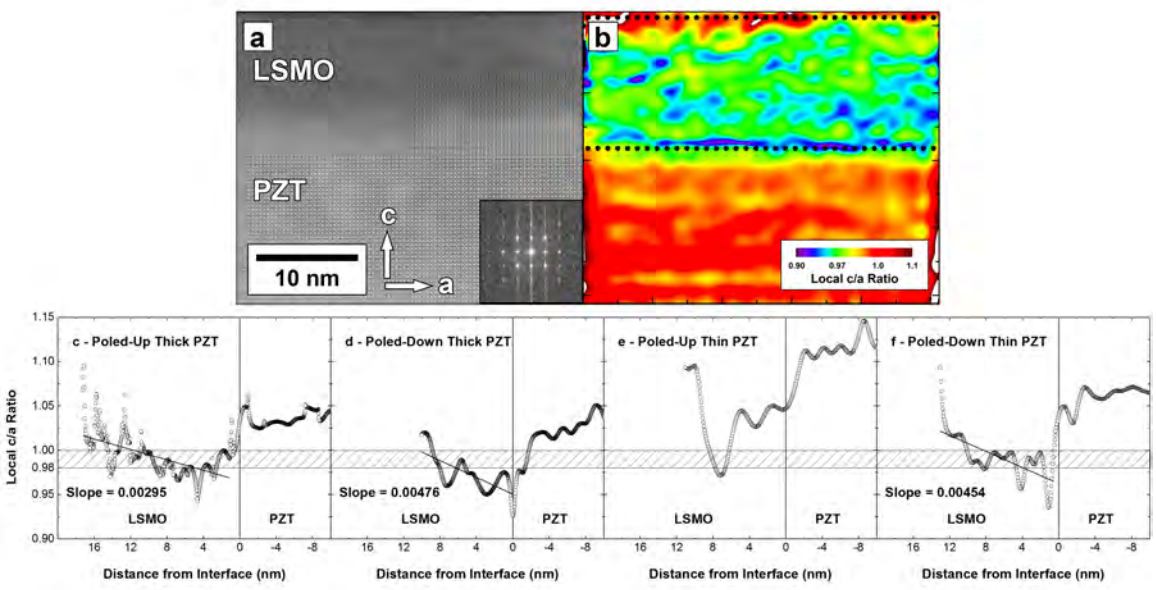

Figure 5.8: (A) Characteristic STEM-HAADF micrograph of the LSMO / PZT interface; the inset shows the fast Fourier transform of the PZT layer. (B) Characteristic map of local c/a axial ratios in the LSMO and PZT layers. This ratio varies throughout the LSMO but is largest at the vacuum interface. (C-F) Line scans of c/a normal to the LSMO / PZT interface for all four films. The vertical line indicates the PZT boundary, while the horizontal dashed region indicates the c/a range outside of which magnetization is expected to be suppressed.

state is heavily dependent on the tetragonality of the underlying PZT layer, as well as the thickness of the LSMO layer. More importantly, a comparison of the PNR and GPA data shows that in general, a LSMO c/a that deviates outside of the range of $0.98 - 0.995$ coincides with local suppression of magnetization, which agrees well with changes in bulk properties.[314] The observed strain fluctuations may correlate to local spin changes, particularly since they are comparable in magnitude to the strains needed to induce a measurable flexoelectric effect in other systems.[315,316] While direct flexomagnetism is limited to a subset of symmetry classes, indirect flexomagnetism is expected to be present in all magnetoelectrics, wherever polarization and magnetization are coupled.[317]

5.10 Strain Effects on Magnetization

To estimate the strain-induced suppression of magnetization in the samples, we turn to the empirical model of Millis *et al.*[162] and DFT calculations, in which we isolate various contributions to the observed magnetization behavior.

5.10.1 Millis Model

Millis *et al.* proposed a model that relates T_C to the substrate strain-induced enhancement of the Jahn-Teller distortion relative to unstrained bulk LSMO.[162,318] We choose this model since it allows us to directly substitute the averaged local $\langle c/a \rangle$, extracted from the experimental GPA, to obtain an estimate of T_C. We then conducted DFT calculations to explore the electron-lattice effects mediating the microscopic coupling in detail.

For the poled-up PZT samples we find from GPA that $\langle c/a \rangle_{LSMO} \approx 0.99 - 1.01$ and we estimate $T_C \approx 249 - 295$ K for the top LSMO layer using the Millis *et al.* model. These out-of-plane strains appear to greatly suppress the FM ordering of the top layer, as is observed in PNR (Figure 5.7.D,F). In contrast, for the poled-down samples, we find that $\langle c/a \rangle_{LSMO} \approx 0.98 - 0.995$ and we estimate $T_C \approx 319 - 327$ K. These distortions result in a higher T_C and larger average magnetization across the LSMO (Figure 5.7.E,G). The predicted and measured Curie temperatures for the poled-down samples are in excellent agreement (Figure 5.7.C); however, the agreement for the poled-up samples is poorer, perhaps because these samples include two LSMO layers and the measurement of T_C is less accurate.

Using the Millis *et al.* model, T_C for the films was estimated using the average lattice parameters from XRD, as shown in Table 5.3. The values agree relatively well between the calculated and measured T_C for the poled-down PZT samples. However, the calculated T_C deviates significantly for the poled-up films. This discrepancy can be explained by different strain states for the LSMO layers above and below the poled-up PZT interlayer. XRD is insensitive to these small changes because of the superposition of relatively broad LSMO 103 diffraction peaks.

Moreover, it is not possible to rule out chemical changes that would affect the T_C ($\varepsilon = 0$) parameter

Table 5.3: Curie temperatures measured and estimated from the Millis *et al.* model using XRD.

PZT Polarization & Thickness	Measured T_C (K)	Calculated T_C (K)	Upper Bound (K)	Lower Bound (K)
Up Thin	335	300	305	284
Up Thick	331	274	278	259
Down Thin	342	341	345	322
Down Thick	328	313	318	296

in the model. We can estimate the effect of a 5% doping variation using the bulk phase diagram (see bounds in Table 5.3).[309] The agreement with the magnetic data is still excellent for the poled-down PZT samples deposited on SRO, but—even allowing doping fluctuations—the model based on XRD cannot account for the Curie temperature of the poled-up PZT samples deposited on LSMO. This suggests that the LSMO layers are in different local strain states, since EELS shows that the nominal chemistry is the same in all samples, and emphasizes the importance of local strain measurements to deconvolute these strains.

5.10.2 Density Functional Theory

We next perform spin-polarized DFT calculations within the generalized-gradient approximation plus Hubbard-U method on a series of LSMO structures to isolate the contributions of epitaxial strain from interfacial charge-transfer on T_C and Mn e_g orbital polarization. We choose lattice constants consistent with the experimental epitaxial constraints and $\langle c/a \rangle_{LSMO}$ ratios ranging from 0.985 (poled-up thick PZT) to 0.994 (poled-down thick PZT). We note that these axial ratios refer to the metric shape of the simulation cell, not local octahedral elongations, and thus deviations from the local strain measurements determined using GPA are expected. The atomic positions are then fully relaxed, allowing for rotations and bond elongations. First we computed the optimal $\langle c/a \rangle$ for LSMO on (001)-oriented STO and obtained a value of 0.985, which is consistent with the average $\langle c/a \rangle$ of LSMO on poled-up thick PZT. We then applied 0.5% and 1% uniaxial strain along the [001]-direction to simulate the range of observed axial ratios (Figure 5.9), as a means to disentangle the strain contributions from interface effects due to coherent strain of LSMO with varying PZT thickness and polarization. We then calculated a mean-field theoretical ferromagnetic Curie temperature, T_C^{MFT}, following the procedure in references 319 and 320.

Our DFT results indicate that out-of-plane stretching monotonically increases T_C^{MFT} from 292 K (0%) to 323 K (1%) at the highest $\langle c/a \rangle$ state. Our T_C^{MFT} trend compares favorably with our measured poled-up PZT samples that have LSMO underlayers as well as the model calculations following Millis *et al.* To quantify the orbital occupancy, we calculated the electron orbital polarization, $P = \frac{n_{x^2-y^2} - n_{z^2}}{n_{x^2-y^2} + n_{z^2}}$, of Mn e_g orbitals from the partial density of states (PDOS) spectra, where $n_{x^2-y^2}$ and n_{z^2} are the area under the curve for $d_{x^2-y^2}$ and d_{z^2} orbitals, respectively, integrated up to the Fermi level.[321] A positive value for

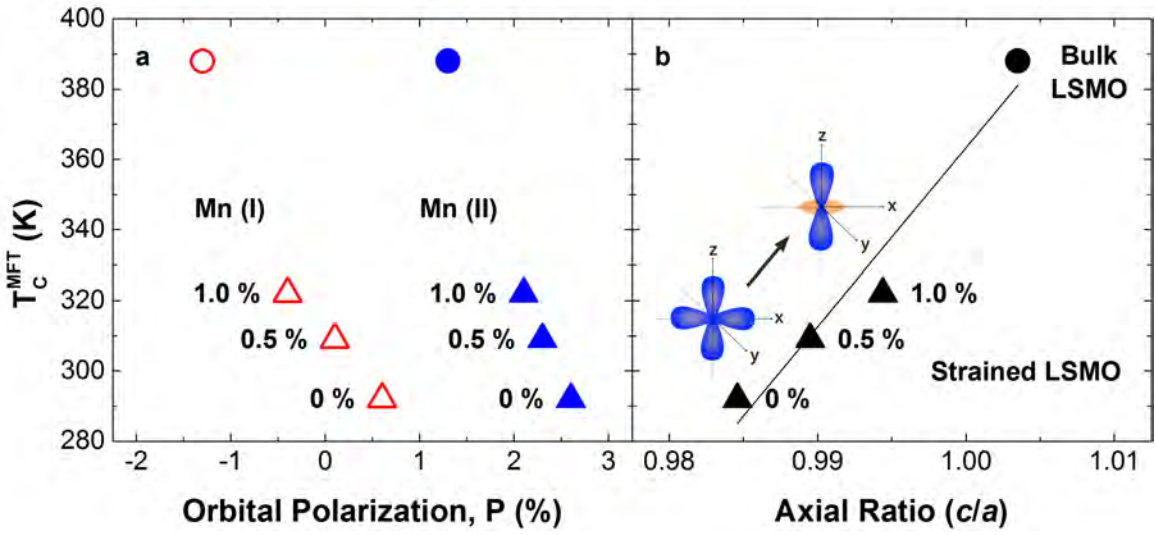

Figure 5.9: (A) Relationship between T_C^{MFT} (K) and P (in %) for various simulation cells as calculated from DFT. Positive value for P indicates the percentage excess of Mn e_g electrons filling $d_{x^2-y^2}$ orbital relative to the d_{z^2} orbital and vice versa. The 30-atom supercell contains two distinct Mn atoms, Mn (I) (open, red) and Mn (II) (filled, blue). (B) Relationship between T_C^{MFT} (K) and axial ratio (c/a) as calculated from DFT. A clear trend emerges between c/a, P, and T_C^{MFT}. In unstrained LSMO, both $d_{x^2-y^2}$ and d_{z^2} are filled. The application of in-plane tensile strain promotes preferential $d_{x^2-y^2}$ filling in both Mn atoms; simultaneously T_C^{MFT} decreases. However, out-of-plane stretching gradually promotes transfer of charge to d_{z^2} orbitals and a corresponding gradual increase in T_C^{MFT} is found. Circles correspond to bulk LSMO and triangles are epitaxially strained LSMO (under uniaxial strain varying from 0–1% along the [001] direction).

P indicates that electrons favor $d_{x^2-y^2}$ orbital occupancy and a negative P value indicates that electrons favor d_{z^2} occupancy. We find that in bulk unstrained LSMO, P takes both negative and positive values, and the magnitude of P is roughly the same for both Mn sites (Figure 5.9 and Figure 5.5); T_C^{MFT} for bulk LSMO is estimated to be 388 K. Application of an in-plane tensile strain alone promotes preferential $d_{x^2-y^2}$ orbital filling; P takes only positive values at both Mn sites and T_C^{MFT} reduces drastically to 292 K, which agrees well with our experimental measurements made on poled-up samples. Uniaxial strain along [001] gradually transfers charge to the Mn d_{z^2} orbital aligned along the z-direction, as expected.[168,169,322] At 1% elongation, P becomes both negative and positive ($T_C^{MFT} \approx 322$ K), albeit reduced relative to unstrained LSMO. Commensurate with the filling of d_{z^2} orbitals as a function of out-of-plane stretching, T_C^{MFT} is also found to increase, indicating a direct association between the c/a axial ratio, macroscopic T_C^{MFT} and P in LSMO.

Although a clear trend emerges between c/a, T_C and P, in agreement with previous literature,[323,324] we recognize that our DFT calculations do not fully capture the T_C behavior of the poled-up samples.

While these samples have the largest average $\langle c/a \rangle$ value (as measured by XRD), their measured T_C is lower than that of other samples, indicating the existence of an additional competing mechanism not captured in our simulations. We also note that these calculations are done assuming a uniform uniaxial strain, in contrast to the changing strain observed in GPA; nonetheless, we believe that these results provide a valuable insight into how increasing tetragonality affects electronic and magnetic ordering.

5.11 Electron Energy Loss Spectroscopy

To probe other possible coupling mechanisms, such as chemistry changes or charge-transfer screening, we have conducted EELS mapping of the LSMO / PZT interface. The Mn $L_{2,3}$ white lines near 640-665 eV are measured in this study since they contain information about excitations from the spin-orbit split $2p_{3/2}$ and $2p_{1/2}$ levels to available states in the $3d$ band.[19,197,325–328] Screening of surface charge from the adjacent PZT layer gives rise to a change in the local $3d$ band occupancy, reflected in a deviation from the nominal Mn^{3+} / Mn^{4+} ratio of ∼3.3.[329,330]

Figure 5.10 shows the results of STEM-EELS maps at the LSMO / PZT interface for the thick samples. We find that the interfaces are quite sharp, with the EELS signal limited to one to two atomic planes away from the interface; however, because STEM is a localized technique it is impossible to completely rule out some intermixing in either interface. Both samples possess a bulk valence of ∼3.4 (near the nominal 3.3), but at the interface the value for the poled-up sample drops to ∼2.63 while that of the poled-down sample increases to ∼4.26. Additionally, there is a clear shift of the Mn L_3 edge toward lower energy in the poled-up sample (Figure 5.10.B), indicating lower valence; however, the shift in the poled-down sample is not as pronounced.[327,329] The valence change is spread over 3–4 u.c. at the interface, with an average valence at ∼3.02 for poled-down and ∼3.89 for poled-up—a difference of ∼0.87. It should be noted that the error bars on this data are still rather large, ruling out more detailed analysis of the induced valence, but there is clearly an interfacial change likely resulting from interaction with the adjacent ferroelectric layer.

Thus, while local strain fluctuations suppress magnetization across larger length scales, it appears that charge-transfer screening operates in a ∼2 nm interface region at the PZT boundary (Figure 5.7.D-G), in line with prior estimates.[133,135,175] PNR measurements show that the change between states in the

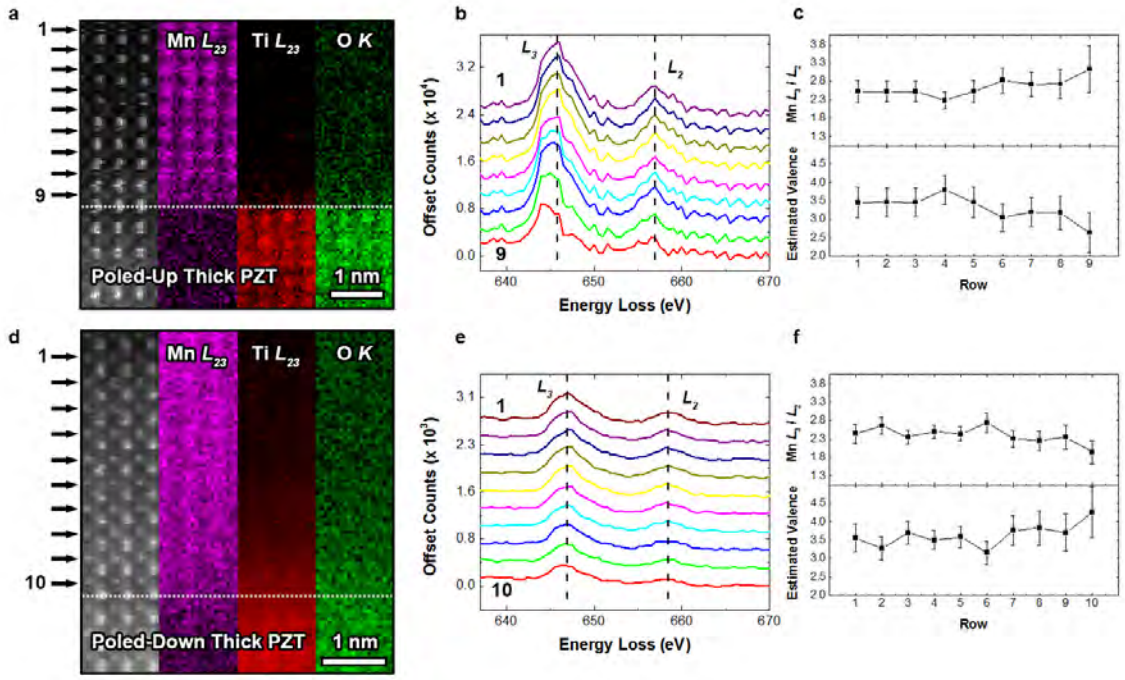

Figure 5.10: STEM-HAADF images and EELS maps of the top LSMO / PZT interface in the poled-up (A) and poled-down (D) thick PZT samples. The numbers indicate the atomic rows across which average spectra were collected and correspond to the Mn $L_{2,3}$ spectra in (B, E). (C, F) Calculated Mn L_3 / L_2 ratios and estimated Mn valences from each row. Error bars correspond to the standard error of the Gaussian fits to the edges. Although both samples possess the same valence in the bulk (∼3.4), they diverge near the PZT interface, indicating screening of surface charge from the adjacent PZT layer.

thick samples at 298 K is $\Delta m = m_{down} - m_{up} = 0.88 - 0.22 = 0.66\ \mu_B\ \mathrm{Mn}^{-1}$, while, for the thin samples, $\Delta m = 0.54 - 0.34 = 0.20\ \mu_B\ \mathrm{Mn}^{-1}$. These values agree well with previous magneto-optical studies of ultrathin LSMO that found $\Delta m = 0.76\ \mu_B\ \mathrm{Mn}^{-1}$.[138]

5.12 Conclusions

Several trends are now clear. We find that it is possible to self-pole PZT through the use of an appropriate substrate material, a method which may be extended to many other systems. Macroscopic bulk magnetization measurements show that M_S and T_C depend on both PZT polarization and thickness. PNR measurements reveal that M_S varies locally and is most suppressed at the LSMO / vacuum interface, where the GPA-measured LSMO c/a axial ratio is largest. Furthermore, we find evidence for large strain gradients (∼10^6 m^{-1}) in the LSMO. Phenomenological models show that local strains affect the

Mn e_g electronic distribution and play a role in suppressing the LSMO T_C. EELS and PNR also reveal the presence of a $\sim$2 nm charge-transfer screening region that affects magnetization at the PZT interface. However, the magnitude of the induced magnetization does not directly agree with the previous work of Vaz *et al.*, suggesting that other factors may be at work.[138]

Collectively the results obtained in this study suggest a more complex model of strain- and charge-mediated magnetization in FE / FM composites. We find that the tetragonality of the PZT has a pronounced effect on the interfacial strain in the LSMO: a larger PZT c/a corresponds to a larger interfacial c/a in the LSMO, which gradually increases near the vacuum surface. In the ultrathin limit ($<$ 4 nm), strain fluctuations in LSMO are minimal and charge-transfer screening drives coupling. As the LSMO thickness increases, local strain fluctuations soon overwhelm the magnetization of the layer, indicating that layer geometries are crucial components in the design of these materials. In excess of the ultrathin limit, our PNR results indicate that local strain can induce much larger changes in the magnetization profile of LSMO than charge-transfer screening. By tuning the PZT tetragonality through doping or an appropriate substrate, it is possible to reshape magnetization gradients in the FM. Our results suggest that a piezoelectric substrate may be used to actively control local strain and directly vary the spin state of the FM. Moreover, it is possible that such strain may actually act to rotate the magnetization of the LSMO layer. The wealth of insight provided by this suite of techniques shows that local probes of magnetization, strain, and chemistry are an invaluable way to understand coupling of multiple degrees of freedom in MEs and emerging flexomagnets.

Chapter 6: Screening-Induced Magnetic Phase Gradients at LSMO / PZT Interfaces

6.1 Introduction

In this section we continue our study of LSMO / PZT / LSMO trilayers and explore the relationship between FE polarization and charge screening in the manganites. We measure the local FE polarizations at the PZT interface that result in asymmetric charge-transfer screening lengths. We suggest that this charge screening is responsible for a local phase transition at the manganite interface.

Magnetoelectric LSMO / PZT thin-film heterostructures offer a window into the rich and varied interactions of structure, chemistry, and magnetic order at oxide interfaces. However, the current picture of coupling in this system is clouded by a insufficient understanding of local ferroelectric polarization and its effect on the formation of interfacial magnetic and electronic phases. Here we present direct, local measurements of electron energy loss, ferroelectric polarization, and magnetization, which we use to map the phases present at the LSMO / PZT interface. We combine these experimental results with density functional theory calculations to elucidate the microscopic interactions governing the interfacial response in this system. We draw two main conclusions from our experiments: namely, that there exists a magnetic phase transition at the LSMO / PZT interface that depends on local PZT polarization direction and magnitude; and that a metal-insulator transition at the interface gives rise to significantly different charge-transfer screening lengths. Collectively these results help establish a framework by which to understand the fundamental asymmetries of magnetoelectric coupling in oxide heterostructures.

6.2 Background

Doped La_{1-x}"A"$_x MnO_3$ manganese perovskite oxides have received considerable attention for spintronic applications, since they offer many handles for structural control of magnetism and possess a relatively high ferromagnetic Curie temperature ($T_C \approx 360$ K).[35,309,331] In these compounds "A" is an alkaline earth such as Ba^{2+}, Sr^{2+}, or Ca^{2+}; for alloying in the range of $0 < x < 1$, the charge state of Mn ions is between the nominal values, 3+ and 4+.[35] The electronic configuration for such a $3d$ $Mn^{3+\delta}$ cation

in an octahedral crystal-field can be written as t_{2g}^3 and e_g^δ, where the magnitude of δ depends on the concentration of x and the degree of hybridization with the neighboring O $2p$ states in the MnO_6 octahedra. In the present work, we focus specifically on the $La_{1-x}Sr_xMnO_3$ (LSMO) system at compositions near x $\approx$ 0.3, where double-exchange interactions dominate, e_g^δ electrons become delocalized, and a completely spin-polarized FM ground-state is stabilized.[35]

One of the intriguing aspects of t_{2g}^3 and e_g^δ configuration is the δ-electrons in the e_g electronic states. Practically one may achieve control of e_g^δ electrons by interfacing LSMO with a functional substrate, such as a ferroelectric material like PZT, BTO, and BFO, through controlled growth in a thin-film heterostructure.[7,70,332] In this class of *artificial* magnetoelectrics, it has been shown that the magnetic order is coupled to the ferroelectric order at the interface, thereby permitting reversible electric-field tuning of T_C and transport properties.[7,57] The use of a ferroelectric substrate provides several mechanisms to control magnetization, including the screening of bound surface charge from the ferroelectric by metallic carriers in the ferromagnet.[145,332,333] Poling of the ferroelectric toward or away from the ferromagnet changes the effective charge state at the interface, resulting in a reversible change in local Mn ion valence and spin state.[143,163] This charge-transfer screening phenomenon, already widely employed in semiconductor *p-n* junctions, typically operates over a few u.c. and greatly depends on interface structure and chemistry.[133,333,334]

There are many unresolved questions about the nature of this coupling mechanism in the LSMO / PZT system. Pioneering X-ray absorption spectroscopy and magnetooptical studies by Vaz *et al.* found evidence for charge-transfer screening that is estimated to occur over 1–2 u.c. at the interface and depends on the PZT polarization direction.[138,140,143,163] However, this effect alone was insufficient to explain the measured interface magnetization, so the authors suggested that an associated spin structure change may also occur. We have recently shown that charge-transfer screening acts in concert with local strain fluctuations to mediate coupling, and that the dominant coupling mechanism appears to depend on film geometry.[335] Moreover, it is known that a suppression of ferroelectric polarization may occur at interfaces, but it is unclear how this may play a role in the LSMO / PZT system.[304] Recently, Lu *et al.* have proposed a theoretical mechanism whereby charge-transfer screening electrostatically

dopes an interface region of the LSMO into a paramagnetic insulating state, which might explain the larger screening lengths we and others have measured.[146,335,336] More insight is clearly needed into local ferroelectric polarization and the presence of such a "doping-induced double layer," which would have fundamental implications for oxide-based electronics.

Aberration-corrected STEM is an ideal technique to study local ferroelectric polarization, valence, and interfacial phases at spatial regimes inaccessible by traditional surface probes. Here we directly probe chemistry and valence across the LSMO / PZT / LSMO heterostructure, which we then relate to local magnetization, ferroelectric polarization and DFT. Using EELS we explore changes in the O *K* edge fine structure, which captures the evolution in Mn valence across the heterointerface. We find that the local ferroelectric polarization is different at each interface and that this leads to gradients in the associated magnetic and electronic interfacial phases.

6.3 Sample Growth

We have used a substrate-induced self-poling technique to spontaneously pole the PZT layer during growth, as described in Section 5.3.[335] We first deposited a ~12 nm $La_{0.7}Sr_{0.3}MnO_3$ layer onto a bulk STO (001) substrate using PLD. This method sets the appropriate electrostatic boundary conditions to spontaneously self-pole the PZT "up" or away from the STO substrate.[300–304,335] We then deposited a ~37 nm thick $PbZr_{0.2}Ti_{0.8}O_3$ layer and a second ~19 nm thick LSMO layer. Assuming a uniform, nearly monodomain configuration, this single sample will possess two different LSMO interface charge states: the top layer will be in a hole charge depletion state and the bottom layer will be in an accumulation state.[138]

6.4 Electron Energy Loss Spectroscopy – O *K* Edge

EELS line scans were collected from several parts of the film to study the spatial evolution of local Mn valence normal to the PZT interface. We employ an enhanced linescan method, termed a "SMART" linescan; this approach averages a larger area of the interface, reducing the risk of beam damage to the film and increasing the signal-to noise ratio of the scan, thus ensuring an accurate interpretation of the EELS fine structure.[337] Figure 6.1.A shows an aberration-corrected STEM-high-angle annular dark

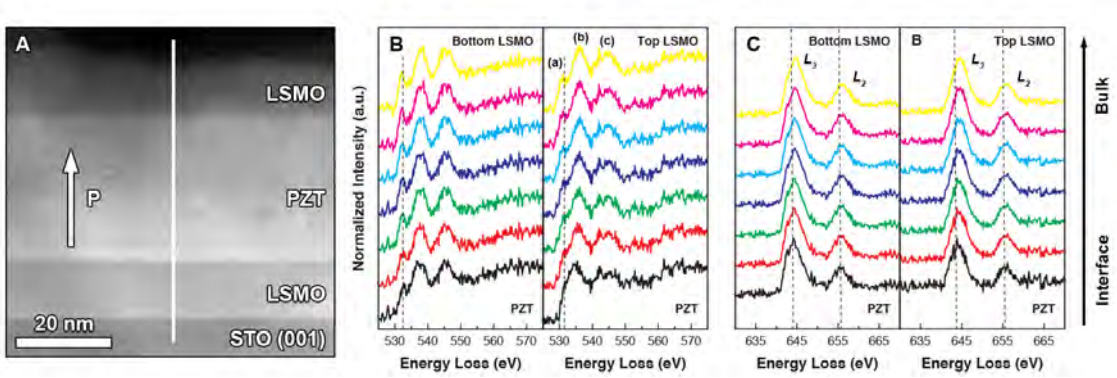

Figure 6.1: Structural and chemical mapping of the heterostructure. (A) Cross-sectional STEM-HAADF micrograph of the film structure, with the direction of ferroelectric polarization and SMART linescan region indicated. (B) Power-law subtracted EEL spectra corresponding to the O K edge, collected every lattice plane beginning at the LSMO / PZT interface. **(a)** and **(b)** correspond to the pre- and main-peak features, respectively. (C) Power-law subtracted EEL spectra corresponding to the Mn $L_{2,3}$ edge. The direction of the bulk LSMO is indicated by the arrow for both scans. We note that only the first ∼10 nm of the top LSMO layer remain after sample thinning.

field (STEM-HAADF) image of the overall heterostructure, in which all the layers are clearly resolved. Spectra for the O K and Mn $L_{2,3}$ edges were measured as a function of position normal to the interface and are shown in Figures 6.1.B,C (the La $M_{4,5}$ and Ti $L_{2,3}$ edges, also resolved, are not shown here). These scans allow us to measure fine structure changes in both the vicinity of the PZT and the bulk of the LSMO layers.

The O K edge is highly sensitive to the local bonding environment and can be used as an indicator of Mn valence changes.[197,327,338] This edge, in the dipole approximation, selectively probes the density of unoccupied states of O atoms with 2p character arising from the first-order transition of electrons from O 1s to 2p states. The configuration interaction, *via* hybridization, between the unoccupied states of O 2p and Mn 3d symmetry manifests as unique pre-peak spectral signatures, whose weight and peak positions reflect the oxidation state or valence of the Mn cations.[197,327,339,340] Here we probe the O K edge at both the top and bottom LSMO / PZT interfaces to directly map and link the magnitude and direction of ferroelectric polarization to Mn valence state.

The O K edge fine structure for the bottom and top interfaces is shown in Figure 6.1.B, in which both the pre- and main-peak are clearly resolved. We observe three prominent features (labeled **a**-**c**), which correspond to excitations associated with hybridized states of O 2p states with Mn 3d, La 5d / Sr

4d and Mn 4sp bands, respectively.[197] We find that the pre- to main-peak energy separation ($\Delta E_{O(b-a)}$) changes in the vicinity of the LSMO / PZT interface, as shown in Figures 6.2.A,B. In both cases the samples display a decrease in separation from a bulk value of ∼5.5–6 eV; this decrease is small for the bottom LSMO (Figure 6.2.A), ∼0.5 eV over 1 nm, but is nearly double for the top LSMO (Figure 6.2.B), ∼1.0 eV over 2.5–3 nm. These energy separations ($\Delta E_{O(b-a)}$) may be correlated to changes in the Mn valence near the interface;[197] however, because it is difficult to draw comparisons to absolute valence, we instead focus on the overall trends in behavior (these trends are further supported by shifts in the pre-peak intensity, shown in Figure D.1).

6.5 Density Functional Theory

To probe the structural and chemical origin of these EELS features, as well as their relationship to local phases, we have conducted DFT+U calculations using the planewave pseudopotential method as implemented in the QUANTUM ESPRESSO package;[341] the O K edge X-ray absorption spectra were calculated with the help of XSPECTRA package.[342,343] We note that although EELS and XAS are not strictly speaking equivalent, these spectroscopy techniques probe the same electronic states: comparisons of experimental and theoretical spectra across the two techniques thus provide invaluable insight and are commonly used to rationalize observed trends and fine structure features. The core and valence electrons were treated with ultrasoft pseudopotentials[344] and PBEsol exchange-correlation functional.[345] We apply the plus Hubbard-U correction within the Dudarev formalism,[346] using $U_{eff} = 2$ eV to treat the Mn 3d orbitals (see Appendix 6.3). We consider three unique chemical compositions: $La_{0.6}Sr_{0.4}MnO_3$, $La_{0.7}Sr_{0.3}MnO_3$, and $La_{0.8}Sr_{0.2}MnO_3$, permitting us to explore the electronic structure trends for a broad range of chemical doping. All compositions have a rhombohedral crystal structure (space group $R\bar{3}c$) but they differ in the magnitude of octahedral rotations.[347–350] From the $La_{1-x}Sr_xMnO_3$ phase diagram,[36] the ground state for the three compositions is expected to be ferromagnetic and metallic. We also note that the "nominal" charge state of Mn is expected to be different in the three compositions, which we confirmed from the calculated magnetic moments (see Appendix 6.3). Our main goal is to disentangle the effect of Mn valence, magnetic spin order, and octahedral rotations on the O K edge spectral features.

The La and Sr partial occupancies were simulated by following an approach adapted by Burton *et*

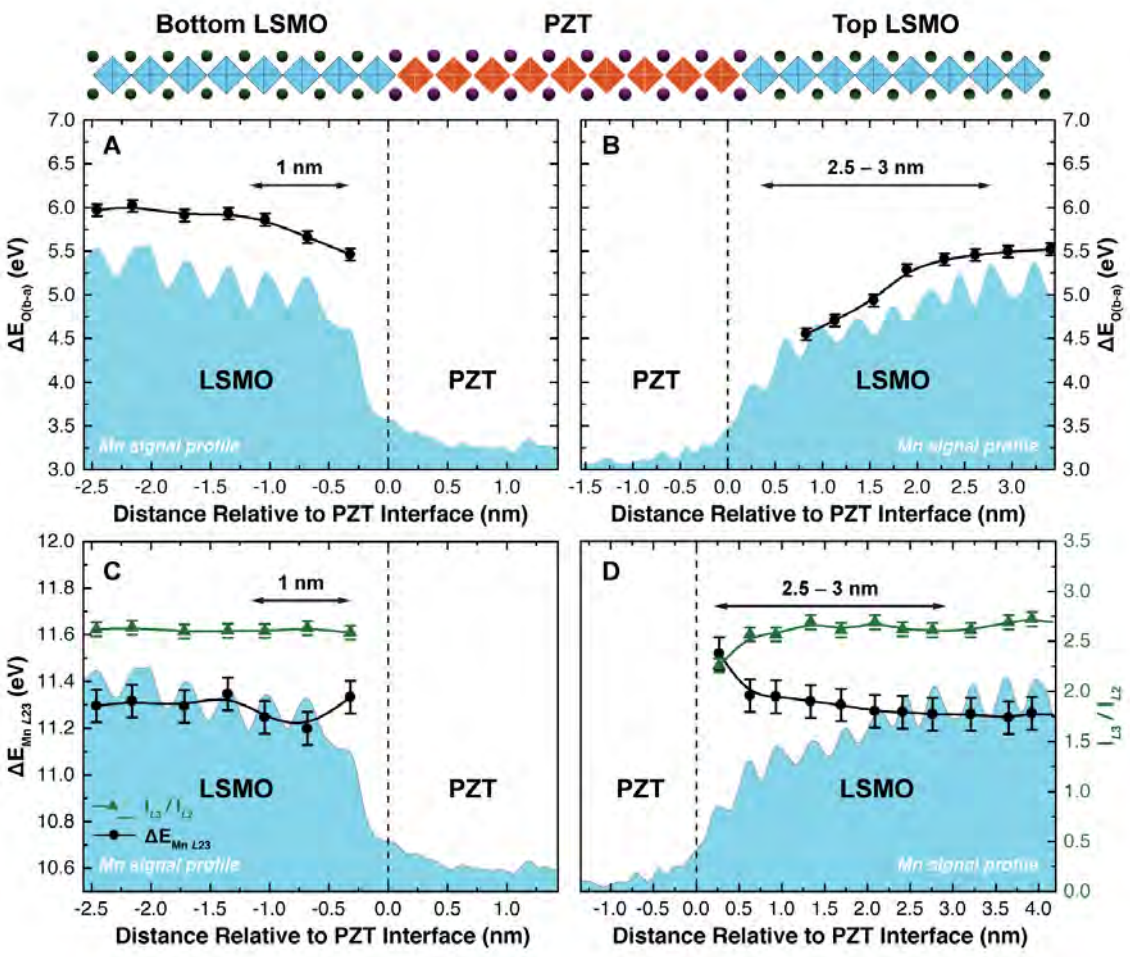

Figure 6.2: Electron energy loss spectroscopy (EELS) measurements of local changes in O K edge fine structure, overlaid with an illustration of the heterostructure. (A, B) show the O K pre- to main-peak separation ($\Delta E_{O(b-a)}$) in the vicinity of the PZT interface for the bottom and top LSMO layers, respectively. The bottom layer exhibits a small (∼0.5 eV) change, while the top layer exhibits a much larger (∼1 eV) change. The bottom layer shows this change over less than 1 nm, while the top layer shows a much broader region of change, nearly 2.5–3 nm. (C, D) show the difference in EELS Mn $L_{2,3}$ edge peak position (black circles) and L_3/L_2 peak intensity ratio (green triangles) in the vicinity of the PZT interface for the bottom and top LSMO layers, respectively. This figure is a combination of scans from different parts of the film and the scales for both curves are the same for panels C and D. The edges were fitted using a combination of Gaussian functions in OriginPro and the error of each fit was calculated. The difference in bulk energy separations is likely the result of different sample thicknesses on either side of the PZT formed during sample preparation.

al.[351,352] In this approach we construct an *effective* pseudopotential for a "fictitious" atom, whose cutoff radii and valence electron configuration were assumed to be that of a La atom, but whose valence charge is modified to mimic the valence of La / Sr partial site occupancy. For example, in our simulation for $La_{0.7}Sr_{0.3}MnO_3$, the valence charge for the La / Sr atom was taken to be equal to 2.7+. Because of the

constraints placed on the La / Sr partial occupancy, we neither relaxed the internal atomic coordinates nor the unit cell parameters: instead, we considered the bulk experimental structures and calculated their charge density. As a result, our DFT calculations do not directly simulate the complex LSMO / PZT / LSMO heterostructure. Instead, we perform systematic calculations on the three bulk structures and uncover trends in the O *K* edge spectra that we may qualitatively correlate to our experimental O *K* edge EEL spectra.

In Figure 6.3, we show the calculated O *K* edge XAS spectra. We find excellent agreement between the experimental (Figure 6.1.B) and our calculated O *K* edge spectra; specifically the three features (**a**, **b**, and **c**) in Figure 6.1.B are well-reproduced in our calculated spectra. For the remainder of the present work, we will focus mainly on the pre-peak and the main peak. In Figure 6.3.A, we show the total (spin up + spin down) XAS spectra for the ferromagnetic spin order for the three chemical compositions.

We find that as the Mn "nominal" valence increases, the spectral weight on the pre-peak feature (corresponding to the O 2*p* – Mn 3*d* hybridized orbitals) decreases and shifts slightly to lower energies. The main peak (O 2*p* – La 5*d* hybridized orbitals), on the other hand, shifts to a higher energy with increasing Mn "nominal" valence. We identify two key features: namely, the spectral weight of the pre-peak and the energy difference between the pre- and main-peak, as indicators of changes in the Mn valence state in the O *K* edge. We next repeated the calculations; however, this time we imposed antiferromagnetic-*A* (AF-*A*) spin order on the Mn atoms. The results for the pre-peak spectral features are shown in Figure 6.3.B.* We find two critical signatures in the pre-peak that differentiate ferromagnetic from AF-*A* spin orders: as a general trend, we find that AF-*A* spin order increases the spectral weight of the pre-peak features and also shifts the pre-peak towards lower energies relative to their ferromagnetic counterparts. Our DFT calculations corroborate the hypothesis that we can use the pre-peak spectral feature from O *K* edge measurements to probe the local variation in the Mn valence and the magnetic configurations. This is an important finding, because earlier works on LSMO magnetoelectric heterostructures have shown an antiferromagnetic spin order near the interface arising from the magnitude and direction of ferroelectric polarization.[138,143] However, it has been challenging to experimentally probe the spin alignment of

*The main peak spectral features show little variation between the ferromagnetic and AF-*A* spin orders.

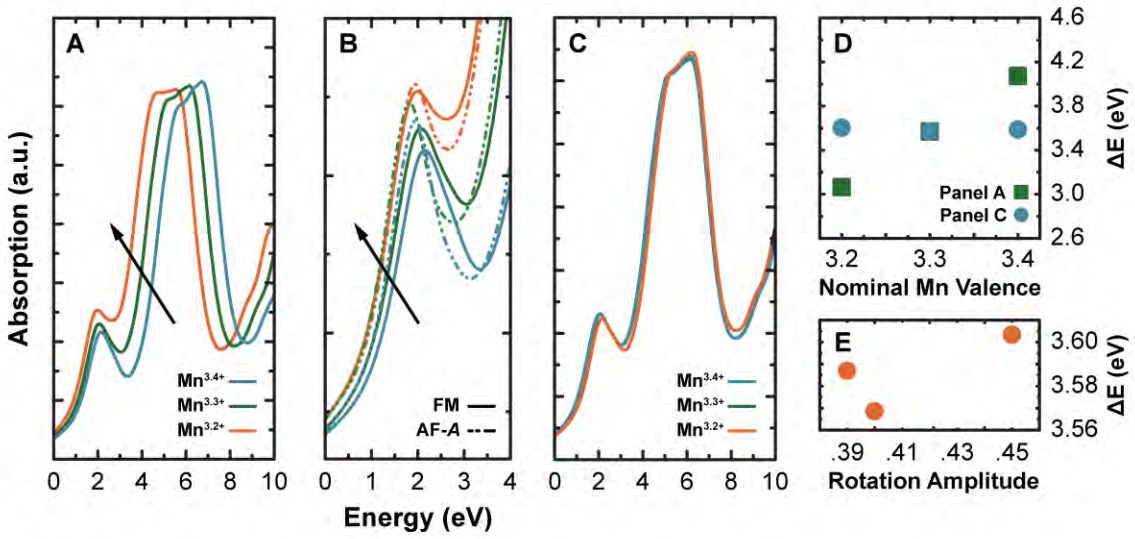

Figure 6.3: Total (spin up + spin down) O *K* edge spectra calculated from density functional theory (DFT). (A) For the bulk structures of $La_{0.6}Sr_{0.4}MnO_3$ (blue), $La_{0.7}Sr_{0.3}MnO_3$ (green), and $La_{0.8}Sr_{0.2}MnO_3$ (orange) compositions with ferromagnetic (FM) spin order. There is a clear shift to higher energy with increasing Mn valence, as indicated by the arrow, in agreement with our experimental measurements (Figure 6.1). (B) Comparison of the spectral weight and energies of the pre-peak feature (O 2*p* – Mn 3*d* hybridized orbitals) between FM (continuous line) and AF-*A* (dotted line) spin configurations on the Mn atom for the three compositions. For the AF-*A* compositions, the spectral weight increases and the pre-peak shifts to a lower energy, relative to the FM compositions. (C) Pre- and main-peak spectral features for the three bulk structures (FM spin order), where we constrain the valence charge of the La / Sr site to be nominally 2.7+ charge so that the chemical composition of the bulk perovskite compound is fixed at $La_{0.7}Sr_{0.3}MnO_3$ for the three structures. We note that in this simulation the rotation amplitudes for the MnO_6 octahedra are varied. The effect on the EEL spectra is negligible in this case. (D) Calculated energy difference (ΔE in eV) between the pre-and the main peaks from (A) and (C) shown as circles and triangles, respectively. (E) Calculated ΔE for different Mn octahedra rotation amplitudes from (C), showing a negligible change.

Mn atoms near the interface. Our DFT calculations indicate that layer (depth)-resolved O *K* edge EELS measurements may offer insights to capture the unique spin behavior of LSMO films.

In addition to the two spin configurations, we also probed the effect of octahedral rotations on the O *K* edge spectral features. Our calculations involved taking the three bulk structures, but we constrained the valence charge of the La / Sr site to be nominally 2.7+. This fixes the chemical composition of the bulk perovskite compound at $La_{0.7}Sr_{0.3}MnO_3$ for the three structures, but allows for different octahedral rotation amplitudes. The resulting O *K* edge spectra for the ferromagnetic spin order are shown in Figure 6.3.C. We find that the octahedral rotations (within the constraints imposed in our calculations) have

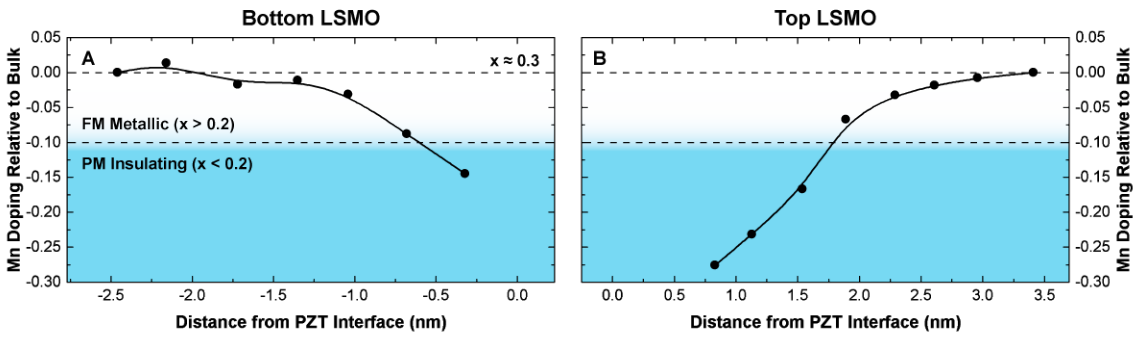

Figure 6.4: Map of local Mn doping relative to bulk $La_{0.7}Sr_{0.3}MnO_3$ as a function of position normal to the LSMO / PZT interface for the bottom (A) and top (B) LSMO layers. The boundaries of the associated magnetic and electronic phases are overlaid and estimated from the bulk LSMO phase diagram.[36]

little effect on the O *K* edge spectra. In Figures 6.3.D,E we quantify, from the DFT calculations, the energy difference between the pre- and main-peak spectral features for the ferromagnetic spin configuration. It is clear that the Mn valence has a dominating influence in determining the energy levels of the hybridized orbitals relative to the octahedral distortions.

We now interpret our experimental EELS measurements of the O *K* edge fine structure to estimate the local phases present at the LSMO / PZT interface. We first compare our measured O *K* pre- to main-peak energy separation ($\Delta E_{O(b-a)}$) to our DFT calculations and standards investigated by Varela *et al.*, as we have already shown in Figures 6.2.A,B.[197] Far from the interface we find that the LSMO is in a bulk-like state, with a nominal Mn valence corresponding to the expected $La_{0.7}Sr_{0.3}MnO_3$ ($Mn^{\sim 3.3+}$) doping. We have confirmed this nominal doping using angle-resolved X-ray photoelectron spectroscopy (XPS) (Figure D.2). We are then able to calculate the effective change in Mn doping relative to this bulk-like state, which we plot as a function of position in Figures 6.4.A,B. Finally, by comparing this changing doping to the bulk LSMO phase diagram at room-temperature, we are able to estimate the local electronic and magnetic phases present in the vicinity of the PZT interface.

Our analysis shows that for the bottom LSMO layer (Figure 6.4.A), the effective Mn doping retains its bulk value up to approximately three lattice planes from the interface, where it drops by ∼0.15 over a nanometer. In contrast, the top LSMO layer (Figure 6.4.B) shows a larger ∼0.26 drop over a broad 2.5–3 nm region. This measurement reveals a clear spatial asymmetry about the PZT layer:

the top layer displays a wide region of valence shift, while the bottom layer displays a more narrow region. Furthermore, a comparison of these values to the bulk phase diagram at room-temperature shows that the bottom LSMO is almost uniformly ferromagnetic and metallic, while the top LSMO should be broadly paramagnetic and insulating at the interface.[36] We note that previous studies have found evidence to support the formation of an antiferromagnetic phase at low-temperature.[138,143] However, at room-temperature the transition to a paramagnetic, insulating phase has previously been invoked to explain the anomalously large screening lengths observed in LSMO / BTO and may be responsible for the similarly large lengths we observe here.[146] Interestingly, while a *decrease* in valence is expected for the top LSMO (depletion state), an *increase* in valence is actually expected for the bottom LSMO (accumulation state).[138] However, we find that *both* interfacial valences decrease near the PZT interface, although the magnitude of the drop for the top LSMO is much larger. The valence decrease of the bottom LSMO may arise from depolarization of the PZT interface, incomplete charge screening and/or intermixing.[302,353]

6.6 Electron Energy Loss Spectroscopy – Mn $L_{2,3}$ Edge

We have also studied changes in the Mn $L_{2,3}$ edge, which is associated with excitations from the spin-orbit split $2p_{3/2}$ and $2p_{1/2}$ levels to available states in the $3d$ band.[19,197] We focus on the chemical shift of the Mn $L_{2,3}$ edge, which only depends on core-level energy and the effective charge of the atom.[195] This method directly measures atomic charge, independent of background subtraction and sample thickness.[338] Figure 6.1.C shows the Mn $L_{2,3}$ edge fine structure for both the bottom and top LSMO layers. Taking the dashed lines as a guide to the eye, there is a clear shift to lower energy in the vicinity of the PZT interface, indicating local chemical state changes. Figures 6.2.C,D show that in both cases the edge intensity ratio (I_{L_3}/I_{L_2}) remains nearly constant throughout the LSMO. However, the Mn $L_{2,3}$ edge separation ($\Delta E_{MnL_{2,3}}$) displays very different behavior for the two interfaces. In both cases the samples display a bulk value of ∼11.2–11.3 eV that deviates in the vicinity of the PZT interface; the bottom LSMO (Figure 6.2.C) displays a slight fluctuation of ∼0.1 eV over 1 nm, while the top LSMO (Figure 6.2.D) displays a steady increase of nearly ∼0.2–0.3 eV over a broad 2.5–3 nm region. The spatial extent of these regions in particular agrees well with the trends observed in the O K edge energy

separation (Figures 6.2.A,B).

6.7 Polarized Neutron Reflectometry

Our EELS and DFT results have raised the interesting possibility of spatial gradients in the magnetic and electronic phases at the LSMO / PZT interface. Intuitively, one would expect that the transition from ferromagnetic metallic to paramagnetic insulating phases at the top LSMO interface would significantly reduce room-temperature magnetization. To probe this we use PNR, a scattering technique that allows us to measure the depth-resolved magnetic structure and is used to isolate individual magnetic layers in a thin-film heterostructure.[221,222,225,335,354]

Figure 6.5 shows the result of PNR measurements conducted at 298 K with a 1 T field applied along the substrate [100] direction. These measurements were performed on the Magnetism Reflectometer at the Spallation Neutron Source, Oak Ridge National Laboratory.[355] Figure 6.5.B shows the measured non-spin-flip reflectivity, which indicates clear spin-splitting resulting from the magnetization of the sample. The calculated fit is overlaid on the data and the resulting scattering length density depth profiles are shown in Figure 6.5.A. The depth profile reveals that the magnetization of the two LSMO layers is strongly asymmetric: the top LSMO displays a greatly suppressed magnetization throughout ($M_S^{Avg} \approx 0.70\,\mu_B$ Mn^{-1}), while the bottom LSMO displays a large magnetization ($M_S^{Avg} \approx 2.9\,\mu_B$ Mn^{-1}) that is only reduced at the STO interface. We have previously shown that the broad suppression of magnetization near the vacuum surface can result from strain fluctuations; however, at the interface the charge-transfer screening effect largely controls the magnetization.[335] Our results suggest a uniformly ferromagnetic character for the bottom interface, in agreement with the phase map in Figure 6.4.A. In contrast, the top LSMO layer possesses a strongly suppressed magnetization near the interface, where strain fluctuations are expected to be minimal, as shown in Figure 6.4.B.[335] This further supports the idea of magnetic and electronic phase transitions at the interface, in agreement with our EELS and DFT results.

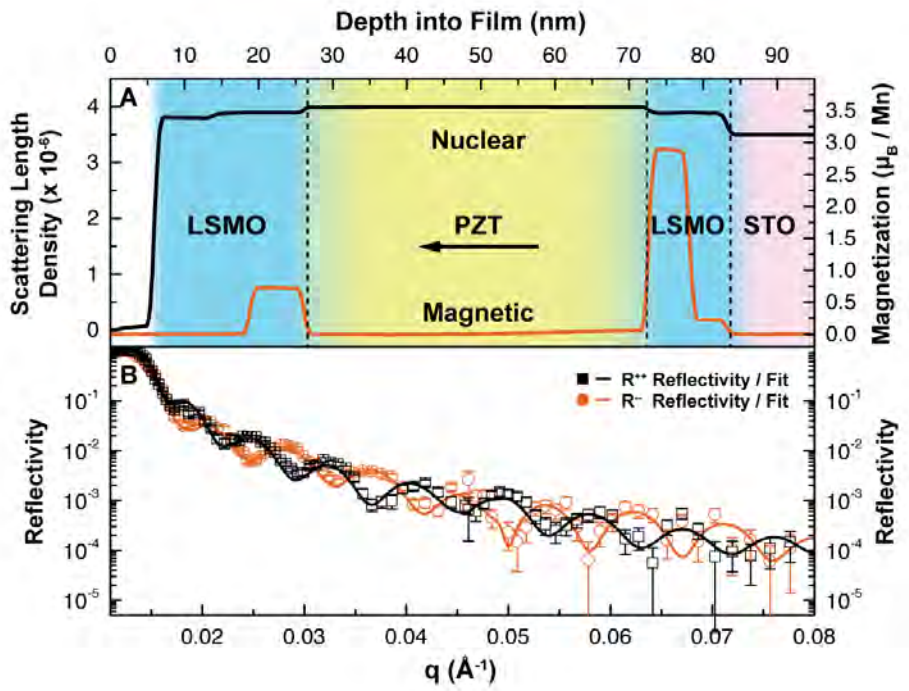

Figure 6.5: Polarized neutron reflectometry (PNR) measurements conducted at 298 K, with a 1 T field applied along the substrate [100] direction in the plane of the film. (A) shows the resulting nuclear scattering length densities (black) obtained from the fit to the data and the associated estimated magnetization (orange). We note some change in nuclear scattering length density near the surface, as well as a reduced magnetization at the STO interface. The arrow indicates the direction of ferroelectric polarization. (B) shows the measured non-spin-flip reflectivities (shapes), overlaid with a fit to the data (lines).

6.8 Polarization Screening Effects on Valence

The valence and magnetic changes described in the previous section are the result of a complex interplay of phenomena, including interfacial charge-transfer screening and possible electronic phase transitions.[146,323,335] As already mentioned, the local screening of bound surface charge is expected to significantly affect Mn ion valence, as well as the formation of interfacial phases; thus, it is important to understand the local ferroelectric polarization at both LSMO / PZT interfaces. Conventional scanning probe techniques, such as PFM, are confined to surfaces and are generally of limited use in studying interfaces.[356] However, using aberration-corrected STEM-HAADF it is possible to directly measure cation displacements with picometer precision, allowing us to characterize local ferroelectric polarization at each LSMO / PZT interface (see Appendix D.3).

These results, shown in Figure 6.6, reveal different polarization behavior for each LSMO / PZT interface. At the bottom interface (Figures 6.6.C,D), the PZT polarization $P_S \approx (53 \pm 15)\,\mu\text{C cm}^{-2}$ is nominally constant over the interface region. However, the top LSMO interface (Figures 6.6.A,B) behavior is markedly different: the average PZT polarization $P_S \approx (70 \pm 15)\,\mu\text{C cm}^{-2}$ is more than 30% larger than the bottom; moreover, within the interface region the polarization is reduced, likely due incomplete charge screening and/or intermixing with the LSMO. The magnitude of the top polarization agrees well with previous displacement current measurements ($P_S \approx 85\,\mu\text{C cm}^{-2}$),[138] but our local measurements show that this polarization can be quite different for each interface.

We may estimate the effective bulk alloying change induced by charge-transfer screening, assuming that the polarization is nominally constant parallel to the interface and fully screened by free carriers in the the LSMO across a 2–3 u.c. ($\sim$1.2 nm) screening length. Based off of Lu *et al.*'s calculations, we may estimate $\Delta x = P_S \times a$, where $a \approx 0.0041\,\text{cm}^2\ \mu\text{C}^{-1}$.[146] For $P_{S,top} \approx (70 \pm 15)\,\mu\text{C cm}^{-2}$ then, we find $\Delta x \approx 0.29 \pm 0.06$, while for $P_{S,bottom} \approx (53 \pm 15)\,\mu\text{C cm}^{-2}$, we find $\Delta x \approx 0.22 \pm 0.06$. This suggests that the magnitude, as well as the direction, of the screening effect will be different for the top and bottom interfaces. A comparison of this calculation to our EELS phase map shows a striking agreement between the magnitude of bulk valence change (Figure 6.4.B). Our calculation further supports the idea of a transition from ferromagnetic and metallic to paramagnetic and insulating at this interface at room-temperature. The magnitude of the change for the bottom interface is also reduced in both our calculation and our EELS phase map (Figure 6.4.A), but the sign of this change is not fully consistent with the charge-transfer screening model.

There has been considerable debate as to the spatial extent of this screening, since calculations of the Thomas-Fermi screening length vary.[135,138,140,146,175,335,357] In the present study we find that the Mn valence change for the top interface occurs over a broader region than is expected from pure charge-transfer screening ($<$ 1.9 nm).[175,357] Lu *et al.* have proposed a qualitative model for LSMO / BTO that may begin to reconcile both the discrepancies in screening length as well as the interface phase transitions we observe.[146] The authors describe PFM measurements of polarization screening, which yield a large $\sim$3 nm screening length. They propose that local screening of surface charge acts to push

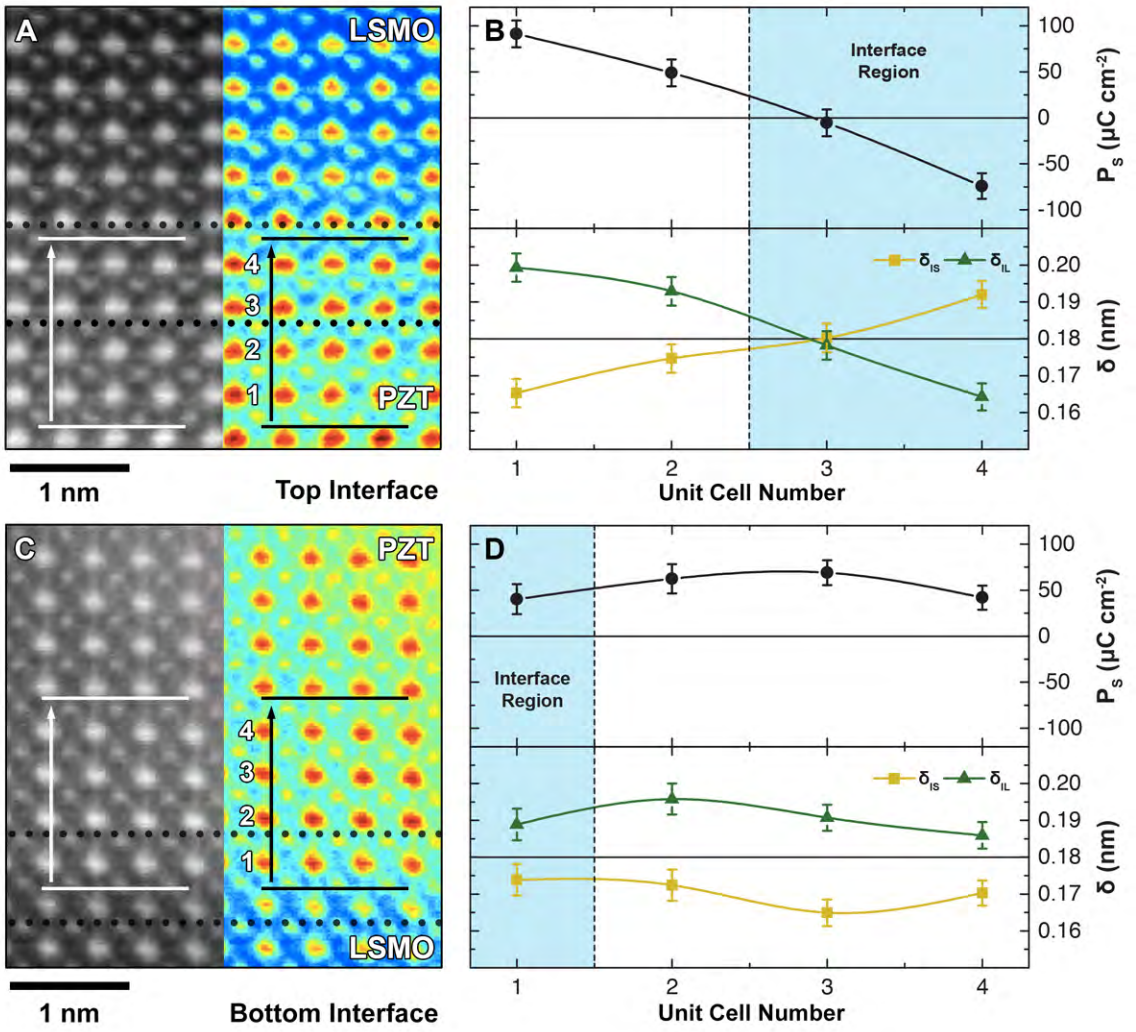

Figure 6.6: Measurement of local ferroelectric polarization. (A) and (C) show STEM-HAADF grayscale and colorized images for the top and bottom interfaces, respectively. The dashed lines indicate the interface region and the numbers mark the position of the measured unit cells. (B) and (D) show the long (δ_{IL}) and short (δ_{IS}) Ti^{4+} cation displacement directions, as well as the calculated spontaneous polarization (P_S) for the top and bottom interfaces, respectively. These displacements are the result of averaging over three to five positions parallel to the interface.

an interface layer of $La_{0.7}Sr_{0.3}MnO_3$ into the paramagnetic insulating region of the phase diagram at room-temperature, increasing the effective hole doping, and thereby expanding the screening region. Our EELS results (Figure 6.4) show that the measured effect on valence is more than sufficient to push the top interface region into the paramagnetic insulating phase at room-temperature. Because charge must be screened over this insulating region, the effective screening length is increased. In contrast, the bottom interface is expected to be almost uniformly ferromagnetic and metallic at room-temperature,

with an associated short screening length. This is supported by our local measurements of ferroelectric polarization, which show that the magnitude of the bound surface charge at the top interface is adequate to induce such a change, while an approximately 30% smaller effect is expected for the bottom interface. This mechanism accounts for the behavior we have observed in our EELS results and supported by DFT calculations, as well as the asymmetric magnetization behavior revealed by PNR. Using local probes we are able to attain direct insight into these features for the first time and we are able to resolve the associated electronic and magnetic phases with unprecedented atomic-scale resolution.

6.9 Conclusions

Our results begin to unravel the connections between charge, valence, and spin configurations in these materials. Using EELS we are able to quantify the extent of charge-transfer screening effects and we show that they depend on the polarization direction. We directly measure the local Mn valence and associated O K edge fine structure changes to construct a map of interfacial phases. Our DFT calculations lend support to the presence of asymmetric magnetic phase transitions, as reflected in EELS fine structure changes, which we are able to qualitatively reproduce. Our STEM-HAADF measurements of local ferroelectric polarization reveal that the local ferroelectric polarization at the top interface is nearly 30% larger than the bottom interface and is large enough to induce a transition deep into a insulating, paramagnetic phase at the LSMO interface at room-temperature. We combine these local chemical analyses with PNR measurements, which reveal a strongly asymmetric magnetic ordering about the PZT layer, likely originating from charge-transfer screening.

Collectively, these results suggest a magnetic phase transition at the LSMO / PZT interface, in agreement with other studies.[138,358,359] We find that the local ferroelectric polarization differs at each interface, which affects the magnitude of the charge-transfer screening effect in each LSMO layer. Our EELS data, supported by DFT calculations, suggest a large change in Mn valence at the top LSMO interface, which gives rise to the suppression in magnetization that we measure in PNR. We believe that the functionality of devices based on similar heterostructures will be greatly affected by intrinsic spontaneous polarization of the chosen ferroelectric. For instance, for $Pb(Zr_{0.55}Ti_{0.45})O_3$, $P_S \approx 70-85\,\mu C\ cm^{-2}$, while for BTO and BFO, $P_S \approx 48\,\mu C\ cm^{-2}$ and $P_S \approx 50-60\,\mu C\ cm^{-2}$, respectively.[105,138,146] Any suppression

or enhancement of ferroelectric polarization will be even more pronounced in the latter compounds. It may be possible to tune the boundary region with polarization by further reducing the hole doping of the system, which may be achieved by increasing Sr doping, at the cost of reducing T_C from its maximum in $La_{0.7}Sr_{0.3}MnO_3$. More study into the the polarization- and composition-dependent phase diagram is needed; the stacking sequence of the layers in the heterostructure may also play a critical role in device performance. Regardless, it is clear that models of magnetoelectric coupling in the manganites and related systems must begin to account for interfacial phase transitions, which may drastically alter coupling behavior.

Chapter 7: Conclusions and Future Work

The work presented in this thesis has utilized a novel, local approach to correlate structure and magnetic properties in thin-film oxide materials. Previous approaches, which have laid the groundwork for the present study, have typically employed non-local techniques, such as X-ray diffraction and spectroscopy. These methods, while extremely valuable, are generally insensitive to the local features that might affect magnetization. Using TEM we have shown that the local strain and chemical states of these materials vary greatly in the vicinity of interfaces. In particular, we find that the c/a axial ratio of these compounds fluctuates, which results in a changing electronic polarization throughout the heterostructure. This results in a suppression of FM Curie temperature, in turn producing graded magnetization profiles. We find that these strain gradients operate over large length scales ($>$ 4 nm), whereas charge-transfer screening effects are confined to the interface ($<$ 4 nm). Moreover, it is possible to reshape these gradients by tuning the tetragonality of the underlying FE. We also find that there is an intrinsic asymmetry to the polarization screening effect arising from changes in local ferroelectric polarization. Using EELS and STEM we are able to visualize these polarization effects and their associated effects to map the magnetic phases present at the LSMO / PZT interface. We combine these results with DFT calculations and PNR measurements, which provide strong evidence for magnetic phase gradients at the interface for the first time.

Collectively our results illustrate the importance of local probes of structure and magnetism to studies of these compounds. We are able to construct a more realistic model for ME coupling in these composites, and we suggest ways to tune coupling by varying layer geometries and local strain state. Moving forward, we are currently exploring dynamic changes in coupling under the application of electric fields. This will allow us to directly measure the effect of electric field changes in magnetization *in situ*. Furthermore, to map the electronic and magnetic phases present in these compounds, it is necessary to do further PNR measurements across a range of temperatures. This will allow us to fully map the interfacial phase diagram in this system. Nonetheless, the work presented in this thesis has illuminated the fundamental

mechanisms underlying ME coupling in this system, as well as begun to disentangle the various strain and charge contributions to magnetization. This new insight will guide designers of the next generation of spintronic materials, while the suite of characterization techniques assembled for this study may be used to explore many other ME heterostructure systems.

Bibliography

[1] G. A. Prinz. Magnetoelectronics. *Science*, 282(5394):1660–1663, 1998.

[2] S. A. Wolf, D. D. Awschalom, R. A. Buhrman, J. M. Daughton, S. von Molnár, M. L. Roukes, A. Y. Chtchelkanova, and D. M. Treger. Spintronics: A Spin-Based Electronics Vision for the Future. *Science*, 294(5546):1488–1495, November 2001.

[3] M. Ye. Zhuravlev, S. S. Jaswal, E. Y. Tsymbal, and R. F. Sabirianov. Ferroelectric switch for spin injection. *Appl. Phys. Lett.*, 87(22):222114, 2005.

[4] Scott a Chambers. Epitaxial growth and properties of doped transition metal and complex oxide films. *Advanced Mater.*, 22(2):219–48, January 2010.

[5] R. F. C. Farrow. The role of molecular beam epitaxy in Res. on giant magnetoresistance and interlayer exchange coupling. *IBM J. Res. and Development*, 42(1):43–52, January 1998.

[6] Darrell G. Schlom, Long-Qing Chen, Chang-Beom Eom, Karin M Rabe, Stephen K Streiffer, and Jean-Marc Triscone. Strain Tuning of Ferroelectric Thin Films. *Ann. Rev. Mater. Res.*, 37(1):589–626, August 2007.

[7] Yao Wang, Jiamian Hu, Yuanhua Lin, and Ce-Wen Nan. Multiferroic Magnetoelectric Composite Nanostructures. *NPG Asia Mater.*, 2(2):61–68, 2010.

[8] Manish K. Niranjan, Chun-Gang Duan, Sitaram S. Jaswal, and Evgeny Y. Tsymbal. Electric field effect on magnetization at the Fe/MgO(001) interface. *Appl. Phys. Lett.*, 96(22):222504, 2010.

[9] G. Srinivasan. Magnetoelectric Composites. *Ann. Rev. Mater. Res.*, 40(1):153–178, June 2010.

[10] Manfred Fiebig. Revival of the magnetoelectric effect. *J. Phys. D: Appl. Phys.*, 38(8):R123–R152, April 2005.

[11] G. Binasch, P. Grünberg, F. Saurenbach, and W. Zinn. Enhanced magnetoresistance in layered magnetic structures with antiferromagnetic interlayer exchange. *Phys. Rev. B*, 39(7):4828–4830, March 1989.

[12] M. N. Baibich, J. M. Broto, A. Fert, F. Nguyen Van Dau, and F. Petroff. Giant Magnetoresistance of (001)Fe/(001)Cr Magnetic Superlattices. *Phys. Rev. Lett.*, 61(21):2472–2475, November 1988.

[13] J.M. Coey. *Magnetism and Magnetic Mater.* Cambridge University Press, Cambridge, 2009.

[14] D. Monroe. Focus: Nobel Focus: Sensitive Magnetic Sandwich, 2007.

[15] A. Fert and I. Campbell. Two-Current Conduction in Nickel. *Phys. Rev. Lett.*, 21(16):1190–1192, October 1968.

[16] N. F. Mott. The Electrical Conductivity of Transition Metals. *Proc. R. Soc. A*, 153(880):699–717, February 1936.

[17] S.D. Bader and S.S.P. Parkin. Spintronics. *Ann. Rev. Cond. Mat. Phys.*, 1(1):71–88, August 2010.

[18] R Ramesh and V G Keramidas. Metal-Oxide Heterostructures. *Ann. Rev. Mater. Science*, 25(1):647–678, August 1995.

[19] M. Varela, A.R. Lupini, K. Van Benthem, A.Y. Borisevich, M.F. Chisholm, N. Shibata, E. Abe, and S.J. Pennycook. Mater. Characterization in the Aberration-Corrected Scanning Transmission Electron Microscope. *Ann. Rev. Mater. Res.*, 35(1):539–569, August 2005.

[20] Shinji Yuasa, Taro Nagahama, Akio Fukushima, Yoshishige Suzuki, and Koji Ando. Giant room-temperature magnetoresistance in single-crystal Fe/MgO/Fe magnetic tunnel junctions. *Nat. Mater.*, 3(12):868–71, December 2004.

[21] S. Parkin, C. Kaiser, A. Panchula, K. Roche, and M. Samant. Magnetically engineered spintronic sensors and memory. *Proceedings of the IEEE*, 91(5):661–680, May 2003.

[22] J. Orna, L. Morellon, P.A. Algarabel, J.A. Pardo, S. Sangiao, C. Magen, E. Snoeck, J.M. De Teresa, and M.R. Ibarra. Fe_3O_4 /MgO/Fe Heteroepitaxial Structures for Magnetic Tunnel Junctions. *IEEE Trans. Magn.*, 44(11):2862–2864, November 2008.

[23] M. Fechner, I. Maznichenko, S. Ostanin, a. Ernst, J. Henk, P. Bruno, and I. Mertig. Magnetic phase transition in two-phase multiferroics predicted from first principles. *Phys. Rev. B*, 78(21):212406, December 2008.

[24] Chun Li and A. J. Freeman. Giant monolayer magnetization of Fe on MgO: A nearly ideal two-dimensional magnetic system. *Phys. Rev. B*, 43(1):780–787, January 1991.

[25] P Bertoncini, P. Wetzel, D. Berling, A. Mehdaoui, B. Loegel, G. Gewinner, R. Poinsot, and V. Pierron-Bohnes. Magnetic anisotropy of epitaxial Fe layers grown on Si (001). *J. Magn. Magn. Mater.*, 237(2):191–205, December 2001.

[26] M. Buchmeier, R. Schreiber, D. Bürgler, and C. Schneider. Thickness dependence of linear and quadratic magneto-optical Kerr effects in ultrathin Fe (001) films. *Phys. Rev. B*, 79(6):1–7, February 2009.

[27] A. Di Bona, C. Giovanardi, and S. Valeri. Growth and structure of Fe on MgO (001) studied by modulated electron emission. *Surf. Sci.*, 498(1):193–201, 2002.

[28] G. Wedler, C. Schneider, A. Trampert, and R. Koch. Strain Relief of Heteroepitaxial BCC-Fe (001) Films. *Phys. Rev. Lett.*, 93(23):236101, November 2004.

[29] S. Jordan, R Schad, A. Keen, M Bischoff, D. Schmool, and H. van Kempen. Nanoscale Fe islands on MgO(001) produced by molecular-beam epitaxy. *Phys. Rev. B*, 59(11):7350–7353, March 1999.

[30] L M Falicov, Daniel T Pierce, S. D. Bader, R. Gronsky, Kristl B. Hathaway, Herbert J. Hopster, David N. Lambeth, S. S. P. Parkin, Gary Prinz, Myron Salamon, Ivan K. Schuller, and R. H. Victora. Surface, interface, and thin-film magnetism. *J. Mater. Res.*, 5(06):1299–1340, January 2011.

[31] D Sander, A Enders, and J Kirschner. Magnetoelastic coupling and epitaxial misfit stress in ultrathin Fe(100)-films on W(100). *J. Magn. Magn. Mater.*, 198-199:519–521, June 1999.

[32] R. Skomski. *Simple Models of Magnetism*. Oxford University Press, 2012.

[33] J.H Wolfe, R.K Kawakami, W.L Ling, Z.Q Qiu, Rodrigo Arias, and D.L Mills. Roughness induced in plane uniaxial anisotropy in ultrathin Fe films. *J. Magn. Magn. Mater.*, 232(1-2):36–45, June 2001.

[34] L.W. Martin, Y.-H. Chu, and R. Ramesh. Advances in the growth and characterization of magnetic, ferroelectric, and multiferroic oxide thin films. *Mater. Sci. Eng.: R: Reports*, 68(4-6):89–133, May 2010.

[35] Vasily Moshnyaga and Konrad Samwer. Ferromagnetic Manganite Films. In H. Kronmueller and Stuart S P Parkin, editors, *Handbook of Magnetism and Advanced Magnetic Mater.* Wiley, 2003.

[36] Pavlo Zubko, Stefano Gariglio, Marc Gabay, Philippe Ghosez, and Jean-Marc Triscone. Interface Physics in Complex Oxide Heterostructures. *Ann. Rev. Cond. Mat. Phys.*, 2(1):141–165, March 2011.

[37] J. M. D. Coey, M. Viret, and S. von Molnar. Mixed-valence manganites. *Advances in Phys.*, 48(2):167–293, March 1999.

[38] J. Mira, J. Rivas, F. Rivadulla, C. Vázquez-Vázquez, and M. López-Quintela. Change from first- to second-order magnetic phase transition in $La_{2/3}(Ca, Sr)_{1/3}MnO_3$ perovskites. *Phys. Rev. B*, 60(5):2998–3001, August 1999.

[39] V. M. Goldschmidt. Die Gesetze der Krystallochemie. *Die Naturwissenschaften*, 14(21):477–485, May 1926.

[40] A.J. Millis, B.I. Shraiman, and R Mueller. Dynamic Jahn-Teller Effect and Colossal Magnetoresistance in $La_{1-x}Sr_xMnO_3$. *Phys. Rev. lett.*, 77(1):175–178, July 1996.

[41] J.H. Park, E. Vescovo, H.J. Kim, and C Kwon. Direct evidence for a half-metallic ferromagnet. *Nat.*, 392(April):794–796, 1998.

[42] M. Quijada, J. Černe, H. D. Drew, K. H. Ahn, A. J. Millis, R. Shreekala, R. Ramesh, M. Rajeswari, and T. Venkatesan. Optical conductivity of manganites:Crossover from Jahn-Teller small polaron to coherent transport in the ferromagnetic state. *Phys. Rev. B*, 58(24):16093–16102, December 1998.

[43] M. Cesaria, A.P. Caricato, G. Maruccio, and M. Martino. LSMO growing opportunities by PLD and applications in spintronics. *J. Phys.: Conference Series*, 292:012003, April 2011.

[44] A. Urushibara, T. Arima, A. Asamitsu, G. Kido, and Y. Tokura. Insulator-metal transition and giant magnetoresistance in $La_{1-x}Sr_xMnO_3$. *Phys. Rev. B*, 51(20):14103–14109, May 1995.

[45] E. O. Wollan and W C Koehler. Neutron Diffraction Study of the Magnetic Properties of the Series of Perovskite-Type Compounds $La_{1-x}Ca_xMnO_3$. *Phys. Rev.*, 100(2):545–563, October 1955.

[46] C. Zener. Interaction between the d shells in the transition metals. *Phys. Rev.*, 81(3):440, 1951.

[47] P.W. Anderson and H. Hasegawa. Considerations on double exchange. *Phys. Rev.*, 100(2):675, 1955.

[48] HY Hwang, SW Cheong, PG Radaelli, M Marezio, and B. Batlogg. Lattice Effects on the Magnetoresistance in Doped LaMnO3. *Phys. Rev. Lett.*, 75(5):914–917, July 1995.

[49] W. Archibald, J. Zhou, and J.B. Goodenough. First-order transition at T_C in the orthomanganites. *Phys. Rev. B*, 53(21):14445–14449, June 1996.

[50] C. Adamo, X. Ke, H. Q. Wang, H. L. Xin, T. Heeg, M. E. Hawley, W. Zander, J. Schubert, P. Schiffer, D. A. Muller, L. Maritato, and D. G. Schlom. Effect of biaxial strain on the electrical and magnetic properties of (001) $La_{0.7}Sr_{0.3}MnO_3$ thin films. *Appl. Phys. Lett.*, 95(11):112504, 2009.

[51] E. Gommert, H. Cerva, J. Wecker, and K. Samwer. Influence of misfit stress on the magnetoresistive properties of $La_{0.7}Ca_{0.3}MnO_{3\delta}$ thin films. *J. Appl. Phys.*, 85(8):5417, 1999.

[52] M. Bibes, Ll. Balcells, S. Valencia, J. Fontcuberta, M. Wojcik, E. Jedryka, and S. Nadolski. Nanoscale Multiphase Separation at $La_{2/3}Ca_{1/3}MnO_3$ / $SrTiO_3$ Interfaces. *Phys. Rev. Lett.*, 87(6):3–6, July 2001.

[53] R. a. Rao, D. Lavric, T. K. Nath, C. B. Eom, L. Wu, and F. Tsui. Three-dimensional strain states and crystallographic domain structures of epitaxial colossal magnetoresistive $La_{0.8}Ca_{0.2}MnO_3$ thin films. *Appl. Phys. Lett.*, 73(22):3294, 1998.

[54] S. Das, A. Herklotz, E. Jia Guo, and K. Dörr. Static and reversible elastic strain effects on magnetic order of $La_{0.7}Ca_{0.3}MnO_3$ / $SrTiO_3$ superlattices. *J. Appl. Phys.*, 115(14):143902, April 2014.

[55] L. P. Chen and J. Gao. Reversible in situ modulation of competing phases in manganite/ferroelectrics heterostructures. *EPL (Euro. Phys. Lett.)*, 93(4):47009, February 2011.

[56] K. Dörr, O. Bilani-Zeneli, a. Herklotz, a. D. Rata, K. Boldyreva, J.-W. Kim, M. C. Dekker, K. Nenkov, L. Schultz, and M. Reibold. A model system for strain effects: epitaxial magnetic films on a piezoelectric substrate. *Euro. Phys. J. B*, 71(3):361–366, September 2009.

[57] K. Dörr, C. Thiele, J. W. Kim, O. Bilani, K. Nenkov, and L. Schultz. Approaches towards ferroelectric control of thin film magnetism. *Philosophical Magazine Lett.*, 87(3):269–278, March 2007.

[58] C. Thiele, K. Dörr, L. Schultz, E. Beyreuther, and W.-M. Lin. Piezoelectrically Induced Resistance Modulations in $La_{0.7}Sr_{0.3}MnO_3$/Pb(Zr,Ti)O_3 Field Effect Devices. *Appl. Phys. Lett.*, 87(16):162512, 2005.

[59] Ernesto Suaste-Gomez, editor. *Piezoelectric Ceramics*. Sciyo, October 2010.

[60] A. Moulson and J. Herbert. *Electroceramics materials, properties, applications*. Wiley, New York, second edition, 2003.

[61] D.A. Berlincourt, C. Cmolik, and H. Jaffe. No Title. *Proce. IRE*, 48:220.

[62] J. Frantti. Notes of the recent structural studies on lead zirconate titanate. *J. Phys. Chem. B*, 112(21):6521–35, May 2008.

[63] R.E. Newnham. *Properties of Materials: Anisotropy, Symmetry, Structure*. Oxford University Press, 2005.

[64] R. Ranjan, S. K. Mishra, and D. Pandey. Room temperature structure of Pb(Zr_xTi_{1x})O_3 around the morphotropic phase boundary region: a Rietveld study. *J. Appl. Phys.*, 92(6):3266, 2002.

[65] B. Noheda, D. E. Cox, and G. Shirane. Stability of the monoclinic phase in the ferroelectric perovskite $PbZr_{1-x}Ti_xO_3$. *Phys. Rev. B*, 63(1):014103, December 2000.

[66] D. Woodward, J. Knudsen, and I. Reaney. Review of crystal and domain structures in the $PbZr_xTi_{1x}O_3$ solid solution. *Phys. Rev. B*, 72(10):1–8, September 2005.

[67] R Guo, Le Cross, Se Park, B Noheda, De Cox, and G Shirane. Origin of the High Piezoelectric Response in $PbZr_{1-x}Ti_xO_3$. *Phys. Rev. Lett.*, 84(23):5423–5426, June 2000.

[68] Ian MacLaren and Quentin M. Ramasse. Aberration-corrected scanning transmission electron microscopy for atomic-resolution studies of functional oxides. *Int. Mater. Rev.*, 59(3):115–131, April 2014.

[69] J.M. Rondinelli and P. Yu. Multiferroic Heterostructures. In R. Ramesh and L.W. Martin, editors, *Multiferroics. Synthesis, Characterization and Applications*, pages 1–27. 2011.

[70] W. Eerenstein, N.D. Mathur, and J.F. Scott. Multiferroic and magnetoelectric materials. *Nat.*, 442(7104):759–65, August 2006.

[71] H. Béa, M. Gajek, M. Bibes, and A. Barthélémy. Spintronics with multiferroics. *J. Phys.: Cond. Mat.*, 20(43):434221, October 2008.

[72] C. Binek, X. He, Y. Wang, and S. Sahoo. Electrically controlled magnetism. *Proceedings of SPIE*, 7036(111):70360X–70360X–8, 2008.

[73] W. C. Röntgen. Ueber die durch Bewegung eines im homogenen electrischen Felde befindlichen Dielectricums hervorgerufene electrodynamische Kraft. *Annalen der Physik und Chemie*, 271(10):264–270, 1888.

[74] P. Curie. Sur la symétrie dans les phénomènes physiques, symétrie d'un champ électrique et d'un champ magnétique. *J. Phys. Theor. Appl.*, 3(1):393–415, 1894.

[75] P. Debye. Bemerkung zu einigen neuen Versuchen über einen magneto-elektrischen Richteffekt. *Z. Phys.*, 36(4):300–301, April 1926.

[76] I. E. Dzyaloshinskii. The magnetoelectric effect in antiferromagnetic materials. *Zh. Eksp. Teor. Fiz.*, 37:881–882, 1959.

[77] D. N. Astrov. The magnetoelectric effect in antiferromagnetic materials. *Zh. Eksp. Teor. Fiz.*, 38:984–985, 1960.

[78] G. Rado and V. Folen. Observation of the Magnetically Induced Magnetoelectric Effect and Evidence for Antiferromagnetic Domains. *Phys. Rev. Lett.*, 7(8):310–311, October 1961.

[79] B.I. Al'shin and D. N. Astrov. No Title. *Sov. Phys.-JETP*, 17:809, 1963.

[80] E. Ascher. Some Properties of Ferromagnetoelectric Nickel-Iodine Boracite, $Ni_3B_7O_{13}I$. *J. Appl. Phys.*, 37(3):1404, 1966.

[81] George Rado. Observation and Possible Mechanisms of Magnetoelectric Effects in a Ferromagnet. *Phys. Rev. Lett.*, 13(10):335–337, September 1964.

[82] T. Watanabe and K. Kohn. Magnetoelectric effect and low temperature transition of $PbFe_{0.5}Nb_{0.5}O_3$ single crystal. *Phase Transitions*, 15(1):57–68, March 1989.

[83] S. Chikazumi. *Phys. of Ferromagnetism*. Oxford University Press, second edition, 2009.

[84] Nicola A Hill. Why Are There so Few Magnetic Ferroelectrics? *The J. Phys. Chem. B*, 104(29):6694–6709, July 2000.

[85] Daniel Khomskii. Classifying multiferroics: Mechanisms and effects. *Phys.*, 2:20, March 2009.

[86] J.-P. Rivera. On definitions, units, measurements, tensor forms of the linear magnetoelectric effect and on a new dynamic method applied to Cr-Cl boracite. *Ferroelectrics*, 161(1):165–180, November 1994.

[87] J.-P. Rivera. The linear magnetoelectric effect in $LiCoPO_4$ Revisited. *Ferroelectrics*, 161(1):147–164, November 1994.

[88] B.B. Krichevtsov, V.V. Pavlov, and R.V. Pisarev. No Title. *JETP Lett.*, 49:535, 1989.

[89] G. Rado, J. Ferrari, and W. Maisch. Magnetoelectric susceptibility and magnetic symmetry of magnetoelectrically annealed $TbPO_4$. *Phys. Rev. B*, 29(7):4041–4048, April 1984.

[90] Darrell G. Schlom, Long-Qing Chen, Craig J. Fennie, Venkatraman Gopalan, David a. Muller, Xiaoqing Pan, Ramamoorthy Ramesh, and Reinhard Uecker. Elastic strain engineering of ferroic oxides. *MRS Bulletin*, 39(02):118–130, February 2014.

[91] S. Picozzi and C. Ederer. First principles studies of multiferroic materials. *J. Phys.: Cond. Mat.*, 21(30):303201, July 2009.

[92] J. Van Den Boomgaard, A. M. J. G. Van Run, and J. Van Suchtelen. Magnetoelectricity in piezoelectric-magnetostrictive composites. *Ferroelectrics*, 10(1):295–298, 1976.

[93] A. M. J. G. Run, D. R. Terrell, and J. H. Scholing. An in situ grown eutectic magnetoelectric composite material. *J. Mater. Science*, 9(10):1710–1714, October 1974.

[94] J. Boomgaard, D. R. Terrell, R. A. J. Born, and H. F. J. I. Giller. An in situ grown eutectic magnetoelectric composite material. *J. Mater. Science*, 9(10):1705–1709, October 1974.

[95] C A. F Vaz. Electric Field Control of Magnetism in Multiferroic Heterostructures. *J. Phys.: Cond. Mat.*, 24(33):333201, August 2012.

[96] S. Lee, W. Ratcliff, S-W. Cheong, and V. Kiryukhin. Electric field control of the magnetic state in $BiFeO_3$ single crystals. *Appl. Phys. Lett.*, 92(19):192906, 2008.

[97] T. Zhao, A. Scholl, F. Zavaliche, K. Lee, M. Barry, A. Doran, M.P. Cruz, Y.H. Chu, C. Ederer, N.A. Spaldin, R.R. Das, D.M. Kim, S.H. Baek, C.B. Eom, and R. Ramesh. Electrical control of antiferromagnetic domains in multiferroic $BiFeO_3$ films at room temperature. *Nat. Mater.*, 5(10):823–9, October 2006.

[98] S. M. Wu, Shane a. Cybart, P. Yu, M. D. Rossell, J. X. Zhang, R. Ramesh, and R. C. Dynes. Reversible electric control of exchange bias in a multiferroic field-effect device. *Nat. Mater.*, 9(July), July 2010.

[99] W.H. Meiklejohn. Exchange AnisotropyA Review. *J. Appl. Phys.*, 33(3):1328, 1962.

[100] W. Meiklejohn and C. Bean. New Magnetic Anisotropy. *Phys. Rev.*, 105(3):904–913, February 1957.

[101] Miguel Kiwi. Exchange bias theory. *J. Magn. Magn. Mater.*, 234:584–595, 2001.

[102] Florin Radu and Hartmut Zabel. Exchange bias effect of ferro-/antiferromagnetic heterostructures. In *Magnetic heterostructures: Advances and Perspectives in Spinstructures and Spintransport*. 2008.

[103] G. Mata, E. Pestana, H. Dreysse, and M. Kiwi. A quantum exchange bias model. *Physica B: Cond. Mat.*, 398(2):262–266, September 2007.

[104] J. Nogués, J. Sort, V. Langlais, V. Skumryev, S. Suriñach, J.S. Muñoz, M.D. Baró, J Nogues, S Surinach, J Munoz, and M Baro. Exchange bias in nanostructures. *Phys. Reports*, 422(3):65–117, December 2005.

[105] J. Wang, J.B. Neaton, H. Zheng, V. Nagarajan, S.B. Ogale, B. Liu, D. Viehland, V. Vaithyanathan, D.G. Schlom, U.V. Waghmare, N.A. Spaldin, K.M. Rabe, M. Wuttig, and R. Ramesh. Epitaxial $BiFeO_3$ multiferroic thin film heterostructures. *Science*, 299(5613):1719–22, March 2003.

[106] A. Palewicz, I. Sosnowska, R. Przenioso, and A.W. Hewat. $BiFeO_3$ Crystal Structure at Low Temperatures. *Acta Physica Polonica A*, 117(2):296–301, 2010.

[107] J. Moreau, C. Michel, R. Gerson, and W. James. Ferroelectric $BiFeO_3$ X-ray and neutron diffraction study. *J. Phys. and Chemistry of Solids*, 32(6):1315–1320, 1971.

[108] F. Kubel and H. Schmid. Structure of a ferroelectric and ferroelastic monodomain crystal of the perovskite $BiFeO_3$. *Acta Cryst. Section B Structural Science*, 46(6):698–702, December 1990.

[109] R. D. Shannon. Revised effective ionic radii and systematic studies of interatomic distances in halides and chalcogenides. *Acta Cryst. Section A*, 32(5):751–767, September 1976.

[110] A. Palewicz, R. Przenioso, I. Sosnowska, and A.W. Hewat. Atomic displacements in $BiFeO_3$ as a function of temperature: neutron diffraction study. *Acta Cryst. B*, 63(Pt 4):537–44, August 2007.

[111] Gustau Catalan and James F. Scott. Phys. and Applications of Bismuth Ferrite. *Advanced Mater.*, 21(24):2463–2485, June 2009.

[112] R. Palai, R. Katiyar, H. Schmid, P. Tissot, S. Clark, J. Robertson, S. Redfern, G. Catalan, and J. Scott. β phase and γ-β metal-insulator transition in multiferroic $BiFeO_3$. *Phys. Rev. B*, 77(1):1–11, January 2008.

[113] S. J. Clark and J. Robertson. Band gap and Schottky barrier heights of multiferroic $BiFeO_3$. *Appl. Phys. Lett.*, 90(13):132903, 2007.

[114] Claude Ederer and Nicola Spaldin. Influence of strain and oxygen vacancies on the magnetoelectric properties of multiferroic bismuth ferrite. *Phys. Rev. B*, 71(22):1–9, June 2005.

[115] P. Ravindran, R. Vidya, a. Kjekshus, H. Fjellvå g, and O. Eriksson. Theoretical investigation of magnetoelectric behavior in $BiFeO_3$. *Phys. Rev. B*, 74(22), December 2006.

[116] Guangyong Xu, H. Hiraka, G. Shirane, Jiefang Li, Junling Wang, and D. Viehland. Low symmetry phase in (001) $BiFeO_3$ epitaxial constrained thin films. *Appl. Phys. Lett.*, 86(18):182905, 2005.

[117] Jiefang Li, Junling Wang, M. Wuttig, R. Ramesh, Naigang Wang, B. Ruette, a. P. Pyatakov, a. K. Zvezdin, and D. Viehland. Dramatically enhanced polarization in (001), (101), and (111) $BiFeO_3$ thin films due to epitiaxial-induced transitions. *Appl. Phys. Lett.*, 84(25):5261, 2004.

[118] V. V. Shvartsman, W. Kleemann, R. Haumont, and J. Kreisel. Large bulk polarization and regular domain structure in ceramic $BiFeO_3$. *Appl. Phys. Lett.*, 90(17):172115, 2007.

[119] Dae Ho Kim, Ho Nyung Lee, Michael D. Biegalski, and Hans M. Christen. Effect of epitaxial strain on ferroelectric polarization in multiferroic $BiFeO_3$ films. *Appl. Phys. Lett.*, 92(1):012911, 2008.

[120] H. Jang, S. Baek, D. Ortiz, C. Folkman, R. Das, Y. Chu, P. Shafer, J. Zhang, S. Choudhury, V. Vaithyanathan, Y. Chen, D. Felker, M. Biegalski, M. Rzchowski, X. Pan, D. Schlom, L. Chen, R. Ramesh, and C. Eom. Strain-Induced Polarization Rotation in Epitaxial (001) $BiFeO_3$ Thin Films. *Phys. Rev. Lett.*, 101(10):3–6, September 2008.

[121] Chung W. Bark, Sangwoo Ryu, Yang M. Koo, Hyun M. Jang, and Hwa S. Youn. Electric-field-induced structural modulation of epitaxial $BiFeO_3$ multiferroic thin films as studied using X-ray microdiffraction. *Appl. Phys. Lett.*, 90(2):022902, 2007.

[122] D. Lebeugle, D. Colson, a. Forget, M. Viret, a. M. Bataille, and a. Gukasov. Electric-Field-Induced Spin Flop in $BiFeO_3$ Single Crystals at Room Temperature. *Phys. Rev. Lett.*, 100(22):1–4, June 2008.

[123] I Sosnowska, T P Neumaier, and E Steichele. Spiral magnetic ordering in bismuth ferrite. *J. Phys. C: Solid State Phys.*, 15(23):4835–4846, August 1982.

[124] Pavel Borisov, Andreas Hochstrat, Xi Chen, Wolfgang Kleemann, and Christian Binek. Magnetoelectric Switching of Exchange Bias. *Phys. Rev. Lett.*, 94(11):1–4, March 2005.

[125] V. Laukhin, V. Skumryev, X. Martí, D. Hrabovsky, F. Sánchez, M. García-Cuenca, C. Ferrater, M. Varela, U. Lüders, J. Bobo, and J. Fontcuberta. Electric-Field Control of Exchange Bias in Multiferroic Epitaxial Heterostructures. *Phys. Rev. Lett.*, 97(22):1–4, November 2006.

[126] J. Dho, X. Qi, H. Kim, J.L. MacManus-Driscoll, and M.G. Blamire. Large Electric Polarization and Exchange Bias in Multiferroic $BiFeO_3$. *Advanced Mater.*, 18(11):1445–1448, June 2006.

[127] H. Bea, M. Bibes, S. Cherifi, F. Nolting, B. Warot-Fonrose, S. Fusil, G. Herranz, C. Deranlot, E. Jacquet, K. Bouzehouane, and a. Barthelemy. Tunnel magnetoresistance and robust room temperature exchange bias with multiferroic $BiFeO_3$ epitaxial thin films. *Appl. Phys. Lett.*, 89(24):242114, 2006.

[128] H. Bea, M. Bibes, M. Sirena, G. Herranz, K. Bouzehouane, E. Jacquet, S. Fusil, P. Paruch, M. Dawber, J.-P. Contour, and A. Barthelemy. Combining half-metals and multiferroics into epitaxial heterostructures for spintronics. *Appl. Phys. Lett.*, 88(6):062502, 2006.

[129] Ying-Hao Chu, Lane W Martin, Mikel B Holcomb, Martin Gajek, Shu-Jen Han, Qing He, Nina Balke, Chan-Ho Yang, Donkoun Lee, Wei Hu, Qian Zhan, Pei-Ling Yang, Arantxa Fraile-Rodríguez, Andreas Scholl, Shan X Wang, and R Ramesh. Electric-field control of local ferromagnetism using a magnetoelectric multiferroic. *Nat. Mater.*, 7(6):478–82, June 2008.

[130] Lu You, Chengliang Lu, Pan Yang, Guchang Han, Tom Wu, Ulrike Luders, Wilfrid Prellier, Kui Yao, Lang Chen, and Junling Wang. Uniaxial Magnetic Anisotropy in La(0.7)Sr(0.3)MnO(3) Thin Films Induced by Multiferroic BiFeO(3) with Striped Ferroelectric Domains. *Advanced Mater.*, 117602:4964–4968, August 2010.

[131] P. Yu, J.-S. Lee, S. Okamoto, M. Rossell, M. Huijben, C.-H. Yang, Q. He, J. Zhang, S. Yang, M. Lee, Q. Ramasse, R. Erni, Y.-H. Chu, D. Arena, C.-C. Kao, L. Martin, and R. Ramesh. Interface Ferromagnetism and Orbital Reconstruction in BiFeO_{3}-La_{0.7}Sr_{0.3}MnO_{3} Heterostructures. *Phys. Rev. Lett.*, 105(2):1–5, July 2010.

[132] Lane W Martin, Ying-hao Chu, Mikel B Holcomb, Mark Huijben, Pu Yu, Shu-jen Han, Donkoun Lee, Shan X Wang, and R Ramesh. Nanoscale control of exchange bias with $BiFeO_3$ thin films. *Nano lett.*, 8(7):2050–5, July 2008.

[133] C. H. Ahn, M. Di Ventra, J. N. Eckstein, C. Daniel Frisbie, M. E. Gershenson, A. M. Goldman, I. H. Inoue, J. Mannhart, Andrew J. Millis, Alberto F. Morpurgo, Douglas Natelson, and Jean-Marc Triscone. Electrostatic Modification of Novel Mater. *Rev. Mod. Phys.*, 78(4):1185–1212, November 2006.

[134] S.M. Sze. *Phys. of Semiconductor Devices*. Wiley-Interscience, 1981.

[135] X. Hong, A. Posadas, and C. H. Ahn. Examining the Screening Limit of Field Effect Devices *Via* the Metal-Insulator Iransition. *Appl. Phys. Lett.*, 86(14):142501, 2005.

[136] Shufeng Zhang. Spin-Dependent Surface Screening in Ferromagnets and Magnetic Tunnel Junctions. *Phys. Rev. Lett.*, 83(3):640–643, July 1999.

[137] Manish Niranjan, Julian Velev, Chun-Gang Duan, S. Jaswal, and Evgeny Tsymbal. Magnetoelectric effect at the Fe_3O_4/BaTiO3 (001) interface: A first-principles study. *Phys. Rev. B*, 78(10):104405, September 2008.

[138] C. A. F. Vaz, J. Hoffman, Y. Segal, J. W. Reiner, R. D. Grober, Z. Zhang, C. H. Ahn, and F. J. Walker. Origin of the Magnetoelectric Coupling Effect in $Pb(Zr_{0.2}\ Ti_{0.8})O_3$ / $La_{0.8}\ Sr_{0.2}\ MnO_3$ Multiferroic Heterostructures. *Phys. Rev. Lett.*, 104(12):127202, March 2010.

[139] H Ohno, D Chiba, F Matsukura, T Omiya, E Abe, T Dietl, Y Ohno, and K Ohtani. Electric-field control of ferromagnetism. *Nat.*, 408(6815):944–6, 2000.

[140] C. A. F. Vaz, Y. Segal, J. Hoffman, R. D. Grober, F. J. Walker, and C. H. Ahn. Temperature Dependence of the Magnetoelectric Effect in $Pb(Zr_{0.2}\ Ti_{0.8})O_3$ / $La_{0.8}Sr_{0.2}MnO_3$ Multiferroic Heterostructures. *Appl. Phys. Lett.*, 97(4):042506, 2010.

[141] Elbio Dagotto, Takashi Hotta, and Adriana Moreo. Colossal magnetoresistant materials: the key role of phase separation. *Phys. Reports*, 344(1-3):1–153, April 2001.

[142] Y Tokura. Critical features of colossal magnetoresistive manganites. *Reports on Progress in Phys.*, 69(3):797–851, March 2006.

[143] C.A.F. Vaz, J. Hoffman, Y. Segal, M.S.J. Marshall, J.W. Reiner, Z. Zhang, R.D. Grober, F.J. Walker, and C.H. Ahn. Control of magnetism in $Pb(Zr_{0.2}Ti_{0.8})O_3$ / $La_{0.8}Sr_{0.2}MnO_3$ multiferroic heterostructures. *J. Appl. Phys.*, 109(7):07D905, 2011.

[144] J. Burton and E. Tsymbal. Prediction of electrically induced magnetic reconstruction at the manganite/ferroelectric interface. *Phys. Rev. B*, 80(17):174406, November 2009.

[145] Z Fang, Iv Solovyev, and K Terakura. Phase Diagram of Tetragonal Manganites. *Phys. Rev. Lett.*, 84(14):3169–3172, April 2000.

[146] H. Lu, T. A. George, Y. Wang, I. Ketsman, J. D. Burton, C.-W. Bark, S. Ryu, D. J. Kim, J. Wang, C. Binek, P. A. Dowben, A. Sokolov, C.-B. Eom, E. Y. Tsymbal, and A. Gruverman. Electric Modulation of Magnetization at the $BaTiO_3/La_{0.67}Sr_{0.33}MnO_3$ Interfaces. *Appl. Phys. Lett.*, 100(23):232904, 2012.

[147] Martin Weisheit, Sebastian Fähler, Alain Marty, Yves Souche, Christiane Poinsignon, and Dominique Givord. Electric field-induced modification of magnetism in thin-film ferromagnets. *Science*, 315(5810):349–51, January 2007.

[148] T Maruyama, Y Shiota, T Nozaki, K Ohta, N Toda, M Mizuguchi, A A Tulapurkar, T Shinjo, M Shiraishi, S Mizukami, Y Ando, and Y Suzuki. Large voltage-induced magnetic anisotropy change in a few atomic layers of iron. *Nat. Nanotech.*, 4(3):158–61, March 2009.

[149] I. B. Misirlioglu, a. L. Vasiliev, M. Aindow, S. P. Alpay, and R. Ramesh. Threading dislocation generation in epitaxial (Ba,Sr)TiO_3 films grown on (001) $LaAlO_3$ by pulsed laser deposition. *Appl. Phys. Lett.*, 84(10):1742, 2004.

[150] C L Canedy, Hao Li, S P Alpay, L. Salamanca-Riba, A L Roytburd, and R Ramesh. Dielectric properties in heteroepitaxial $Ba_{0.6}Sr_{0.4}TiO_3$ thin films: Effect of internal stresses and dislocation-type defects. *Appl. Phys. Lett.*, 77(11):1695, 2000.

[151] S. P. Alpay, I. B. Misirlioglu, V. Nagarajan, and R. Ramesh. Can interface dislocations degrade ferroelectric properties? *Appl. Phys. Lett.*, 85(11):2044, 2004.

[152] R. V. Chopdekar and Y. Suzuki. Magnetoelectric coupling in epitaxial $CoFe_2O_4$ on $BaTiO_3$. *Appl. Phys. Lett.*, 89(18):182506, 2006.

[153] Y. Lee, S. Park, Y. Hyun, J. Kim, V. Prokhorov, V. Komashko, and V. Svetchnikov. Microstructural and magnetotransport properties of $La_{0.7}Ca_{0.3}MnO_3$ / $BaTiO_3$ and $La_{0.7}Sr_{0.3}MnO_3$ / $BaTiO_3$ bilayered films. *Phys. Rev. B*, 73(22):224413, June 2006.

[154] MK Lee, TK Nath, CB Eom, MC Smoak, and F. Tsui. Strain modification of epitaxial perovskite oxide thin films using structural transitions of ferroelectric BaTiO substrate. *Appl. Phys. Lett.*, 77(22):3547, 2000.

[155] Yi Zhang, Chaoyong Deng, Jing Ma, Yuanhua Lin, and Ce-Wen Nan. Enhancement in magnetoelectric response in $CoFe_2O_4BaTiO_3$ heterostructure. *Appl. Phys. Lett.*, 92(6):062911, 2008.

[156] Sangwoo Ryu, Jung H. Park, and Hyun M. Jang. Magnetoelectric coupling of [00l]-oriented $Pb(Zr_{0.4}Ti_{0.6})O_3$-$Ni_{0.8}Zn_{0.2}Fe_2O_4$ multilayered thin films. *Appl. Phys. Lett.*, 91(14):142910, 2007.

[157] M. Ziese, a. Bollero, I. Panagiotopoulos, and N. Moutis. Magnetoresistance switch effect in a multiferroic $Fe_3O_4BaTiO_3$ bilayer. *Appl. Phys. Lett.*, 88(21):212502, 2006.

[158] Y. G. Ma, W. N. Cheng, M. Ning, and C. K. Ong. Magnetoelectric effect in epitaxial $Pb(Zr_{0.52}Ti_{0.48})O_3$ / $La_{0.7}Sr_{0.3}MnO_3$ composite thin film. *Appl. Phys. Lett.*, 90(15):152911, 2007.

[159] Jia-Mian Hu, Ce-Wen Nan, and Long-Qing Chen. Size-dependent electric voltage controlled magnetic anisotropy in multiferroic heterostructures: Interface-charge and strain comediated magnetoelectric coupling. *Phys. Rev. B*, 83(13):1–15, April 2011.

[160] Jia-Mian Hu and C. W. Nan. Electric-field-induced magnetic easy-axis reorientation in ferromagnetic/ferroelectric layered heterostructures. *Phys. Rev. B*, 80(22):224416, December 2009.

[161] N. Pertsev. Giant magnetoelectric effect via strain-induced spin reorientation transitions in ferromagnetic films. *Phys. Rev. B*, 78(21):212102, December 2008.

[162] A. J. Millis, T. Darling, and A. Migliori. Quantifying Strain Dependence in "Colossal" Magnetoresistance Manganites. *J. Appl. Phys.*, 83(3):1588, 1998.

[163] Hajo J. A. Molegraaf, Jason Hoffman, Carlos A. F. Vaz, Stefano Gariglio, Dirk van der Marel, Charles H. Ahn, and Jean-Marc Triscone. Magnetoelectric Effects in Complex Oxides with Competing Ground States. *Adv. Mater.*, 21(34):3470–3474, September 2009.

[164] C Xiong, J Sun, and B Shen. Dependence of magnetic anisotropy of the La0.67Ca0.33MnO3 films on substrate and film thickness. *Solid State Comm.*, 134(7):465–469, May 2005.

[165] C. Booth, F. Bridges, G. Kwei, J. Lawrence, a. Cornelius, and J. Neumeier. Direct Relationship between Magnetism and MnO6 Distortions in La1-xCaxMnO3. *Phys. Rev. Lett.*, 80(4):853–856, January 1998.

[166] Q. Qian, T. Tyson, C.-C. Kao, W. Prellier, J. Bai, a. Biswas, and R. Greene. Strain-induced local distortions and orbital ordering in Nd0.5Sr0.5MnO3 manganite films. *Phys. Rev. B*, 63(22):3–6, May 2001.

[167] Y. Uozu, Y. Wakabayashi, Y. Ogimoto, N. Takubo, H. Tamaru, N. Nagaosa, and K. Miyano. Intrinsic Colossal Magnetoresistance Effect in Thin-Film Pr0.5Sr0.5MnO3 through Dimensionality Switching. *Phys. Rev. Lett.*, 97(3):3–6, July 2006.

[168] J.-L. L. Maurice, F. Pailloux, A. Barthélémy, O. Durand, D. Imhoff, R. Lyonnet, A. Rocher, J.-P. P. Contour, and A. Barthelemy. Strain Relaxation in the Epitaxy of $La_{2/3}Sr_{1/3}MnO_3$ Grown By Pulsed-Laser Deposition on $SrTiO_3$(001). *Philos. Mag.*, 83(28):3201–3224, October 2003.

[169] M. Angeloni, G. Balestrino, N. G. Boggio, P. G. Medaglia, P. Orgiani, and A. Tebano. Suppression of the Metal-Insulator Transition Temperature in Thin $La_{0.7}Sr_{0.3}MnO_3$ Films. *J. Appl. Phys.*, 96(11):6387, 2004.

[170] L. Ranno, A. Llobet, R. Tiron, and E. Favre-Nicolin. Strain-Induced Magnetic Anisotropy in Epitaxial Manganite Films. *Appl. Surf. Sci.*, 188(1-2):170–175, March 2002.

[171] Y. Suzuki, H. Y. Hwang, S-W. Cheong, and R. B. van Dover. The role of strain in magnetic anisotropy of manganite thin films. *Appl. Phys. Lett.*, 71(1):140, 1997.

[172] H. L. Liu, M. X. Kuo, J. L. Her, K. S. Lu, S. M. Weng, L. M. Wang, S. L. Cheng, and J. G. Lin. Thickness-dependent optical properties of $La_{0.7}Sr_{0.3}MnO_3$ thin films. *J. Appl. Phys.*, 97(11):113528, 2005.

[173] T. Hezareh, F. S. Razavi, R. K. Kremer, H.-U. Habermeier, O. I. Lebedev, D. Kirilenko, and G. Van Tendeloo. Effect of $PbZr_{0.52}Ti_{0.48}O_3$ Thin Layer on Structure, Electronic and Magnetic Properties of $La_{0.65}Sr_{0.35}MnO_3$ and $La_{0.65}Ca_{0.30}MnO_3$ Thin-Films. *J. Appl. Phys.*, 109(11):113707, 2011.

[174] Ionela Vrejoiu, Michael Ziese, Annette Setzer, Pablo D. Esquinazi, Balaji I. Birajdar, Andriy Lotnyk, Marin Alexe, and Dietrich Hesse. Interfacial Strain Effects in Epitaxial Multiferroic Heterostructures of $PbZr_xTi_{1x}O_3$ / $La_{0.7}Sr_{0.3}MnO_3$ Grown by Pulsed-Laser Deposition. *Appl. Phys. Lett.*, 92(15):152506, 2008.

[175] M. Dzero, Gor'Kov L. P., V. Z. Kresin, and L. P. Gor'Kov. On Magnetoconductivity of Metallic Manganite Phases and Heterostructures. *Int. J. Mod. Phys. B*, 17(10):2095–2115, April 2003.

[176] K. Yoshimatsu, K. Horiba, H. Kumigashira, E. Ikenaga, and M. Oshima. Thickness dependent electronic structure of $La_{0.6}Sr_{0.4}MnO_3$ layer in $SrTiO_3$ / $La_{0.6}Sr_{0.4}MnO_3$ / $SrTiO_3$ heterostructures studied by hard X-ray photoemission spectroscopy. *Appl. Phys. Lett.*, 94(7):071901, 2009.

[177] M. Huijben, L. W. Martin, Y.-H. Chu, M. B. Holcomb, P. Yu, G. Rijnders, D. H. a. Blank, and R. Ramesh. Critical thickness and orbital ordering in ultrathin $La_{0.7}Sr_{0.3}MnO_3$ films. *Phys. Rev. B*, 78(9):1–7, September 2008.

[178] J. Z. Sun, D. W. Abraham, R. A. Rao, and C. B. Eom. Thickness-dependent magnetotransport in ultrathin manganite films. *Appl. Phys. Lett.*, 74(20):3017, 1999.

[179] Milton Ohring. *Mater. Science of Thin Films*. Academic Press, second edition, 2001.

[180] T.J. Zhu, L. Lu, and M.O. Lai. Pulsed laser deposition of lead-zirconate-titanate thin films and multilayered heterostructures. *Appl. Phys. A*, 81(4):701–714, April 2005.

[181] H M Christen and G Eres. *J. Phys. Cond. Matter, mendeley-groups = A Thesis, month = jul, number = 26, pages = 264005, pmid = 21694339, title = Recent advances in pulsed-laser deposition of complex oxides., url = http://www.ncbi.nlm.nih.gov/pubmed/21694339, volume = 20, year = 2008*.

[182] B.D. Cullity. *Elements of X-Ray Diffraction*. Addison-Wesley Publishing Company, Inc., 1956.

[183] Miho Yasaka. X-ray thin-film measurement techniques. *The Rigaku J.*, 26(2):1–9, 2010.

[184] Matts Björck and Gabriella Andersson. GenX : An Extensible X-Ray Reflectivity Refinement Program Utilizing Differential Evolution. *J. Appl. Crystallogr.*, 40(6):1174–1178, November 2007.

[185] D.B. Williams and C.B. Carter. *Transmission Electron Microscopy*. Springer, 2009.

[186] P.J. Ferreira, K. Mitsuishi, and E.A. Stach. In Situ Transmission Electron Microscopy. *MRS Bulletin*, 33(02):83–90, January 2011.

[187] L. Reimer and H. Kohl. *Transmission Electron Microscopy: Phys. of Image Formation*. 2008.

[188] R Egerton. *Physical Principles of Electron Microscopy: An Introduction to TEM, SEM, and AEM*. Springer, 2008.

[189] Volkan Ortalan, Alper Uzun, Bruce C Gates, and Nigel D Browning. Direct imaging of single metal atoms and clusters in the pores of dealuminated HY zeolite. *Nat. Nanotech.*, 5(7):506–10, July 2010.

[190] K. Kambe. Visualization of bloch waves of high energy electrons in high resolution electron microscopy. *Ultramic.*, 10(3):223–227, January 1982.

[191] F. Fujimoto. Periodicity of crystal structure images in electron microscopy with crystal thickness. *Phys. Status Solidi (a)*, 45(1):99–106, January 1978.

[192] Pierre Stadelmann. Jems image simulation, September 2004.

[193] Total Resolution Inc. Mactempasx, April 2014.

[194] C.T. Koch. *Determination of Core Structure Periodicity and Point Defect Density Along Dislocations*. PhD thesis, Arizona State University, 2002.

[195] R F Egerton. Electron energy-loss spectroscopy in the TEM. *Reports on Progress in Phys.*, 72(1):016502, January 2009.

[196] D a Muller, L Fitting Kourkoutis, M Murfitt, J H Song, H Y Hwang, J Silcox, N Dellby, and O L Krivanek. Atomic-scale chemical imaging of composition and bonding by aberration-corrected microscopy. *Science*, 319(5866):1073–6, February 2008.

[197] M. Varela, M. Oxley, W. Luo, J. Tao, M. Watanabe, A. Lupini, S. Pantelides, and S. Pennycook. Atomic-Resolution Imaging of Oxidation States in Manganites. *Phys. Rev. B*, 79(8):085117, February 2009.

[198] Martin J. Hÿtch and Andrew M. Minor. Observing and measuring strain in nanostructures and devices with transmission electron microscopy. *MRS Bulletin*, 39(02):138–146, February 2014.

[199] M.J. Hÿtch and F. Houdellier. Mapping Stress and Strain in Nanostructures by High-Resolution Transmission Electron Microscopy. *Microelectron. Eng.*, 84(3):460–463, March 2007.

[200] M.J. Hÿtch, E. Snoeck, and R. Kilaas. Quantitative Measurement of Displacement and Strain Fields From HREM Micrographs. *Ultramic.*, 74(3):131–146, August 1998.

[201] Florian Hüe, Martin Hÿtch, Hugo Bender, Florent Houdellier, and Alain Claverie. Direct Mapping of Strain in a Strained Silicon Transistor by High-Resolution Electron Microscopy. *Phys. Rev. Lett.*, 100(15):156602, April 2008.

[202] J Norpoth, D Su, H Inada, S Sievers, Y Zhu, and Ch Jooss. Interfacial reconstruction and superconductivity in cupratemanganite multilayers of YBa 2 Cu 3 O 7 δ and Pr 0.68 Ca 0.32 MnO 3. *New J. Phys.*, 14(9):093009, September 2012.

[203] J. Loudon, L. Kourkoutis, J. Ahn, C. Zhang, S.-W. Cheong, and D. Muller. Valence Changes and Structural Distortions in Charge Ordered Manganites Quantified by Atomic-Scale Scanning Transmission Electron Microscopy. *Phys. Rev. Lett.*, 99(23):1–4, December 2007.

[204] M.-J. Casanove, C. Roucau, P. Baulès, J Majimel, J.-C. Ousset, D. Magnoux, and J.F. Bobo. Growth and relaxation mechanisms in La0.66Sr0.33MnO3 manganites deposited on SrTiO3(0 0 1) and MgO(0 0 1). *Appl. Surf. Sci.*, 188(1-2):19–23, March 2002.

[205] Frédéric Pailloux, Rose Lyonnet, Jean-luc Maurice, and Jean-Pierre Contour. Twinning and lattice distortions in the epitaxy of La0.67Sr0.33MnO3 thin films on (0 0 1) SrTiO3. *Appl. Surf. Sci.*, 177(4):263–267, June 2001.

[206] L. Reimer. *Scanning Electron Microscopy*. Springer, second edition, 1998.

[207] Charles Kittel. *Introduction to Solid State Phys.* Wiley, 8 edition, 2004.

[208] FEI Corporation. FEI Titan Themis S/TEM, 2014.

[209] B. Sparber, S.R. Spurgeon, F Hanejko, and Mitra L. Taheri. A Study of Additive Diffusion in Ferrous Powder Metal Compacts Using Scanning Electron Microscopy and Energy Dispersive X-Ray Spectroscopy. In *PowderMet Conference*, 2011.

[210] B.D. Cullity and C.D. Graham. *Introduction to Magnetic Mater.* John Wiley and Sons, Hoboken, N.J., second edition, 2009.

[211] Z.Q. Qui and S.D. Bader. Surface magneto-optic Kerr effect. *Rev. Sci. Instr.*, 71:1243, August 2000.

[212] K. Postava, D. Hrabovský, J. Hamrlová, J. Pištora, a. Wawro, L.T. Baczewski, I. Sveklo, and a. Maziewski. Selective sensitivity of ellipsometry to magnetic nanostructures. *Thin Solid Films*, 519(9):2627–2632, December 2010.

[213] R. Morales, Zhi-Pan Li, O. Petracic, X. Batlle, Ivan K. Schuller, Justin Olamit, and Kai Liu. Magnetization depth dependence in exchange biased thin films. *Appl. Phys. Lett.*, 89(7):072504, 2006.

[214] S Bader. SMOKE. *J. Magn. Magn. Mater.*, 100(1-3):440–454, November 1991.

[215] H. R. Hulme. The Faraday Effect in Ferromagnetics. *Proc. R. Soc. A*, 135(826):237–257, February 1932.

[216] Petros Argyres. Theory of the Faraday and Kerr Effects in Ferromagnetics. *Phys. Rev.*, 97(2):334–345, January 1955.

[217] D A Allwood, Gang Xiong, M D Cooke, and R P Cowburn. Magneto-optical Kerr effect analysis of magnetic nanostructures. *J. Phys. D: Appl. Phys.*, 36(18):2175–2182, September 2003.

[218] F Lucari. Magneto-optical study of exchange-biased sputtered Co/CoO films. *J. Magn. Magn. Mater.*, 272-276:E837–E838, May 2004.

[219] M R Fitzsimmons and C F Majkrzak. Application of polarized neutron reflectometry to studies of artificially structured magnetic materials. Technical report, NIST NCNR, Gaithersburg, 2008.

[220] Institut Laue-Langevin. Some introductory elements, 2014.

[221] M Fitzsimmons. Neutron scattering studies of nanomagnetism and artificially structured materials. *J. Magn. Magn. Mater.*, 271(1):103–146, April 2004.

[222] J Ankner. Polarized-neutron reflectometry. *J. Magn. Magn. Mater.*, 200(1-3):741–754, October 1999.

[223] D.J. Hughes. *Pile Neutron Res.* Addison-Wesley, Cambridge, 1953.

[224] C F Majkrzak, K V O Donovan, and N F Berk. Polarized Neutron Reflectometry. 2004.

[225] J.-H. Kim, I. Vrejoiu, Y. Khaydukov, T. Keller, J. Stahn, a. Rühm, D. K. Satapathy, V. Hinkov, and B. Keimer. Competing interactions at the interface between ferromagnetic oxides revealed by spin-polarized neutron reflectometry. *Phys. Rev. B*, 86(18):180402, November 2012.

[226] Nikolay Kardjilov, Ingo Manke, André Hilger, Markus Strobl, and John Banhart. Neutron imaging in materials science. *Mater. Today*, 14(6):248–256, June 2011.

[227] Surendra Singh, M R Fitzsimmons, T Lookman, H Jeen, A Biswas, M A Roldan, and M. Varela. Measurement of the coupling between applied stress and magnetism in a manganite thin film. *Arxiv*, 3, January 2012.

[228] Kieron Burke and Lucas O. Wagner. DFT in a nutshell. *Int. J. Quantum Chemistry*, 113(2):96–101, January 2013.

[229] R.M. Martin. *Electronic Structure: Basic Theory and Practical Methods*. Cambridge University Press, 2004.

[230] A. Szabo and N.S. Ostlund. *Modern Quantum Chemistry*. MacMillan, New York, 1982.

[231] J. Slater. The Theory of Complex Spectra. *Phys. Rev.*, 34(10):1293–1322, November 1929.

[232] L. H. Thomas. The calculation of atomic fields. *Mathematical Proceedings of the Cambridge Philosophical Society*, 23(05):542, October 1927.

[233] E. Fermi. Eine statistische Methode zur Bestimmung einiger Eigenschaften des Atoms und ihre Anwendung auf die Theorie des periodischen Systems der Elemente. *Z. Phys.*, 48(1-2):73–79, January 1928.

[234] Y W Yin, J D Burton, Y-m Kim, A Y Borisevich, S J Pennycook, S M Yang, T W Noh, A Gruverman, X G Li, E Y Tsymbal, and Qi Li. Enhanced tunnelling electroresistance effect due to a ferroelectrically induced phase transition at a magnetic complex oxide interface. *Nat. Mater.*, (February):1–6, February 2013.

[235] Hossein Raanaei, Hans Lidbaum, Andreas Liebig, Klaus Leifer, and Björgvin Hjörvarsson. Structural coherence and layer perfection in Fe/MgO multilayers. *J. Phys.: Cond. Mat.*, 20(5):055212, February 2008.

[236] Th. Mühge, A. Stierle, N. Metoki, H. Zabel, and U. Pietsch. Structural properties of high-quality sputtered Fe films on Al2O3(1120) and MgO(001) substrates. *Appl. Phys. A Solids and Surfaces*, 59(6):659–665, December 1994.

[237] BM Lairson, AP Payne, S. Brennan, NM Rensing, BJ Daniels, and BM Clemens. In situ x-ray measurements of the initial epitaxy of Fe (001) films on MgO (001). *J. Appl. Phys.*, 78(7):4449–4455, 1995.

[238] Y. Y. Huang, C. Liu, and G. P. Felcher. Magnetization of ultrathin bcc Fe films on MgO. *Phys. Rev. B*, 47(1):183–189, January 1993.

[239] C Liu, Y. Park, and S.D. Bader. Resistance minimum in ultrathin ferromagnetic films of Fe on MgO(100). *J. Magn. Magn. Mater.*, 111(3):L225–L230, June 1992.

[240] R Fan, SJ Lee, JP Goff, RCC Ward, SG Wang, A Kohn, C Wang, AR Wildes, and SP Collins. The influence of interfacial roughness on the coherence of structure and magnetic coupling across barriers in Fe/MgO multilayers. *J. Phys.: Cond. Mat.*, 22:226004, 2010.

[241] M Arita, K Wakasugi, K Ohta, K Hamada, Y Takahashi, and J Choi. Microstructure and electric property of MgO/Fe/MgO tri-layer films forming a nano-granular system. *Micro. Eng.*, 85(12):2445–2450, December 2008.

[242] M. Tsujikawa, S. Haraguchi, T. Oda, Y. Miura, and M. Shirai. A comparative ab initio study on electric-field dependence of magnetic anisotropy in MgO/Fe/Pt and MgO/Fe/Au films. *J. Appl. Phys.*, 109(7):07C107, 2011.

[243] F. Cebollada, a. Hernando-Mañeru, a. Hernando, C. Martínez-Boubeta, a. Cebollada, and J. González. Anisotropy, hysteresis, and morphology of self-patterned epitaxial Fe/MgO/GaAs films. *Phys. Rev. B*, 66(17):1–8, November 2002.

[244] C. Martínez Boubeta, C. Clavero, J. García-Martín, G. Armelles, a. Cebollada, Ll. Balcells, J. Menéndez, F. Peiró, a. Cornet, and Michael Toney. Coverage effects on the magnetism of FeMgO(001) ultrathin films. *Phys. Rev. B*, 71(1):13–15, January 2005.

[245] P Luches, S Benedetti, M Liberati, F Boscherini, I Pronin, and S Valeri. Absence of oxide formation at the Fe/MgO(001) interface. *Surf. Sci.*, 583:191–198, May 2005.

[246] X.-G. Zhang, W. Butler, and Amrit Bandyopadhyay. Effects of the iron-oxide layer in Fe-FeO-MgO-Fe tunneling junctions. *Phys. Rev. B*, 68(9):6–9, September 2003.

[247] Chao Wang, Shouguo Wang, Amit Kohn, Roger C C Ward, and Amanda. K. Petford-Long. Transmission Electron Microscopy Study of the Interface for Magnetic Tunnel Junctions. *IEEE Trans. Magn.*, 43(6):2779–2781, June 2007.

[248] C. Tiusan, M. Sicot, M. Hehn, C. Belouard, S. Andrieu, F. Montaigne, and a. Schuhl. FeMgO interface engineering for high-output-voltage device applications. *Appl. Phys. Lett.*, 88(6):062512, 2006.

[249] H. Meyerheim, R. Popescu, N. Jedrecy, M. Vedpathak, M. Sauvage-Simkin, R. Pinchaux, B. Heinrich, and J. Kirschner. Surface x-ray diffraction analysis of the MgO/Fe(001) interface: Evidence for an FeO layer. *Phys. Rev. B*, 65(14):1–7, April 2002.

[250] Ivan Rungger, Alexandre Reily Rocha, Oleg Mryasov, Olle Heinonen, and Stefano Sanvito. Electronic transport through Fe/MgO/Fe(100) tunnel junctions. *J. Magn. Magn. Mater.*, 316(2):481–483, September 2007.

[251] P. A. van Aken, V. J. Styrsa, B. Liebscher, A. B. Woodland, and G. J. Redhammer. Microanalysis of Fe^{3+} / ΣFe in oxide and silicate minerals by investigation of electron energy-loss near-edge structures (ELNES) at the Fe $M_{2,3}$ edge. *Phys. and Chem. Miner.*, 26(7):584–590, August 1999.

[252] C. Colliex, T. Manoubi, and C. Ortiz. Electron-energy-loss-spectroscopy near-edge fine structures in the iron-oxygen system. *Phys. Rev. B*, 44(20):11402–11411, November 1991.

[253] Frederic Cosandey, Jafar F Al-Sharab, Fadwa Badway, Glenn G Amatucci, and Pierre Stadelmann. EELS spectroscopy of iron fluorides and FeFx/C nanocomposite electrodes used in Li-ion batteries. *Microscopy and Microanalysis*, 13(2):87–95, April 2007.

[254] J. Graetz, C. C. Ahn, R. Yazami, and B. Fultz. An Electron Energy-Loss Spectrometry Study of Charge Compensation in LiNi 0.8 Co 0.2 O 2. *The J. Physical Chemistry B*, 107(13):2887–2891, April 2003.

[255] F Cosandey, D Su, M Sina, N Pereira, and G G Amatucci. Fe valence determination and Li elemental distribution in lithiated FeO(0.7)F(1.3)/C nanocomposite battery materials by electron energy loss spectroscopy (EELS). *Micron*, 43(1):22–29, June 2012.

[256] Toru Kanaji, Takami Kagotani, and S Nagata. Auger and loss spectroscopy study of surface contamination effect on the growth mode of iron epitaxial films on MgO(001). *Thin Solid Films*, 32(2):217–219, March 1976.

[257] G Fahsold, A Pucci, and K.H. Rieder. Growth of Fe on MgO (001) studied by He-atom scattering. *Phys. Rev. B*, 61(12):8475–8483, 2000.

[258] Martin Siegert and Michael Plischke. Solid-on-solid models of molecular-beam epitaxy. *Phys. Rev. E*, 50(2):917–931, August 1994.

[259] M. Johnson, C. Orme, A. Hunt, D. Graff, J Sudijono, L. Sander, and B. Orr. Stable and unstable growth in molecular beam epitaxy. *Phys. Rev. Lett.*, 72(1):116–119, January 1994.

[260] Yongsup Park, Eric E Fullerton, and S D Bader. Growth-induced uniaxial in-plane magnetic anisotropy for ultrathin Fe deposited on MgO(001) by oblique-incidence molecular beam epitaxy. *Appl. Phys. Lett.*, 66(16):2140, 1995.

[261] K. Thürmer, R. Koch, M. Weber, and K. Rieder. Dynamic Evolution of Pyramid Structures during Growth of Epitaxial Fe (001) Films. *Phys. Rev. Lett.*, 75(9):1767–1770, August 1995.

[262] G. Fahsold, a. Bartel, O. Krauth, and a. Lehmann. In-situ investigation of Fe ultrathin film growth by infrared transmission spectroscopy. *Surf. Sci.*, 433-435:162–166, August 1999.

[263] D. Petti, M. Cantoni, C. Rinaldi, S. Brivio, R. Bertacco, J. Gazquez, and M. Varela. Sharp Fe/MgO/Ge(001) epitaxial heterostructures for tunneling junctions. *J. Appl. Phys.*, 109(8):084909, 2011.

[264] J. L. JL Vassent, M. Dynna, A. Marty, B. Gilles, and G. Patrat. A study of growth and the relaxation of elastic strain in MgO on Fe(001). *J. Appl. Phys.*, 80(10):5727, 1996.

[265] Stuart L. Blank and Joseph a. Pask. Diffusion of Iron and Nickel in Magnesium Oxide Single Crystals. *J. the American Ceramic Society*, 52(12):669–675, December 1969.

[266] R. a. Weeks, J. Gastineau, and E. Sonder. Distribution of Fe3+ in iron-doped MgO single crystals. *Phys. Status Solidi (a)*, 61(1):265–274, September 1980.

[267] Yu. V. Goryunov, N. N. Garifyanov, G. G. Khaliullin, I. A. Garifullin, L. Tagirov, F. Schreiber, Th. Mühge, and H. Zabel. Magnetic anisotropies of sputtered Fe films on MgO substrates. *Phys. Rev. B*, 52(18):13450–13458, November 1995.

[268] P Bruno. Magnetic surface anisotropy of cobalt and surface roughness effects within Neel's model. *J. Phys. F: Metal Phys.*, 18(6):1291–1298, June 1988.

[269] Hiroshi Matsuda, Soichiro Okamura, Tadashi Shiosaki, Hideaki Adachi, and Hiroshi Sakakima. Magnetic and magnetoresistance properties of spin valves using epitaxial Fe_3O_4 (110) as the pinning layer. *J. Appl. Phys.*, 98(6):063903, 2005.

[270] S Schnittger, C Jooss, and S Sievers. Magnetic and structural properties of cobalt ferrite thin films and structures. *J. Phys.: Conference Series*, 200(7):072086, January 2010.

[271] G. Hu, V.G. Harris, and Y. Suzuki. Microstructure and magnetic properties of cobalt ferrite thin films. *Magnetics, IEEE Transactions on*, 37(4):2347–2349, July 2001.

[272] J Camarero, J J de Miguel, R Miranda, and A Hernando. Thickness-dependent coercivity of ultrathin Co films grown on Cu(111). *J. Phys.: Cond. Mat.*, 12(35):7713–7719, September 2000.

[273] M. L. Munford, M. L. Sartorelli, L. Seligman, and A. A. Pasa. Morphology and Magnetic Properties of Co Thin Films Electrodeposited on Si. *J. Electrochem. Soc.*, 149(5):C274, 2002.

[274] a Moschel, Ra Hyman, A Zangwill, and Md Stiles. Magnetization Reversal in Ultrathin Films with Monolayer-Scale Surface Roughness. *Phys. Rev. Lett.*, 77(17):3653–3656, October 1996.

[275] Chen Chen, Osamu Kitakami, and Yutaka Shimada. Particle size effects and surface anisotropy in Fe-based granular films. *J. Appl. Phys.*, 84(4):2184, 1998.

[276] Jian-Wang Cai, Satoshi Okamoto, Osamu Kitakami, and Yutaka Shimada. Large coercivity and surface anisotropy in MgO/Co multilayer films. *Phys. Rev. B*, 63(10):1–7, February 2001.

[277] J. Islam, Y. Yamamoto, Eiji Shikoh, Akihiko Fujiwara, and H. Hori. A comparative study of Co and Fe thin films deposited on GaAs(001) substrate. *J. Magn. Magn. Mater.*, 320(3-4):571–574, February 2008.

[278] C. L. Platt, a. E. Berkowitz, David J. Smith, and M. R. McCartney. Correlation of coercivity and microstructure of thin CoFe films. *J. Appl. Phys.*, 88(4):2058, 2000.

[279] S. K. Chen, F. T. Yuan, and T. S. Chin. Effect of interfacial diffusion on microstructure and magnetic properties of CuFePt bilayer thin films. *J. Appl. Phys.*, 97(7):073902, 2005.

[280] Albert Fert. The Present and the Future of Spintronics. *Thin Solid Films*, 517(1):2–5, November 2008.

[281] M. Stiles and A. Zangwill. Anatomy of Spin-Transfer Torque. *Phys. Rev. B*, 66(1):014407, June 2002.

[282] Jack C. Sankey, Yong-Tao Cui, Jonathan Z. Sun, John C. Slonczewski, Robert A. Buhrman, and Daniel C. Ralph. Measurement of the Spin-Transfer-Torque Vector in Magnetic Tunnel Junctions. *Nat. Phys.*, 4(1):67–71, November 2007.

[283] S.A. Wolf and D. Treger. Spintronics: A new paradigm for electronics for the new millennium. *IEEE Trans. Magn.*, 36(5):2748–2751, 2000.

[284] Albert Fert, Jean-Marie George, Henri Jaffrès, Richard Mattana, and Pierre Seneor. The New Era of Spintronics. *Europhys. News*, 34(6):227–229, November 2003.

[285] W Eerenstein, M Wiora, J L Prieto, J F Scott, and N D Mathur. Giant Sharp and Persistent Converse Magnetoelectric Effects in Multiferroic Epitaxial Heterostructures. *Nat. Mater.*, 6(5):348–351, May 2007.

[286] V Garcia, M Bibes, L Bocher, S Valencia, F Kronast, A Crassous, X Moya, S Enouz-Vedrenne, A Gloter, D Imhoff, C Deranlot, N D Mathur, S Fusil, K Bouzehouane, and A Barthélémy. Ferroelectric Control of Spin Polarization. *Science*, 327(5969):1106–1110, February 2010.

[287] Manuel Bibes and Agnès Barthélémy. Multiferroics: Towards a Magnetoelectric Memory. *Nat. Mater.*, 7(6):425–426, June 2008.

[288] Pavel Lukashev and Renat F. Sabirianov. Flexomagnetic Effect in Frustrated Triangular Magnetic Structures. *Phys. Rev. B*, 82(9):094417, September 2010.

[289] Eugene Eliseev, Anna Morozovska, Maya Glinchuk, and R. Blinc. Spontaneous Flexoelectric/Flexomagnetic Effect in Nanoferroics. *Phys. Rev. B*, 79(16):165433, April 2009.

[290] R. F. Sabirianov and Pavel V. Lukashev. Magneto-Elastic Properties of Frustrated Triangular Magnetic Structure: Flexomagnetic Effect. In *American Physical Society March Meeting*, 2010.

[291] K. Dörr and C. Thiele. Multiferroic Bilayers of Manganites and Titanates. *Phys. Status Solidi B*, 243(1):21–28, January 2006.

[292] R.K. Zheng, Y. Wang, Y.K. Liu, G.Y. Gao, L.F. Fei, Y. Jiang, H.L.W. Chan, X.M. Li, H.S. Luo, and X.G. Li. Epitaxial Growth and Interface Strain Coupling Effects in Manganite Film / Piezoelectric-Crystal Multiferroic Heterostructures. *Mater. Chem. Phys.*, 133(1):42–46, March 2012.

[293] Li Shu, Zheng Li, Jing Ma, Ya Gao, Lin Gu, Yang Shen, Yuanhua Lin, and C. W. Nan. Thickness-Dependent Voltage-Modulated Magnetism in Multiferroic Heterostructures. *Appl. Phys. Lett.*, 100(2):022405, 2012.

[294] Ming Liu, Shandong Li, Ogheneyunume Obi, Jing Lou, Scott Rand, and Nian X. Sun. Electric Field Modulation of Magnetoresistance in Multiferroic Heterostructures for Ultralow Power Electronics. *Appl. Phys. Lett.*, 98(22):222509, 2011.

[295] Miryam Arredondo, Quentin M Ramasse, Matthew Weyland, Reza Mahjoub, Ionela Vrejoiu, Dietrich Hesse, Nigel D Browning, Marin Alexe, Paul Munroe, and Valanoor Nagarajan. Direct Evidence for Cation Non-Stoichiometry and Cottrell Atmospheres Around Dislocation Cores in Functional Oxide Interfaces. *Adv. Mater.*, 22(22):2430–2434, June 2010.

[296] M. Arredondo, M. Weyland, M. Hambe, Q. M. Ramasse, P. Munroe, and V. Nagarajan. Chemistry of Ruddlesden-Popper Planar Faults at a Ferroelectric-Ferromagnet Perovskite Interface. *J. Appl. Phys.*, 109(8):084101, 2011.

[297] J. Chakhalian, A. J. Millis, and J. Rondinelli. Whither the Oxide Interface. *Nat. Mater.*, 11(2):92–94, January 2012.

[298] Stuart A. Wolf, Jiwei Lu, Mircea R. Stan, Eugene Chen, and Daryl M. Treger. The Promise of Nanomagnetics and Spintronics for Future Logic and Universal Memory. *Proc. IEEE*, 98(12):2155–2168, December 2010.

[299] B Raveau, A Maignan, R Mahendiran, D Khomskii, C Martin, S Hébert, M Hervieu, and R Frésard. Instability of Magnetism and Conductivity in CMR Manganites: Role of Mn-Site Doping and Thermal Cycling. *J. Phys. Chem. Solids*, 63(6-8):901–905, June 2002.

[300] Jason Chen, Haidong Lu, Heng-Jui Liu, Ying-Hao Chu, Steve Dunn, Kostya (Ken) Ostrikov, Alexei Gruverman, and Nagarajan Valanoor. Interface Control of Surface Photochemical Reactivity in Ultrathin Epitaxial Ferroelectric Films. *Appl. Phys. Lett.*, 102(18):182904, 2013.

[301] J Karthik, Anoop R Damodaran, and Lane W Martin. Epitaxial Ferroelectric Heterostructures Fabricated by Selective Area Epitaxy of $SrRuO_3$ Using an MgO Mask. *Adv. Mater.*, 24(12):1610–1615, March 2012.

[302] P Yu, W Luo, D Yi, J X Zhang, M D Rossell, C-H Yang, L You, G Singh-Bhalla, S Y Yang, Q He, Q M Ramasse, R Erni, L W Martin, Y H Chu, S T Pantelides, S J Pennycook, and R Ramesh. Interface Control of Bulk Ferroelectric Polarization. *Proc. Natl. Acad. Sci. U. S. A.*, 109(25):9710–9715, June 2012.

[303] V P Afanasjev, A A Petrov, I P Pronin, E A Tarakanov, E Ju Kaptelov, and J Graul. Polarization and Self-Polarization in Thin $PbZr_{1-x}Ti_xO_3$ (PZT) Films. *J. Phys.: Condens. Matter*, 13(39):8755–8763, October 2001.

[304] Chun-Lin Jia, Valanoor Nagarajan, Jia-Qing He, Lothar Houben, Tong Zhao, Ramamoorthy Ramesh, Knut Urban, and Rainer Waser. Unit-Cell Scale Mapping of Ferroelectricity and Tetragonality in Epitaxial Ultrathin Ferroelectric Films. *Nat. Mater.*, 6(1):64–69, January 2007.

[305] Peng Gao, Christopher T Nelson, Jacob R Jokisaari, Seung-Hyub Baek, Chung Wung Bark, Yi Zhang, Enge Wang, Darrell G Schlom, Chang-Beom Eom, and Xiaoqing Pan. Revealing the Role of Defects in Ferroelectric Switching with Atomic Resolution. *Nat. Commun.*, 2:591, January 2011.

[306] Mitsuhiro Saito, Koji Kimoto, Takuro Nagai, Shun Fukushima, Daisuke Akahoshi, Hideki Kuwahara, Yoshio Matsui, and Kazuo Ishizuka. Local Crystal Structure Analysis with 10-pm Accuracy Using Scanning Transmission Electron Microscopy. *J. Electron Microsc.*, 58(3):131–136, June 2009.

[307] P Thévenaz, U E Ruttimann, and M Unser. A Pyramid Approach to Subpixel Registration Based on Intensity. *IEEE Transactions on Image Proccessing*, 7(1):27–41, January 1998.

[308] David Walker, Pam A. Thomas, and Steve P. Collins. A Comprehensive Investigation of the Structural Properties of Ferroelectric $PbZr_{0.2}Ti_{0.8}O_3$ Thin Films Grown by PLD. *Phys. Status Solidi A*, 206(8):1799–1803, August 2009.

[309] Hanghui Chen and Sohrab Ismail-Beigi. Ferroelectric Control of Magnetization in $La_{1-x}Sr_xMnO_3$ Manganites: A First-Principles Study. *Phys. Rev. B*, 86(2):1–13, July 2012.

[310] J W Freeland, J J Kavich, K E Gray, L Ozyuzer, H Zheng, J F Mitchell, M P Warusawithana, P Ryan, X Zhai, R H Kodama, and J N Eckstein. Suppressed Magnetization at the Surfaces and Interfaces of Ferromagnetic Metallic Manganites. *J. Phys.: Condens. Matter*, 19(31):315210, August 2007.

[311] F Tsui, M C Smoak, T. K. Nath, and C. B. Eom. Strain-Dependent Magnetic Phase Diagram of Epitaxial $La_{0.67}Sr_{0.33}MnO_3$ Thin Films. *Appl. Phys. Lett.*, 76(17):2421, 2000.

[312] Jinbo Cao and Junqiao Wu. Strain Effects in Low-Dimensional Transition Metal Oxides. *Mater. Sci. Eng.: R: Reports*, 71(2-4):35–52, January 2011.

[313] Teruo Kanki, Hidekazu Tanaka, and Tomoji Kawai. Anomalous Strain Effect in $La_{0.8}Ba_{0.2}MnO_3$ Epitaxial Thin Film: Role of the Orbital Degree of Freedom in Stabilizing Ferromagnetism. *Phys. Rev. B*, 64(22):224418, November 2001.

[314] F. Yang, N. Kemik, M. D. Biegalski, H. M. Christen, E. Arenholz, and Y. Takamura. Strain Engineering to Control the Magnetic and Magnetotransport Properties of $La_{0.67}Sr_{0.33}MnO_3$ Thin Films. *Appl. Phys. Lett.*, 97(9):092503, 2010.

[315] P. Zubko, G. Catalan, A. Buckley, P. Welche, and J. Scott. Strain-Gradient-Induced Polarization in $SrTiO_3$ Single Crystals. *Phys. Rev. Lett.*, 99(16):167601, October 2007.

[316] E. A. Eliseev, M. D. Glinchuk, V. Khist, V. V. Skorokhod, R. Blinc, and A. N. Morozovska. Linear Magnetoelectric Coupling and Ferroelectricity Induced by the Flexomagnetic Effect in Ferroics. *Phys. Rev. B*, 84(17):174112, November 2011.

[317] Pavlo Zubko, Gustau Catalan, and Alexander K. Tagantsev. Flexoelectric Effect in Solids. *Ann. Rev. Mater. Res.*, 43(1):387–421, July 2013.

[318] SY Park, YP Lee, and VG Prokhorov. Effects of Lattice-Strain-Induced Distortion and Jahn-Teller Coupling in $La_{0.8}Sr_{0.2}MnO_3/La_{0.8}Ca_{0.2}MnO_3$ Epitaxial Films. *J. Korean Phys. Soc.*, 45(1):47–50, 2004.

[319] J. Kübler, A. William, and C. Sommers. Formation and Coupling of Magnetic Moments in Heusler Alloys. *Phys. Rev. B*, 28(4):1745–1755, August 1983.

[320] Nathascia Lampis, Cesare Franchini, Guido Satta, Alessandra Geddo-Lehmann, and Sandro Massidda. Electronic Structure of $PbFe_{1/2}Ta_{1/2}O_3$: Crystallographic Ordering and Magnetic Properties. *Phys. Rev. B*, 69(6):064412, February 2004.

[321] Antonio Cammarata and James M. Rondinelli. Octahedral Engineering of Orbital Polarizations in Charge Transfer Oxides. *Phys. Rev. B*, 87(15):155135, April 2013.

[322] P. Dey, T. K. Nath, and A. Taraphder. Effect of Substrate-Induced Strain on Transport and Magnetic Properties of Epitaxial $La_{0.67}Sr_{0.33}MnO_3$ Thin Films. *Appl. Phys. Lett.*, 91(1):012511, 2007.

[323] A-M. Haghiri-Gosnet and J-P. Renard. CMR Manganites: Physics, Thin Films and Devices. *J. Phys. D: Appl. Phys.*, 36(8):R127–R150, April 2003.

[324] D Pesquera, G Herranz, A Barla, E Pellegrin, F Bondino, E Magnano, F Sánchez, and J Fontcuberta. Surface Symmetry-Breaking and Strain Effects on Orbital Occupancy in Transition Metal Perovskite Epitaxial Films. *Nat. Commun.*, 3:1189, January 2012.

[325] D. B. Loomer, T. A. Al, L. Weaver, and S. Cogswell. Manganese Valence Imaging in Mn Minerals at the Nanoscale Using STEM-EELS. *American Mineralogist*, 92(1):72–79, January 2007.

[326] Amish Shah, Xiaofang Zhai, Bin Jiang, Jian-Guo Wen, James Eckstein, and Jian-Min Zuo. Electron Energy-Loss Study of the Electronic Structure of Atomic Scale $SrTiO_3$-$SrMnO_3$-$LaMnO_3$ Superlattices. *Phys. Rev. B*, 77(11):2–7, March 2008.

[327] Amish B Shah, Quentin M Ramasse, Xiaofang Zhai, Jian Guo Wen, Steve J May, Ivan Petrov, Anand Bhattacharya, Peter Abbamonte, James N Eckstein, and Jian-Min Zuo. Probing Interfacial Electronic Structures in Atomic Layer $LaMnO_3$ and $SrTiO_3$ Superlattices. *Adv. Mater.*, 22(10):1156–1160, March 2010.

[328] A. Shah, Q. Ramasse, S. May, Jerald Kavich, J. Wen, X. Zhai, J. Eckstein, J. Freeland, A. Bhattacharya, and J. Zuo. Presence and Spatial Distribution of Interfacial Electronic States in $LaMnO_3$-$SrMnO_3$ Superlattices. *Phys. Rev. B*, 82(11):1–10, September 2010.

[329] H K Schmid and W Mader. Oxidation States of Mn and Fe in Various Compound Oxide Systems. *Micron*, 37(5):426–432, January 2006.

[330] L. Samet, D. Imhoff, J.-L. Maurice, J.-P. Contour, A. Gloter, T. Manoubi, A. Fert, and C. Colliex. EELS Study of Interfaces in Magnetoresistive LSMO/STO/LSMO Tunnel Junctions. *Eur. Phys. J. B*, 34(2):179–192, July 2003.

[331] Yurii a Izyumov and Yu N Skryabin. Double exchange model and the unique properties of the manganites. *Phys.-Usp.*, 44(2):109–134, February 2001.

[332] C. A. F. Vaz and Urs Staub. Artificial multiferroic heterostructures. *J. Mater. Chemistry C*, 2013.

[333] C H Ahn, J-M Triscone, and J Mannhart. Electric field effect in correlated oxide systems. *Nat.*, 424(6952):1015–8, August 2003.

[334] Matthew Dawber and James F. Scott. Models of Electrode-Dielectric Interfaces in Ferroelectric Thin-Film Devices. *Japanese J. Appl. Phys.*, 41(Part 1, No. 11B):6848–6851, November 2002.

[335] Steven R Spurgeon, Jennifer D Sloppy, Despoina Maria Demie Kepaptsoglou, Prasanna V Balachandran, Siamak Nejati, J Karthik, Anoop R Damodaran, Craig L Johnson, Hailemariam Ambaye, Richard Goyette, Valeria Lauter, Quentin M Ramasse, Juan Carlos Idrobo, Kenneth K S Lau, Samuel E Lofland, James M Rondinelli, Lane W Martin, and Mitra L Taheri. Thickness-dependent crossover from charge- to strain-mediated magnetoelectric coupling in ferromagnetic/piezoelectric oxide heterostructures. *ACS Nano*, 8(1):894–903, January 2014.

[336] S. Brivio, M. Cantoni, D. Petti, and R. Bertacco. Near-room-temperature control of magnetization in field effect devices based on $La_{0.67}Sr_{0.33}MnO_3$ thin films. *J. Appl. Phys.*, 108(11):113906, 2010.

[337] Kasim Sader, Bernhard Schaffer, Gareth Vaughan, Rik Brydson, Andy Brown, and Andrew Bleloch. Smart acquisition EELS. *Ultramic.*, 110(8):998–1003, July 2010.

[338] Haiyan Tan, Jo Verbeeck, Artem Abakumov, and Gustaaf Van Tendeloo. Oxidation state and chemical shift investigation in transition metal oxides by EELS. *Ultramic.*, 116:24–33, May 2012.

[339] Jin Suntivich, Wesley T. Hong, Yueh-Lin Lee, James M. Rondinelli, Wanli Yang, John B. Goodenough, Bogdan Dabrowski, John W. Freeland, and Yang Shao-Horn. Estimating hybridization of transition metal and oxygen states in perovskites from o k-edge x-ray absorption spectroscopy. *J. Phys. Chem. C*, 118(4):1856–1863, 2014.

[340] Hiroki Kurata and Christian Colliex. Electron-energy-loss core-edge structures in manganese oxides. *Phys. Rev. B*, 48(4):2102–2108, July 1993.

[341] Paolo Giannozzi, Stefano Baroni, Nicola Bonini, Matteo Calandra, Roberto Car, Carlo Cavazzoni, Davide Ceresoli, Guido L Chiarotti, Matteo Cococcioni, Ismaila Dabo, Andrea Dal Corso, Stefano de Gironcoli, Stefano Fabris, Guido Fratesi, Ralph Gebauer, Uwe Gerstmann, Christos Gougoussis, Anton Kokalj, Michele Lazzeri, Layla Martin-Samos, Nicola Marzari, Francesco Mauri, Riccardo Mazzarello, Stefano Paolini, Alfredo Pasquarello, Lorenzo Paulatto, Carlo Sbraccia, Sandro Scandolo, Gabriele Sclauzero, Ari P Seitsonen, Alexander Smogunov, Paolo Umari, and Renata M Wentzcovitch. QUANTUM ESPRESSO: a modular and open-source software project for quantum simulations of materials. *J. Phys. Cond. Mat.*, 21(39):395502 (19pp), 2009.

[342] Christos Gougoussis, Matteo Calandra, Ari P. Seitsonen, and Francesco Mauri. First-principles calculations of x-ray absorption in a scheme based on ultrasoft pseudopotentials: From α-quartz to high-T_c compounds. *Phys. Rev. B*, 80:075102, Aug 2009.

[343] C. Gougoussis, M. Calandra, A. Seitsonen, Ch. Brouder, A. Shukla, and F. Mauri. Intrinsic charge transfer gap in NiO from Ni K-edge x-ray absorption spectroscopy. *Phys. Rev. B*, 79:045118, Jan 2009.

[344] David Vanderbilt. Soft self-consistent pseudopotentials in a generalized eigenvalue formalism. *Phys. Rev. B*, 41:7892–7895, Apr 1990.

[345] John P. Perdew, Adrienn Ruzsinszky, Gábor I. Csonka, Oleg A. Vydrov, Gustavo E. Scuseria, Lucian A. Constantin, Xiaolan Zhou, and Kieron Burke. Restoring the Density-Gradient Expansion for Exchange in Solids and Surfaces. *Phys. Rev. Lett.*, 100(13):136406, 2008.

[346] S. L. Dudarev, L.-M. Peng, S. Y. Savrasov, and J.-M. Zuo. Correlation effects in the ground-state charge density of Mott insulating NiO: A comparison of ab initio calculations and high-energy electron diffraction measurements. *Phys. Rev. B*, 61(4):2506–2512, 2000.

[347] C.H. Shen, C.C. Chen, R.S. Liu, R. Gundakaram, S.F. Hu, and J.M. Chen. Internal chemical pressure effect and magnetic properties of $la_{0.6}(sr_{0.4x}ba_x)mno_3$. *J. Solid State Chem.*, 156(1):117 – 121, 2001.

[348] P. G. Radaelli, G. Iannone, M. Marezio, H. Y. Hwang, S-W. Cheong, J. D. Jorgensen, and D. N. Argyriou. Structural effects on the magnetic and transport properties of perovskite $a_{1-x}a_xmno_3$ ($x = 0.25, 0.30$). *Phys. Rev. B*, 56:8265–8276, Oct 1997.

[349] J.A. Dhahri, S. Zemni, K. Cherif, J. Dhahri, M. Oumezzine, M. Ghedira, and H. Vincent. The effect of deficit of strontium on structural, magnetic and electrical properties of $la_{0.8}sr_{0.2x}mno_3$ manganites. *J. Alloys Compd.*, 394(12):51 – 57, 2005.

[350] Branton J. Campbell, Harold T. Stokes, David E. Tanner, and Dorian M. Hatch. *ISODISPLACE*: a web-based tool for exploring structural distortions. *J. Appl. Cryst.*, 39(4):607–614, Aug 2006.

[351] J. D. Burton and E. Y. Tsymbal. Prediction of electrically induced magnetic reconstruction at the manganite/ferroelectric interface. *Phys. Rev. B*, 80:174406, Nov 2009.

[352] Y. W. Yin, J. D. Burton, Y-M. Kim, A. Y. Borisevich, S. J. Pennycook, S. M. Yang, T. W. Noh, A. Gruverman, X. G. Li, E. Y. Tsymbal, and Qi Li. Enhanced tunnelling electroresistance effect due to a ferroelectrically induced phase transition at a magnetic complex oxide interface. *Nat. Mater.*, 12:397–402, 2013.

[353] M. Dawber, C. Lichtensteiger, M. Cantoni, M. Veithen, P. Ghosez, K. Johnston, K. Rabe, and J.-M. Triscone. Unusual Behavior of the Ferroelectric Polarization in PbTiO3/SrTiO3 Superlattices. *Phys. Rev. Lett.*, 95(17):177601, October 2005.

[354] A. Hoffmann, S. May, S. te Velthuis, S. Park, M. Fitzsimmons, G. Campillo, and M. Gómez. Magnetic depth profile of a modulation-doped La1xCaxMnO3 exchange-biased system. *Phys. Rev. B*, 80(5):1–4, August 2009.

[355] Valeria Lauter, Hailemariam Ambaye, Richard Goyette, Wai-Tung Hal Lee, and Andre Parizzi. Highlights from the magnetism reflectometer at the SNS. *Phys. B Cond. Mat.*, 404(17):2543–2546, September 2009.

[356] Sergei V. Kalinin, Brian J. Rodriguez, Stephen Jesse, Edgar Karapetian, Boris Mirman, Eugene A. Eliseev, and Anna N. Morozovska. Nanoscale Electromechanics of Ferroelectric and Biological Systems: A New Dimension in Scanning Probe Microscopy. *Ann. Rev. Mater. Res.*, 37(1):189–238, August 2007.

[357] Martin Gajek, Manuel Bibes, Stéphane Fusil, Karim Bouzehouane, Josep Fontcuberta, Agnès Barthélémy, and Albert Fert. Tunnel junctions with multiferroic barriers. *Nat. Mater.*, 6(4):296–302, April 2007.

[358] R.O. Cherifi, V. Ivanovskaya, L.C. Phillips, A. Zobelli, I.C. Infante, E. Jacquet, V. Garcia, S. Fusil, P.R. Briddon, N. Guiblin, A. Mougin, A.A. Unal, F. Kronast, S. Valencia, B. Dkhil, A. Barthélémy, M. Bibes, and A.A. Ünal. Electric-field control of magnetic order above room temperature. *Nat. Mater.*, (January):1–7, January 2014.

[359] X. Ma, A. Kumar, S. Dussan, H. Zhai, F. Fang, H. B. Zhao, J. F. Scott, R. S. Katiyar, and G. Lüpke. Charge control of antiferromagnetism at $PbZr_{0.52}Ti_{0.48}O_3$ / $La_{0.67}Sr_{0.33}MnO_3$ interface. *Appl. Phys. Lett.*, 104(13):132905, March 2014.

[360] S. de Jong, R. Kukreja, C. Trabant, N. Pontius, C. F. Chang, T. Kachel, M. Beye, F. Sorgenfrei, C. H. Back, B. Bräuer, W. F. Schlotter, J. J. Turner, O. Krupin, M. Doehler, D. Zhu, M. A. Hossain, A. O. Scherz, D. Fausti, F. Novelli, M. Esposito, W. S. Lee, Y. D. Chuang, D. H. Lu, R. G. Moore, M. Yi, M. Trigo, P. Kirchmann, L. Pathey, M. S. Golden, M. Buchholz, P. Metcalf, F. Parmigiani, W. Wurth, A. Föhlisch, C. Schüß ler Langeheine, and H. A. Dürr. Speed limit of the insulator-metal transition in magnetite. *Nat. Mater.*, 12(July):1–5, July 2013.

[361] Jing Ma, Jiamian Hu, Zheng Li, and Ce-Wen Nan. Recent Progress in Multiferroic Magnetoelectric Composites: from Bulk to Thin Films. *Advanced Mater.*, 23:1062–1087, January 2011.

[362] I. I. Oleynik and E. Yu. Tsymbal. Atomic, electronic, and magnetic properties of magnetic tunnel junctions. *J. Appl. Phys.*, 93(10):6429–6431, 2003.

[363] Jagadeesh S. Moodera, Joaquim Nassar, and George Mathon. Spin-Tunneling in Ferromagnetic Junctions. *Ann. Rev. Mater. Science*, 29(1):381–432, August 1999.

[364] J M Slaughter. Mater. for Magnetoresistive Random Access Memory. *Ann. Rev. Mater. Res.*, 39(1):277–296, August 2009.

[365] S. Tehrani, B. Engel, J.M. Slaughter, E. Chen, M. DeHerrera, M. Durlam, P. Naji, R. Whig, J. Janesky, and J. Calder. Recent developments in magnetic tunnel junction MRAM. *IEEE Trans. Magn.*, 36(5):2752–2757, 2000.

[366] The interface is still the device. *Nat. Mater.*, 11(2):91, February 2012.

[367] Hiroyuki Yamada, Yoshihiro Ogawa, Yuji Ishii, Hiroshi Sato, Masashi Kawasaki, Hiroshi Akoh, and Yoshinori Tokura. Engineered interface of magnetic oxides. *Science*, 305(5684):646–8, July 2004.

[368] G. Hu and Y. Suzuki. Negative Spin Polarization of Fe_3O_4 in Magnetite/Manganite-Based Junctions. *Phys. Rev. Lett.*, 89(27):276601, December 2002.

[369] Xuesong Jin, Ciaran McEvoy, and I.V. Shvets. Studies of heteroepitaxial growth of Fe / MgO / Fe_3O_4 multilayer on MgO (100) substrates for fabrication of magnetic tunnel junctions. *J. Magn. Magn. Mater.*, 286:128–133, February 2005.

[370] Ruo-Gu Huang and James R Heath. Silicon Nanowire Charge-Trap Memory Incorporating Self-Assembled Iron Oxide Quantum Dots. *Small*, 8(22):3417–3421, September 2012.

[371] S. Vangelista, R. Mantovan, S. Cocco, A. Lamperti, O. Salicio, and M. Fanciulli. Chemical vapor deposition growth of Fe_3O_4 thin films and Fe/Fe_3O_4 bi-layers for their integration in magnetic tunnel junctions. *Thin Solid Films*, 520(14):4617–4621, May 2012.

[372] F. Greullet, E. Snoeck, C. Tiusan, M. Hehn, D. Lacour, O. Lenoble, C. Magen, and L. Calmels. Large inverse magnetoresistance in fully epitaxial Fe / Fe_3O_4 / MgO / Co magnetic tunnel junctions. *Appl. Phys. Lett.*, 92(5):053508, 2008.

[373] T. Kado, H. Saito, and K. Ando. Room-temperature magnetoresistance in magnetic tunnel junctions with Fe_3O_4 electrode. *J. Appl. Phys.*, 101(9):09J511, 2007.

[374] G. E. Sterbinsky, J. Cheng, P. T. Chiu, B. W. Wessels, and D. J. Keavney. Investigation of heteroepitaxial growth of magnetite thin films. *J. Vacuum Science & Technology B*, 25(4):1389, 2007.

[375] R. G. Delatorre, R. C. Silva, J. S. Cruz, N. Garcia, and A. A. Pasa. Electrodeposited magnetite with large magnetoresistive response at room temperature and low magnetic fields. *J. Solid State Electrochemistry*, 13(6):843–847, July 2008.

[376] H. Takahashi, S. Soeya, J. Hayakawa, K. Ito, A. Kida, H. Asano, M. Matsui, and A. Sample. Half-Metallic Fe_3O_4 Films for High-Sensitivity Magnetoresistive Devices. *IEEE Trans. Magn.*, 40(1):313–318, 2004.

[377] J. C. A. Huang, C. Y. Hsu, Y. F. Liao, M. Z. Lin, and C. H. Lee. Role of interfacial roughness on bias-dependent magnetoresistance and transport properties in magnetic tunnel junctions. *J. Appl. Phys.*, 98(10):103504, 2005.

[378] A A Shokri, Z H Ebrahiminejad, and S F Masoudi. The interfacial roughness effect on spin-dependent transport in nonplanar junctions with double magnetic barriers. *Thin Solid Films*, 519(7):2193–2200, January 2011.

[379] Steven R. Spurgeon, Jennifer D. Sloppy, Runzhe Tao, Robert F. Klie, Samuel E. Lofland, Jon K. Baldwin, Amit Misra, and Mitra L. Taheri. A study of the effect of iron island morphology and interface oxidation on the magnetic hysteresis of Fe-MgO (001) thin film composites. *J. Appl. Phys.*, 112(1):013905, 2012.

[380] J Swerts, S Vandezande, K Temst, and C Van Haesendonck. Surface roughness effects on the magnetization reversal of polycrystalline Fe / Ag thin films. *Solid State Comm.*, 131(6):359–363, August 2004.

[381] TJ Moran and B Lüthi. Elastic and magnetoelastic effects in magnetite. *Phys. Rev.*, 1965, 1969.

[382] R V Chopdekar, B. B. Nelson-Cheeseman, M Liberati, E Arenholz, and Y Suzuki. Role of magnetic anisotropy in spin-filter junctions. *Phys. Rev. B*, 83(22):224426, June 2011.

[383] R.V. Chopdekar, M. Liberati, Y. Takamura, L.F. Kourkoutis, J.S. Bettinger, B.B. Nelson-Cheeseman, E. Arenholz, A. Doran, A. Scholl, D.A. Muller, and Y. Suzuki. Magnetism at spinel thin film interfaces probed through soft X-ray spectroscopy techniques. *J. Magn. Magn. Mater.*, 322(19):2915–2921, October 2010.

[384] Takeshi Kasama, Rafal Dunin-Borkowski, and Wilma Eerenstein. Off-axis electron holography observation of magnetic microstructure in a magnetite (001) thin film containing antiphase domains. *Phys. Rev. B*, 73(10):104432, March 2006.

[385] W. L. Zhou, K.-Y. Wang, C. J. O'Connor, and J. Tang. Granular growth of Fe_3O_4 thin films and its antiphase boundaries prepared by pulsed laser deposition. *J. Appl. Phys.*, 89(11):7398, 2001.

[386] D Margulies, Ft Parker, Fe Spada, Rs Goldman, J Li, R Sinclair, and Ae Berkowitz. Anomalous moment and anisotropy behavior in Fe_3O_4 films. *Phys. Rev. B*, 53(14):9175–9187, April 1996.

[387] D Sander, R Skomski, C Schmidthals, A. Enders, and J Kirschner. Film Stress and Domain Wall Pinning in Sesquilayer Iron Films on W(110). *Phys. Rev. Lett.*, 77(12):2566–2569, September 1996.

[388] A. P. Mihai, J. P. Attane, L. Vila, C. Beigne, J. C. Pillet, and A. Marty. Magnetization reversal dominated by domain wall pinning in FePt based spin valves. *Appl. Phys. Lett.*, 94(12):122509, 2009.

[389] F. Bonell, S. Andrieu, C. Tiusan, F. Montaigne, E. Snoeck, B. Belhadji, L. Calmels, F. Bertran, P. Le Fèvre, and A. Taleb-Ibrahimi. Influence of misfit dislocations on the magnetoresistance of MgO-based epitaxial magnetic tunnel junctions. *Phys. Rev. B*, 82(9):092405, September 2010.

[390] N. Spiridis, J. Barbasz, Z. Lodziana, and J. Korecki. Fe_3O_4(001) films on Fe(001): Termination and reconstruction of iron-rich surfaces. *Phys. Rev. B*, 74(15):155423, October 2006.

[391] S. K. Arora, R. G. S. Sofin, I. V. Shvets, and M. Luysberg. Anomalous strain relaxation behavior of Fe_3O_4 / MgO (100) heteroepitaxial system grown using molecular beam epitaxy. *J. Appl. Phys.*, 100(7):073908, 2006.

[392] Ralph Skomski and J. Coey. Giant energy product in nanostructured two-phase magnets. *Phys. Rev. B*, 48(21):15812–15816, December 1993.

[393] A. Seeger, H. Kronmuller, H. Rieger, and H. Trauble. Effect of Lattice Defects on the Magnetization Curve of Ferromagnets. *J. Appl. Phys.*, 35(3):740, 1964.

[394] Y. K. Kim and M. Oliveria. Magnetic properties of sputtered Fe thin films: Processing and thickness dependence. *J. Appl. Phys.*, 74(2):1233, 1993.

[395] P A A van der Heijden, M G van Opstal, C H W Swueste, P H J Bloemen, J M Gaines, and W J M de Jonge. A ferromagnetic resonance study on ultra-thin Fe_3O_4 layers grown on (001) MgO. *J. Magn. Magn. Mater.*, 182:71–80, 1998.

[396] S. Serrano-Guisan, Han-Chun Wu, C Boothman, M. Abid, B. S. Chun, I. V. Shvets, and H. W. Schumacher. Thickness dependence of the effective damping in epitaxial Fe_3O_4 / MgO thin films. *J. Appl. Phys.*, 109(1):013907, 2011.

[397] Sangeeta Kale, S. Bhagat, S. Lofland, T. Scabarozi, S. Ogale, A. Orozco, S. Shinde, T. Venkatesan, B. Hannoyer, B. Mercey, and W. Prellier. Film thickness and temperature dependence of the magnetic properties of pulsed-laser-deposited Fe_3O_4 films on different substrates. *Phys. Rev. B*, 64(20):205413, November 2001.

[398] F.J.A. den Broeder, W. Hoving, and P.J.H. Bloemen. Magnetic anisotropy of multilayers. *J. Magn. Magn. Mater.*, 93:562–570, February 1991.

[399] M. Pardavi-Horvath. Coercivity of epitaxial magnetic garnet crystals. *IEEE Trans. Magn.*, 21(5):1694–1699, September 1985.

[400] M Li, YP Zhao, GC Wang, and HG Min. Effect of surface roughness on magnetization reversal of Co films on plasma-etched Si (100) substrates. *J. Appl. Phys.*, 83(11):6287, 1998.

[401] S. Middelhoek. Domain Walls in Thin NiFe Films. *J. Appl. Phys.*, 34(4):1054, 1963.

[402] A.J. Freeman, Ruqian Wu, Miyoung Kim, and V.I. Gavrilenko. Magnetism, magneto-crystalline anisotropy, magnetostriction and MOKE at surfaces and interfaces. *J. Magn. Magn. Mater.*, 203:1–5, 1999.

[403] J. Woods, A. Ushioda, M.M. Donovan, S. W. Sun, M. Tobise, and R. C. O'Handley. Magnetization depth profiling with low-energy electron spectroscopy and MOKE. *J. Appl. Phys.*, 63(8):3669–3671, 1988.

[404] M.J. Donahue and D.G. Porter. OOMMF User's Guide, Version 1.0. Interagency Report NISTIR 6376. Technical report, National Institute of Standards and Technology, Gaithersburg, MD.

[405] Qing-feng Zhan, Stijn Vandezande, Kristiaan Temst, and Chris Van Haesendonck. Magnetic anisotropies of epitaxial Fe / MgO (001) films with varying thickness and grown under different conditions. *New J. Phys.*, 11(6):063003, June 2009.

[406] J. Orna, P. A. Algarabel, L. Morellón, J. A. Pardo, J. M. de Teresa, R. López Antón, F. Bartolomé, L. M. García, J. Bartolomé, J. C. Cezar, and A. Wildes. Origin of the giant magnetic moment in epitaxial Fe_3O_4 thin films. *Phys. Rev. B*, 81(14):144420, April 2010.

[407] F. A. Stevie, C. B. Vartuli, L. A. Giannuzzi, T. L. Shofner, S. R. Brown, B. Rossie, F. Hillion, R. H. Mills, M. Antonell, R. B. Irwin, and B. M. Purcell. Application of focused ion beam lift-out specimen preparation to TEM, SEM, STEM, AES and SIMS analysis. *Surf. and Int. Anal.*, 31(5):345–351, May 2001.

[408] N. D. Browning, D.J. Wallis, P.D. Nellist, and S.J. Pennycook. EELS in the STEM: Determination of materials properties on the atomic scale. *Micron*, 28(5):333–348, October 1997.

[409] R.L. Hadimani, Y. Melikhov, J.E. Snyder, and D.C. Jiles. Determination of Curie Temperature by Arrott Plot Technique in $Gd_5(Si_xGe_{1x})_4$ for x > 0.575. *J. Magn. Magn. Mater.*, 320(20):e696–e698, October 2008.

[410] Anthony Arrott. Criterion for Ferromagnetism from Observations of Magnetic Isotherms. *Phys. Rev.*, 108(6):1394–1396, December 1957.

[411] Jiyu Fan, Li Pi, Lei Zhang, Wei Tong, Langsheng Ling, Bo Hong, Yangguang Shi, Weichun Zhang, Di Lu, and Yuheng Zhang. Investigation of Critical Behavior in $Pr_{0.55}Sr_{0.45}MnO_3$ by Using the Field Dependence of Magnetic Entropy Change. *Appl. Phys. Lett.*, 98(7):072508, 2011.

[412] O L Krivanek, G J Corbin, N Dellby, B F Elston, R J Keyse, M F Murfitt, C S Own, Z S Szilagyi, and J W Woodruff. An Electron Microscope for the Aberration-Corrected Era. *Ultramic.*, 108(3):179–95, February 2008.

[413] D R G Mitchell and B Schaffer. Scripting-Customized Microscopy Tools for Digital Micrograph. *Ultramic.*, 103(4):319–332, July 2005.

[414] Craig Johnson, Jan Bording, and Yimei Zhu. Structural Inhomogeneity and Twinning in $YBa_2Cu_3O_{7-\delta}$ Superconductors: High-Resolution Transmission Electron Microscopy Measurements. *Phys. Rev. B*, 78(1):014517, July 2008.

[415] S. L. Dudarev, S. Y. Savrasov, C. J. Humphreys, and A. P. Sutton. Electron-Energy-Loss Spectra and the Structural Stability of Nickel Oxide: An LSDA+U Study. *Phys. Rev. B*, 57(3):1505–1509, January 1998.

[416] Matteo Cococcioni and Stefano de Gironcoli. Linear Response Approach to the Calculation of the Effective Interaction Parameters in the LDA+U Method. *Phys. Rev. B*, 71(3):035105, January 2005.

[417] Andrew Rappe, Karin Rabe, Efthimios Kaxiras, and J. Joannopoulos. Optimized Pseudopotentials. *Phys. Rev. B*, 41(2):1227–1230, January 1990.

[418] John P. Perdew, Kieron Burke, and Matthias Ernzerhof. Generalized Gradient Approximation Made Simple. *Phys. Rev. Lett.*, 77(18):3865–3868, October 1996.

[419] John Perdew, Adrienn Ruzsinszky, Gábor Csonka, Oleg Vydrov, Gustavo Scuseria, Lucian Constantin, Xiaolan Zhou, and Kieron Burke. Restoring the Density-Gradient Expansion for Exchange in Solids and Surfaces. *Phys. Rev. Lett.*, 100(13):136406, April 2008.

[420] Nicola Marzari, David Vanderbilt, Alessandro De Vita, and M. Payne. Thermal Contraction and Disordering of the Al(110) Surface. *Phys. Rev. Lett.*, 82(16):3296–3299, April 1999.

[421] Hendrik J. Monkhorst and James D. Pack. Special Points for Brillouin-Zone Integrations. *Phys. Rev. B*, 13(12):5188–5192, June 1976.

[422] Chunlan Ma, Zhongqin Yang, and Silvia Picozzi. *Ab Initio* Electronic and Magnetic Structure in $La_{0.67}Sr_{0.33}MnO_3$: Strain and Correlation Effects. *J. Phys.: Condens. Matter*, 18(32):7717–7728, August 2006.

[423] H. Ju, H.-C. Sohn, and Kannan Krishnan. Evidence for O2p Hole-Driven Conductivity in La1-xSrxMnO3 (0 x 0.7) and La0.7Sr0.3MnOz Thin Films. *Phys. Rev. Lett.*, 79(17):3230–3233, October 1997.

[424] Mark C. Biesinger, Brad P. Payne, Andrew P. Grosvenor, Leo W.M. Lau, Andrea R. Gerson, and Roger St.C. Smart. Resolving Surface Chemical States in XPS Analysis of First Row Transition Metals, Oxides and Hydroxides: Cr, Mn, Fe, Co and Ni. *Appl. Surf. Sci.*, 257(7):2717–2730, January 2011.

[425] A. J. Nelson, John G. Reynolds, and Joseph W. Roos. Core-Level Satellites and Outer Core-Level Multiplet Splitting in Mn Model Compounds. *J. Vac. Sci. Technol., A*, 18(4):1072–1076, 2000.

[426] H.W. Nesbitt and D. Banerjee. Interpretation of XPS Mn(2p) Spectra of Mn Oxyhydroxides and Constraints on the Mechanism of MnO_2 Precipitation. *Am. Mineral.*, 83(1994):305–315, 1998.

[427] Lewys Jones and Peter D Nellist. Identifying and correcting scan noise and drift in the scanning transmission electron microscope. *Microsc. Microanal.*, 19(4):1050–60, August 2013.

[428] Caroline A Schneider, Wayne S Rasband, and Kevin W Eliceiri. NIH Image to ImageJ: 25 years of image analysis. *Nat. Methods*, 9(7):671–675, June 2012.

[429] A. M. Glazer and S. A. Mabud. Powder profile refinement of lead zirconate titanate at several temperatures. II. Pure PbTiO3. *Acta Cryst. B*, 34(4):1065–1070, April 1978.

[430] Nicola Marzari, David Vanderbilt, Alessandro De Vita, and M. C. Payne. Thermal Contraction and Disordering of the Al(110) Surface. *Phys. Rev. Lett.*, 82:3296–3299, Apr 1999.

[431] Hendrik J. Monkhorst and James D. Pack. Special points for Brillouin-zone integrations. *Phys. Rev. B*, 13:5188–5192, Jun 1976.

[432] P.A. Kienzle, K.V. O'Donovan, J.F. Ankner, N.F. Berk, and C.F. Majkrzak. NIST NCNR ReflPak Software Suite. `http://www.ncnr.nist.gov/reflpak`, 2000-2006.

Appendix A: Strain Effects on Magnetization in Ferrous Thin-Films

A.1 Introduction

In this chapter we conduct a follow-up study to our previous work on ferrous thin film heterostructures. We explore the effects of interfacial misfit dislocations on magnetic properties and provide insight into how to tune these properties *via* structure.

Magnetic thin-film heterostructures play an important role in the performance of many devices, including magnetic tunnel junctions, multiferroic memories, and magnetoresistive random access memories.[360–365] Many of the fundamental properties that make these systems so attractive are dictated by interactions arising near interfaces, where surface termination and symmetry breaking induce exotic behavior.[366,367] Iron and iron oxides in particular offer considerable versatility for these electronic and magnetic systems.[368–370] For instance, Fe_3O_4 has proven to be a promising candidate for these systems because of its high ferromagnetic Curie temperature and structural compatibility.[371–376] Interface effects, such as strain and roughness, can also significantly affect the performance of these devices.[369,377–379] Interfacial roughness results in greater area of interfacial contact and can enhance demagnetizing effects, while strain can introduce magnetoelastic effects.[380,381]

A.2 Background

Many questions remain about how interface structure affects the evolution of uniaxial anisotropy in ferrite composites. Abrupt changes in magnetic anisotropy are known to occur at Fe_3O_4 interfaces in spin valves.[382] The origin of this effect is debated, but it has been found that Fe_3O_4 can induce magnetic proximity effects in adjacent layers.[383] Furthermore, the connection between interfacial misfit dislocations and coercivity is poorly understood. Previous studies have focused extensively on antiphase boundaries in Fe_3O_4[384–386], but the presence of misfit dislocations Fe / Fe_3O_4 composites has only received cursory attention.[22] Such defects can act to pin magnetic domain walls and can greatly affect tunneling magnetoresistance in MgO-based tunnel junctions.[387–389] This necessitates a more predictive understanding of

the relationship between coercivity, domain wall motion, and misfit dislocations.

Here we examine the Fe / Fe_3O_4 / MgO thin-film system using XRD, TEM, VSM, and MOKE magnetometry. We explore the structure and magnetic behavior of these composites while varying the thickness and surface roughness of the top Fe layer. We find a significant density of misfit dislocations that depend on Fe layer thickness, and show that this acts in concert with epitaxial strain to control coercivity of these compounds. These observations are supported by micromagnetic simulations that accurately reproduce the shape of the experimental data.

A.3 Sample Growth

Nominally 45 nm Fe_3O_4 layers were deposited at a $p_{O_2} \approx 2 \times 10^{-6}$ Torr onto MgO (001) substrates, at a substrate temperature of 250 °C, using MBE. 20, 25, and 30 nm Fe layers were then deposited without substrate heating.

A.4 X-Ray Diffraction

Our structural characterization indicates that the films are of nominal composition and thickness, and free of impurity phases. XRD and XRR scans of the samples are shown in Figure A.1. We observe a sharp MgO (002) substrate reflection at $q = 2.982$ Å^{-1} and the Fe_3O_4 (002) peak at $q = 1.525$ Å^{-1}. There are clear shifts in the position of the α–Fe (002) peak that indicate changes in its strain state (Figure A.1.B). As shown in Table A.1, between 10 and 20 nm Fe there is a near doubling of out-of-plane compression, which gradually relaxes with increasing Fe thickness. A simple calculation of the epitaxial mismatch between Fe / MgO and Fe / Fe_3O_4 predicts Fe layer strains of $\varepsilon_\perp = -4.57\%$ and $\varepsilon_\parallel = 3.77\%$ for the former and $\varepsilon_\perp = -4.07\%$ and $\varepsilon_\parallel = 3.36\%$ for the latter, considering that there is only a small ($\sim 0.3\%$) mismatch between Fe_3O_4 and MgO.[22,390] These estimated strains are significantly larger than the measured strains in Table A.1, suggesting that misfit dislocations act to relax it. This is expected, considering that the critical thickness for strain relaxation by misfit dislocations for Fe on MgO ($\sim 3.77\%$ mismatch) is around $t_c = 2-3$ nm (in contrast, Fe_3O_4 on MgO displays a t_c in excess of several hundred nm).[28,391]

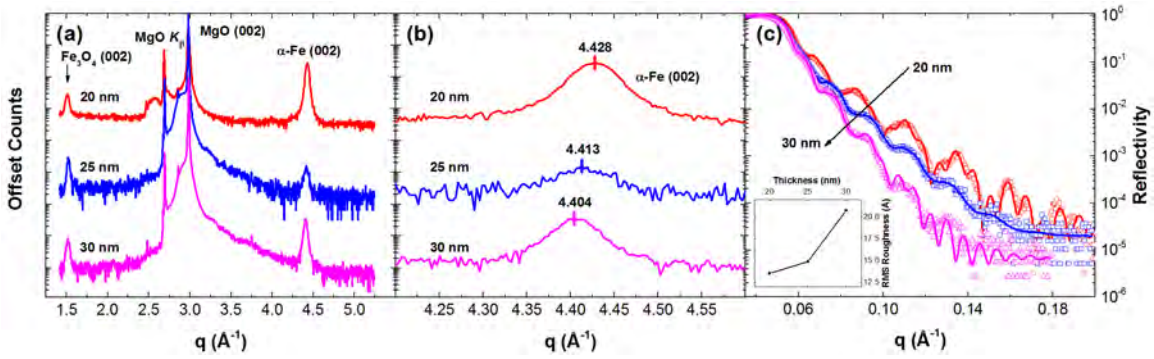

Figure A.1: $\theta - 2\theta$ XRD patterns measured on each film and normalized by the intensity of the MgO (002) substrate reflection. (A) shows the full pattern, confirming the presence of the desired phases. (B) shows more detail of the region between 4.25–4.55 Å^{-1}, indicating a shift in the α-Fe (002) peak. (C) shows XRR measurements and respective fits, with the inset quantifying the increase in root mean squared (σ_{rms}) surface roughness with increasing Fe thickness. We note the presence of spurious MgO K_β and W L_α reflections.

Table A.1: X-ray diffraction analysis of the α–Fe (002) peak. The measured c lattice parameters are compared to the bulk value ($c = 2.87$ Å) to calculate the out-of-plane strain ($\varepsilon_\perp$).[13] The in-plane strain is estimated using the Fe elastic constants as $\varepsilon_\parallel = -\frac{c_{11}}{2c_{12}}\varepsilon_\perp$.[207,267]

Sample	$q_{(002)}$ (Å^{-1})	c (Å)	$\varepsilon_\perp$ (%)	$\varepsilon_\parallel$ (%)
20 nm Fe / Fe_3O_4	4.427	2.839	-1.10	0.90
25 nm Fe / Fe_3O_4	4.415	2.846	-0.83	0.68
30 nm Fe / Fe_3O_4	4.406	2.852	-0.62	0.51

A.5 Transmission Electron Microscopy

To further explore the interface dislocations and strain relaxation of these films, TEM was conducted. Figure A.2 shows a series of bright field cross-sectional TEM micrographs, which indicate that the Fe_3O_4 / MgO interface is quite sharp and dislocation free, as shown in the insets. This is expected, considering the small $\sim$ 0.3% epitaxial mismatch between the layers. The Fe / Fe_3O_4 interface, on the other hand, displays many dislocations (Figure A.3). From these micrographs we are able to estimate the dislocation line density in the 20 nm film at $\rho \approx 0.175$ nm^{-1} to $\rho \approx 0.25$ nm^{-1} in the 25 nm film, and $\rho \approx 0.125$ nm^{-1} in the 30 nm film. These values compare favorably to the 0.195 nm^{-1} previously reported.[389] These dislocations are present at the Fe / Fe_3O_4 interface, depend on Fe thickness, and act to partially relax the epitaxial strain, which explains the difference between the calculated and measured lattice strains. As will be discussed, both dislocations and epitaxial strain can greatly influence the

magnetization of these materials.

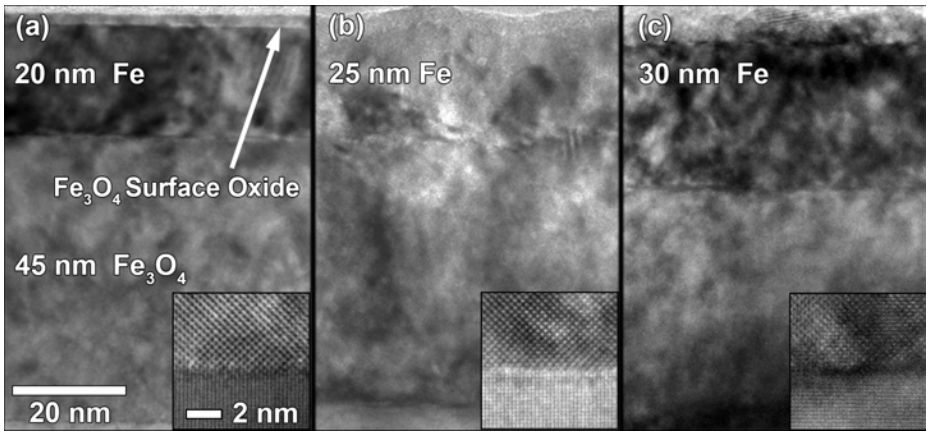

Figure A.2: (A-C) Series of cross-section TEM images of the 20 / 45 nm Fe / Fe_3O_4, 25 / 45 nm Fe / Fe_3O_4, and 30 / 45 nm Fe / Fe_3O_4 samples, respectively. The insets show high-resolution TEM images representative of the high quality and epitaxy of the Fe_3O_4 / MgO interface.

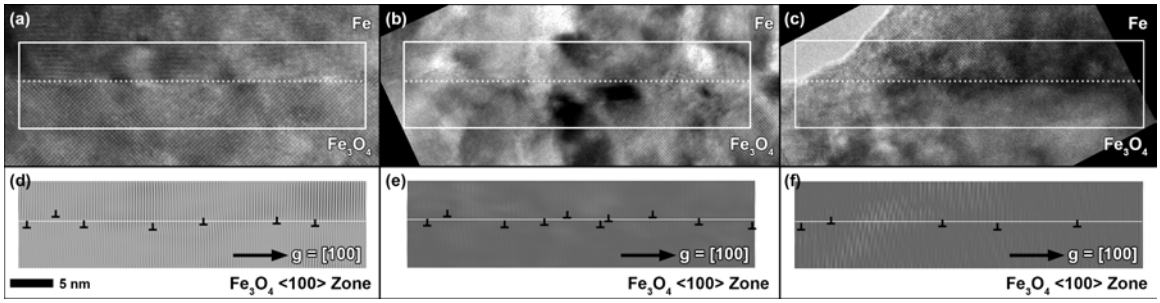

Figure A.3: (A-C) Cross-section TEM images of the Fe / Fe_3O_4 interface in the 20, 25, and 30 nm films, respectively, taken parallel to the Fe_3O_4 <001> zone axis. (D-F) Inverse fast Fourier transforms of the masked $\mathbf{g} = [100]$ reflection, showing the presence of multiple edge dislocations. The dislocation density increases from $\rho \approx 0.175$ nm^{-1} to ~ 0.255 nm^{-1} between 20 and 25 nm and then decreases to ~ 0.125 nm^{-1} for the 30 nm film.

In addition to the epitaxial strain effects, we note the presence of both surface oxidation and roughness with increasing Fe thickness. HRTEM micrographs (Figure A.4) reveal the presence of a 2–3 nm surface oxide, which we identify as Fe_3O_4, in agreement with the XRD data. TEM also shows evidence for increasing surface roughness; to quantify this we fit our XRR data, which shows that the root mean squared roughness increases from $\sigma_{rms} = 13.5 - 20.8$ Å, as the Fe layer thickness increases from 20–30 nm (Figure A.1.C).

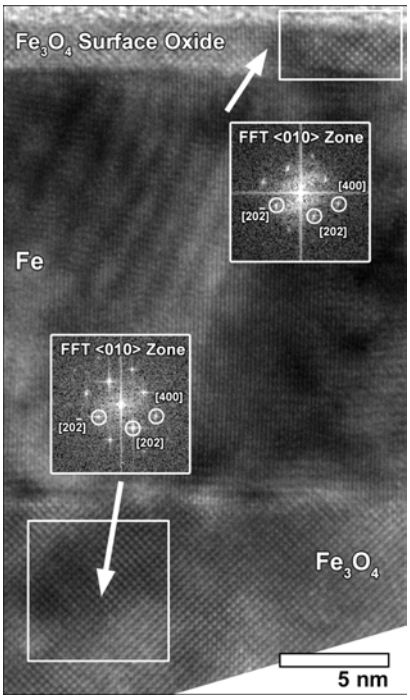

Figure A.4: High-resolution TEM image of the 20 / 45 nm Fe / Fe_3O_4 interface taken along the Fe_3O_4 <010> zone axis. The insets show fast Fourier transforms of the Fe_3O_4 underlayer and surface oxide, confirming that the oxide is Fe_3O_4.

A.6 Structural Effects on Magnetization

We next discuss the effect of the aforementioned structural changes on magnetization. Figure A.5 shows in-plane magnetic hysteresis measured by the VSM (Figure A.5.A) and MOKE (Figure A.5.B) techniques at 300 K along the MgO <100> direction. Both techniques show that the coercivity of the bilayers increases with Fe thickness, reaching a maximum near 25 nm (Figure A.5.C). We also observe the onset of a small exchange bias with increasing Fe thickness, coinciding with the growth of the Fe_3O_4 surface oxide detected by XRD and TEM.

To disentangle the contributions of the different magnetic layers, we consider the different hysteresis behavior measured by VSM and MOKE. The former technique samples the entire composite and shows a sheared, soft loop (Figure A.5.A). In contrast, the MOKE technique only samples the first 20–25 nm of the film—largely the Fe layer (Figure A.5.B). This measurement reveals a squarer, hard loop, which results from an exchange interaction between the Fe and Fe_3O_4 on either side of it. Formerly free spins in the FM Fe layer are pinned by the ferrimagnetic Fe_3O_4, giving rise to a harder loop shape.

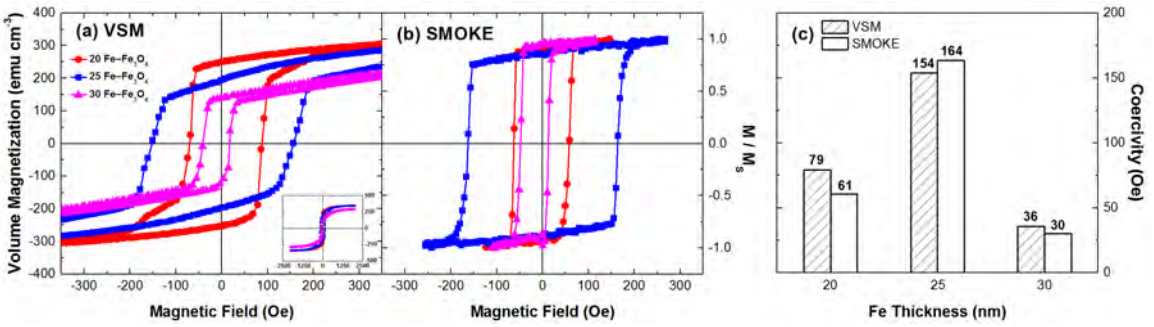

Figure A.5: In-plane magnetic hysteresis loops measured by VSM (A) and MOKE (B) at 25 °C along the MgO <100> direction, with the Fe layer thickness indicated. The inset of (A) shows the high field response of the samples. There is a clear exchange bias in the 30 nm film, which is more pronounced in the MOKE measurement. (C) shows the magnetic coercivity (H_C) as a function of Fe layer thickness measured by each technique. The coercivity increases between 20 and 25 nm, then significantly decreases for 30 nm.

Interpreting the observed trends in coercivity is more difficult. TEM images indicate that the Fe_3O_4 surface oxide ranges from 2–3 nm in all the samples, so it is unlikely that this layer is responsible for the jump in coercivity. However, the coercivity behavior does agree quite well with the increase and subsequent decrease in misfit dislocation density. The inhomogeneous stress distribution around the dislocations can pin domain walls, leading to a linear increase in anisotropy with lattice deformation.[387,392,393] XRD also shows that there is a near halving of out-of-plane strain ($\varepsilon_\perp = -1.1$ to -0.62%) between the 20 and 30 nm Fe samples. Dislocations and misfit strain can introduce a magnetoelastic contribution to the in-plane uniaxial anisotropy of the Fe layer.[267]

We can describe the magnetoelastic contribution of epitaxial strain to in-plane uniaxial anisotropy (K_u^{ME}) of this layer as,

$$\frac{2K_u^{ME}}{M} = -\frac{2B_1}{M}(\varepsilon_\perp - \varepsilon_\parallel) \tag{A.1}$$

where $\varepsilon_\perp - \varepsilon_\parallel$ is the difference in out-of- and in-plane strains measured by XRD and B_1 is the magnetoelastic coefficient of Fe.[267] From this relation we are able to estimate K_u^{ME}, as shown in Figure A.6.A. This shows that between 10 and 20 nm the in-plane anisotropy of the Fe layer nearly doubles and that it begins to decrease between 20 and 30 nm.

Previous ferromagnetic resonance (FMR) and other studies have shown that the anisotropy of Fe and

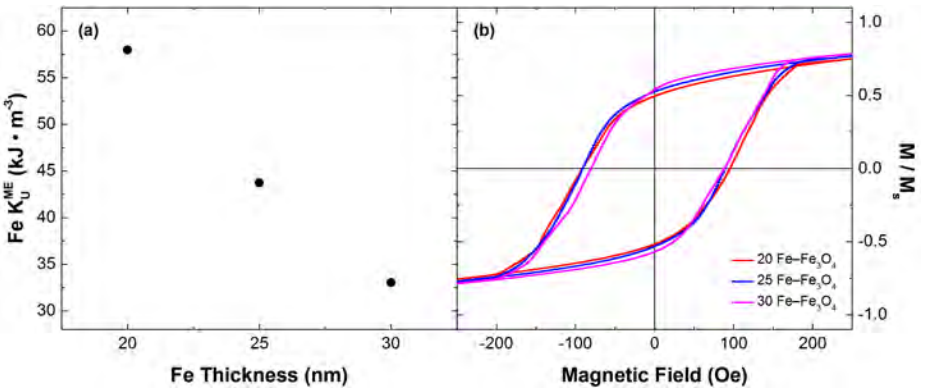

Figure A.6: (A) Calculated in-plane uniaxial anisotropies resulting from substrate-induced strain, overlayed with a cubic fit to the data, and (B) micromagnetics simulations conducted along the MgO <100> direction using these anisotropies. The shape of the loops shows good agreement with the measured data, but the trend in coercivity is only qualitatively reproduced.

Fe_3O_4 thin-films can be described in terms of surface and volume anisotropy contributions.[267,394–397] The MCA consists of a cubic term (K_1) and an uniaxial term (K_u), both of which scale with film thickness—though the former is much weaker than the latter.[395] Both terms consist of magnetoelastic and shape contributions that scale with increasing layer thickness as,

$$K_u^{eff} = K_v + \frac{2K_s}{t_{film}} \tag{A.2}$$

where K_v and K_s are the volumetric and interface contributions, respectively. The t^{-1} dependence implies that the uniaxial anisotropy eventually converges to the volumetric term as the film thickness increases. Put another way, this indicates that as the film's thickness increases, it begins to relax to an unstrained bulk anisotropy.[267]

This relaxation is typically achieved by the formation of interfacial misfit dislocations, which can act to pin magnetic domain walls (as shown in Figure A.3). The addition of dislocations lying in the plane of the domain wall adds a contribution to the interface anisotropy, which is described by,

$$H_c^d = \frac{3G\lambda b}{2M_s} \tag{A.3}$$

where λ is the magnetostrictive coefficient, G is the shear modulus, b is the Burgers vector, and M_s is the

saturation magnetization.[398,399] The strain fields associated with the dislocations act as pinning centers, imposing a "drag" on magnetic domain walls that impinge upon them.[387] As the dislocation density increases, the number of pinning sites also increases and a concomitant change in coercivity is expected, as we observe in Figures A.3 and A.5.

Knowing this, we can conduct micromagnetics simulations to evaluate the effect of a changing uniaxial anisotropy on the overall hysteresis of the composite. We will assume the cubic anisotropy of the layers is constant over the present thickness range, and we will not attempt to model the exchange bias present in the 30 nm film. The results of these simulations are shown in Figure A.6.B. The simulations uphold the general decrease in coercivity with increasing Fe thickness, in line with a gradual relaxation of strain and transition to bulk-like anisotropies. However, our model does not fully capture the doubling of coercivity between 20 and 25 nm Fe observed in our experimental data, indicating that there are other factors not accounted for—most likely the presence of pinning from misfit dislocations. Nonetheless, it is clear that the evolution of in-plane anisotropies induced by epitaxial strain is a major factor in determining the shape of the resulting hysteresis. This indicates that the bilayer geometry may be used to tune magnetic properties for a particular application.

Since our simulations are unable to accurately model the jump in coercivity between 20 and 25 nm, we will now discuss other possible factors mediating this behavior, namely surface roughness and domain wall type. XRR indicates that the roughness of each composite increases with increasing Fe thickness. The presence of such roughness can induce an additional in-plane surface anistoropy.[268,380,400] Roughness introduces local strain magnetic fields around asperities and leads to a loss of the two-dimensional character of a film. Roughness effects are particularly significant in thinner films, whose behavior begins to approach that of an ensemble of interacting single domain particles. Our films fall well within this limit and so may be affected by roughness.

We may also consider the transition from Bloch to Néel magnetic domain wall types with increasing Fe thickness. Kim *et al.* have calculated the wall formation energies of each and found that for Fe films there is a crossover around 25–30 nm.[394] This crossover is associated with a different coercivity dependence: in the case of Bloch walls coercivity is inversely proportional to film thickness, while for

Néel walls it is directly proportional. This explanation has been confirmed theoretically in calculations based on the total wall energy density and has also been observed in similar ferrite and permalloy thin-film systems.[401] Our results support the idea of a change in domain wall type, which acts in concert with the aforementioned changes in uniaxial anisotropy to modify coercivity.

A.7 Conclusions

We have investigated the microstructure and magnetic properties of a Fe / Fe_3O_4 thin-film system using XRD, TEM, VSM, and MOKE. We find that there is a large increase in coercivity between 20 and 25 nm Fe thickness, which subsequently decreases with increasing Fe layer thickness. This is associated with a similar trend in dislocation density, as confirmed by TEM. We show that such strain acts to impose an in-plane uniaxial anisotropy on the composite that depends on thickness. Micromagnetics simulations using our calculated in-plane anisotropies can qualitatively reproduce the trend in our experimental loops, but more accurate calculations of coercivity must account for the presence of pinning from dislocations and other features, such as surface roughness and domain wall type. Our results suggest that the precise engineering of interfacial strain and misfit dislocations through the use of different substrate materials may be used to tune coercivity for a particular application.

A.8 Experimental Methods

Commercial 1×1 cm^2 MgO (001) substrates were purchased from MTI International and cleaned using acetone and isopropyl alcohol. Nominally 45 nm Fe_3O_4 layers were deposited at a $p_{O_2} \approx 2 \times 10^{-6}$ Torr and a substrate temperature of 250 °C using MBE. 20, 25, and 30 nm Fe layers were then deposited without substrate heating. These Fe thicknesses were chosen to coincide with measured penetration thickness of the MOKE signal for our system.

XRD measurements were conducted to obtain structural information; scans were performed from $2\theta = 20 - 80°$ at room-temperature using Cu K_α ($\lambda = 1.541$ Å) radiation on a Panalytical Empyrean diffractometer. The patterns were normalized to the intensity of the MgO (002) substrate reflection for comparison and analyzed using the Jade software package. The α–Fe (002) peak was fitted using a Gaussian profile in the OriginPro software. X-ray reflectivity (XRR) measurements were also conducted

from 0.3-2.5° grazing angle at room-temperature to quantify surface roughness. The reflectivity data were fitted using the GenX software package.[184]

Cross-section TEM samples were prepared using conventional polishing techniques. Small sections were glued to one another using Epotek brand M-Bond epoxy and then cured for several hours at 100 °C. These sections were polished to ∼10 μm thickness using a low-speed polishing wheel and diamond lapping film. They were then ion milled using a Fischione 1010 Low-Angle Ion Mill operating at $0.5-1.5$ keV and $10-15°$ incidence angle. Bright field and diffraction images were taken using a JEOL 2100 LaB_6 TEM operating at 200 keV. HRTEM was used to determine the quality of interfaces and surface morphology.

We combine TEM measurements with MOKE magnetometry to correlate local microstructure to magnetization. The latter technique measures the rotation induced in a polarized laser upon reflection from the surface of a magnetic film and has been used extensively to examine magnetic properties of thin-film systems, specifically surface and sub-surface effects.[402,403] These measurements were conducted using a custom-designed MOKE magnetometer at 25 °C along the in-plane MgO <100> direction. Bulk in-plane hysteresis was also measured using a Quantum Design PPMS VSM at 25 °C with the field applied along the MgO <100> direction.

Micromagnetics simulations were conducted using the Object Oriented Micromagnetic Framework (OOMMF) software package.[404] The program minimizes the Landau-Lifshitz equation,

$$\frac{d\mathbf{M}}{dt} = -|\bar{\gamma}|\mathbf{M}\times\mathbf{H}_{\mathbf{eff}} - \frac{|\bar{\gamma}|\alpha}{M_S}\mathbf{M}\times\left(\mathbf{M}\times\mathbf{H}_{\mathbf{eff}}\right) \tag{A.4}$$

where $\mathbf{M}$ is the magnetization, $\mathbf{H}_{\mathbf{eff}}$ is the effective field, $\bar{\gamma}$ is the Landau-Lifshitz gyromagnetic ratio, and α is the damping constant. In the present study we use the Runge Kutta evolver, with the default values of $\bar{\gamma} = 2.211\times10^5$ m/A · s and $\alpha = 0.5$, which allows the simulation to converge in a reasonable time. A 500×500 nm^2 mesh, with $5\times5\times5$ nm^2 cell size was used, with the thickness of the mesh varied according to the film layers.

Simulations of the Fe / Fe_3O_4 bilayers were conducted in which the Fe_3O_4 layer was fixed at 45 nm and the Fe layer thickness was varied between 20–30 nm. The nominal bulk saturation magnetizations

were used, with $M_{S,Fe} = 1.71 \times 10^6$ A m^{-1} and $M_{S,Fe_3O_4} = 4.8 \times 10^5$ A m^{-1}.[13] For the Fe_3O_4 layer, a cubic magnetocrystalline anisotropy constant of $K_{1,Fe_3O_4} = -2.4 \times 10^4$ J m^{-3} and an out-of-plane uniaxial anisotropy of $K_{u,Fe_3O_4} = 2.5 \times 10^5$ J m^{-3} were used. For Fe a constant cubic anisotropy of $K_{1,Fe} = 4.8 \times 10^4$ J m^{-3} was used, with the in-plane uniaxial anisotropy ranging from 3.3×10^4 to 5.796×10^4 J m^{-3}. These values are in line with previous experiments.[13,267,395,396,405,406] A six neighbor exchange interaction energy was used, with exchange coefficients $A_{Fe-Fe} = 21$ pJ m^{-1},$A_{Fe-Fe_3O_4} = 14$ pJ m^{-1}, and $A_{Fe_3O_4-Fe_3O_4} = 7$ pJ m^{-1}.[386] Demagnetization was also included. A magnetic field was then applied along the substrate [100] direction from 250 to –250 Oe in 2 Oe steps and the magnetization in the [100] direction was calculated.

Appendix B: Interface Effects on Magnetization in Ferrous Thin-Films

B.1 Experimental Methods

Fe / MgO samples were first synthesized by electron beam deposition and were then characterized by a combination of structural and magnetic analyses. X-ray diffraction, electron microscopy, and spectroscopy were used to confirm the crystallinity and local structure of the films.

Commercial 1 × 1 cm^2 square MgO (001) substrates purchased from MTI International were annealed for 12 hours at 300 °C in a vacuum chamber at a base pressure of $\sim 10^{-7}$ Torr. Fe films of three thicknesses (10, 20, and 30 nm) were then electron beam deposited at 500 °C at a rate of 0.2 nm s^{-1}. Each film was subsequently capped in a nominal 5 nm layer of Au, deposited at 30 °C and a rate of 0.5 nm s^{-1}. X-ray diffraction and fluorescence measurements were performed on the samples to confirm the orientation, crystallinity, and thicknesses of the Fe films. SEM micrographs were captured at 10 keV accelerating voltage with an FEI Strata DB235 Dual-Beam Focused Ion Beam (FIB) system. Cross-section TEM samples were then prepared by a "lift out" technique on the same DB235 system operating between 5–10 keV ion beam current.[407] Sputter redeposition and damage were cleaned with a Fischione 1010 Low-Angle Ion Mill operating at 0.5–1.5 keV and 4–6° incidence angle. Images were captured on a JEOL 2100 LaB_6 TEM operating at 200 keV.

EDS maps were subsequently collected in STEM mode on a JEOL 2010F S/TEM operating at 200 keV with a convergence angle of 15 mrad and a collection angle of 28 mrad. STEM-EDS can provide the local chemical information needed to develop a qualitative understanding of diffusion and oxidation at the interface. The same system was used to measure EEL spectra at various points across the Fe / MgO interface. EELS enables quantification of the relative oxidation state of the Fe atoms across the interface region.[408] The curves presented in Figure 4.4 are the sum of five spectra collected at each measurement point. The background was removed and the energy was calibrated using the known position of the Fe L_3 edge. L_3/L_2 edge intensity ratios were calculated by taking the second derivative of the measured data and then integrating the positive areas under each peak. This method is independent of background

removal and does not depend on the method used to determine the continuous L edge contribution.[255] Fe valences were estimated using the values provided by Cosandey *et al.*[255]

In-plane magnetic hysteresis loops curves were measured on the as-deposited samples at 300 K along the Fe <100> and <110> directions with a Quantum Design VSM.

Appendix C: Substrate-Induced Polarization Effects in LSMO / PZT

C.1 Bulk Magnetometry

To study the possibility of substrate misalignment effects on bulk saturation magnetization, we conducted bulk VSM hysteresis measurements along the substrate [100] and [110] directions, as shown in Figure C.1. The difference between these directions is negligible, indicating that the changes in macroscale saturation magnetization between polarization states are real.

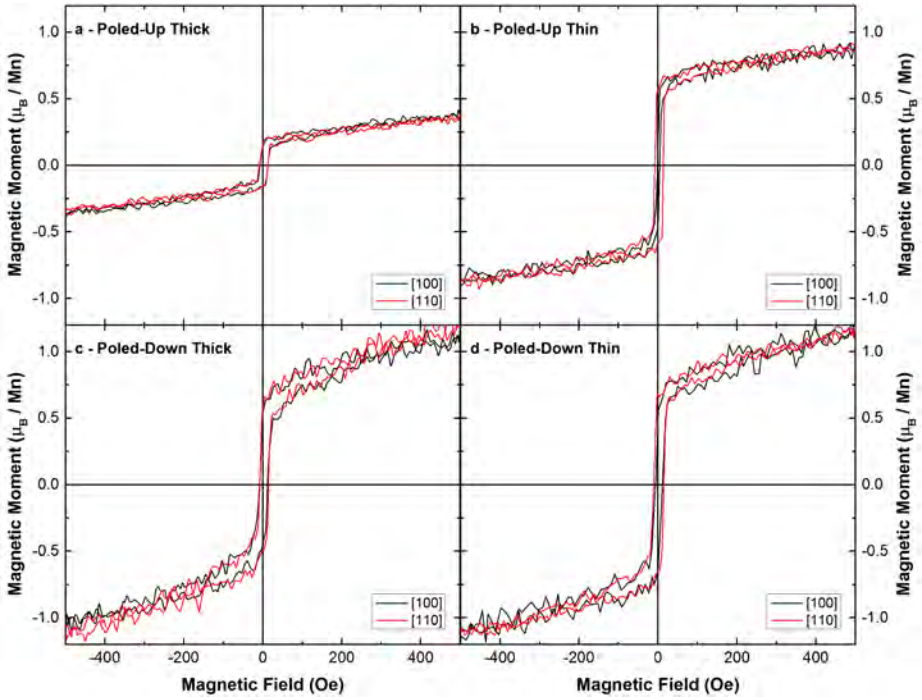

Figure C.1: (A-D) Bulk vibrating sample magnetometry measurements conducted at 305 K along the in-plane [100] and [110] directions, showing no difference in saturation or coercivity.

To confirm the accuracy of the Curie temperature measurements, an Arrott-Belov analysis was conducted on the poled-up thick PZT sample. This technique is a highly accurate method to determine Curie temperature, independent of an applied magnetic field and thermal effects.[409] As shown in Figure C.2.A, isothermal magnetic moment *versus* field measurements were conducted at 4 K intervals between 300 and 356 K. The sample holder background was removed and the data was plotted according to the $M^{1/\beta} \propto (H/M)^{1/\gamma}$ relation from the Weiss-Brillouin molecular field theory.[410] Figure C.2.B shows the

result of a plot with critical exponents $\beta = 0.5$ and $\gamma = 1.0$ assumed from the Landau mean-field approximation. The experimental exponents were then fit using the Widom scaling and universal relations as starting points, yielding $\beta = 0.492$ and $\gamma = 1.029$.[411] A simple extrapolation of the fits to zero yields a Curie temperature of 328 K. To correlate this to the measured moment *versus* temperature plots, a logistic fit was applied, followed by a second derivative. The minima of these curves were located and show that in the case of the poled-down thick PZT sample, the minimum corresponds to 313 K compared to the 328 K from the Arrott-Belov analysis (Figure C.3). *Assuming the samples are self-consistent*, it is possible to apply a shift of the difference (15 K) to the minima to estimate T_C. These results are listed in Table C.1.

Table C.1: Curie temperatures estimated from Arrott-Belov analysis, assuming the samples are self-consistent.

PZT Polarization & Thickness	Measured T_C (K)
Up Thin	335
Up Thick	331
Down Thin	342
Down Thick	328

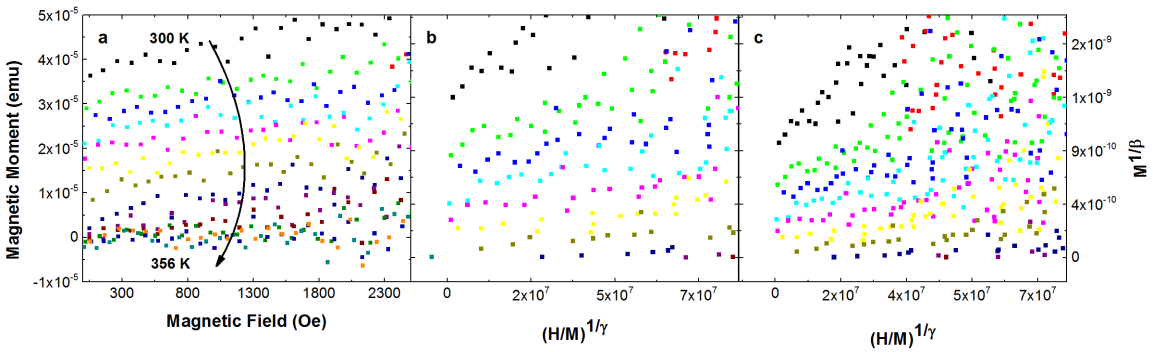

Figure C.2: Arrott-Belov temperature isotherms for the poled-up thick PZT sample. (A) Magnetic moment *versus* field plots taken in 4 K increments from 300–356 K with the sample holder background removed. (B) M^2 *vs.* H/M plots assuming critical exponents of $\beta = 0.5$ and $\gamma = 1.0$, while (C) shows $M^{1/\beta}$ *vs.* $(H/M)^{1/\gamma}$ plots, with critical exponents of $\beta = 0.492$ and $\gamma = 1.029$ estimated from the Widom and universal relations.

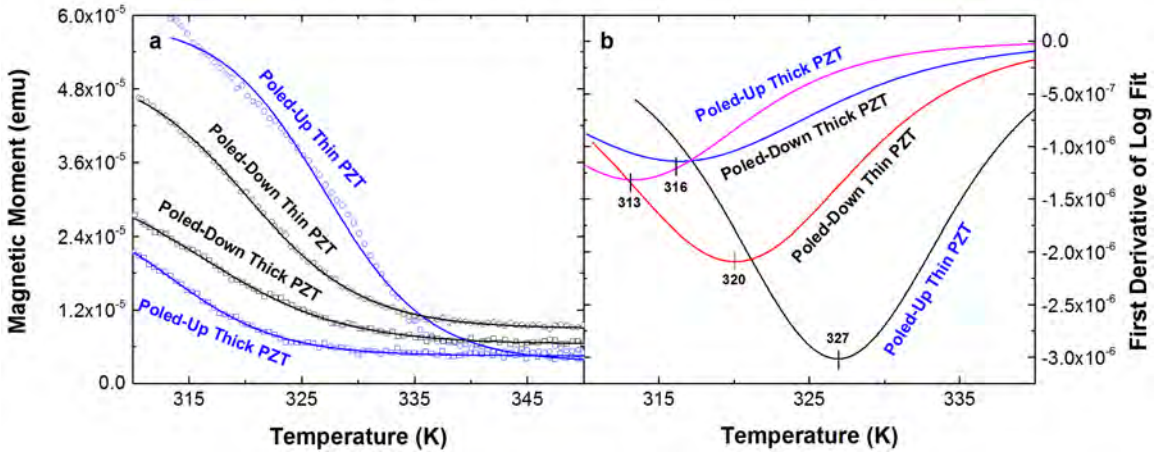

Figure C.3: (A) Logistic fits to the measured moment *versus* temperature data and (B) the first derivative of these fits, with the minima marked on each curve.

C.2 Polarized Neutron Reflectometry

As described in Section 5.8, we find that the magnetization of the top LSMO layer is greatly suppressed in the vicinity of the vacuum and PZT interfaces. As shown in Figure C.4, this asymmetry is quite pronounced for both poled-up samples, and is likely the result of varying strain states, as well as asymmetric boundary conditions about the PZT.

Care was taken during the fitting of the PNR data to maintain a very similar nuclear scattering length density between samples and fitting types, as shown in Figure C.5 and listed in Table C.2. Only minimal variation was allowed between samples. Our models were selected based on the quality of the spin asymmetry fit (Figure C.6), as well as on the overall fits to the non-spin-flip reflectivity (Figures C.7,C.8). The fits were iteratively refined using inputs from XRD, TEM, and GPA. In general the graded magnetization profile represents a better fit to the data (Figure C.7 *cf.* Figure C.8) and is more consistent with our EELS, GPA, and DFT results.

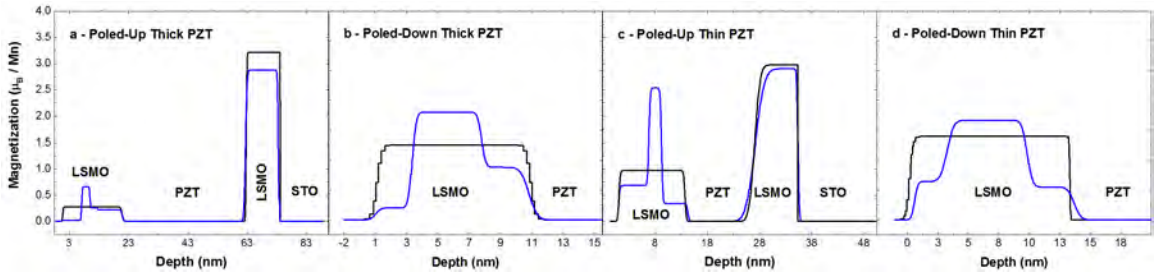

Figure C.4: (A-D) Magnetization depth profiles for uniform (black) and graded magnetization (blue) models.

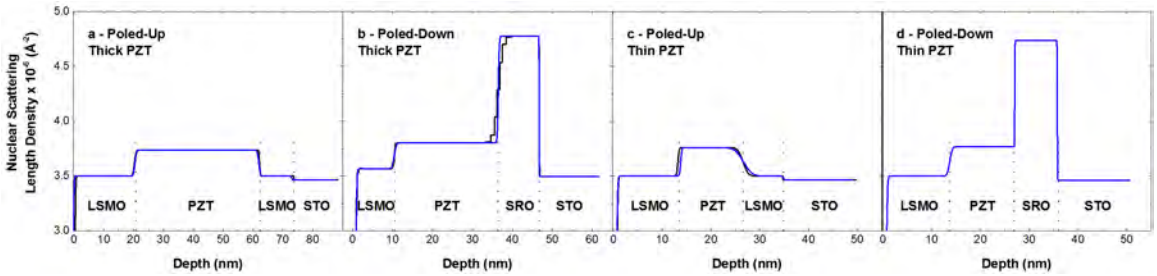

Figure C.5: (A-D) Nuclear scattering length density profiles for uniform (black) and graded magnetization (blue) models.

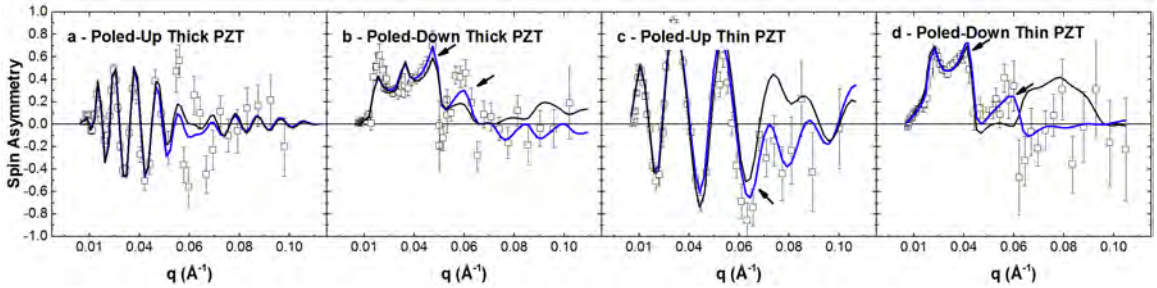

Figure C.6: (A-D) Polarized neutron reflectometry spin asymmetry (circles) and model fits, with the arrows indicating regions of improved fit. The black model assumes a uniform magnetization, while the blue model accounts for a graded magnetization, the only different fitting parameters being the number of magnetic sublayers and their magnetizations.

Table C.2: Comparison of the theoretical and fitted nuclear scattering length densities (SLDs) from Figure C.5. Values are given in units of $\times 10^{-6}$ $Å^{-2}$.[a]

Layer	Theoretical	Poled-Up Thick	Poled-Down Thick	Poled-Up Thin	Poled-Down Thin
LSMO	3.59	3.50	3.57	3.50	3.50
PZT	3.85	3.74	3.80	3.76	3.77
SRO	5.11	—	4.78	—	4.74
STO	3.53	3.46	3.50	3.46	3.46

[a]Theoretical SLDs were obtained using the NIST SLD calculator (`http://www.ncnr.nist.gov/resources/activation/`), assuming nominal bulk densities.

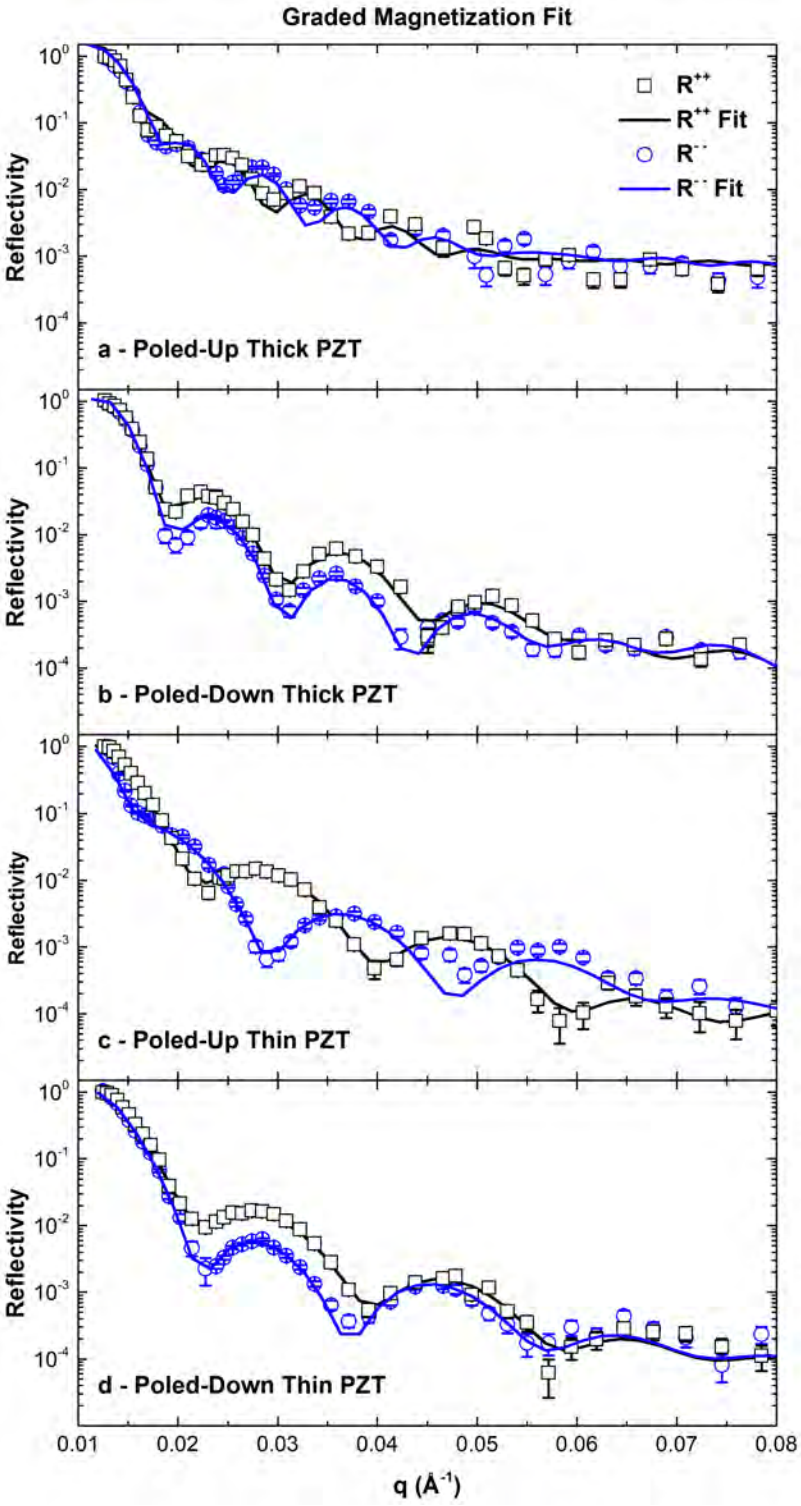

Figure C.7: (A-D) Measured non-spin-flip reflectivities (shapes) and calculated fits to the data (solid lines), assuming a *graded* magnetization.

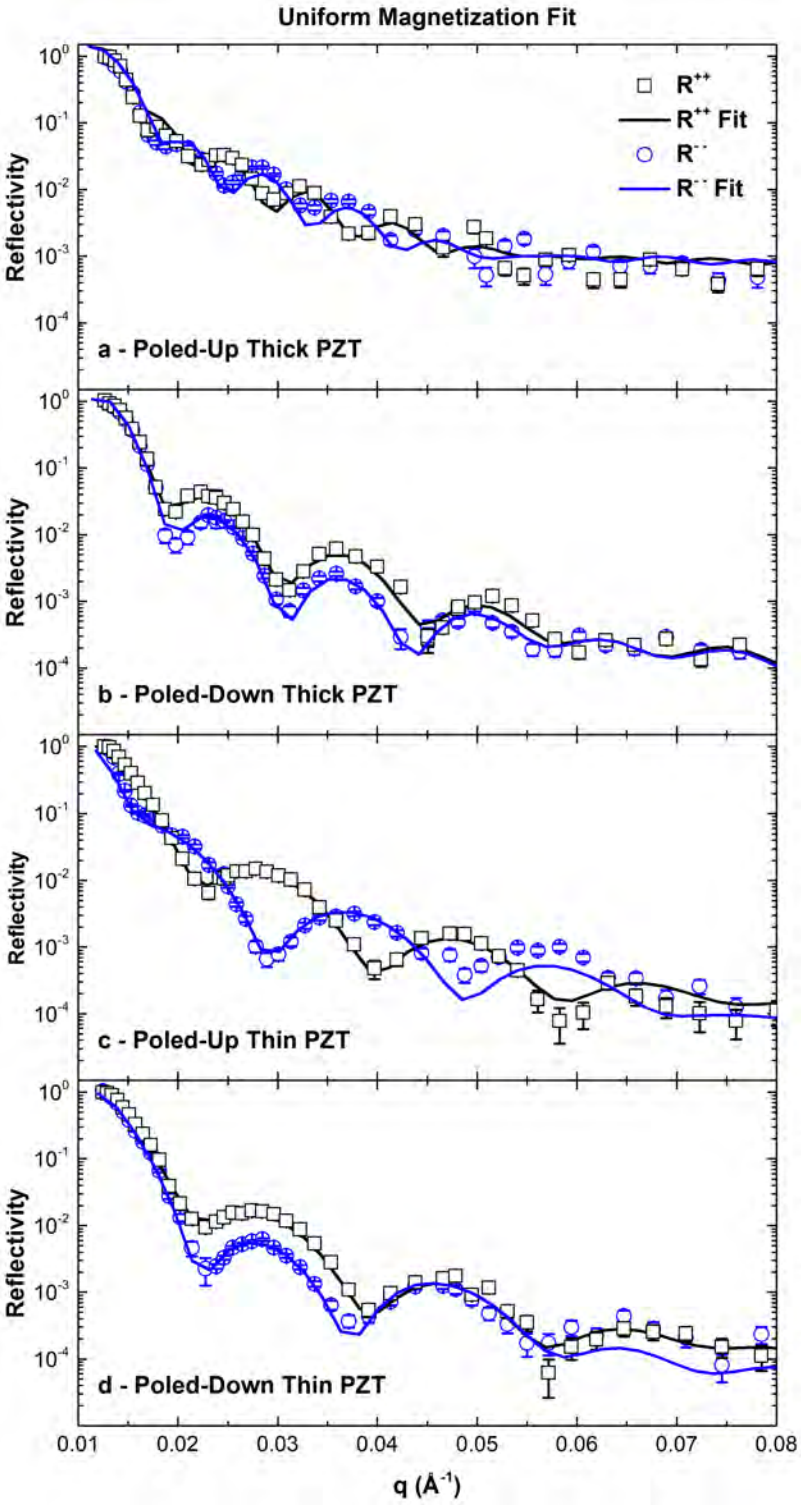

Figure C.8: (A-D) Measured non-spin-flip reflectivities (shapes) and calculated fits to the data (solid lines), assuming a *uniform* magnetization.

C.3 Experimental Methods

$SrRuO_3$ and $Pb(Zr_{0.2}Ti_{0.8})O_3$ films were grown by PLD at 635 °C at 100 and 200 mTorr pO_2, with laser repetition rates of 12 and 3 Hz, and laser fluences of 1.75 and 2 J cm^{-2}, respectively. The $La_{0.7}Sr_{0.3}MnO_3$ layers were grown at 650 °C at 200 mTorr of oxygen with a laser repetition rate of 2 Hz and a fluence of 1.5 J cm^{-2}. Films were then cooled to room-temperature in 760 Torr pO_2.

The crystallinity of the as-grown films was measured by XRD with Cu K_α radiation ($\lambda = 0.15418$ nm) on a Panalytical Empyrean diffractometer. Reciprocal space maps were made around the STO 103 diffraction condition. Layer thickness was studied by XRR as measured on a Rigaku SmartLab diffractometer.

Bulk magnetometry was conducted with a Quantum Design VSM at 305 K along the [100] and [110] in-plane substrate directions, with no discernable difference in hysteresis. T_C was measured in the range of 310–350 K under an applied in-plane magnetic field of 100 Oe. An Arrott-Belov analysis was conducted to determine T_C, assuming self-consistent samples.

PNR was conducted at 298 K with an in-plane magnetic field of 1 T applied along the [100] substrate direction. Non-spin-flip specular reflectivites were measured from $q = 0.005 - 0.1$ Å^{-1}. The reflectivity data were then fit with the ReflPak software package and refined in conjunction with XRD. A fit was conducted with uniform magnetization in the LSMO layers and a second fit was conducted in which the magnetization was allowed to vary. The latter resulted in a better fit to the measured spin asymmetry, particularly at higher q.

Samples were prepared for TEM by conventional mechanical polishing and ion milling. HRTEM images were captured at 200 keV on a JEOL 2100 LaB_6. BF-STEM and STEM-HAADF micrographs were also captured on a C_S-corrected FEI Titan STEM operating at 300 keV. EELS maps and HAADF images were measured on a C_S-corrected Nion UltraSTEM™100 operating at 100 keV, with a convergence angle of 30 mrad and an effective energy resolution of 0.6–0.7 eV.[412] The background was removed from each scan using a power law fit and spectra were extracted from each map row-by-row with a $\sim 0.1\times$ 0.8–1 nm^2 window. Hartree-Slater cross-sections were subtracted from each edge and the spectra were processed with the EELSTools package in the Digital Micrograph to extract Mn $L_{2,3}$ ratios from the

positive component of the second derivative.[413]

Cation displacements were determined from a series of 10–40 STEM-HAADF acquisitions, which were captured at 5 μs intervals and cross-correlated and averaged with the ImageJ program with the StackReg plugin. Image simulations along the PZT [100] direction were conducted with the multislice method in the QSTEM program.[194] This allows us to achieve a precision to measure the atomic displacements better than ∼8 pm.[306] A 69 × 70 × 160 supercell consisting of 80 slices was used. A 400 × 400 pixel array with a 0.05 × 0.05 Å^2 resolution and 20 × 20 Å^2 window size was used, along with the imaging parameters from the microscope ($V = 100$ kV, $C_3 = 0.005$ mm, $C_C = 1$ mm, convergence angle = 30 mrad, collection angle = 86–190 mrad). Final simulations were conducted with 30 thermal diffuse scattering (TDS) runs, a source size of 1.1 Å and an oversampling of 10.

GPA was conducted on STEM-HAADF and HRTEM images displaying minimal drift or scan error. First maps of local reciprocal lattice vectors corresponding to out-of-plane (g_1) and in-plane (g_2) directions were constructed. The ratio of these two maps (g_2/g_1) then gives the local c/a.[414] The line profiles shown in Figure 5.8 were measured by integrating 3–5 nm in-plane to minimize noise. It should be noted that local contrast and thickness fluctuations can give rise to local spikes in the measured ratio, so we only discuss broader trends in c/a.

To calculate in- (ε_{xx}) and out-of-plane (ε_{yy}) LSMO strains, references were chosen in either the STO or PZT layers—in the latter the measured strain values have been shifted to account for the average strain across the PZT layer. The measured strains in the top LSMO layer were converted relative to bulk LSMO according to

$$\varepsilon_{relative} = \left(\varepsilon_{measured} + \frac{c_{STO,bulk} - c_{LSMO,bulk}}{c_{STO,bulk}} \right) \frac{c_{STO,bulk}}{c_{LSMO,bulk}} \tag{C.1}$$

where $c_{STO,bulk} = 3.905$ Åand $c_{LSMO,bulk} = 3.87$ Å. T_C was estimated from these GPA strains using the empirical model of Millis *et al.*[162]

$$T_C(\varepsilon) = T_C(\varepsilon = 0) \left(1 - \alpha \varepsilon_B - \frac{1}{2} \Delta \varepsilon_{JT}^2 \right) \tag{C.2}$$

where $\varepsilon_B = (2\varepsilon_{xx} + \varepsilon_{yy})$ and $\varepsilon_{JT} = \sqrt{2/3}(\varepsilon_{yy} - \varepsilon_{xx})$. $T_C(\varepsilon = 0)$ is the bulk LSMO T_C of ~360 K while α and Δ are empirical constants that represent the weighting of the bulk strain and Jahn-Teller distortion of MnO_6 octahedra, respectively. Typical values are $\alpha \approx 10$ and $\Delta \approx 270$.[318]

DFT calculations were performed within the spin-polarized generalized gradient approximation (GGA) plus Hubbard-U method as implemented in the Quantum-ESPRESSO package version 5.0.[415] The Cococcioni and de Gironcoli approach[416] was followed to include an effective Hubbard term of 3 eV for unstrained LSMO and 2 eV for LSMO on STO to accurately treat the correlated Mn 3d electrons. The core and valence electrons were treated with the ultrasoft pseudopotential[417] and the PBE exchange-correlation functional.[418,419] The Brillouin-zone integrations were performed with a Marzari-Vanderbilt smearing[420] of 0.02 Ry over a 7 × 7 × 5 Monkhorst-Pack k-point mesh[421] centered at Γ, and a 60 Ry plane-wave cut-off. For density of states (DOS) calculations, a denser 14 × 14 × 12 Monkhorst-Pack k-point mesh sampling was used. Atomic positions were allowed to converge until the Hellmann-Feynman forces became less than 2 meV $Å^{-1}$. Structure optimization was performed using the Broyden-Fletcher-Goldfarb-Hanno (BFGS) algorithm. The Ma *et al.* approach was used to simulate the crystal structure of LSMO.[422] P was calculated using the formula,

$$P = \frac{n_{x^2-y^2} - n_{z^2}}{n_{x^2-y^2} + n_{z^2}} \tag{C.3}$$

where $n_{x^2-y^2}$ and n_{z^2} are the area under the partial density of states spectra of $d_{x^2-y^2}$ and d_{z^2} orbitals respectively (for both spins) within the energy window from the Fermi level to -8 eV below it. The nearest-neighbor exchange coupling constant J_0 was calculated within the mean-field approximation[319,320] with,

$$J_0 = \frac{E_F - E_{AFM-A}}{\frac{1}{2}\left(\sum S_1^F S_2^F - \sum S_1^{AFM-A} S_2^{AFM-A}\right)} \tag{C.4}$$

where E_F and E_{AFM-A} are the total energies (eV) of spin-polarized FM ordered and spin-polarized A-type AF ordered calculations, respectively, S_1 is the calculated atomic magnetic moment of Mn(I) atom, and S_2 is the calculated atomic magnetic moment of Mn(II) atom. From J_0, $\hat{T}_C$ was estimated by the mean-

field theory approximation $\hat{T}_C = \frac{2}{3}S(S+1)\frac{J_0}{k_B}$ [319,320], where $S = \left(4 * S_1^F) + (2 * S_2^F)\right)/6$ is the weighted average of the magnetic moments of Mn in the FM spin order configuration.

Appendix D: Screening-Induced Magnetic Phase Gradients at LSMO / PZT Interfaces

D.1 Electron Energy Loss Spectroscopy – O K Edge

In addition to the measurements of the O K pre- to main-peak separation ($\Delta E_{O(b-a)}$) described in Section 6.4, we also measure the relative intensity of the O K edge pre-peak in the vicinity of the PZT interface. This is another well-known indicator of changing valence and density of states in the manganites.[197] As shown in Figure D.1, the relative pre-peak intensity of the bottom LSMO layer fluctuates over a 1–1.5 nm region at the interface, but deviates only slightly from the bulk value of ∼0.62. In contrast, the top LSMO layer shows a significant change over a ∼2 nm region at the interface. There is a large increase in pre-peak intensity from a bulk value of ∼0.58 to ∼0.69 at the interface. This suggests that at the top interface excitations to $2t_{2g}^{\downarrow}$ states increase. This again points toward an asymmetry in the spatial extent of screening about the PZT, as well as a changing local density of states at the interface, in agreement with our other EELS data.[423]

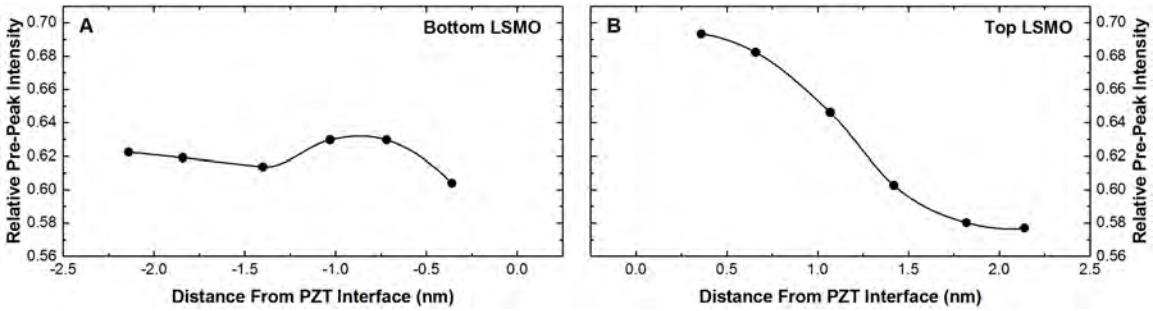

Figure D.1: Relative intensity of the O K pre-peak as a function of position for the bottom (A) and top (B) LSMO / PZT interfaces. There is a significant increase in the pre-peak intensity of the top layer near the PZT interface, which is spread out over a ∼2 nm distance. This figure is a combination of two scans from different parts of the film.

D.2 Angle-Resolved X-ray Photoelectron Spectroscopy

Because of the difficulty in quantifying bulk valence from STEM-EELS, we have conducted angle-resolved X-ray photoelectron spectroscopy (XPS) on the sample. This technique allows us to measure valence in the bulk as well as closer to the top LSMO / PZT interface. As shown in Figure D.2, a shift of ∼0.2 eV was

measured in the Sr 3*d* peak, along with a shift in the binding energy of the Mn $2p_{3/2}$ and $2p_{1/2}$ spin-orbit doublet, indicating a transition from Mn^{3+} to Mn^{4+} oxidation state in the interface region.[424–426] From this we calculate a reduction in Mn^{3+} / Mn^{4+} ratio from ∼2.3 to ∼1.5, in excellent agreement with our STEM-EELS results.

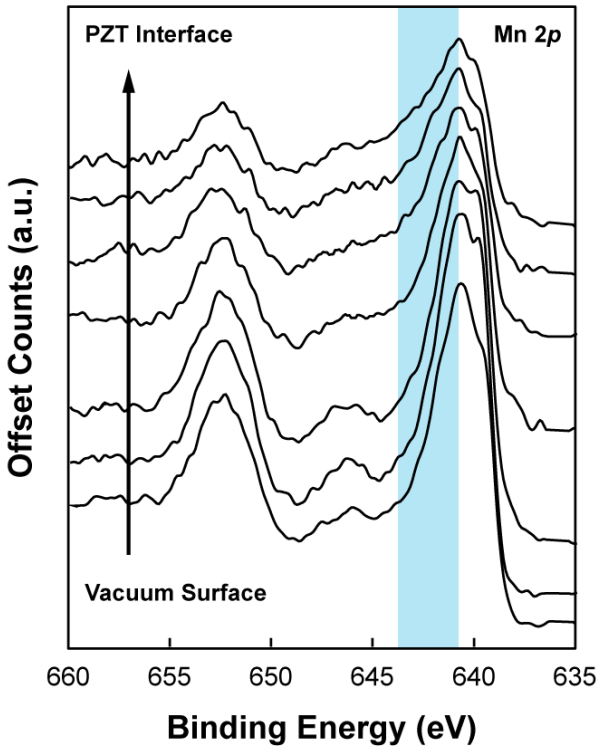

Figure D.2: Angle-resolved X-ray photoelectron (AR-XPS) spectra showing a shift in Mn 2*p* spin-orbit doublet binding energy near the LSMO / PZT interface. We note the presence of a weak shake up satellite near ∼647 eV, indicating a Mn^{2+} species arising from contamination.

D.3 Local Mapping of Ferroelectric Polarization

The local ferroelectric polarization at the LSMO / PZT interface was estimated from STEM-HAADF images following the method described by Jia *et al.*[304] STEM-HAADF images were first processed using the Jitterbug program.[427] Image contrast was then enhanced using the ImageJ program[428] and a series of line profiles were collected normal to the interface. The positions of each atomic column were fitted using Gaussian functions in OriginPro and the error of each fit was calculated. We find that this error is < 1 pm for each fitted position. These fitted peak positions were then used in the following calculation.

We first assume that the Ti and O cations are shifted in the same direction, as is the case for $PbTiO_3$.[304,429] We are then able to estimate the ferroelectric polarization (P_S) through the linear relation,[304]

$$P_S = \kappa \Delta_{Ti} \tag{D.1}$$

where κ is a constant with units of $\mu C\ cm^{-2}\ nm^{-1}$. Following Jia *et al.*,[304] it can be shown that,

$$P_S = \kappa(\delta_O - \delta_{Ti}) \tag{D.2}$$

and that,

$$\delta_O = \frac{\kappa - 1,390}{\kappa - 2,275}\delta_{Ti} \tag{D.3}$$

For bulk $PbTiO_3$ this yields $\kappa = 2,726\ \mu C\ cm^{-2}\ nm^{-1}$ and the following relation,

$$P_S = 2.96(\kappa\delta_{Ti}) \tag{D.4}$$

Using the values of δ_{IL} and δ_{IS} measured from our STEM-HAADF images, we are able to estimate the relative displacement of the Ti^{4+} cations as,

$$\delta_{Ti} = \frac{\delta_{IL} - \delta_{IS}}{2} \tag{D.5}$$

which we substitute into Equation D.4 to estimate the local polarization. These various displacements are schematically illustrated in Figure D.3. The ferroelectric polarization measurements presented in the main text is an average of three to five positions parallel to the LSMO / PZT interface.

D.4 Density Functional Theory

We explored three $La_{1-x}Sr_xMnO_3$ compositions, where x = 0.2, 0.3, and 0.4. When x = 0.2, 0.3, and 0.4, the nominal valence of Mn atoms are 3.2, 3.3, and 3.4, respectively. All compositions have

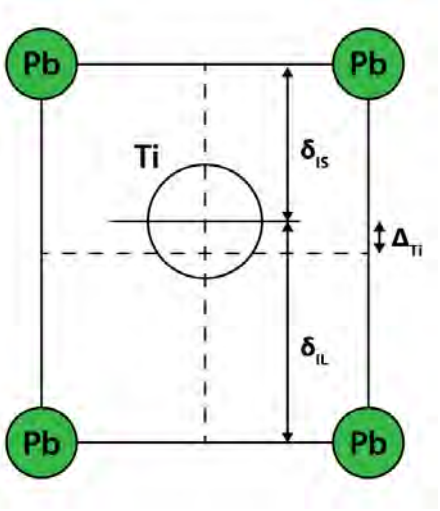

Figure D.3: Illustration of the PZT unit cell and the displacements used to calculate the ferroelectric polarization from STEM-HAADF images. δ_{IS} and δ_{IL} correspond to the short and long axes of Ti^{4+} cations, respectively, while Δ_{Ti} refers to the absolute vertical displacement of the Ti^{4+} cations relative to the center of the unit cell. After Jia *et al.*[304]

a rhombohedral crystal structure (space group $R\bar{3}c$), but they differ in the magnitude of octahedral rotations (see Table D.1). The exact crystal structure data were taken from the literature. The $R\bar{3}c$ space group dictates that the La and Sr atoms are randomly distributed in the lattice. Therefore, the La / Sr partial site occupancies were simulated by constructing a "fictititous" atom; in this approach, we assume a pseudopotential cutoff radius corresponding to the La atom, but we modify its valence to mimic the "nominal" charge corresponding to the $La_{1-x}Sr_x$ partial occupancy. In our DFT calculations, we neither optimize the cell shape nor the internal coordinates. We note that in an octahedral crystal field (such as MnO_6 octahedra in a perovskite), the Mn^{3+} and Mn^{4+} cations have $3d^4$, $t_{2g}^3 e_g^1$ and $3d^3$, t_{2g}^3 electronic configurations, respectively. As a result, the Mn^{3+} and Mn^{4+} cations are expected to have atomic magnetic moments (Mn_μ) of 4 and 3 μ_B, respectively. However, hybridization between Mn $3d$ and O $2p$ states could cause a slight reduction in the Mn_μ value. In $La_{1-x}Sr_xMnO_3$ series, as the concentration of hole-doping (x) increases, the Mn_μ is expected to decrease. We tested the validity of the "fictitious" atom approximation by comparing the Mn_μ in the three compositions. In Table D.1, the crystallographic and magnetic data for the three compositions in FM spin order are given. As expected, the Mn_μ value decreased with increasing x, suggesting that our "fictitious" atom approximation is valid.

Table D.1: Theoretically explored LSMO compositions. The Mn atomic magnetic moments (Mn_μ) are in Bohr magnetons (μ_B) units. The rotation amplitude correspond to out-of-phase MnO_6 rotations ($a^-a^-a^-$ in Glazer notation) in Ångström (Å) units.

x	Mn_μ (μ_B)	Rotation amplitude (Å)
0.2	3.397	0.39
0.3	3.288	0.40
0.4	3.206	0.45

D.5 Experimental Methods

$PbZr_{0.2}Ti_{0.8}O_3$ films were grown by PLD at 635 °C at 100 and 200 mTorr pO_2, with laser repetition rates of 12 and 3 Hz, and laser fluences of 1.75 and 2 J cm^{-2}, respectively. The $La_{0.7}Sr_{0.3}MnO_3$ layers were grown at 650 °C at 200 mTorr of oxygen with a laser repetition rate of 2 Hz and a fluence of 1.5 J cm^{-2}. Films were then cooled to room-temperature in 760 Torr pO_2.

Samples were prepared for TEM by conventional mechanical polishing and ion milling. HRTEM images were captured at 200 keV on a JEOL 2100 LaB_6. EELS maps and STEM-HAADF images were collected on a C_S-corrected Nion UltraSTEM™100 operating at 100 keV, with a convergence angle of 30 mrad and an effective energy resolution of 0.4–0.7 eV (depending on the energy dispersion used: a higher dispersion was chosen for improved precision on the energy shift measurements, specifically for the O K and Mn $L_{2,3}$ fine structure analysis, while lower dispersions allowed for detection of the largest possible range of edges for overall chemical profiling of the films).[412] The background was removed from each scan using a power law fit. The spectra were offset to the known onset of the O K edge. To improve the signal-to-noise ratio of the HAADF data while minimizing sample damage, a high-speed time series was recorded (5 µs per pixel). This data set was first rigid registered to eliminate any sample or stage drift.* High frequency scan-noise was then compensated using the Jitterbug software;† importantly the scan-noise was compensated in each individual frame of the series before averaging across the series.[427] The data were not smoothed or filtered in any way. Measurements of local ferroelectric polarization are described in Appendix D.3.

*L. Jones *et al.* "Smart Align – A New Tool for Robust Rigid and Non-Rigid Registration of STEM Data." In preparation.
†Available from HREM Research (`http://www.hremresearch.com`).

In our DFT calculations, we explored both FM and *A*-type AF spin configurations. In AF spin order, the in-plane Mn atoms are FM aligned, whereas the out-of-plane Mn atoms are AF coupled to one another. Semicore 3*s* and 3*p* states were included in the valence electron electron configuration for the Mn atom.[‡] We used a 90 Ry plane-wave cutoff for the wavefunctions, an effective Hubbard-U value of 2 eV to treat the correlated Mn 3*d* electrons, the Marzari-Vanderbilt smearing method[430] with a width of 0.02 Ry, a Monkhorst-Pack $6\times6\times3$ k-grid[431] centered at Γ for the self-consistent field (scf) calculation, a 10^{-8} eV convergence threshold for the total energy in the scf calculation, and a $4\times4\times4$ mesh with 64 k-points in the irreducible Brillouin zone for the O K edge XAS calculation. We introduced a core-hole into the O-pseudopotential of the absorbing atom, which we compensated in our scf calculation by adding a background charge of $+1e$. We used a $2\times1\times1$ supercell and a [100] X-ray polarization vector direction to mimic our EELS experiment. Additional calculation details for the O K edge spectra include: a 0.5 eV broadening parameter, a 10^{-5} eV convergence threshold for the Lanczos method, and a 900 Ry cutoff for the kinetic energy.

PNR was conducted at 298 K with an in-plane magnetic field of 1 T applied along the [100] substrate direction on the Magnetism Reflectometer at the Spallation Neutron Source, Oak Ridge National Laboratory. Non-spin-flip specular reflectivites were measured from $q = 0.005-0.1$ Å^{-1}. The reflectivity data were then fit with the ReflPak software package[432] and refined in conjunction with XRD data. A fit was conducted with uniform magnetization in the LSMO layers and a second fit was conducted in which the magnetization was allowed to vary. It was found that the some variation in the chemical scattering length density near the surface was needed to fit the data most accurately.

[‡]For La, Mn, and O atoms we used the valence electron configuration of $5s^25p^66s^25d^1$, $3s^23p^63d^54s^2$, and $2s^2p^4$, respectively.

Vita

Steven Richard Spurgeon

Contact Information

Drexel University, Department of Materials Science and Engineering
3141 Chestnut Street
Philadelphia, Pennsylvania, United States 19104

cell: +1 719 330 0441
email: spurgeon@drexel.edu
web: www.stevenspurgeon.com

Dissertation Topic

Studied interfacial magnetoelectric coupling in thin film oxide heterostructures using transmission electron microscopy and polarized neutron reflectometry. Developed *in situ* electrical biasing techniques for polarized neutron scattering and vibrating sample magnetometry to correlate local atomic structure and chemistry to induced magnetization.

Education

Drexel University — **Philadelphia, PA**

Ph.D. in Materials Science and Engineering — June 2009 – June 2014

Department of Defense NDSEG Fellow
National Science Foundation IGERT Fellow
Advisor: Mitra Taheri, Ph.D.

Carnegie Mellon University — **Pittsburgh, PA**

B.S. in Materials Science and Engineering — August 2005 – May 2009

Professional Experience

National Institute of Standards and Technology | Center for Neutron Research — **Gaithersburg, MD**

Visiting Researcher — 2010 – 2014

Developed a first-of-its-kind *in situ* electrical biasing technique for polarized neutron reflectometry.
Advisor: Brian Kirby, Ph.D.

Oak Ridge National Laboratory | Spallation Neutron Source — **Oak Ridge, TN**

Visiting Researcher — 2011 – 2012

Collaborated to apply electric fields to manganite thin films during neutron measurements on the Magnetism Reflectometer.
Advisor: Valeria Lauter, Ph.D.

Drexel University | Department of Materials Science — **Philadelphia, PA**

Teaching Assistant — 2009 – 2013

Graded assignments, taught lectures, ran laboratory sessions for several dozen students, and planned experiments.
Instructor: Mitra Taheri, Ph.D.

Carpenter Specialty Alloys | High Temperature Alloys Research — **Reading, PA**

Metallurgy Intern — 2008

Conducted magnetic, mechanical, and chemical testing of new magnetic steel alloys and wrote interdepartmental whitepaper on magnetic product lines.
Advisor: Paul Novotny, M.S.

Carnegie Mellon University | Department of Materials Science — **Pittsburgh, PA**

Senior Design Project — 2008 – 2009

Studied synthesis and thermomechanical processing of Fe-Co nanocomposite ribbons, which were directly implemented in a production setting.
Advisor: Michael McHenry, Ph.D.

Research Assistant — 2007 – 2008

Studied synthesis of $Sr_2Nb_2O_7$ and $La_2Ti_2O_7$ reduced oxides using pulsed laser deposition. Deposited films, fabricated mixed oxide targets, and treated substrate surfaces.
Advisor: Paul Salvador, Ph.D.

Professional Experience

University of Colorado | Liquid Crystals Materials Research Center — **Boulder, CO**

National Science Foundation Research Experiences for Undergraduates (REU) Intern — 2007

Engineered anisotropic lyotropic liquid crystal "salt-bridge" for Li-ion polymer batteries.
Advisor: Douglas Gin, Ph.D.

Honors and Awards

Gold Graduate Student Research Award, Materials Research Society Fall Meeting	2013
Second Place Poster Award, Microscopy and Microanalysis Conference	2013
Presidential Student Award, Microscopy Society of America	2013
GMAG Travel Award, American Physical Society March Meeting	2013
Travel Award, American Conference on Neutron Scattering	2012
Forum on Graduate Student Affairs Travel Award, American Physical Society	2012
National Defense Science & Engineering (NDSEG) Fellowship, Department of Defense	2011–2014
School on Neutron and X-Ray Scattering Scholarship, Argonne + Oak Ridge National Laboratories	2010
Axel-Madsen Conference Grant, Center for Powder Metallurgy Technology	2010
SMART Fellowship Semi-Finalist, Department of Defense	2010
School on High Resolution Electron Microscopy Scholarship, Arizona State University	2010
IGERT Fellowship, National Science Foundation	2009–2011
Provost's Fellowship, Drexel University	2009–2011
"Steel Engineering Education Link" Scholarship, Assoc. of Iron and Steel Technology	2007–2009
Chairperson's Educational Assistance Scholarship, ASM International	2007

Research Grants

Carnegie Mellon University — Pittsburgh, Pennsylvania

Small Undergraduate Research Grant (SURG) — **2007**

"Synthesis of oxynitride ABO_2N thin films using a two-step processing approach."

Patents

Taheri, M.L., Sunday, K.J., Spurgeon, S.R., and S.J. May. (2013). "Soft composites for electric motors." U.S. Provisional Patent Application № 61/921,030.

Skills and Techniques

Instrumentation Design: Constructed a magneto-optical Kerr effect (MOKE) magnetometer with *in situ* electrical biasing capability for dynamic measurements of magnetoelectric thin films

Materials Characterization: JEOL JEM2100 Transmission Electron Microscope; FEI Strata DB235 Dual Beam Focused Ion Beam; FEI XL30 Scanning Electron Microscope; Rigaku SmartLab X-Ray Diffractometer

Magnetic Characterization: Quantum Design PPMS and MPMS; Magneto-Optical Kerr Effect Magnetometer; NIST NCNR PBR Polarized Neutron Reflectometer; ORNL SNS Magnetism Reflectometer

Materials Analysis: OOMMF, ReflPak, GenX, Origin Pro, CrystalMaker, CrystalDiffract, SingleCrystal

3D Modeling and Illustration: SketchUp, AutoCAD, Adobe Photoshop, Adobe InDesign, Adobe Illustrator

Programming: C++, Java, Mathematica, HTML, CSS, Adobe Dreamweaver

Professional Affiliations

Materials Research Society Member
Microscopy Society of America Member
Reviewer for MRS Fall Conference Proceedings
Former MAGNET Graduate Student Society Officer

IEEE / IEEE Magnetics Society Member
American Physical Society Member
Reviewer for IEEE Transactions on Magnetics
Former ASM Honor Society Vice President

Community Outreach

Materials Research Society Bulletin Contributing Writer	2011 – Present
Philadelphia Science Festival Volunteer	2013
Philly Materials Science and Engineering Day Guide	2011 – 2014
NSF Research Experiences for Undergraduates Program Reviewer	2011
Drexel University High School and Freshman Visit Days Guide	2010 – 2013
Undergraduate Senior Project Mentor	2009 – 2014

Peer-Reviewed Publications

Spurgeon, S.R., Balachandran, P.V., Kepaptsoglou, D.M., Damodaran, A.R., Karthik, J., Nejati, S., Jones, L., Ambaye, H., Lauter, V., Ramasse, Q.M., Lau, K.K.S., Martin, L.W., Rondinelli, J.M., and M.L. Taheri. "Polarization screening-induced magnetic phase gradients at complex oxide interfaces." *Nature Communications*, In review.

Spurgeon, S.R., Sloppy, J.D., Kepaptsoglou, D.M., Balachandran, P.V., Nejati, S., Karthik, J., Damodaran, A.R., Johnson, C.L., Ambaye, H., Goyette, R., Lauter, V., Ramasse, Q.M., Idrobo, J.C., Lau, K.K.S., Lofland, S.E., Rondinelli, J.M., Martin, L.W., and M.L. Taheri. "Thickness-dependent crossover from charge- to strain-mediated magnetoelectric coupling in ferromagnetic / piezoelectric oxide heterostructures." *ACS Nano*, 8.1. (2014): 894-903. DOI:10.1021/nn405636c

Spurgeon, S.R., Sloppy, J.D., Tao, R., Klie, R.F., Lofland, S.E., Baldwin, J.K., Misra, A., and M.L. Taheri. "A study of the effect of iron island morphology and interface oxidation on the magnetic hysteresis of Fe – MgO (001) thin film composites." *Journal of Applied Physics*, 112 (2012): 013905. DOI:10.1063/1.4730630

Carroll, K.J., Huba, Z., Spurgeon, S.R., Qian, M., Khanna, S.N., Hudgins, D.M., Taheri, M.L., and E.E. Carpenter. "Magnetic properties of Co_2C and Co_3C nanoparticles and their assemblies." *Applied Physics Letters*, 101 (2012): 012409. DOI:10.1063/1.4733321

Carroll, K.J., Hudgins, D.M., Spurgeon, S., Kemner, K.M., Mishra, B., Boyanov, M.I., Brown, L.W., Taheri, M.L., and E.E. Carpenter. "One-pot aqueous synthesis of Fe and Ag core/shell nanoparticles." *Chemistry of Materials*, 22.23 (2010): 6291–6296. DOI:10.1021/cm101996u

Havelia, S., Balasubramaniam, K., Spurgeon, S., Cormack, F., and P. Salvador. "Growth of $La_2Ti_2O_7$ and $LaTiO_3$ thin films using pulsed laser deposition." *Journal of Crystal Growth*, 310.7–9 (2008): 1985–1990. DOI:10.1016/j.jcrysgro.2007.12.006

Book Reviews

Spurgeon, S.R. "Experimental Neutron Scattering, by B.T.M. Willis and C.J. Carlile.." *Contemporary Physics*, 55.3 (2014). DOI:10.1080/00107514.2014.907352

Invited Talks

Spurgeon, S.R. "Static and Dynamic Studies of Charge- and Strain-Mediated Magnetoelectric Coupling in Ferromagnetic / Piezoelectric Oxide Heterostructures Using Polarized Neutron Reflectometry and Transmission Electron Microscopy." Pacific Northwest National Laboratory. Richland, WA. 27 Jun 2014.

Spurgeon, S.R. "Static and Dynamic Studies of Charge- and Strain-Mediated Magnetoelectric Coupling in Ferromagnetic / Piezoelectric Oxide Heterostructures Using Polarized Neutron Reflectometry and Transmission Electron Microscopy." National Institute of Standards and Technology – Center for Neutron Research. Gaithersburg, MD. 10 Feb 2014.

Contributed Talks

Spurgeon, S.R., McDonald, I.J., Huang, E., Vasudevan, R., Lofland, S.E., Kirby, B.J., Valanoor, N., and M.L. Taheri. "*In Situ* Electrical Biasing Studies of Interfacial Magnetoelectric Coupling in $La_{1-x}Sr_xMnO_3$ – $PbZr_xTi_{1-x}O_3$ Thin Film Oxide Heterostructures." American Physical Society March Meeting, 3 Mar 2014.

Spurgeon, S.R., McDonald, I.J., Huang, E., Vasudevan, R., Lofland, S.E., Kirby, B.J., Valanoor, N., and M.L. Taheri. "*In Situ* Electrical Biasing Studies of Interfacial Magnetoelectric Coupling in $La_{1-x}Sr_xMnO_3$ – $PbZr_xTi_{1-x}O_3$ Thin Film Oxide Heterostructures." Materials Research Society Fall Meeting, 2 Dec 2013.

Spurgeon, S.R., Sloppy, J.D., Kepaptsoglou, D.M., Balachandran, P.V., Nejati, S., Karthik, J., Damodaran, A.R., Johnson, C.L., Ambaye, H., Goyette, R., Lauter, V., Ramasse, Q.M., Idrobo, J.C., Lau, K.K.S., Lofland, S.E., Rondinelli, J.M., Martin, L.W., and M.L. Taheri. "Graduate Student Award Session: Thickness-Dependent Crossover from Charge- to Strain-Mediated Magnetoelectric Coupling in Ferromagnetic/Piezoelectric Oxide Heterostructures." Materials Research Society Fall Meeting, 3 Dec 2013.

Spurgeon, S.R., Sloppy, J.D., Kepaptsoglou, D.M., Balachandran, P.V., Nejati, S., Karthik, J., Damodaran, A.R., Johnson, C.L., Ambaye, H., Goyette, R., Lauter, V., Ramasse, Q.M., Idrobo, J.C., Lau, K.K.S., Lofland, S.E., Rondinelli, J.M., Martin, L.W., and M.L. Taheri. "Thickness-Dependent Crossover from Charge- to Strain-Mediated Magnetoelectric Coupling in Ferromagnetic/Piezoelectric Oxide Heterostructures." Materials Research Society Fall Meeting, 3 Dec 2013.

Jablonski, M., Spurgeon, S.R., Marshall, M.S.J., Arredondo, M., Ahn, C.H., Martin, L.W., and M.L. Taheri. "*In Situ* Transmission Electron Microscopy Studies of Domain Wall Motion in Ferroelectric Perovskite Oxides." Materials Research Society Fall Meeting, 4 Dec 2013.

Spurgeon, S.R., Sloppy, J.D., Kepaptsoglou, D.M., Balachandran, P.V., Nejati, S., Karthik, J., Damodaran, A.R., Johnson, C.L., Ambaye, H., Goyette, R., Lauter, V., Ramasse, Q.M., Idrobo, J.C., Lau, K.K.S., Lofland, S.E., Rondinelli, J.M., Martin, L.W., and M.L. Taheri. "A combined TEM, STEM-EELS, and neutron reflectometry study of charge- and strain-mediated magnetoelectric coupling in LSMO/PZT thin-film heterostructures." Materials Science and Technology Conference, 8 Oct 2012.

Spurgeon, S.R., Sloppy, J.D., Kepaptsoglou, D.M., Balachandran, P.V., Nejati, S., Karthik, J., Damodaran, A.R., Johnson, C.L., Ambaye, H., Goyette, R., Lauter, V., Ramasse, Q.M., Idrobo, J.C., Lau, K.K.S., Lofland, S.E., Rondinelli, J.M., Martin, L.W., and M.L. Taheri. "A combined TEM, STEM-EELS, and neutron reflectometry study of charge- and strain-mediated magnetoelectric coupling in LSMO/PZT heterostructures." Microscopy and Microanalysis Conference, 2 Aug 2012. DOI:10.1017/S1431927612011415

Spurgeon, S.R., Sloppy, J.D., Nejati, S., Karthik, J., Damodaran, A.R., Johnson, C.L., Ambaye, H., Goyette, R., Lauter, V., Idrobo, J.C., Lau, K.K.S., Lofland, S.E., Martin, L.W., and M.L. Taheri. "A polarized neutron and transmission electron microscopy study of magnetoelectric coupling in thin film PZT-LSMO heterostructures." American Conference on Neutron Scattering, 25 Jun 2012.

Spurgeon, S.R., Sloppy, J.D., Nejati, S., Karthik, J., Damodaran, A.R., Johnson, C.L., Ambaye, H., Goyette, R., Lauter, V., Idrobo, J.C., Lau, K.K.S., Lofland, S.E., Martin, L.W., and M.L. Taheri. "A study of strain- and charge-mediated magnetoelectric coupling in PZT-LSMO heterostructures using transmission electron microscopy and polarized neutron reflectometry." Materials Research Society Fall Meeting, 29 Nov 2011.

Spurgeon, S.R., Lofland, S.E., Misra, A., and M.L. Taheri. "A study of the interfacial magnetic and atomic structure of oxide-coated ferrous powder metals." PowderMet Conference, 20 May 2011.

Spurgeon, S.R., Winkler, C.R., Kirby, B.J., and M.L. Taheri. "A multi-scale analysis of the structural and magnetic properties of oxide coatings for iron powders used in electromagnetic applications." PowderMet Conference, 29 Jun 2010.

S.R. Spurgeon "Engineering anisotropic lyotropic liquid crystal nano-architectures." National Science Foundation Research Experiences for Undergraduates Program. University of Colorado, 9 Aug 2007.

Poster Presentations

Spurgeon, S.R., Sloppy, J.D., Kepaptsoglou, D.M., Balachandran, P.V., Nejati, S., Karthik, J., Damodaran, A.R., Johnson, C.L., Ambaye, H., Goyette, R., Lauter, V., Ramasse, Q.M., Idrobo, J.C., Lau, K.K.S., Lofland, S.E., Rondinelli, J.M., Martin, L.W., and M.L. Taheri. "Evidence for a thickness-dependent crossover from charge- to strain-mediated magnetoelectric coupling in $La_{0.7}Sr_{0.3}MnO_3$ / $PbZr_{0.2}Ti_{0.8}O_3$ thin film oxide heterostructures." Microscopy and Microanalysis Conference, 8 Aug 2013. DOI:110.1017/S1431927613011811

Spurgeon, S.R., Sloppy, J.D., Kepaptsoglou, D.M., Balachandran, P.V., Nejati, S., Karthik, J., Damodaran, A.R., Johnson, C.L., Ambaye, H., Goyette, R., Lauter, V., Ramasse, Q.M., Idrobo, J.C., Lau, K.K.S., Lofland, S.E., Rondinelli, J.M., Martin, L.W., and M.L. Taheri. "Thickness-dependent crossover from charge- to strain-mediated magnetoelectric coupling in $La_{0.7}Sr_{0.3}MnO_3$ / $PbZr_{0.2}Ti_{0.8}O_3$ thin film heterostructures." Drexel University Research Day, 18 Apr 2013.

Spurgeon, S.R., Sloppy, J.D., Kepaptsoglou, D.M., Balachandran, P.V., Nejati, S., Karthik, J., Damodaran, A.R., Johnson, C.L., Ambaye, H., Goyette, R., Lauter, V., Ramasse, Q.M., Idrobo, J.C., Lau, K.K.S., Lofland, S.E., Rondinelli, J.M., Martin, L.W., and M.L. Taheri. "A local study of magnetoelectric coupling in PZT-LSMO thin film heterostructures using transmission electron microscopy and polarized neutron reflectometry." American Physical Society March Meeting, 21 Mar 2013.

McDonald, I.J, Spurgeon, S.R., Beckett, D., May, S.J., and M.L. Taheri. "Development of a unique surface magneto-optical Kerr magnetometer to study correlation of magnetism and structure at iron / oxide interfaces." PowderMet Conference, 11 Jun 2012.

McDonald, I.J, Spurgeon, S.R., Beckett, D., May, S.J., and M.L. Taheri. "Development of a unique surface magneto-optical Kerr effect magnetometer to correlate magnetism and structure in coated ferrous thin films and powders." Materials Research Society Fall Meeting, 29 Nov 2011.

Taheri, M.L., Winkler, C.R., Sloppy, J.D., Spurgeon, S.R., Martin, L.W., Idrobo, J.C., Phatak, C., Wen, J., and D.J. Miller. "A quantitative understanding of domain relaxation behavior in $BiFeO_3$-based multiferroic systems using *in situ* TEM." Materials Research Society Fall Meeting, 28 Nov 2011.

Spurgeon, S.R., Sloppy, J.D, Lofland, S.E., Baldwin, J.K., Misra, A., and M.L. Taheri. "The effect of film morphology and interface structure on the magnetic properties of Fe - MgO (001) thin films." Microscopy and Microanalysis Conference, 9 Aug 2011. DOI:10.1017/S1431927611008099

Sloppy, J.D., Idrobo, J.C., Sundaram, S., Spurgeon, S.R., Winkler, C.R., Valanoor, N., Munroe, P., and M.L. Taheri. "Interfacial chemistry, defects, and strain in multiferroic heterostructures." Microscopy and Microanalysis Conference, 10 Aug 2011. DOI:10.1017/S1431927611007781

Sparber, B.A., Spurgeon, S.R., Hanejko, F.J., and M.L. Taheri. "A study of additive diffusion in ferrous powder metal compacts using scanning electron microscopy and energy dispersive X-ray spectroscopy." PowderMet Conference, 19 May 2011.

Spurgeon, S.R., Kikkawa, J., Baldwin, J.K., Misra, A., and M.L. Taheri. "A structural and magnetic study of interfacial spin coupling in Fe–MgO ferromagnetic-dielectric thin film composites." Materials Research Society Fall Meeting, 19 Nov 2010.

Barr, C.M., Vetterick, G., Scotto D'Antuono, D., Winkler, C.R., Spurgeon, S.R., Kirk, M.A., Knight, R., and M.L. Taheri. "Multi-scale examination of the effect of $\Sigma 3_n$ CSL boundaries on radiation-induced degradation in stainless steels." Materials Research Society Fall Meeting, 19 Nov 2010.

Spurgeon, S.R., Winkler, C.R., Kirby, B.J., Johnson, C.L., and M.L. Taheri. "Correlating interfacial structure and magnetism in Fe–MgO thin films using electron microscopy, X-ray and neutron reflectometry." Microscopy and Microanalysis Conference, 3 Aug 2010.

Spurgeon, S.R., Winkler, C.R., Kirby, B.J., Johnson, C.L., Atthipalli, G., Gray, J., and M.L. Taheri. "A multi-scale correlation of the structural and magnetic properties of complex metal oxide thin film composites." Materials Research Society Spring Meeting, 6 Apr 2010.

MRS Bulletin Articles

S. Spurgeon. "Navy SeaPerch competition spreads STEM awareness." *Materials Research Society Bulletin*, 38 (2013): 780. DOI:10.1557/mrs.2013.246

S. Spurgeon. "Electric field utilized to locally pin magnetic domain walls." *Materials Research Society Bulletin*, 38 (2013): 598. DOI:10.1557/mrs.2013.190

S. Spurgeon. "Epitaxial strain tunes spintronic behavior of $BiFeO_3$." *Materials Research Society Bulletin*, 38 (2013): 529. DOI:10.1557/mrs.2013.164

S. Spurgeon. "Superdiffusive electron transport mediates laser-induced demagnetization." *Materials Research Society Bulletin*, 38 (2013): 296. DOI:10.1557/mrs.2013.89

S. Spurgeon. "Drexel hosts Philly Materials Day." *Materials Research Society Bulletin*, 37 (2012): 888-889. DOI:10.1557/mrs.2012.261

S. Spurgeon. "Spin bag model proposed for room-temperature ferromagnetism in $Sr_3YCo_4O_{10+\delta}$." *Materials Research Society Bulletin*, 37 (2012): 881. DOI:10.1557/mrs.2012.244

S. Spurgeon. "Inverse spin Hall effect observed in silicon." *Materials Research Society Bulletin*, 37 (2012): 186. DOI:10.1557/mrs.2012.69

S. Spurgeon. "Functional ferroelectric tunnel-junction memories demonstrated." *Materials Research Society Bulletin*, 37 (2012): 101. DOI:10.1557/mrs.2012.15

S. Spurgeon. "Room-temperature electrical control of ferromagnetic ordering in cobalt demonstrated." *Materials Research Society Bulletin*, 36 (2011): 953. DOI:10.1557/mrs.2011.316

S. Spurgeon. "Thin-film heterostructures of Fe- and Co-$BaTiO_3$ exhibit interface multiferroicity at room temperature." *Materials Research Society Bulletin*, 36 (2011): 843. DOI:10.1557/mrs.2011.282

S. Spurgeon. "SPM reveals nanoscale understanding of oxygen reactions in fuel cells and batteries." *Materials Research Society Bulletin*, 36 (2011): 741. DOI:10.1557/mrs.2011.248

S. Spurgeon. "A (111)–ordered Sr_2FeRuO_6 superlattice displays room-temperature magnetic ordering." *Materials Research Society Bulletin*, 36 (2011): 478. DOI:10.1557/mrs.2011.161

S. Spurgeon. "Modified SPM allows high resolution mapping of lithium-ion diffusion." *Materials Research Society Bulletin*, 35 (2010): 836. DOI:10.1557/mrs2010.723